Universidad del País Vasco Euskal Herriko Unibertsitatea

NAZIOARTEKO BIKAINTASUN CAMPUSA
CAMPUS DE EXCELENCIA INTERNACIONAL

CIC biomaGUNE
Biomaterialetako Ikerkuntza Kooperatiboko Zentroa
Centro de Investigación Cooperativa en Biomateriales

Towards Near-Infrared Photoactivation of Anticancer Metal Complexes

Emmanuel Ruggiero

2016

Table of Contents

Resumen

La terapia fotodinámica (photodynamic therapy, PDT) es un tratamiento contra el cáncer clínicamente aprobado como alternativa a la tradicional quimioterapia. Esta estrategia terapéutica es mínimamente invasiva y altamente selectiva. Combina oxígeno celular, un profármaco (un derivado de porfirina) y luz roja de baja energía para generar citotoxicidad localizada en el área irradiada. La fotoactivación del profármaco permite el control espacio-temporal de los efectos citotóxicos, disminuye la toxicidad sistémica del tratamiento y limita los efectos secundarios no deseados. Cabe destacar que prácticamente cualquier órgano puede ser irradiado por dispositivos con fibra óptica flexible. Por esta razón, la PDT se puede utilizar para tratar diferentes tipos de cáncer como el de piel, cabeza, cuello, pulmón, páncreas, esófago, vejiga, próstata o neoplasmas.

A pesar de este éxito y de sus prometedores desarrollos, esta fototerapia tiene diversas desventajas, las cuales limitan actualmente su aceptación en clínica como un tratamiento rutinario de quimioterapia. La principal carencia de la PDT es la dependencia de oxígeno en su mecanismo de acción. Dado que los tumores sólidos contienen regiones con muy baja concentración de oxígeno (hipoxia) por lo que las células en dichas zonas resultan ser resistentes a los protocolos de PDT.

Inspirados en la PDT, otras estrategias prometedoras que empleen luz han sido investigadas tales como el uso de complejos metálicos anticancerígenos y fotoactivables.

Los profármacos basados en complejos metálicos usados para fotoquimioterapia deben ser no tóxicos y estables en la oscuridad en condiciones fisiológicas y que al mismo tiempo generen especies citotóxicas una vez que han sido irradiados. Resulta importante mencionar que la quimioterapia de fotoactivación basada en compuestos inorgánicos combina las ventajas de dos tratamientos: la selectividad de la PDT y el uso clínico ya consolidado de la quimioterapia con fármacos de platino. De hecho, los derivados anticancerígenos de platino (p. ej. cisplatino, carboplatino, oxaliplatino) son administrados globalmente a casi la mitad de los pacientes que comienzan un

tratamiento de quimioterapia para el cáncer. Además, los profármacos basados en complejos metálicos fotoactivables ofrecen una ventaja importante: su mecanismo de fototoxicidad es independiente de la presencia de oxígeno.

El principal obstáculo que impide el progreso de la quimioterapia fotoactivable con compuestos inorgánicos hacia fases preclínicas y clínicas es la carencia de buena absorción de luz y reactividad de dichos compuestos en la ventana fototerapéutica (650–1000 nm). Normalmente, requieren luz UV-azul de alta energía para inducir su actividad antineoplástica, pero la activación con UV-azul no es adecuada para aplicaciones terapéuticas debido a su baja penetración en el tejido y el daño celular que tiene a dichas longitudes de onda.

Para abordar esta cuestión, aquí se presenta una estrategia innovadora, en la cual nanopartículas de conversión ascendente (upconverting nanoparticles, UCNPs) son funcionalizadas con profármacos de rutenio y de platino que una vez irradiados con luz de infrarrojo cercano (near infrared, NIR), altamente penetrante en el tejido, conduzca a la generación in situ de especies metálicas activas. UCNPs son nanocristales dopados con lantánidos que se caracterizan por convertir la luz de infrarrojo cercano (980 nm) en luz UV-visible, coincidiendo con la demanda de los complejos metálicos, los cuales requieren una excitación de luz UV-azul de alta energía. Las UCNPs son generalmente nanocristales de $NaYF_4$ o $NaGdF_4$ dopados con lantánidos como Yb, Er y Tm.

El principal objetivo de este trabajo de doctorado es explorar la combinación de las UCNPs y los complejos metálicos como una estrategia viable con el objeto de proporcionar nuevos enfoques en fotoquimioterapia, los cuales están basados en el uso de la luz NIR y de un mecanismo de acción no dependiente de la presencia de oxigeno. Además, las UCNPs presentan características únicas de multimodalidad en imagen (MRI/PET/UCL), lo que hace que estos nanosistemas híbridos (UCNP-complejos metálicos) se podrían usarse con fines terapéuticos y de diagnostico (teranóstica).

El **Capítulo 1** define la validez y limitaciones de la actualmente usada PDT y se ilustra el potencial de los complejos metálicos fotoactivables para los tratamientos antineoplásticos.

El **Capítulo 2** describe la síntesis de las UCNPs y sus propiedades químicas y ópticas. Además, se expone lo descrito hasta ahora sobre el papel que desempeñan las UCNPs en la fotoquímica de los complejos metálicos bajo de irradiación de luz NIR.

El **Capítulo 3** demuestra por primera vez con claras evidencias espectroscópicas que los nanocristales $NaYF_4:Yb^{3+}/Er^{3+}$ pueden desencadenar la fotoquímica de un complejo metálico. En concreto, la luz de 980 nm se usa para inducir la fotodisociación del ligando piridilo en *cis*-$[Ru^{II}(bpy)_2(py)_2]Cl_2$ (donde bpy = 2,2'-bipiridina, py = piridina) en presencia de las UCNPs. Este complejo de Ru, no exhibiendo ninguna actividad biológica, resulta ser un modelo interesante para otros complejos polipiridílicos de rutenio que sí son biológicamente activos.

> *"Near-Infrared Photolysis of a Ru Polypyridyl Complex by Upconverting Nanoparticles" E. Ruggiero, A. Habtemariam, L. Yate, J. C. Mareque-Rivas, L. Salassa, Chem. Commun., 2014, 50, 1715.*

El **Capítulo 4** ilustra la fotoactivación de *cis,cis,trans*-$[Pt^{IV}(NH_3)_2(Cl)_2(O_2CCH_2CH_2CO_2H)_2]$ mediante la excitación con luz NIR de las UCNPs de $NaYF_4:Yb^{3+}/Tm^{3+}@NaYF_4$. El complejo metálico seleccionado es un precursor fotoactivable del cisplatino. Bajo excitación con UVA, el complejo de platino libera dos ligandos axiales succinato y genera fotoproductos de Pt^{IV} y Pt^{II} (p. ej. cisplatino) con actividad antineoplástica. En este caso, *cis,cis,trans*-$[Pt^{IV}(NH_3)_2(Cl)_2(O_2CCH_2CH_2CO_2H)_2]$ fue anclado a la superfície de las UCNPs mediante la funcionalización de un fosfolípido pegilado biocompatible a través de técnicas de bioconjugación. La activación del

complejo de Pt^{IV} inducida con NIR fue un resultado destacable, teniendo en cuenta la ausencia de bandas de absorción de dicho compuesto por encima de 400 nm.

> *"Near-Infrared Activation of an Anticancer Pt^{IV} Complex by Tm-Doped Upconversion Nanoparticles" E. Ruggiero, J. Hernández-Gil, J. C. Mareque-Rivas, L. Salassa, Chem. Commun., 2015, 51, 2091.*

El **Capítulo 5** extiende la fotoactivación inducida por UCNP a otra clase de compuestos de rutenio, denominados complejos con geometría de taburete de piano (piano-stool) Ru^{II}-areno. Para este trabajo, dos nuevos complejos areno de Ru^{II} fueron sintetizados, $[(\eta^6\text{-}p\text{-cym})Ru^{II}(bpy)(m\text{-CCH-Py})][PF_6]_2$ y $[(\eta^6\text{-}p\text{-cym})Ru^{II}(bpm)(m\text{-CCHPy})][PF_6]_2$ (donde *p*-cym = *p*-cimeno, bpm = 2,2'-bipirimidina, y *m*-CCH-Py = 3-etinilpiridina). La fotoquímica de estos derivados fue totalmente caracterizada con diferentes métodos, incluyendo cálculos DFT y medidas de rendimiento cuántico. Al irradiar con luz azul, ambos complejos liberan selectivamente el ligando piridilo y una molécula de agua entra en la esfera de coordinación del rutenio. El derivado bpm $[(\eta^6\text{-}p\text{-cym})Ru^{II}(bpm)(m\text{-CCHPy})][PF_6]_2$ exhibió mayor rendimiento en la fotorreacción por lo que fue elegido para su funcionalización con un brazo fosfonato para decorar la superficie de las UCNPs $NaYF_4:Yb^{3+}/Tm^{3+}@NaYF_4$. El grupo fosfonato tiene un papel importante, ya que tiene buena afinidad por la superficie de la UCNP. El nanosistema UCNP-complejo Ru así obtenido, experimentó la fotoactivación con NIR y produjo los correspondientes fotoproductos que se unen al modelo de base de ADN guanosina 5'-monofosfato.

> *"Upconverting Nanoparticles Prompt Remote Near-Infrared Photoactivation of Ru(II)–Arene Complexes" E. Ruggiero, C. Garino, J. C. Mareque-Rivas, A. Habtemariam, L. Salassa, Chem. Eur. J., 2016, 22, 2801.*

Además de los trabajos arriba mencionados, durante mi doctorado también he contribuido al desarrollo de otros proyectos de investigación y a la preparación de artículos de revisión bibliográfica. Estas actividades fueron herramientas para consolidar mi formación en el área de los compuestos de coordinación fotoactivables y nanopartículas inorgánicas. El resultado de mi participación produjo (no enseñados en esta tesis) 6 artículos publicados en revistas internacionales revisionadas por pares y 1 artículo de divulgación.

"Light Harvesting and Photoemission by Nanoparticles for Photodynamic Therapy" A. G. Arguinzoniz, E. Ruggiero, A. Habtemariam, J. Hernández-Gil, L. Salassa, J. C. Mareque-Rivas, Part. Part. Syst. Charact., 2014, 31, 46.

"Quantum Dot Photoactivation of Pt(IV) Anticancer Agents: Evidence of an Electron Transfer Mechanism Driven by Electronic Coupling" I. Infante, J. M. Azpiroz, N. Gomez Blanco, E. Ruggiero, J. M. Ugalde, J. C. Mareque-Rivas, L. Salassa, J. Phys. Chem. C, 2014, 118, 8712.

"The Photochemistry of Transition Metal Complexes and Its Application in Biology and Medicine" E. Ruggiero, S. Alonso-de Castro, A. Habtemariam, L. Salassa, Struct. Bond., 2014, 165, 69.

"Rare-Earth Doped Colour Tuneable Up-Conversion ZBLAN Phosphor for Enhancing Photocatalysis" J. Méndez-Ramos, P. Acosta-Mora, J. C. Ruiz-Morales, M. Sierra, A. Redondas, E. Ruggiero, L. Salassa, M. E. Borges, P. Esparza, Optical Materials, 2015, 41, 98.

"Nuevos Materiales de Conversión Ascendente para Fotoquimioterapia con Complejos de Metales de Transición" S. Alonso-de Castro, E. Ruggiero, L. Salassa, CIC Network Ciencia y Tecnología, 2015, 15, 40.

"Photorelease of Pyridyl Esters in Organometallic Ru(II) Arene Complexes" A. Habtemariam, C. Garino, E. Ruggiero, S. Alonso-de Castro, J. C. Mareque-Rivas, L. Salassa, Molecules, 2015, 20, 7276.

"Upconverting Nanoparticles for the Near Infrared Photoactivation of Transition Metal Complexes: New Opportunities And Challenges In Medicinal Inorganic Photochemistry" E. Ruggiero, S. Alonso-de Castro, A. Habtemariam, L. Salassa, Dalton Trans., 2016, submitted.

Summary

Photodynamic therapy (PDT) is a clinically-approved cancer treatment alternative to traditional chemotherapy. This therapeutic approach is minimally invasive and highly selective. It combines cellular oxygen, a prodrug (porphyrin derivative) and low energy red light to generate localized cytotoxicity in the irradiated area. Light activation of the prodrug allows spatiotemporal control of the cytotoxic effects, decreases systemic toxicity of the treatment and limits unwanted side effects. Importantly, any organs can be virtually irradiated by flexible fiber optic devices. For this reason, PDT can be employed to treat different types of cancer such as skin, head, neck, lung, pancreas, esophagus, bladder, prostate and neoplasms.

Despite its success and promising developments, PDT has a number of drawbacks, which currently limit its clinical acceptance as routine chemotherapeutic treatment. The main shortcoming of PDT is the oxygen dependency of its mechanism of action. As solid tumors contain regions of very low oxygen concentrations (hypoxia), cells in these regions are in fact resistant to PDT protocols.

Inspired by PDT, others strategies based on light activation have been investigated. Among them, the use of photoactivatable anticancer metal complexes is one of the most promising. Metal prodrugs for photochemotherapy obviously must be nontoxic and stable in the dark under physiological conditions, but at the same time, upon light irradiation, they should be capable of generating cytotoxic species. Importantly, the inorganic photochemotherapy approach merges the advantages of two clinical treatments: the selectivity of PDT and the well consolidated clinical use of Pt chemotherapy. Anticancer Pt complexes (e.g. cisplatin, carboplatin, oxaliplatin) are administered globally almost to half of the patients undertaking cancer chemotherapy. Moreover, photoactivatable metal-based prodrugs potentially offer a significant advantage: their phototoxicity mechanism is oxygen independent.

The main obstacles that hamper the progress of inorganic photochemotherapy towards preclinical and clinical stages are the weak light absorption properties and reactivity of metal complexes in the phototherapeutic window (650–1000 nm).

Coordination and organometallic compounds typically require high-energy UV-blue light to induce their antineoplastic activity. UV-blue activation is not ideal for therapeutic applications due to its low tissue penetration and the cellular damage that occur at such wavelengths.

To address this issue, an innovative strategy is presented herein, where Ru and Pt anticancer prodrugs candidates are integrated with upconverting nanoparticles (UCNPs) in order to use near-infrared light (highly penetrating) for the in situ generation of metal-based bioactive species. UCNPs are lanthanide doped nanocrystals which convert near-infrared light (NIR, 980 nm) into UV-visible light, meeting the demand of metal complexes for high-energy UV-blue light excitation. UCNPs are generally $NaYF_4$ or $NaGdF_4$ nanocrystals doped with lanthanides such as Yb, Er and Tm.

The main aim of this Ph.D. work is to explore the combination of UCNPs and metal complexes as viable strategy to provide novel photochemotherapeutic approaches which rely on NIR light and on O_2-independent mechanisms of action. Furthermore, UCNPs have unique multimodal imaging capabilities (UCL/MRI/PET/SPECT) which make hybrid nanosystems (UCNP-metal complexes) encouraging candidates for theranostics (simultaneous therapy and diagnosis).

Chapter 1 defines strengths and limitations of currently used PDT and the potentialities of photoactivatable metal complexes for antineoplastic treatments are illustrated.

Chapter 2 describes the synthesis of UCNPs and their chemical and optical properties. In addition, it reports on the state of art of UCNP-assisted photochemistry of metal complexes upon NIR excitation.

Chapter 3 demonstrates for the first time, with clear spectroscopic evidences that $NaYF_4$:Yb^{3+}/Er^{3+} nanocrystals can trigger the photochemistry of a metal complex. In

particular, 980-nm light is used to induce the photodissociation of the pyridyl ligand in *cis*-$[Ru^{II}(bpy)_2(py)_2]Cl_2$ (where bpy = 2,2'-bipyridine, py = pyridine) in the presence of UCNPs. This Ru complex is an attractive model for biologically active ruthenium polypyridyl complexes.

> *"Near Infrared Photolysis of a Ru Polypyridyl Complex by Upconverting Nanoparticles" E. Ruggiero, A. Habtemariam, L. Yate, J. C. Mareque-Rivas and L. Salassa, Chem. Commun., 2014, 50, 1715.*

Chapter 4 illustrates the photoactivation of *cis,cis,trans*-$[Pt^{IV}(NH_3)_2(Cl)_2(O_2CCH_2CH_2CO_2H)_2]$ by $NaYF_4:Yb^{3+}/Tm^{3+}@NaYF_4$ UCNPs upon NIR light excitation. The metal complex selected is a light-activatable cisplatin precursor. Under UVA excitation, the platinum complex releases the two axial succinate ligands and generates Pt^{IV} and Pt^{II} photoproducts with antineoplastic activity (e.g. cisplatin). *Cis,cis,trans*-$[Pt^{IV}(NH_3)_2(Cl)_2(O_2CCH_2CH_2CO_2H)_2]$ was anchored on the surface of the UCNPs through its functionalization with a biocompatible PEGylated phospholipid via bio-conjugation techniques. The NIR-induced activation of Pt^{IV} complex was a remarkable result, particularly considering the lack of absorption bands for the compound above 400 nm.

> *"Near Infrared Activation of an Anticancer Pt^{IV} Complex by Tm-Doped Upconversion Nanoparticles" E. Ruggiero, J. Hernández-Gil, J. C. Mareque-Rivas, L. Salassa, Chem. Commun., 2015, 51, 2091.*

Chapter 5 extends UCNP-induced photoactivation to another class of anticancer Ru compounds, namely piano-stool Ru^{II}-arene complexes. For this work, two new Ru^{II}-arene complexes were synthesized, $[(\eta^6\text{-}p\text{-cym})Ru^{II}(bpy)(m\text{-CCH-Py})][PF_6]_2$ and $[(\eta^6\text{-}p\text{-cym})Ru^{II}(bpm)(m\text{-CCHPy})][PF_6]_2$ (where *p*-cym = *p*-cymene, bpm = 2,2'-bipyrimidine, and *m*-CCH-Py = 3-ethynylpyridine). The photochemistry of these derivates was fully characterized with a range of methods, including DFT calculations and photodissociation quantum yield measurements. Upon blue irradiation, both

complexes selectively release the pyridyl ligand and coordinate a water molecule, forming aqua photoproducts. The bpm derivate $[(\eta^6\text{-}p\text{-cym})Ru^{II}(bpm)(m\text{-CCHPy})][PF_6]_2$ displayed higher photoaquation yield and was then chosen for further functionalization with a phosphonate arm to decorate the surface of $NaYF_4:Yb^{3+}/Tm^{3+}@NaYF_4$ UCNPs. The phosphonate group has good affinity for the UCNP surface. The so-obtained nanosystem UCNP-Ru complex underwent NIR photoactivation and produced the corresponding aqua photoproducts that bound the DNA-model base guanosine 5'-monophosphate.

> *"Upconverting Nanoparticles Prompt Remote Near-Infrared Photoactivation of Ru(II)–Arene Complexes" E. Ruggiero, C. Garino, J. C. Mareque-Rivas, A. Habtemariam, L. Salassa, Chem. Eur. J., 2016, 22, 2801.*

In addition to the aforementioned work, during my Ph.D. I have also contributed to the development of other research projects and to the preparation of review articles. These activities were instrumental in consolidating my expertise in the area of photoactive coordination compounds and inorganic nanoparticles. The result of my involvement produced (not reported in this thesis) 6 articles published in international peer-reviewed journals and 1 outreach journal article.

> *"Light Harvesting and Photoemission by Nanoparticles for Photodynamic Therapy" A. G. Arguinzoniz, E. Ruggiero, A. Habtemariam, J. Hernández-Gil, L. Salassa, J. C. Mareque-Rivas, Part. Part. Syst. Charact., 2014, 31, 46.*

> *"Quantum Dot Photoactivation of Pt(IV) Anticancer Agents: Evidence of an Electron Transfer Mechanism Driven by Electronic Coupling" I.*

Infante, J. M. Azpiroz, N. Gomez Blanco, E. Ruggiero, J. M. Ugalde, J. C. Mareque-Rivas, L. Salassa, J. Phys. Chem. C, 2014, 118, 8712.

"The Photochemistry of Transition Metal Complexes and Its Application in Biology and Medicine" E. Ruggiero, S. Alonso-de Castro, A. Habtemariam, L. Salassa, Struct. Bond., 2014, 165, 69.

"Rare-Earth Doped Colour Tuneable Up-Conversion ZBLAN Phosphor for Enhancing Photocatalysis" J. Méndez-Ramos, P. Acosta-Mora, J. C. Ruiz-Morales, M. Sierra, A. Redondas, E. Ruggiero, L. Salassa, M. E. Borges, P. Esparza, Optical Materials, 2015, 41, 98.

"Nuevos Materiales de Conversión Ascendente para Fotoquimioterapia con Complejos de Metales de Transición" S. Alonso-de Castro, E. Ruggiero, L. Salassa, CIC Network Ciencia y Tecnología, 2015, 15, 40.

"Photorelease of Pyridyl Esters in Organometallic Ru(II) Arene Complexes" A. Habtemariam, C. Garino, E. Ruggiero, S. Alonso-de Castro, J. C. Mareque-Rivas, L. Salassa, Molecules, 2015, 20, 7276.

"Upconverting Nanoparticles for the Near Infrared Photoactivation of Transition Metal Complexes: New Opportunities And Challenges In Medicinal Inorganic Photochemistry" E. Ruggiero, S. Alonso-de Castro, A. Habtemariam, L. Salassa, Dalton Trans., 2016, submitted.

1

Light in Medicine: Photodynamic Therapy and Light-Activatable Metal-Based Prodrugs

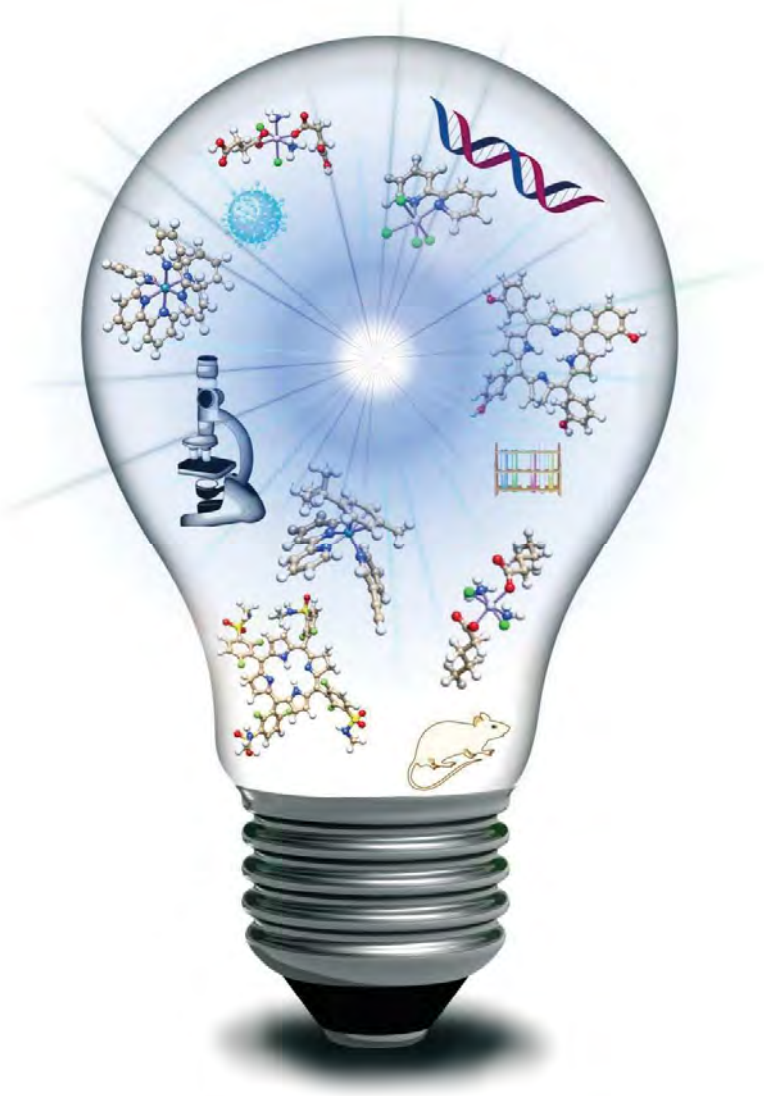

1.1 Photodynamic therapy (PDT)

The therapeutic properties of light have been known for more than 3000 years. [1] Ancient Egyptians, Indians and Chinese have exploited sun light to treat skin diseases. Nowadays, one of the most important clinically used light-based remedies is photodynamic therapy (PDT).

PDT is a minimally invasive clinical procedure utilized for the treatment of nonmalignant diseases and tumors (skin, head, neck, lung, pancreas, esophagus, bladder, prostate and neoplasms). The mechanism of action of PDT is based in the generation of cytotoxic reactive oxygen species (ROS) upon irradiation with visible light in the presence of a photosensitizing compound (PS). [2,3] The individual components of PDT are not toxic, per se, but the total sum conspires to kill cells via different mechanisms: apoptosis, necrosis and autophagic death. [2,3]

The PS structure is mostly based on tetrapyrrole macrocycles, which display highly conjugated electron systems that permit the efficient absorption of visible light. As shown in Fig. 1, a number of PSs are available nowadays for clinical use and some porphyrin and phthalocyanine derivatives are undergoing clinical trials. [2]

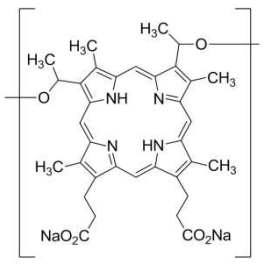

Porfimer sodium

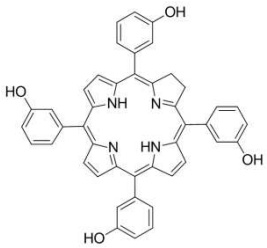

Temoporfin

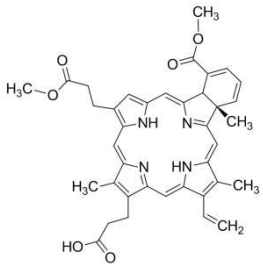

Verteporfin

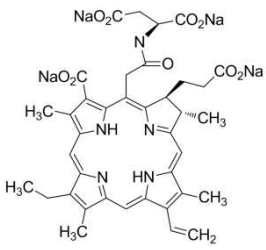

Talaporfin sodium

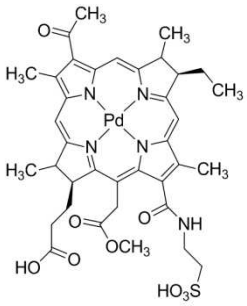

Padeliporfin

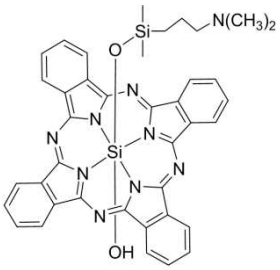

Silicon Phthalocyanine

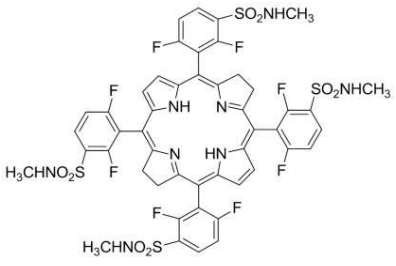

Redaporfin

Fig. 1. Selected structures of clinically approved PSs. [2]

Upon visible light irradiation, the PS absorbs photons and reaches the singlet excited state (Fig. 2). Such a state has very short lifetime and either decays back to the ground state radiatively (fluorescence), or undergoes intersystem crossing (ISC) to yield the triplet excited state (^{3}PS*). The ^{3}PS* state can in turn either decay radiatively to the ground state (phosphorescence) or react with the surrounding molecules by two pathways (Type I and Type II). In the Type I pathway, the excited photosensitizer interacts with the cellular environment, extracting an electron or a hydrogen atom to form radical species. Subsequently, these radicals react with cellular oxygen and provide ROS (e.g. peroxides, superoxide, hydroxyl radical, or singlet oxygen). The type II mechanism relies on the direct energy transfer between the photosensitizer and molecular oxygen, which has a triplet ground state ($^3O_2$). Upon energy transfer, the excited photosensitizer returns to the ground state and oxygen reaches the excited singlet state ($^1O_2$), which is a highly-reactive specie. Both mechanisms involve the interaction with cellular oxygen to form ROS, which is the cause of cytotoxicity via oxidative stress mechanisms in the cell. [2,3]

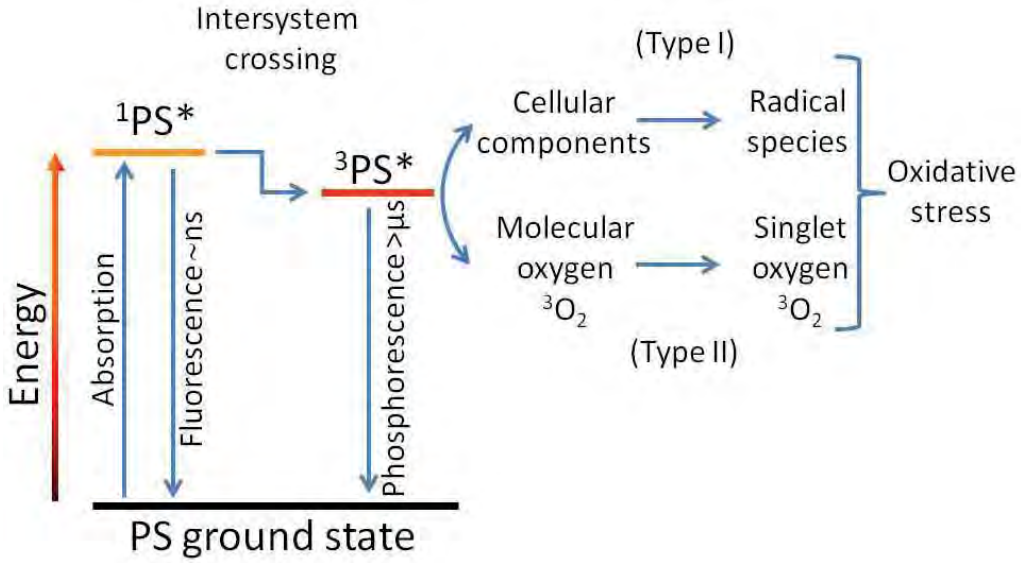

Fig. 2. Energy level diagram depicting the generation of reactive oxygen species in photodynamic therapy.

Most of the photosensitizers are expected to undergo thorough Type II process. Due to the high reactivity and short half-life of the ROS, PDT directly affects only cells that are in the vicinity of the site where ROS are produced. The cyclic sequence of light

absorption, PS excitation and ROS generation continues until photosensitizer decomposition. The ideal PS should localize selectively in tumors, be non-toxicity in the dark, have a rapid clearance from healthy tissues and display high quantum yields for ROS production. ROS generated during PDT lead to tumor elimination principally by three pathways:

(a) Direct cancer cell death due to the damage of cellular compartment; [4]

(b) Deterioration of tumor microcirculation vessels, which can cause reduction of the nutrient supply to the cancer or hemorrhage or even platelet aggregation; [5,6]

(c) Inflammatory reaction that can induce an immunostimulatory or immunosuppressive response. [7]

In the clinic, the PDT procedure is divided into phases (Fig. 3). In the first stage, the PS is administered to the patient, which has to wait a definite period of time to maximize the drug concentration in the tumor to occur. This time, also named drug-to-light interval, can span from a minimum of 15 min to a maximum of 72 h, depending on the kind of tumor and the PS employed. [2] The last stage involves the irradiation of the target cancer tissue and, as a consequence, the localized generation of antineoplastic species.

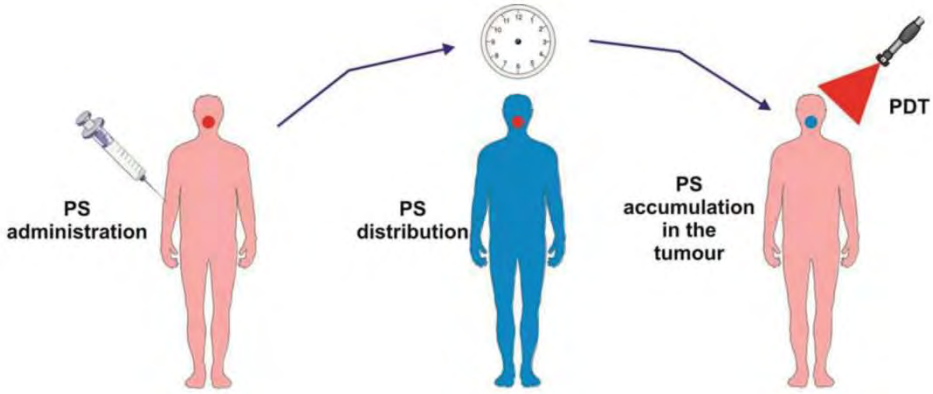

Fig. 3. Different phases in the application of photodynamic therapy. The circle represents the patient's tumor. The figure is reproduced from reference [3].

Importantly, any organ can be virtually irradiated by flexible fiber optic devices. Since the light can be easily oriented to the area of interest and the PS is preferentially absorbed by hyper proliferative cancer cells. PDT is highly selective, avoiding systemic toxicity and damage to adjacent healthy tissues. Figures 4 and 5 display two examples

of clinical PDT applications to treat pre-cancerous conditions of Barrett's oesophagus and lip cancers. [8]

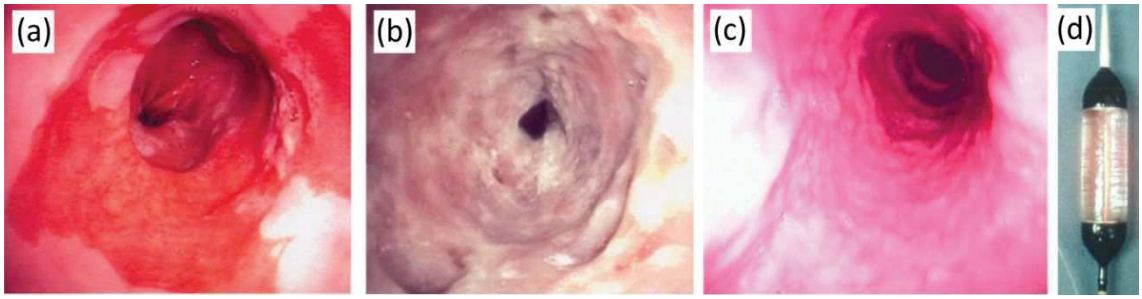

Fig. 4. Clinical PDT application for pre-cancerous conditions of Barrett's oesophagus. (a) The oesophagus before therapy; (b) The oesophageal mucosa destruction, one day after PDT treatment; (c) One month after, normal lining of the oesophagus is regenerated; (d) The tool employed to irradiate the oesophagus. Figure is taken from reference [8].

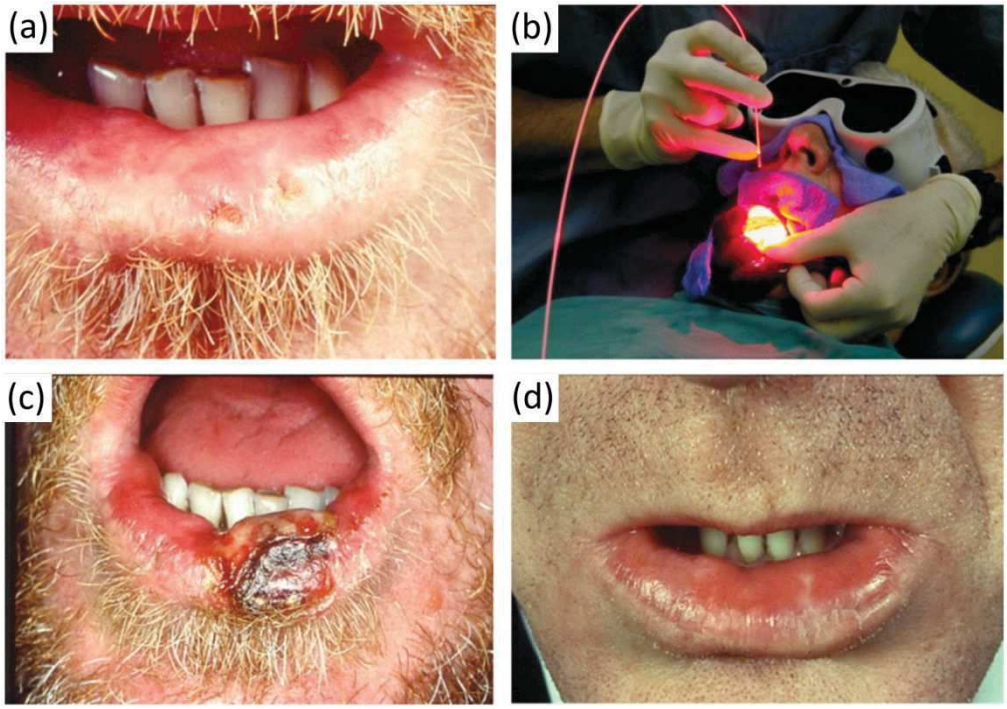

Fig. 5. Clinical PDT for the treatment of lip cancer. (a) The two brown spots are lip tumors; (b) Light irradiation of cancers, two days after administration of porfimer sodium; (c) Complete destruction of tumor and surrounding tissue after four days; (d) One month after PDT treatment. The figure is adapted from reference [8].

At present, more than 400 PDT clinical trials have been performed or are ongoing as recorded by U.S. National Institutes of Health. [9] It is worth highlighting that PDT can be employed in combination with other treatments (radiotherapy, chemotherapy and surgery) in consideration of the localized PDT-toxicity and the absence of possible cross-resistance with other anticancer therapies.

Despite the promising antitumor results achieved by PDT, this therapeutic approach still suffers some important deficiencies that limit the efficacy of the treatment:

(a) Photosensitizers are activated upon visible light, which is not the most advantageous to achieve ideal tissue penetration. Tissues are most phototransparent between 650 and 1000 nm;

(b) Cells can evolve mechanisms of resistance based on the doses of light and PS employed; [10]

(c) Hypoxic solid tumor microenvironment (lack of O_2) makes these cancers resistant to PDT treatment. [11,12] *In vivo* studies demonstrated that induction of tissue hypoxia, abolished the PDT effects, since PDT mechanism is oxygen dependent. [13] Moreover, oxygen shortage can arise as a result of the photochemical consumption of oxygen during the photodynamic process. [14]

Such drawbacks are intrinsic to the photophysical nature of PSs and the PDT mechanism of action. Alternative O_2-independent phototherapies are under development to improve PDT potential, such as: photothermal therapy using NPs, [15,16] photo-induced pH imbalance by the release of sulfonium salts, [17] photoisomerization of organic compounds [18] and photoactivation of inorganic prodrugs. [19] Among these, the use of photosensitive anticancer metal complexes, which do not need oxygen to stimulate their cytotoxicity, is one of the approaches with most prospective. Light activation of anticancer metal complexes conserves the spatiotemporal control of cytotoxic effects, but most likely allows the chemotherapeutic action in oxygen poor tissues such as hypoxic tumors.

In the following section, a brief overview of the potential of photoactive transition metal complexes in medicine is described.

1.2 Photoactivatable metal-based prodrugs

Viable alternatives to PDT are light-activatable metal-based anticancer agents. The extensive knowledge acquired over the years in medicinal inorganic chemistry and its application in cancer therapies [20] has led to the exploitation of the rich photochemistry of metal complexes [21] and to design innovative photosensitive metal-based prodrugs. These prodrugs are nontoxic and stable in the dark under physiological conditions but capable of generating species which selectively interact with cellular vital functions under light irradiation. Indeed, transition metal complexes exhibit a large variety of easily accessible electronic excited states which can be used for the photostimulation of ligand substitution, structure rearrangement and redox reactions on metal centers. [22,23,24]

Therefore, metal complexes potentially offer diverse and unique toxicity mechanisms which do not rely on ROS development. Furthermore, they can also integrate multiple functionalities in a single agent (e.g. luminescence properties, targeting ability, release of bioactive agents). Over the last decades, different promising agents, which have therapeutic oxygen-independent mechanisms of action, have been discovered. These agents function by targeting DNA (e.g. DNA-crosslinking, [25] photocleavage of DNA, [26] gene silencing [27]), inhibiting crucial enzymes, [28] and activating gasotransmitters (NO, CO). [29,30]

In this section, selected representative examples of light-activatable metal complexes which demonstrated promising photoinduced antineoplastic action *in vitro* and, in few cases also in animal models will be discussed.

1.2.1 Metal-based anticancer prodrugs

Platinum

Platinum-based drugs play a pivotal role in cancer therapy. Square planar platinum (II) complexes are administered almost to 50% of patients under cancer treatment worldwide (such as cisplatin, carboplatin and oxaliplatin, Fig. 6). [20]

The anticancer activity of Pt compounds primarily arises from their interaction with DNA. These complexes hydrolyze once they enter the cell, losing one or more ligands and forming Pt aqua species which react with nucleophilic sites of DNA. [20] In

such a way, Pt drugs give mono and bis adducts as well as intra- and interstrand crosslinked DNA structures which eventually lead to cellular apoptosis. [31,32]

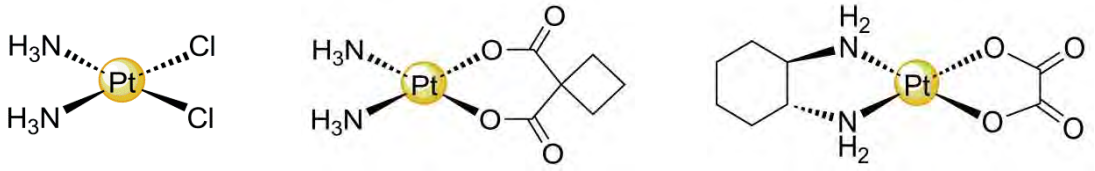

Cisplatin Carboplatin Oxaliplatin

Fig. 6. Square planar Pt^{II} drugs which have achieved the global marketing authorization for human use.

The clinical success and drawbacks (e.g. systemic toxicity and drug resistance) of Pt^{II} anticancer drugs have inspired the investigation of new generations of platinum chemotherapeutic agents. Many efforts have been put in the design of octahedral Pt^{IV} complexes as Pt^{II} prodrugs with lower side-effects. These octahedral platinum compounds show high inertness and stability towards ligand substitution reactions, however under certain conditions Pt^{IV} complexes can be activated by reduction to their Pt^{II} counterparts, which portray cytotoxic effects. The reduction of Pt^{IV} complexes is generally accompanied by the release of the two axial ligands and the change of geometry from octahedral to square planar. [33] The activation mechanism can be triggered from external or internal stimuli, e.g. light activation or cellular environment such as biological reducing agents (like ascorbic acid, glutathione). [34,35] In addition, the octahedral geometry of Pt^{IV} introduces two extra ligand sites in contrast to Pt^{II} drugs, offering superior possibilities for drug design. Pt^{IV} coordination chemistry has been used to modify the pharmacokinetic parameters of prodrugs, including the rate of reduction and lipophilicity, and to allow the inclusion of ligands with biological activity (e.g. enzyme inhibition, immunomodulation) or tumor-targeting capacity. [36,37,38,39]

To illustrate the capability of Pt^{IV} compounds, two representative complexes which function as photoactivatable prodrugs with outstanding antineoplastic activity have

been selected: *trans,trans,trans*-[Pt(N$_3$)$_2$(OH)$_2$(py)(NH$_3$)] (where py = pyridine, Fig. 7a) and *cis,trans*-[Pt(N$_3$)$_2$(Sub)$_2$(*t*Bu$_2$bpy)] (where Sub = suberoyl-bis-hydroxamic and *t*Bu$_2$bpy = 4,4'-di-*tert*-butyl-2,2'-bipyridine acid, Fig. 7b).

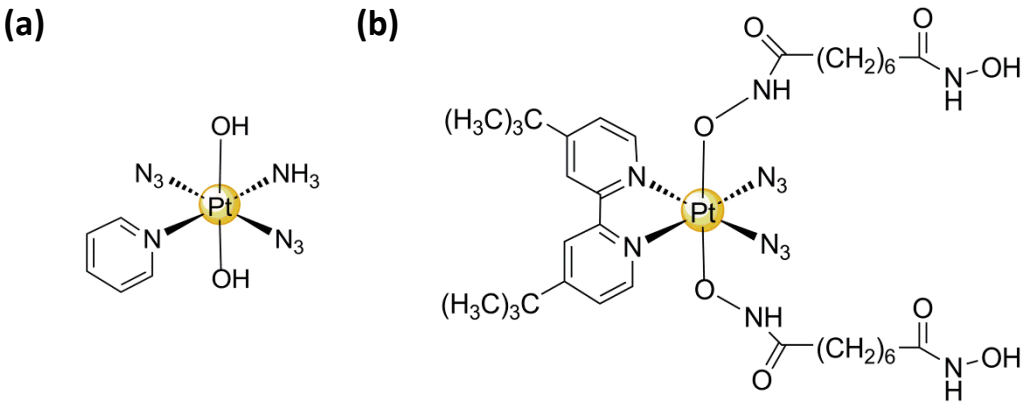

Fig. 7. Schematic representation of the Pt^{IV} prodrug candidates (a) *trans,trans,trans*-[Pt(N$_3$)$_2$(OH)$_2$(py)(NH$_3$)] and (b) *cis,trans*-[Pt(N$_3$)$_2$(Sub)$_2$(*t*Bu$_2$bpy)].

Trans,trans,trans-[Pt(N$_3$)$_2$(OH)$_2$(NH$_3$)(py)] was published by the Sadler's group, who have been investigating the photochemistry of numerous Pt^{IV} diazido complexes over the years.

The group observed that the irradiation of Pt^{IV} diazido complexes (range UVA–green light) caused photodissociation and/or photodecomposition of the azido ligands and reduction of Pt^{IV} to Pt^{II}. When the irradiation was undertaken in cells, a potent cytotoxic effect was induced, which was not observed either in the dark, or with irradiation of the cells in the absence of the Pt complex. [40,41]

In 2012, the Sadler group published the first *in vivo* study of the octahedral phototoxic Pt^{IV}-azido complex, *trans,trans,trans*-[Pt(N$_3$)$_2$(OH)$_2$(NH$_3$)(py)] (Fig. 7a). [42] Upon UVA light activation and in the presence of guanosine 5'-monophosphate (GMP, DNA model base), the prodrug candidate rapidly led to formation of Pt^{II} square planar species and mono and bis-GMP adducts, *trans*-[Pt(N$_3$)(NH$_3$)(py)(GMP)] and *trans*-[Pt(NH$_3$)(py)(GMP)$_2$], respectively. [43] In the dark the Pt^{IV} prodrug did not bind to the GMP and fluorescence microscopy studies of the Pt^{IV} complex in HL60 cells showed that the prodrug did not cause any alteration in cellular morphology, conversely to cisplatin administration, which displays morphologic hallmarks of apoptosis.

The phototoxicity of this *trans,trans,trans*-[$Pt(N_3)_2(OH)_2(NH_3)(py)$] was studied in 13 cancer cell lines. IC_{50} values (the drug concentration causing 50% inhibition of a specific biological process) ranged from 29 μM for bladder carcinoma RT-112 cells to 137 μM for bladder carcinoma epithelial RT-4 cells with the average IC_{50} of 55 μM (λ_{irr} = 365 nm with 0.12 mW/cm^2). [42]

Curiously, the photostimulated toxicity of *trans,trans,trans*-[$Pt(N_3)_2(OH)_2(NH_3)(py)$] led to cell death through an autophagy pathway, in contrast to the apoptosis mechanism found for cisplatin, as demonstrated by the high levels of the microtubule-associated protein light chain (LC3) and sequestodome 1 (p62). [42]

The antitumor activity of *trans,trans,trans*-[$Pt(N_3)_2(OH)_2(NH_3)(py)$] was also confirmed in OE19 xenograft bearing mice. [42] After 35 days of phototherapy, two out of the seven mice treated with the Pt^{IV} complex under irradiation were alive, while none of the ones treated under non-irradiation conditions or without Pt metallodrug survived. Interestingly, the prodrug did not show any systemic toxicity in the animals, even when the complex was administered at about ten times more than the maximum tolerated dose for cisplatin. Such results highlighted that the platinum agent was active *in vivo* and displayed lower side-effects in comparison to other anticancer agents.

Recently, Brabec and coworkers proposed the photosensitive bifunctional platinum azido complex, *cis,trans*-[$Pt(N_3)_2(Sub)_2(tBu_2bpy)$] (Fig. 7b) as a dual function anticancer agent. [44]

Upon UVA or 458 nm light excitation, such complex also underwent photoreduction and axial ligands release, generating bioactive Pt^{II} adducts. These Pt^{II} species bound to DNA, forming DNA adducts, as established by mammalian DNA-binding experiments, which subsequently led to cellular death.

Importantly, the released Sub ligands displayed simultaneously a secondary biological action. In the cells, DNA is packed around proteins called histones to make up the chromatin. Sub acts as a competitive histone deacetylase inhibitor, which is a class of enzymes that remove acetyl groups, necessary in the regulation of DNA expression. [45] The reduced activity of this enzyme increases the histone hyper-

acetylation, which limits the ability of histones to wrap the DNA tightly and can increase DNA accessibility for drug binding.

Notably, Sub alone inhibited cancer cell proliferation, but it can also synergistically operate with equimolar concentration of anticancer Pt agents. In fact, Sub exerted cooperative interaction with oxaliplatin, inhibiting the survival of colorectal cancer CRC cells *in vitro* experiments. [46,47,48,49] Brabec and coworkers rationalized that such synergy based on reduced chromatin condensation could be exploited to promote DNA platination.

The inhibitory effect of *cis,trans*-[$Pt(N_3)_2(Sub)_2(tBu_2bpy)$] was confirmed after light irradiation, determining the values of histone deacetylase in ovarian carcinoma A2780 cells. [44]

The double functionality of this Pt prodrug led to remarkable photostimulated cytotoxic effects in A2780 and cisplatin-resistant A2780cisR cells. After 458-nm light irradiation, the IC_{50} values of Pt prodrug in A2780 and A2780cisR cells were 8.4 and 10.2 μM, respectively with an enhancement of 3–4 times with respect to dark conditions (IC_{50} 31 and 24 μM). Remarkably, cisplatin in the same condition displayed less potent cytotoxic effect, with IC_{50} of 19 μM in A2780 cells and 50 μM in A2780cisR cells.

To demonstrate the synergetic effect of Sub and Pt^{II} species, photoactivatable Pt^{IV} analogues containing biologically inactive axial ligands (hydroxide and acetate) were tested *in vitro* in the same conditions as negative control. Although the cytotoxicity of these derivatives was also increased upon irradiation, the enhancement was significantly lower than for *cis,trans*-[$Pt(N_3)_2(Sub)_2(tBu_2bpy)$].

These results encourage conjugation of biologically active ligands to photoactivatable Pt^{IV} compounds in order to expand the effectiveness of inorganic photochemotherapy.

Rhodium

Rh complexes are well-known class of octahedral metal compounds, which show cisplatin-like mode of action upon light excitation. The group of Morrison has led research on Rh polypyridyl derivatives, demonstrating the complexes could bind

covalently to nucleic acids under light-irradiation, causing phototoxicity *in vitro* and *in vivo*.

The parent compound *cis*-$[Rh(phen)_2Cl_2][Cl]$ (where phen = 1,10-phenanthroline, Fig. 8a) was reported for the first time in 1989. [50,51] This Rh complex acted as "photocisplatin" since upon UVB irradiation (Φ_{311} = 0.026) it photoreleased one chloride ligand and coordinated a water molecule, forming an aqua photoproduct. Moreover, light excitation at 330 nm triggered the formation of Rh-DNA mono-adducts.

After years of refinement based on structure-activity relationship studies, in 2006 Morrison`s group designed the Rh prodrug candidate $[Rh(3,4,7,8\text{-Me-phen})_2Cl_2][Cl]$ (Fig. 8b), a methylated analog of the parent Rh complex described. [52]

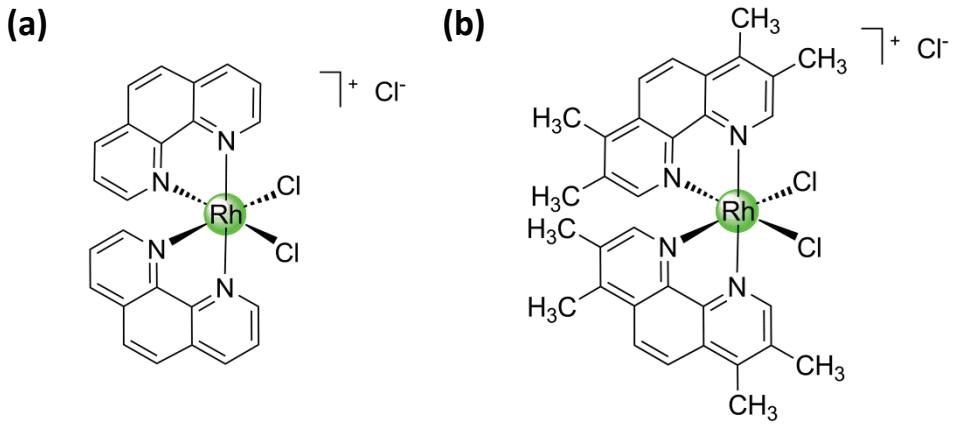

Fig. 8. Schematic representation of the Rh^{III} prodrug candidates (a) *cis*-$[Rh(phen)_2Cl_2][Cl]$ and (b) $[Rh(3,4,7,8\text{-Me-phen})_2Cl_2][Cl]$.

The ring methylation improved two key features of the complex: hydrophobicity and photoreactivity. It is well known that the introduction of methyl groups on the aromatic rings can increase the hydrophobicity of these compounds, which conveniently favors cellular uptake. In fact, in nasopharyngeal carcinoma cells a considerable uptake of the methylated Rh complex was observed. Moreover, this complex showed an improved photoaquation yield (Φ_{254} = 0.061, Φ_{311} = 0.20, Φ_{347} = 0.63) with efficiencies up to tenfold higher than the non-methylated parent Rh compound at the same wavelength (λ_{irr} = 311 nm). [50]

[Rh(3,4,7,8-Me-phen)$_2$Cl$_2$][Cl] displayed photocytotoxicity against several types of tumors: nasopharyngeal carcinoma, bladder, pancreatic and colon cancers. Moreover, the Rh complex showed promising activity against melanoma cells such as SKMEL-5 and UACC6-2. [53] In the case of SKMEL-5 cells, a 100 μM concentration of Rh prodrug was sufficient to cause 40% cell death under irradiation at 311 nm, while no toxicity was observed in the control experiments.

Because of these encouraging results, [Rh(3,4,7,8-Me-phen)$_2$Cl$_2$][Cl] was tested on SKMEL-5 xenograft bearing mice. The metallodrug was administered intravenously and via intraperitoneal injections. The Rh complex was more efficient in diminishing tumor size at early stage as well as in delaying tumor progression in comparison with cisplatin. The authors rationalized the finding with the appearance of drug resistance towards cisplatin in SKMEL-5 cells. [53] Furthermore, cellular studies pointed out that cell-death mechanism relied on apoptosis pathways since a significant increase of apoptotic cells in tumor tissues treated with the photoactivatable [Rh(3,4,7,8-Me-phen)$_2$Cl$_2$][Cl] was observed. [53]

Ruthenium

Ruthenium is another important metal in the design of light-activatable anticancer prodrugs. Its photophysical and photochemical properties are well suited for medical applications. Ruthenium has several oxidation states available under physiological conditions, e.g. Ru^{II}, Ru^{III}, and Ru^{IV}, [54] and ruthenium complexes are often considered less toxic than Pt^{II} complexes. Furthermore, Ru derivatives can be effective against cisplatin-resistant tumors. [55] The literature regarding the coordination chemistry of ruthenium and its biomedical applications is extensive. Herein two noted classes of Ru^{II} compounds for photoactivated chemotherapy, Ru polypyridyl and Ru arene complexes, will be illustrated.

Over the years, Turro and coworkers have been among the major players in the application of Ru chemistry towards the development of photoactivatable anticancer prodrug systems. They exploited complexes such as *cis*-[Ru(phpy)(phen)(CH_3CN)$_2$][PF_6] (phpy= 2-phenylpyridine, Fig 9a) to control the photosubstitution (λ_{irr} = 500 nm) of the

two acetonitrile ligands with molecules of water, [56,57] and generate an aqua product able to bind to DNA. Ruthenation of DNA induced changes in its tertiary structure resembling cisplatin. The cisplatin-resistant OVCAR-5 cell line (human advanced ovarian epithelial cancer) was employed for assessing the photocytotoxicity of such Ru complex upon 690 nm excitation. A IC_{50} value of 70 nM was found (15 h exposure) under the tested experimental conditions, corresponding to a 14-fold increase compared to the action of the complex in the dark. [57]

The Glazer group designed other two interesting polypyridyl complexes, $[Ru(phen)_2(biq)][PF_6]_2$ (Fig. 9b) and $[Ru(phen)(biq)_2][PF_6]_2$ (Fig. 9c, where biq = 2,2'-biquinoline). [58]

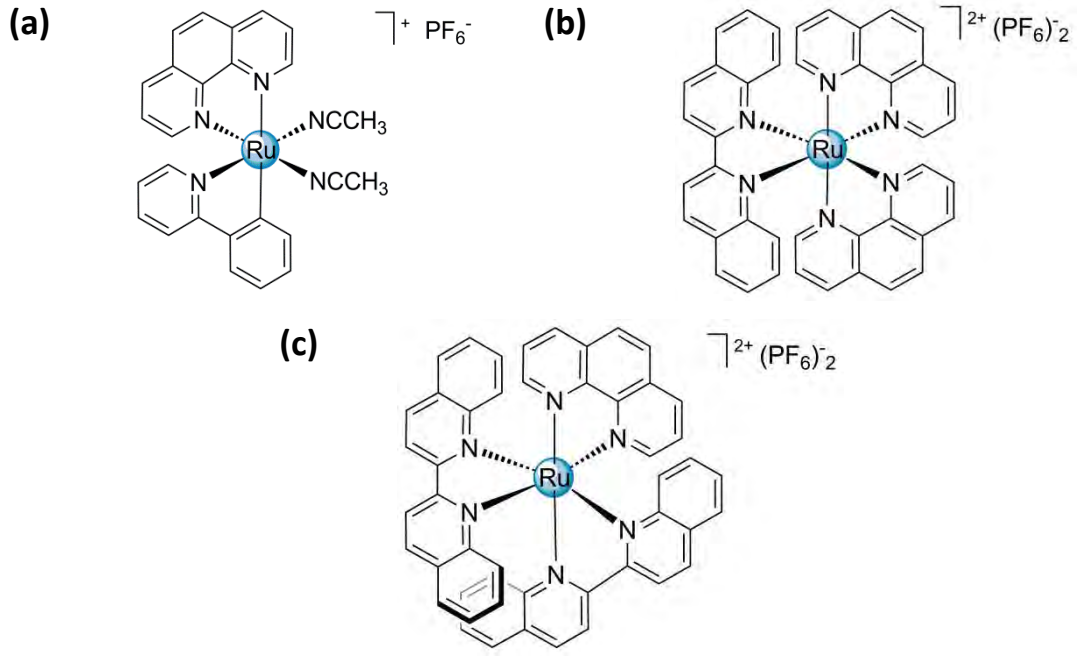

Fig. 9. Schematic representation of the polypyridyl Ru^{II} metal prodrug complexes (a) *cis*-$[Ru(phpy)(phen)(CH_3CN)_2][PF_6]$, (b) $[Ru(phen)_2(biq)][PF_6]_2$ and (c) $[Ru(phen)(biq)_2][PF_6]_2$.

The photoactivity of these Ru^{II} complexes was modulated by the sterically demanding biq ligand which introduced significant structural distortions in the complex, reducing the bond-dissociation energy and improving the efficiency of ligand photoejection.

In fact, both Ru complexes selectively photoreleased one biq ligand with high efficiency and afforded reactive bis-aqua species in controllable manner. Furthermore, introduction of biq ligands in the octahedral Ru scaffold extended the tail of lowest-energy absorption band as far as 800 nm. No release of the phen ligand was observed under the experimental conditions employed.

In the presence of plasmid DNA, both complexes were able to form photoadducts with the macromolecule. Based on mobility studies, DNA cross-links were most likely obtained as for cisplatin, while intercalation and cleavage did not appear to occur. Although blue light (λ_{irr} = 400 nm) was more effective, red light (λ_{irr} = 600 nm) and near-infrared (λ_{irr} = 650 nm) were still capable of inducing photobinding. Both Ru compounds displayed similar toxicity in GK-60 human leukemia cell line under 400 nm excitation, having IC_{50} values of 1–2 μM, which were similar to cisplatin (IC_{50} 3 μM). Remarkably, the two Ru complexes showed much lower toxicity under dark condition (IC_{50} around 50 μM). Antineoplastic activity decreased using red light, however increasing light dose led to higher potency. Upon light irradiation at 600 nm $[Ru(phen)(biq)_2][PF_6]_2$ was more phototoxic than $[Ru(phen)_2(biq)][PF_6]_2$ consistent with the absorption profile of the two complexes.

Another class of Ru complexes of promising anticancer activity is the photoactivatable Ru^{II} arene. These complexes have piano-stool geometry, where the η^6-arene ligand occupies three coordination sites of the complex, leaving the others three positions available for coordination.

Sadler and coworkers have developed several photoactivatable Ru^{II} arene complexes with general formula $[(\eta^6\text{-arene})Ru(N,N')(L)]^{2+}$ (where N,N' is a bidentate chelating ligand and L is a monodentate ligand, Fig 10a). [59,60] Upon visible light irradiation, such Ru compounds photodissociated selectively the monodentate ligand L and generated reactive aqua species able to strongly bind DNA or other bio-macromolecules. [60] Calf thymus (CT)-DNA-binding studies showed that, once irradiated, the complexes bound to CT-DNA whereas the non-irradiated forms bound negligibly. Studies of CT-DNA interactions in cell-free media suggested combined weak monofunctional coordinative and intercalative binding modes. [60]

In 2011, Sadler and Marchán functionalized the Ru^{II} arene scaffold with two different targeting peptides: Arg-Gly-Asp (RGD) and octreotide ([(η^6-*p*-cym)Ru(bpy)(py-peptide)][PF_6]$_2$, Fig 10b). [61]

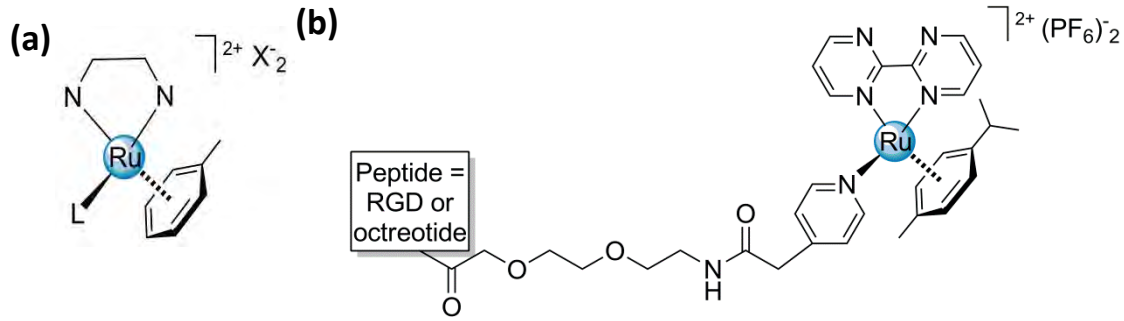

Fig. 10. Schematic representation of piano-stool Ru^{II} metal prodrugs (a) [(η^6-arene)Ru(N,N')(L)][X]$_2$ and (b) [(η^6-*p*-cym)Ru(bpy)(py-peptide)][PF_6]$_2$ (where peptide = RGD or octreotide).

RGD is a tripeptide whose sequence is recognized by integrins α(v)β(3), which play an important role in angiogenesis and are overexpressed on tumoral endothelial cells among others during cancer growth and metastasis. [62,63] In contrast, octreotide is an octapeptide with specific affinity for somatostatin receptors SSTR-2 and SSTR-5, which are also widely distributed in a variety of tumors and cancer cell lines. These peptides might not only increase the selectivity versus tumor cells, but also improve the cellular uptake of the complex. Interestingly, both peptides can be exploited also for molecular imaging by delivering radionuclides. In fact, many RGD and octreotide derivatives have been labeled with ^{18}F, ^{64}Cu, ^{68}Ga or ^{99m}Tc and tracked by PET and SPECT imaging. [64]

The two peptide-functionalized complexes were nonreactive in water solution in the dark, but once irradiated at 420 nm-light the pyridine-peptide ligands were substituted with a water molecule. The resulting aqua adduct [(η^6-*p*-cym)Ru(bpy)(H_2O)]$^{2+}$ bound both model DNA nucleobase 9-ethylguanine and guanines of two DNA sequences, $^{5'}$dCATGGCT and $^{5'}$dAGCCATG. It is worth highlighting that when the Ru complex was irradiated in presence of the oligonucleotides, a new binding mode was observed. The photoproduct displaced not only the pyridine but also *p*-cymene, forming a double adduct and showing a multidentate DNA-coordination ability.

Iridium

Iridium compounds were investigated for their anticancer activity after the discovery of cisplatin. Actually, the square planar complex [Ir(acetylacetonate)(1,5-cyclooctadiene)] cured mice bearing Ehrlich ascites and inhibited growth of subcutaneous Lewis lung carcinoma. [65]

Unlike other metals, iridium complexes do not have wide spread notoriety in the phototoxicity panorama. They are highly stable towards ligand photosubstitution and display long-lived emission and large Stokes' shifts, which make these derivatives promising candidates in optical bioimaging applications. [66,67]

In the context of phototherapy, the Meggers' group reported the unique case of a light-triggered cytotoxic Ir complex, namely [Ir(Me)(SeCN)(DBCO)(pyridocarbazole)] (where DBCO = dibenzo[a,e]cyclooctatetraene, Fig 11). [68]

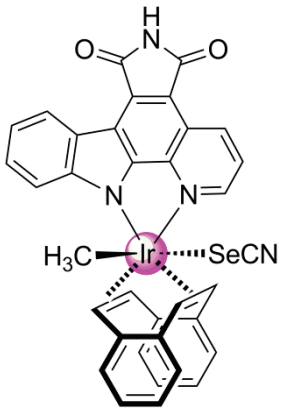

(DBCO)

Fig. 11. Schematic representation of the Ir^{I} complex [Ir(Me)(SeCN)(DBCO)(pyridocarbazole)].

This complex displayed a dual complementary antitumor activity. It acted as light independent kinase inhibitor and as photo apoptosis-inducing agent.

[Ir(Me)(SeCN)(DBCO)(pyridocarbazole)] selectively blocked the activity of kinase VEGFR3, which is an enzyme with important role in tumor and metastases development. [69] VEGFR3 requires the co-substrate ATP for enzymatic catalysis. The Ir complex bound to the ATP binding site of the protein kinase with the pyridocarbazole moiety occupying the adenine pocket and inhibiting its enzymatic

activity. Incubation of 5 μM metallodrug for 24-h in HUVEC cells, which overexpress VEGFR, induced strong cell apoptosis.

In addition, [Ir(Me)(SeCN)(DBCO)(pyridocarbazole)] displayed also phototriggered cytotoxicity upon irradiation (λ_{irr} = 450 nm) with an IC_{50} of 0.23 μM against HeLa cells, 34-fold higher than in the dark. Such phototoxicity relied on the replacement of selenocyanate ligand. In fact, ^{1}H-NMR studies showed that irradiation of [Ir(Me)(SeCN)(DBCO)(pyridocarbazole)] in the presence of chloride (tetrabutylammonium chloride) led to a facile replacement of selenocyanate by chloride. This photoinduced labilization of the selenocyanate ligand induced the cellular death by apoptosis, although the full mechanism is not entirely clear yet. Control experiments were performed with different analogues of the Ir prodrug to ensure that the two apoptotic mechanisms (in the presence and absence of light) relied on different mechanisms.

1.2.2 Small molecules

NO is a small molecule of high relevance in biology since it plays important roles in vasodilation and neurotransmission and can control immune response and apoptotic cell death. [70] Hence there is a growing interest in the potential applications of compounds that release NO in a controlled manner (e.g. by light excitation).

More recently, biological studies have also demonstrated that carbon monoxide is a bioregulator. [71,72] CO is implicated in a number of different physiological effects, including preventing organ graft rejection, reducing ischemia-reperfusion injury and promoting wound healing. [73,74]

For these reasons, NO is already used in the clinic, [75] while several clinical trials are currently ongoing to evaluate the therapeutic activity of CO. [76]

Consequently, a number of NO and CO releasing systems have been developed over the last decades. [77,78,79] Among these, transition metal complexes (Cr, Mn, Fe, Ru) with metal nitrosyls, nitrates, and nitrites function as photoactivatable nitric oxide releasing moieties (photoNORMs). [77,78] Whilst, various M-CO complexes (Cr, Mn, Fe, Mo, W, Re) are analogously investigated as photoactivated carbon monoxide

releasing moieties (photoCORMs), taking advantage of the rich metal-carbonyl coordination chemistry. [79]

In the area of NO and CO medical research, two representative examples of the classes of metal-based compounds are selected to illustrate how controlled photorelease of NO and CO provides a promising alternative for chemotherapy.

NO

Ruthenium nitrosyl complexes are robust in physiological condition, but under light irradiation display pronounced NO-lability. Such properties have attracted significant attention on these compounds as potential photoNORMs. [77,78]

The group of Mascharak developed octahedral Ru-nitrosyl complexes of general formula [(R_2bYb)Ru(NO)(L)] (where R = H, Me, OMe and Y= pyridine (bPb) and quinoline (bQb), L = Cl^-, pyridine, OH^-, Fig. 12), where the R_2bYb tetradentate ligands ensured outstanding photochemical behavior. The carboxamido nitrogens of these ligands acted as donors, stabilizing the higher oxidation states of Ru. This effect promoted the efficient release of NO and the production of Ru photoproducts.

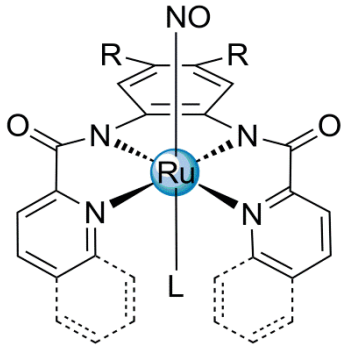

Fig. 12. Schematic representation of the Ru^{III} photoNORMs [(R_2bYb)Ru(NO)(L)] (where R = H, Me, OMe, Y= pyridine (bPb) and quinoline (bQb) and L = Cl^-, pyridine, OH^-, resorufin (Resf)).

Furthermore, the structure of the tetradentate ligand R_2bYb could be opportunely modified to tune the optical properties of the compounds. [80] Mascharak and coworkers rationally designed substitutions on both the R_2bYb ligand framework, and on the axial ligand L coordinates trans to NO. The work allowed to red-shift the

absorption band of the complexes. Through synthetic modifications, they achieved shifting the maximum of the lowest-energy absorption band from 390 nm in the case of [(bPb)Ru(NO)(Cl)] up to 500 nm for [((OMe)$_2$bQb)Ru(NO)(Cl)].

In 2007, the same group reported the complex [(Me$_2$bPb)Ru(NO)(Resf)] (Fig. 12) where the dye resorufin (Resf) was directly coordinated to the Ru center in the axial L position. [81]

Resf is a potent light harvesting chromophore, which displays a strong absorbance in the visible region (λ_{max} = 600 nm, ε = 105 000 M^{-1} cm^{-1}). After metal-coordination Resf absorption maximum shifted to lower wavelengths, overlapping with the photo-band of the nitrosyl complex. Blue shift improved the photosensitivity of the resulting nitrosyl-dye conjugates to visible light excitation. In fact, [(Me$_2$bPb)Ru(NO)(Resf)] showed a very strong absorption at 500 nm (ε = 12 000 M^{-1} cm^{-1}) and dramatically higher quantum yield compared to its hydroxyl analogue [(Me$_2$bPb)Ru(NO)(OH)] (Φ_{500} = 0.052 vs 0.001, respectively). [29] Mascharak rationalized that the improved photoreactivity was due to the energy transfer between the coordinated dye and the Ru-NO moiety. Hence, Resf acted as light harvesting antenna for the Ru complex.

Furthermore, free Resf in water is highly fluorescent, however when the dye was caged in [(Me$_2$bPb)Ru(NO)(Resf)] its emission was strongly quenched (~90 %). Nevertheless, the residual fluorescence of the nitrosyl-dye conjugate could be still exploited to visualize its behavior in cell environment under the microscope.

The rapid NO photorelease combined with fluorescence capacity makes [(Me$_2$bPb)Ru(NO)(Resf)] an ideal agent for studying NO-induced apoptosis in cancer cells. In fact, Mascharak and coworkers demonstrated that 200 μM of this photoNORM led to apoptosis in human mammary cancer MDA-MB-231 cells under 465-nm light irradiation. On the contrary, the complex in the dark did not give any apoptosis signs. [29]

Shortly after, the same group used S- and Se-analogues of Resf (Thionol and Selenophore) to take advantage of the heavy-atom effect for photosensitizing NO release and further shift the absorption band of this class of Ru-photoNORM. They successfully demonstrated that moving from Resf to S- and Se-analogues increased NO dissociation quantum yields at all the excitation wavelengths and extended the excitation window to 600 nm. [82]

CO

The majority of reported photoCORMs are metal carbonyl complexes of group 6, 7 and 8 (e.g. Cr, Mn, Fe, Mo, W, Re), since these metal form stable CO-compounds.

Schatzschneider and co-workers were the first to introduce a Mn-photoCORM with the purpose of inducing CO-toxicity in tumor cells upon light-activation. The Mn-photoCORM took advantage of the structural and electronic features of the Mn^{I} tricarbonyl fragment and the tripodal ligand tris(pyrazolyl)methane (tpm). [30]

$[Mn(CO)_3(tpm)][PF_6]$ (Fig 13) could be excited at 365 nm (ε = 2080 M^{-1} cm^{-1}) to prompt the release of 1.96 eq. of CO in solution. At 100 µM the irradiated Mn complex reduced the amount of cell biomass of HT29 human colon tumor to about 30%, which was comparable with the effect of the clinically approved antineoplastic drug 5-fluorouracil at 20 µM. The Mn-photoCORM was completely inactive and stable in the dark at concentrations up to 100 µM in HT29 cells.

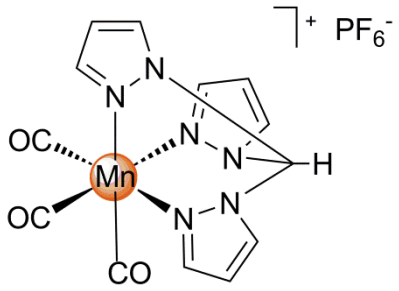

Fig. 13. Schematic representation of the Mn^{I} photoCORM $[Mn(CO)_3(tpm)][PF_6]$.

In addition the Mn complex had good uptake in HT29 human colon cancer cells at various compound concentrations. Cellular Mn increased in a linear fashion with increasing incubation concentration of $[Mn(CO)_3(tpm)][PF_6]$. Moreover, no saturation effects up to 100 µM was observed indicating that uptake occurs by passive diffusion rather active transport. [83]

Remarkably, the tripodal ligand tpm has great synthetic versatility since the acidic methyl proton can be replaced with a variety of different functional groups without influencing dramatically the photochemistry of the complex, maintaining CO-release capacity upon UV irradiation.

Schatzschneider prepared a series of $[Mn(CO)_3(R\text{-tpm})][PF_6]$ complexes by modifying the tpm with pendant arms. [84,85,86] As an example, a tpm functionalized with an alkyne group was used to attach by click chemistry the pentapeptide, Threonine-Phenylalanine-Serine-Aspartic acid-Leucine for cancer targeting. [84] The peptide sequence is part of the transactivation domain of the tumor suppressor protein p53 with the regulatory protein MDM2 (murine double minute 2). This complex illustrated a convenient approach to achieve targeted delivery of $[Mn(CO)_3(R\text{-tpm})][PF_6]$ to cancer cells.

1.2.3 Enzyme-inhibitor release

In addition to NO and CO, the scaffold of octahedral metal complex has also been used to deliver more sophisticated ligands, which display biological activity. In the context of cancer phototherapy, caging of enzyme inhibitors is considered a new strategy to develop prodrugs which are capable of affecting cell survival by targeting specific proteins after light activation.

Adopting this concept, Turro and Kodanko studied light-activatable release of the cysteine cathepsins inhibitor Ac-Phe-$NHCH_2CN$ (where Ac-Phe = acetate-phenylalanine) from the Ru complex, $[Ru(bpy)_2(Ac\text{-}Phe\text{-}NHCH_2CN)_2][PF_6]_2$ (Fig 14a), under physiological conditions. [28]

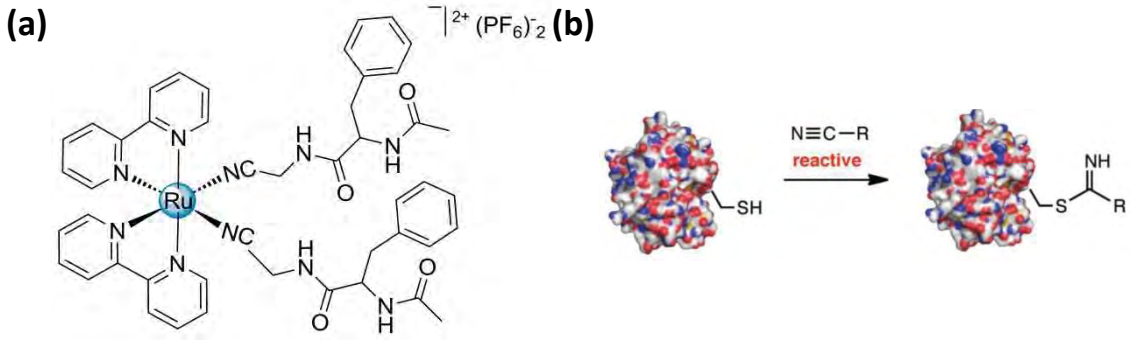

Fig. 14. Schematic representation of (a) the Ru^{II} complex $[Ru(bpy)_2(Ac\text{-}Phe\text{-}NHCH_2CN)_2][PF_6]_2$ and (b) the nitrile-based inhibition mechanism of cysteine protease. The figure 14b is adapted from reference [28].

Cysteine cathepsins are cysteine proteases overexpressed in several tumors. [87] *In vivo* results show that their inhibition reduces tumor growth, migration, invasion, angiogenesis and metastasis. For these reasons, cysteine cathepsins are a viable target for chemotherapy. [88,89] Electrophilic nitrile groups, as in Ac-Phe-$NHCH_2CN$, react with the cysteine nucleophilic thiolates present in the active site of the proteases, blocking their activity (Fig 14b).

$[Ru(bpy)_2(Ac\text{-}Phe\text{-}NHCH_2CN)_2][PF_6]_2$ displayed complete stability in the dark, while, under light excitation, acted as inhibitor for different cysteine cathepsins, like cathepsins B, K, and L. Upon 395 nm-light irradiation, the complex selectively released 2 eq. of Ac-Phe-$NHCH_2CN$ and generated 1 eq. of the aqua complex $[Ru(bpy)_2(H_2O)_2]^{2+}$.

In vitro photoirradiation experiments with human cell lysates were performed to determine the inhibitory activity of the complex towards cathepsin B. In particular, the lysates selected were from DU145 prostate carcinoma and primary human bone marrow stromal (hBMSCs) cells, in both cases cysteine cathepsins B exhibited high activity. Activated $[Ru(bpy)_2(Ac\text{-}Phe\text{-}NHCH_2CN)_2]^{2+}$ caused higher enzyme inhibition compared to Ac-Phe-$NHCH_2CN$ alone. In both cell lysates, the IC_{50} value for human cathepsins B inhibition was approx. 85 µM for the Ru complex upon 395-nm excitation, whereas the IC_{50} value was approx. 180 µM for the cathepsins inhibitor alone, in agreement with the release of 2 eq. of Ac-Phe-$NHCH_2CN$ molecules per Ru complex. Importantly, this metal prodrug candidate in the dark was 7-fold less strong then under light condition, displaying an IC_{50} value approx. of 619 µM.

Although not investigated in the study, Turro and Kodanko highlighted that *in situ* formation of $[Ru(bpy)_2(H_2O)_2]^{2+}$ may serve to unleash multiple anticancer activity, since this aqua photoproduct is known to have DNA binding properties and cytotoxic activity. [90]

1.3 Light-activatable tools for chemical biology

The synthetic versatility and rich photochemistry of Ru polypyridine complexes has been exploited to develop innovative chemical biology tools for neuroscience.

Neuroscience is one of the fields where caged molecules are increasingly employed to manipulate neuronal circuits with light. [91]

In this context, the group of Etchenique used the capacity of Ru ions to coordinate amine groups for realizing visible light photouncaging of neurochemicals, among which in Fig. 15 are shown glutamate (Glu, [92]), nicotine (Nic, [93]), gamma aminobutyric acid (GABA, [94]) and 4-aminopyridine (AP, [95]).

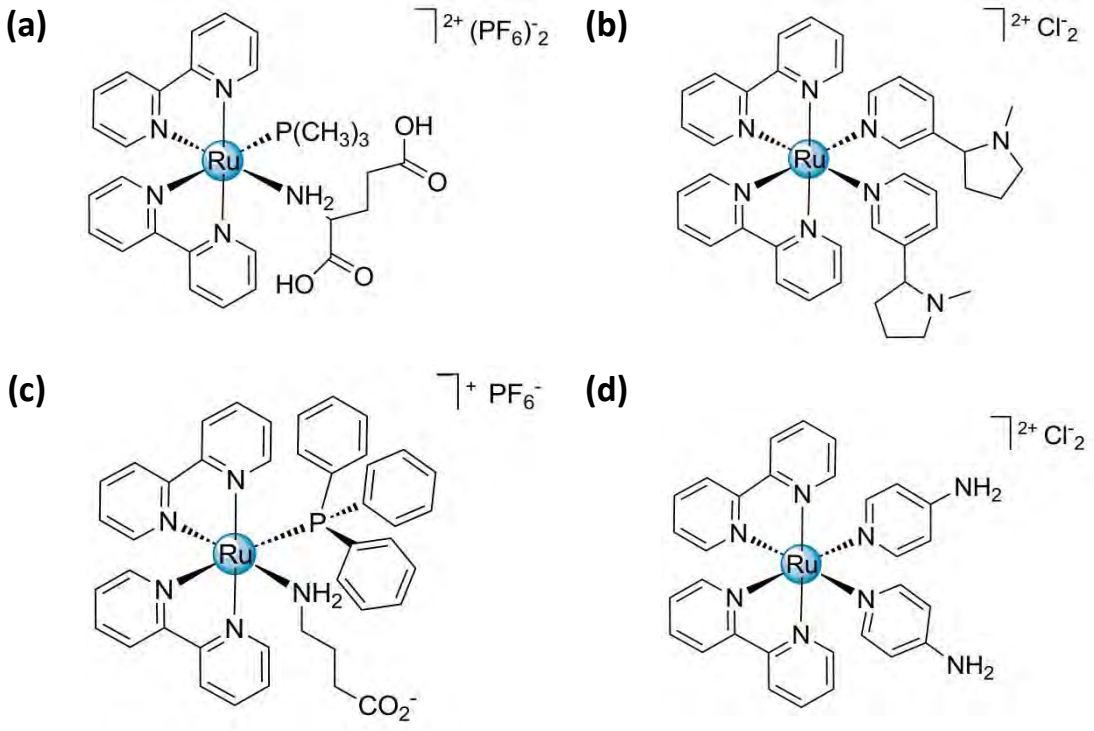

Fig. 15. Schematic representation of Ru^{II} caged compounds (a) $[Ru(bpy)_2(PMe_3)(Glu)][PF_6]_2$, (b) $[Ru(bpy)_2(Nic)_2][Cl]_2$, (c) $[Ru(bpy)_2(PPh_3)(GABA)][PF_6]$ and (d) $[Ru(bpy)_2(AP)_2][Cl]_2$.

Complexes containing the $Ru(bpy)_2$-unit (Fig. 15) were very stable in aqueous environments and released neurochemicals in a single step without secondary reactions, with high efficiency. This type of complexes has been employed to elicit neuron responses, both *in vitro* and *in vivo*. [93,96]

In this section the study of $[Ru(bpy)_2(PMe_3)(Glu)][PF_6]_2$ and $[Ru(bpy)_2(Nic)_2][Cl]_2$ (Fig. 15a and 15b) as representative examples of metal-based caged compounds in neuroscience will be discussed.

In 2009 Etchenique published the first Ru glutamate caged complex, $[Ru(bpy)_2(PMe_3)(Glu)][PF_6]_2$. [92] Glutamate is the most ubiquitous excitatory neurotransmitter in the mammalian central nervous system. The ability to deliver glutamate with a precise spatial and temporal control is crucial to modulate the activity of neural circuits. $[Ru(bpy)_2(PMe_3)(Glu)][PF_6]_2$ could be activated by visible light in the range of 400–540 nm, but also displayed light-induced reactivity upon excitation at 800–900 nm in the 2-photons regime. Its quantum yield of glutamate photorelease was 0.13 at pH=7, whereas the complex was completely stable in the dark.

The capacity of $[Ru(bpy)_2(PMe_3)(Glu)][PF_6]_2$ to activate glutamate receptors in a controlled fashion was investigated by incubating the complex with slices of pyramidal neurons from the mouse neocortex. As shown in Fig. 16, 2-photons light irradiation of the complex at 800 nm led to glutamate release and generated a measurable action potential of the irradiated neuron (nerve impulse).

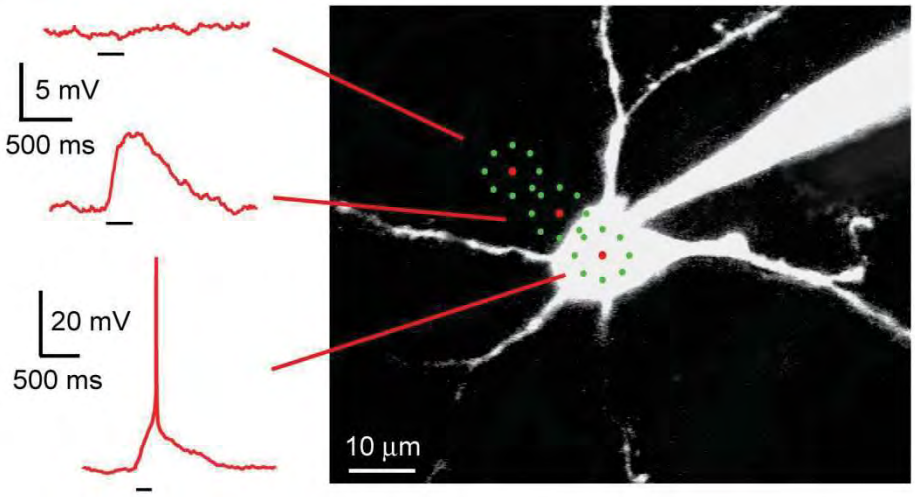

Fig. 16. Action potentials of pyramidal neuron measured under 2-photons light beam in different positions. When the beam was placed on the soma, the photouncaging of the complex elicited an action potential, while moving the beam away from the soma, did not produce neuronal response. Figure is taken from reference [92].

In order to demonstrate spatial resolution of this approach, Etchenique and coworkers showed that only irradiation of the neuron soma caused significant neuronal response. Indeed, they proved that little or no response was detectable when the light beam was shifted away from the soma (Fig. 16).

The $[Ru(bpy)_2(Nic)_2][Cl]_2$ complex (Fig 15b) exploited the same photochemistry principles to photodeliver the alkaloid nicotine. [93]

Nicotine is a strong stimulant of the parasympathetic nervous system, because it is an agonist of the nicotinic acetylcholine receptors, which are located in several tissues like brain, ganglia and muscles. [97]

Under blue or green light excitation, $[Ru(bpy)_2(Nic)_2][Cl]_2$ efficiently released nicotine (Φ_{450} =0.23), whereas no decomposition was detected after even two days in the dark. Irradiated solutions of the complex in the presence of Retzius neurons of leech ganglia displayed an increase of the neuron firing rate due to the release of nicotine. Such firing increase was determined in many ganglia and several animals. Importantly, $[Ru(bpy)_2(nic)_2][Cl]_2$ resulted completely as nontoxic up to 1 mM concentration.

The examples discussed above show how Ru caged systems can be conveniently used for mapping the synaptic inputs of neurons and determining gating kinetic of neurotransmitters. Moreover, their two-photon excitation allows the study of neuroresponses with high cell precision. [98,99,100]

1.4 References

[1] M. D. Daniell, J. S. Hill, *Aust. N. Z. J. Surg.*, **1991**, *61*, 340.

[2] J. M. Dąbrowski, L. G. Arnaut, *Photochem. Photobiol. Sci.*, **2015**, *14*, 1765.

[3] P. Agostinis, K. Berg, K. A. Cengel, T. H. Foster, A. W. Girotti, S. O. Gollnick, S. M. Hahn, M. R. Hamblin, A. Juzeniene, D. Kessel, M. Korbelik, J. Moan, P. Mroz, D. Nowis, J. Piette, B. C. Wilson, J. Golab, *CA Cancer J. Clin.*, **2011**, *61*, 250.

[4] H. Pass, *J. Natl. Cancer Inst.*, **1998**, *85*, 443.

[5] R. Bhuvaneswari, Y. Y. Gan, K. C. Soo, M. Olivo, *Cell. Mol. Life Sci.*, **2009**, *66*, 2275.

[6] M. T. Tseng, M. W. Reed, D. M. Ackermann, D. A. Schuschke, T. J. Wieman, F. N. Miller, *Photochem. Photobiol.*, **1988**, *48*, 675.

[7] A. P. Castano, P. Mroz, M. R. Hamblin, *Nat. Rev. Cancer*, **2006**, *6*, 535.

[8] S. G. Bown, *Phil. Trans. R. Soc. A*, **2013**, *371*, 20120371.

[9] https://clinicaltrials.gov/ct2/results?term=photodynamic+therapy&Search=Search

[10] A. Casas, G. Di Venosa, T. Hasan, A. Batlle, *Curr. Med. Chem.*, **2011**, *18*, 2486.

[11] J. M. Brown, *Methods Enzymol.*, **2007**, *435*, 297.

[12] Y. Mir, J. E. van Lier, B. Paquette, D. Houde, *Photochem. Photobiol.*, **2008**, *84*, 1182.

[13] C. J. Gomer, N. J. Razum, *Photochem. Photobiol.*, **1984**, *40*, 435.

[14] D. E.J.G.J. Dolmans, D. Fukumura, R. K. Jain, *Nat. Rev. Cancer*, **2003**, *3*, 380.

[15] A. Espinosa, R. Di Corato, J. Kolosnjaj-Tabi, P. Flaud, T. Pellegrino, C. Wilhelm, ACS Nano, 2016, 10, 2436.

[16] G.S. Terentyuk, G. N. Maslyakova, L. V. Suleymanova, N. G. Khlebtsov, B.N. Khlebtsov, G. G. Akchurin, I. L. Maksimova, V. V. Tuchin, *J. Biomed. Opt.*, **2009**, *14*, 21016.

[17] X. Yue, C. O. Yanez, S. Yao, K. D. Belfield, *J. Am. Chem. Soc.*, **2013**, *135*, 2112.

[18] K. M. Scherer, R. H. Bisby, S. W. Botchway, J. A. Hadfield, A. W. Parker, *J. Biomed. Opt.*, **2015**, *20*, 51004.

[19] P. J. Bednarski, F. S. Mackay, P. J. Sadler, *Anticancer Agents Med. Chem.*, **2007**, *7*, 75.

[20] N. J. Wheate, S. Walker, G. E. Craig, R. Oun, *Dalton Trans.*, **2010**, *39*, 8113.

[21] U. Schatzschneider, *Eur. J. Inorg. Chem.*, **2010**, *10*, 1451.

[22] N. J. Farrer, L. Salassa, P. J. Sadler, *Dalton Trans.*, **2009**, *48*, 10690.

[23] U. Schatzschneider, *Eur. J. Inorg. Chem.*, **2010**, *10*, 1451.

[24] D. Crespy, K. Landfester, U. S. Schubert, A. Schiller, *Chem. Commun.*, **2010**, *46*, 6651.

[25] D. Ossipov, S. Gohil, J. Chattopadhyaya, *J. Am. Chem. Soc.*, **2002**, *124*, 13416.

[26] S. A. Poteet, M. B. Majewski, Z. S. Breitbach, C. A. Griffith, S. Singh, D. W. Armstrong, M. O. Wolf, F. M. MacDonnell, *J. Am. Chem. Soc.*, **2013**, *135*, 2419.

[27] L. Marcélis, C. Moucheron, A. Kirsch-De Mesmaeker, *Phil. Trans. R. Soc. A*, **2013**, *371*, 20120131.

[28] T. Respondek, R. N. Garner, M. K. Herroon, I. Podgorski, C. Turro, J. J. Kodanko, *J. Am. Chem. Soc.*, **2011**, *133*, 17164.

[29] M. J. Rose, N. L. Fry, R. Marlow, L. Hinck, P. K. Mascharak, *J. Am. Chem. Soc.*, **2008**, *130*, 8834.

[30] J. Niesel, A. Pinto, H. W. Peindy N'Dongo, K. Merz, I. Ott, R. Gust, U. Schatzschneider, *Chem. Commun.*, **2008**, *15*, 1798.

[31] D. Wang, S. J. Lippard, *Nat. Rev. Drug Discov.*, **2005**, *4*, 307.

[32] B. Lippert, Cisplatin: Chemistry and Biochemistry of a Leading Anticancer Drug, Wiley-VCH, **1999**, 111.

[33] H. P. Varbanov, M. A. Jakupec, A. Roller, F. Jensen, M. Galanski, B. K. Keppler, *J. Med. Chem.*, **2013**, *56*, 330.

[34] K. Lemma K, J. Berglund, N. Farrell, L. Elding, *J. Biol. Inorg. Chem.*, **2000**, *5*, 300.

[35] Y.-R. Zheng, K. Suntharalingam, T. C. Johnstone, S. J. Lippard, *Chem. Sci.*, **2015**, *6*, 1189.

[36] Y.-R. Zheng, K. Suntharalingam, T. C. Johnstone, H. Yoo, W. Lin, J. G. Brooks, S. J. Lippard, *J. Am. Chem. Soc.*, **2014**, *136*, 8790.

[37] V. Novohradsky, L. Zerzankova, J. Stepankova, O. Vrana, R. Raveendran, D. Gibson, J. Kasparkova, V. Brabec, *J. Inorg, Biochem.*, **2014**, *140*, 72.

[38] S. G. Awuah, Y.-R. Zheng, P. M. Bruno, M. T. Hemann, S. J. Lippard, *J. Am. Chem. Soc.*, **2015**, *137*, 14854.

[39] Y. Yuan, R. T. K. Kwok, B. Z. Tang, B. Liu, *J. Am. Chem. Soc.*, **2014**, *136*, 2546.

[40] F. S. Mackay, J. A. Woods, P. Heringová, J. Kašpárková, A. M. Pizarro, S. A. Moggach, S. Parsons, V. Brabec, P. J. Sadler, *Proc. Natl. Acad. Sci. USA*, **2007**, *104*, 20743.

[41] F. S. Mackay, N. J. Farrer, L. Salassa, H.-C. Tai, R. J. Deeth, S. A. Moggach, P. A. Wood, S. Parsons, P. J. Sadler, *Dalton Trans.*, **2009**, *13*, 2315.

[42] A. F. Westendorf, J. A.Woods, K. Korpis, N. J. Farrer , L. Salassa, K. Robinson, V. Appleyard, K. Murray, R. Grünert, A. M. Thompson, P. J. Sadler, P. J. Bednarski, *Mol. Cancer Ther.*, **2012**, *11*, 1894.

[43] F. S. Mackay, J. A. Woods, P. Heringová, J. Kašpárková, A. M. Pizarro, S. A. Moggach, S. Parsons, V. Brabec, P. J. Sadler, *Proc. Natl. Acad. Sci. USA*, **2007**, *104*, 20743.

[44] J. Kasparkova,H. Kostrhunova, O. Novakova, R. Křikavová, J. Vančo, Z. Trávníček, V. Brabec, *Angew. Chem. Int. Ed.*, **2015**, *54*, 14478.

[45] L. Verdone, M. Caserta, E. Di Mauro, *Biochem. Cell. Biol.*, **2005**, *83*, 344.

[46] L. Ning, D. Y. Greenblatt, M. Kunnimalaiyaan, H. Chen, *Oncologist.*, **2008**, *13*, 98.

[47] B. R. You, W. H. Park, Mol. Biol. Rep., **2013**, *40*, 3807.

[48] S. Flis, A. Gnyszka, J. Spławiński, *Biochem. Biophys. Res. Commun.*, **2009**, *387*, 336.

[49] B. R. You, W. H. Park, *Mol. Cell. Biochem.*, **2010**, *344*, 203.

[50] R. E. Mahnken, M. Bina, R. M. Deibel, K. Luebke, H. Morrison, *Photochem. Photobiol.*, **1989**, *49*, 519.

[51] H. L. Harmon, H. Momson, *Inorg. Chem.*, **1995**, *34*, 4937.

[52] D. Loganathan, H. Morrison, *Photochem. Photobiol.*, **2006**, *82*, 237.

[53] M. R. Kim, H. Morrison, S. I. Mohammed, *Anticancer Drugs*, **2011**, *22*, 896.

[54] W. H. Ang, P. J. Dyson. *Eur. J. Inorg. Chem.*, **2006**, *20*, 4003.

[55] A. Bergamo, G. Sava, *Dalton Trans.*, **2011**, *40*, 7817.

[56] R. B. Sears, L. E. Joyce, M. Ojaimi, J. C. Gallucci, R. P. Thummel, C. Turro, *J. Inorg. Biochem.*, **2013**, *121*, 77.

[57] A. M. Palmer, B. Peña, R. B. Sears, O. Chen, M. El Ojaimi, R. P. Thummel, K. R. Dunbar, C. Turro, *Phil. Trans. R. Soc. A*, **2013**, *371*, 20120135.

[58] E. Wachter, D. K. Heidary, B. S. Howerton, S. Parkina, E. C. Glazer, *Chem. Commun.*, **2012**, *48*, 9649.

[59] S. Betanzos-Lara, L. Salassa, A. Habtemariam, P. J. Sadler, *Chem. Commun.*, **2009**, 6622.

[60] S. Betanzos-Lara, L. Salassa, A. Habtemariam, O. Novakova, A. M. Pizarro, G. J. Clarkson, B. Liskova, V. Brabec, P. J. Sadler, *Organometallics*, **2012**, *31*, 3466.

[61] F. Barragán, P. López-Senín, L. Salassa, S. Betanzos-Lara, V. Moreno, P. J. Sadler, V. Marchán, *J. Am. Chem. Soc.*, **2011**, *133*, 14098.

[62] E. Garanger, D. Boturyn, P. Dumy, *AntiCancer Agents Med. Chem.*, **2007**, *7*, 552.

[63] L. Auzzas, F. Zanardi, L. Battistini, P. Burreddu, P. Carta, G. Rassu, C. Curti, G. Casiraghi, *Curr. Med. Chem.*, **2010**, *17*, 1255.

[64] G. Ferro-Flores, F. de M. Ramírez, L. Meléndez-Alafort, C. L. Santos-Cuevas, *Mini-Rev. Med. Chem.*, **2010**, *10*, 87.

[65] T. Giraldi, G. Sava, G. Mestroni, G. Zassinovich, D. Stolfa, *Chem. Biol. Interact.*, **1978**, *22*, 231.

[66] I. M. Dixon, J. P. Collin, J.-P. Sauvage, L. Flamigni, S. Encinas, F. Barigelletti, *Chem. Soc. Rev.*, **2000**, *29*, 385.

[67] Y. You, P. S. Young, *Dalton Trans.*, **2009**, 1267.

[68] A. Kastl, A. Wilbuer, A. L. Merkel, L. Feng, P. Di Fazio, M. Ockerb, E. Meggers, *Chem. Commun.*, **2012**, *48*, 1863.

[69] T. Tammela, G. Zarkada, E. Wallgard, A. Murtomäki, S. Suchting, M. Wirzenius, M. Waltari, M. Hellström, T. Schomber, R. Peltonen, C. Freitas, A. Duarte, H. Isoniemi, P. Laakkonen, G. Christofori, S. Ylä-Herttuala, M. Shibuya, B. Pytowski, A. Eichmann, C. Betsholtz, K. Alitalo, *Nature*, **2008**, *454*, 656.

[70] L. J. Ignarro, Nitric Oxide: Biology and Pathobiology, Elsevier Inc., Second Edition, **2010**.

[71] J. M. Fukuto, S. J. Carrington, D. J. Tantillo, J. G. Harrison, L. J. Ignarro, B. A. Freeman, A. Chen, D. A. Wink, *Chem. Res. Toxicol.*, **2012**, *25*, 769.

[72] L. Wu, R. Wang, *Pharmacol. Rev.*, **2005**, *57*, 585.

[73] L. E. Otterbein, *Antioxid. Redox Sign.*, **2002**, *4*, 309.

[74] H. P. Kim, S. W. Ryter, A. M. K. Choi, *Annu. Rev. Pharmacol. Toxicol.*, **2006**, *46*, 411.

[75] K. D. Bloch, F. Ichinose, J. D. Roberts, W. M. Zapol, *Cardiovasc. Res.*, **2007**, *75*, 339.

[76] R. Motterlini, L. E. Otterbein, *Nat. Rev. Drug. Discov.*, **2010**, *9*, 728.

[77] P. C. Ford, *Nitric Oxide*, **2013**, *34*, 56.

[78] B. J. Heilman, M. A. Gonzalez, P. K. Mascharak, *Prog. Inorg. Chem.*, **2014**, *58*, 185.

[79] R. Alberto, R. Motterlini, *Dalton Trans.*, **2007**, 1651.

[80] A. K. Patra, M. J. Rose, K. M. Murphy, M. M. Olmstead, P. K. Mascharak, *Inorg. Chem.*, **2004**, *43*, 4487.

[81] M. J. Rose , M. M. Olmstead , P. K. Mascharak, *J. Am. Chem. Soc.*, **2007**, *129*, 5342.

[82] M. J. Rose, P. K. Mascharak, *Inorg. Chem.*, **2009**, *48*, 6904.

[83] C. A. Puckett, R. J. Ernst, J. K. Barton, *Dalton Trans.*, **2010**, *39*, 1159.

[84] H. Pfeiffer, A. Rojas, J. Niesel, U. Schatzschneider, *Dalton Trans.*, **2009**, *14*, 4292.

[85] G. Dördelmann, H. Pfeiffer, A. Birkner, U. Schatzschneider, *Inorg. Chem.*, **2011**, *50*, 4362.

[86] G. Dördelmann, T. Meinhardt, T. Sowik, A. Krueger, U. Schatzschneider, *Chem. Commun.*, **2012**, *48*, 11528.

[87] C. Jedeszko, B. F. Sloane, *Biol. Chem.*, **2004**, *385*, 1017.

[88] I. Podgorski, B. E. Linebaugh, M. Sameni, C. Jedeszko, S. Bhagat, M. L. Cher, B. F. Sloane, *Neoplasia*, **2005**, *7*, 207.

[89] I. Podgorski, B. E. Linebaugh, J. E. Koblinski, D. L. Rudy, M. K. Herroon, M. B. Olive, B. F. Sloane, *Am. J. Pathol.*, **2009**, *175*, 1255.

[90] R. N. Garner, J. C. Gallucci, K. R. Dunbar, C. Turro, Inorg. Chem., **2011**, *50*, 9213.

[91] R. Yuste, F. Lanni, A. Konnerth, In Imaging: A Laboratory Manual, Cold Spring Harbor, Cold Spring Harbor Press, **1999**, *25*, 21.

[92] E. Fino, R. Araya, D. S. Peterka, M. Salierno, R. Etchenique, R. Yuste, *Front. Neural. Circuits.*, **2009**, *3*, 2.

[93] O. Filevich, M. Salierno, R. Etchenique, *J. Inorg. Biochem.*, **2010**, *104*, 1248.

[94] L. Zayat, M. G. Noval, J. Campi, C. I. Calero, D. J. Calvo, R. Etchenique, *Chembiochem*, **2007**, *8*, 2035.

[95] L. Zayat, C. Calero, P. Albores, L. Baraldo, R. Etchenique, *J. Am. Chem. Soc.*, **2003**, *125*, 882.

[96] X. Yang, D. L. Rode, D. S. Peterka, R. Yuste, S. M. Rothman, *Ann. Neurol.*, **2012**, *71*, 68.

[97] J.-P. Changeux, *Nat. Rev. Neurosci.*, **2010**, *11*, 389.

[98] E. M. Callaway, L. C. Katz, *Proc. Natl. Acad. Sci. USA*, **1993**, *90*, 7661.

[99] V. Nikolenko, K. E. Poskanzer, R. Yuste, *Nat. Methods.*, **2007**, *4*, 943.

[100] G. M. Shepherd, T. A. Pologruto, K. Svoboda, *Neuron.*, **2003**, *38*, 277.

2

Upconverting Nanoparticles as Tools for the Near-Infrared Photoactivation of Metal Complexes

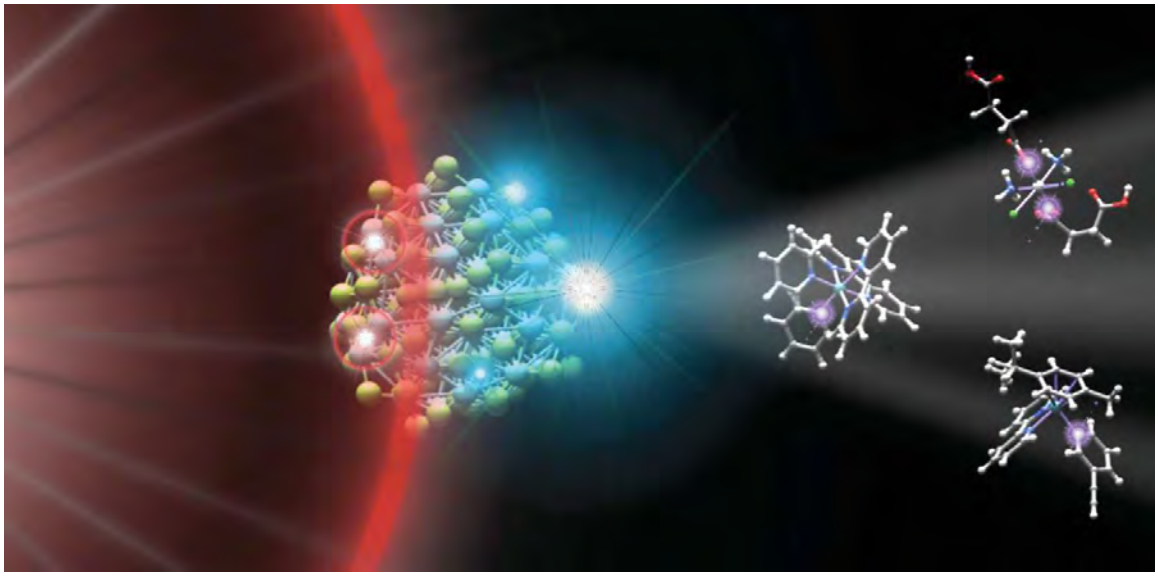

2.1 Near-infrared (NIR) light

The portion of the electromagnetic spectrum that spans from UV to near-infrared (NIR) displays different tissue penetration capacities, as a result of the distinct absorption properties that tissue constituents have. The UV-NIR light spectrum can be divided into the following regions: UVC (100−280 nm), UVB (280−320 nm), UVA (320−400 nm), blue (400−470 nm), green (470−550 nm), yellow (500−630 nm), orange−red (600−650 nm) and NIR (650−1200 nm). As shown in Fig. 1, photons of longer wavelengths have deeper penetration into various tissues (skin, brain, muscle, lung, mammary fat and liver). [1] However, irradiating at wavelengths higher than 1000 nm is not advantageous, since water also absorbs photons in this region, reducing penetration of light and causing overheating of biological components.

Prolonged light-irradiation can seriously damage tissues, especially at short wavelengths (e.g. UVC-A). Thus it is always important for medical applications to consider the maximum permissible exposure (MPE) at the selected light wavelength. The MPE of human skin for visible light (400–700 nm) is 0.2 W cm^{-2}, while MPE for NIR light can reach 1 W cm^{-2}. [2]

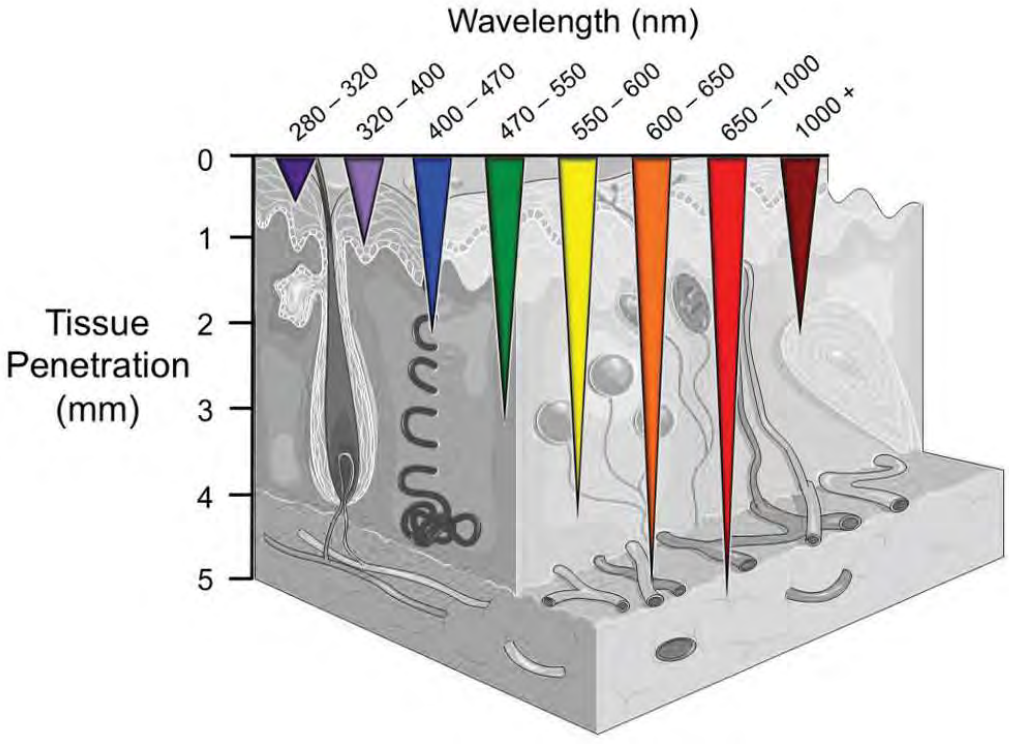

Fig. 1. Penetration depth of light with different wavelengths in skin tissue.

Therefore, NIR light is in the most appropriate range of wavelengths for maximum penetration and limited photodamage. For this reason, the so-called "phototherapeutic window" is considered to be in the range 650–1000 nm. Light of ca. 800 nm being the ideal choice since this does not cause water excitation and heating.

The great majority of light-sensitive metal-based prodrug systems are inactive upon NIR light excitation, since they usually require high-energy UV-visible light (e.g. UVA−blue light) to trigger a photochemical response. The synthetic design of metal complexes active in the phototherapeutic window for medical application is extremely challenging. Very few exceptions have been described where the photochemistry of metal complexes is prompted by red light. [3,4,5] In fact, there is a tradeoff in metal complexes between achieving good absorption in the red region of the spectrum and maintaining high photoreactivity.

This intrinsic feature in the photophysics and photochemistry of metal complexes hampers their current progress for medical applications. However, new and intriguing strategies are under development to overcome such limitations and are providing promising results. One of these strategies exploits the unique optical properties of nanoparticles (NPs) to trigger the photochemistry of metal-based prodrugs.

The work in this thesis aims at exploring the combination of metal complexes and inorganic nanoparticles to achieve activation in the "phototherapeutic window".

2.2 Photoactivation of metal-based prodrug systems by nanoparticles

Over the past few decades, significant progress has been made in the association of nanoparticles with metallodrugs for therapeutic applications. [6] In inorganic medicinal chemistry, nanoscience has attracted growing interest as it promises to solve several issues associated with conventional metal-based therapeutic agents, including their poor water solubility, lack of targeting capability, systemic toxicity, and low therapeutic index.

The combination of nanoparticles with metal complexes offers great advantages, which originate from the different and complementary properties that NPs have compared to the complexes.

The large surface area of NPs offers the opportunity to achieve high loading of different compounds (co-deliver metal complexes, targeting ligands and imaging agents) and protect them from biological degradation during transport. Since nanoparticle uptake pathways are different from the ones exploited by small molecules, drug-NP systems can potentially overcome cell drug resistance. Nanoparticles can also help to cross the blood brain barrier, which is one of the biggest problems encountered by exogenous agents in the body. [7] Moreover, nanoparticles can deliver their payload to a precise location in a controlled manner, combining the pharmacokinetics and biodistribution of different molecules. [8]

Much of the attractiveness of nanomedicine is related to NPs capacity of exploiting cellular passive and active targeting or a combination of both. [6] Passive targeting relies on the enhanced permeability and retention (EPR) effect. Nanoparticles can be preferentially accumulated in cancer tissue through the leaky vasculature of tumors and are then retained in the cancer cells due to their reduced lymphatic drainage. [9,10] Active targeting is achieved by functionalization of the nanomaterial surface with biological ligands with high affinity to tumor cells and tissues. [11] A wide number of targeting vectors have been successfully employed including nucleic acids (aptamers, e.g. A10 2'-fluoropyrimidine RNA [12]), proteins and peptides (antibodies and their fragments, e.g. VEGFR-2 [13]) or other bio-molecules (vitamins, carbohydrates, e.g. folic acid, dextran [14,15]).

In addition to these advantages, nanomaterials can also enhance the light induced reactivity of metal complexes by means of their outstanding photophysical and photochemical properties.

In particular, quantum dots (QDs) were the first class of nanoparticles to be used as triggers for the photoactivation of metal complexes. QDs are semiconductor nanocrystals with unique optical and electrical properties, which are currently employed in biomedical imaging and electronics industries. [16,17] The Ford and

Mareque groups have exploited the strong absorption cross-sections of quantum dots to improve the light-induced photochemistry of metal complexes at higher wavelengths. QDs have absorptions that extend to the red and near-infrared regions and display bright emissions. Both features depend on their composition and size and are key in photoactivation strategies. [16]

As schematized in Fig. 2, QDs can act as an antenna (donor, D) that absorbs light and transfers energy or charges to a metal compound (acceptor, A), ultimately triggering a photochemical response. Indeed, the interaction between the excited donor (D*) and the acceptor relies on three different pathways: (a) D* activates A through radiative and/or non-radiative energy transfer, (b) D* transfers an electron to A, (c) or D* receives an electron from A. [18] Finally, non-radiative deactivation of D* to the ground state can also occur. In all the described scenarios, the interaction between the excited QDs and the metal complex potentially stimulates a chemical reaction.

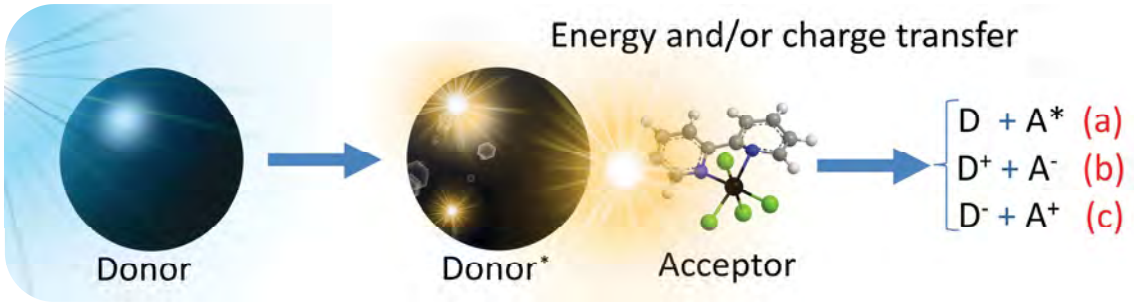

Fig. 2. (a) Schematic representation of a QD (donor, D) which triggers the photochemistry of a metal complex (acceptor, A) upon light irradiation.

In the context of phototherapy, Ford was the first to take advantage of the optical properties of CdSe@ZnS and CdTe QDs to photosensitize NO release from Cr and Ru cage compounds. [18,19,20]

In 2007, he demonstrated that CdSe@ZnS QDs at low concentrations (nM) could improve NO release from solutions of *trans*-[Cr(1,4,8,11-tetraazacyclotetradecane)$(ONO)_2$][BF_4] (CrONO, Fig. 3a) hundred times more concentrated (μM). [18,19] The complex displayed extremely poor absorption in the visible range (ε_{336} = 267 M^{-1} cm^{-1}, ε_{476} = 40 M^{-1} cm^{-1}), and QDs increased up to 6 times

the NO dissociation yield. Whereas the NO photorelease from CrONO alone was possible only at λ < 390 nm, in the CrONO-QD system the photoreaction occured at excitation wavelengths reaching 560 nm. The QD photosensitization relied on an energy transfer mechanism, which was favored by the strong electrostatic interactions between the negatively-charged nanoparticle surface and the positively-charged metal complex.

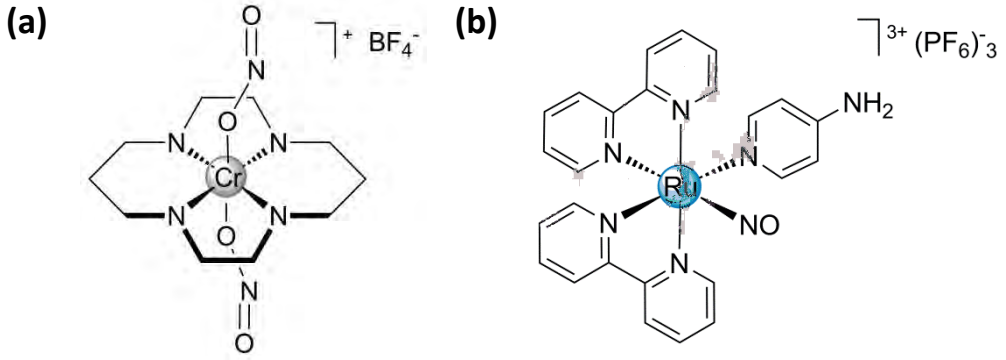

Fig. 3. Schematic representation of photoNORM (a) *trans*-[Cr(1,4,8,11-tetraazacyclotetradecane)$(ONO)_2$][BF_4] and (b) *cis*- [Ru(NO)(4-ampy)$(bpy)_2$][PF_6]$_3$.

Adopting a similar approach, Ford employed CdTe QDs as antenna for activating *cis*- [Ru(NO)(4-ampy)$(bpy)_2$][PF_6]$_3$ (where 4-ampy = 4-amino-pyridina and bpy = 2,2'-bipyridine, Fig. 3b). [20] The photoinduced release of NO from this nanosystem was achieved at 530 nm, with an enhanced efficiency of 8 times compared to direct excitation of the complex. In contrast to the CrONO-QD, CdTe QD system photosensitized the Ru complex by electron transfer.

Similarly, Mareque's efforts were directed in improving with QDs the photoactivation process of Pt^{IV} anticancer prodrugs (Fig. 4), a class of compound which rarely absorbs above 400 nm. [21]

In their first study, the group demonstrated the photosensitization of [$Pt(Cl)_4$(bpy)] (Fig. 4a), employing CdSe and CdSe@ZnS QDs. [22] Upon 530-nm excitation, both types of nanoparticles reduced the octahedral Pt^{IV} precursor to the square planar [$PtCl_2$(bpy)] with an increased efficacy (6 times) compared to the direct irradiation of the Pt complex. Remarkably, core-only CdSe QDs induced Pt reduction in the dark (although at slow rate), indicating that QD shell had a protective role, fundamental for

having a light control of the Pt prodrug activation. As in the case of the Ru-QD system reported by Ford, the mechanism of photosensitization depended on electron transfer between the nanomaterial and the metal agent.

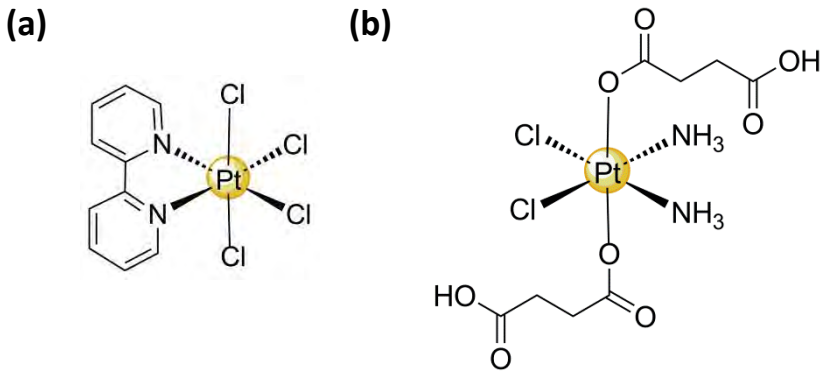

Fig. 4. Schematic representation of the Pt^{IV} prodrug complexes (a) $[Pt(Cl)_4(bpy)]$ and (b) *cis,cis,trans*-$[Pt(NH_3)_2(Cl)_2(O_2CCH_2CH_2CO_2H)_2]$.

In an optimized system, the Mareque's group fabricated water soluble nanoconstructs where the cisplatin prodrug *cis,cis,trans*-$[Pt(NH_3)_2(Cl)_2(O_2CCH_2CH_2CO_2H)_2]$ (Fig. 4b) and QDs were co-loaded in PEGylated micelles. [23] Photoinduced electron transfer by QDs generated cisplatin from inert Pt^{IV} prodrug, switching on Pt^{II} antineoplastic activity in prostate cancer cells under 630-nm irradiation. Moreover, the introduction of *fac*-$[^{99m}Tc(OH_2)_3(CO)_3]^+$ in the micelles made this system suitable for SPECT imaging.

In a recent mechanistic study we observed that the absorption of Pt on the surface of QD reduced the formation of unwanted Pt^{IV} photoproducts and maximized the generation of Pt^{II} species. [24]

Despite these momentous results achieved with CdSe-based QDs, many researchers are convinced that their intrinsic toxicity is hampering their development for biomedical applications. The major cause of QD toxicity is related to the release of Cd^{2+} and Se^{2-} ions, which are both highly toxic to cells. [25] In particular, cadmium binds to thiol groups in mitochondria, causing cellular stress and death. QDs have been found within phagocytic cells in the spleen, lymph nodes and the liver of rodents, many months after injection, demonstrating that QDs sluggish clearance would also be a key issue for medicinal use. [26]

2.3 Upconverting nanoparticles (UCNPs)

Recently, a new class of nanomaterials named upconverting nanoparticles (UCNPs) has been intensely investigated for biological and medical applications due to their exceptional optical and chemical properties. [27]

UCNPs are lanthanide-doped crystals which absorb and convert low energy NIR photons (980 or 800 nm) into high energy UV-visible light. [28,29] Advantageously with respect to QDs, UCNPs can photosensitize metal complexes via energy transfers with high penetrating and less harmful NIR light. Preliminary *in vitro* and *in vivo* studies assert these NPs as biosafe materials. [30,31]

Upconverting emission benefits from the good absorption cross-sections of UCNPs in the NIR and can be obtained by excitation with relatively low power ($0.1–10^2$ W cm^{-2}) continuous-wave lasers. Moreover, the use of UCNPs for NIR activation is advantageous compared to two-photon excitation of metal-based prodrugs. The latter approach requires expensive high-intensity ($10^6–10^9$ W cm^{-2}) pulsed laser sources and metal complexes suffer from low two-photon absorption cross section. [32,33]

Upconversion is a non-linear optical luminescence phenomenon where two or more photons are absorbed by a material and single photon of shorter wavelength (Anti-Stokes shift) is subsequently emitted. This phenomenon can proceed through different mechanisms: excited state absorption (ESA), energy transfer upconversion (ETU), photon avalanche (PA), cooperative energy transfer (CET) and energy migration-mediated upconversion (EMU). [32] In lanthanide-based upconverting nanomaterials, ETU emission is the most common mechanism, although others can occur simultaneously in the same nanosystem. [32]

Typically, UCNPs are composed of a fluorine inert matrix which offers doping sites for optically active lanthanides ions (Ln^{3+}). Ln^{3+} ions are incorporated in the host matrix by displacing the matrix-cations during the UCNP-growing process. The host matrix has high chemical stability, high transparency to NIR irradiation and low phonon-energy crystal lattice in order to reduce non-radiative emissions and maximize the upconverting process. Among all the lattices used through the years, UCNPs made with rare earth elements (RE) are the most efficient materials, in particular $NaYF_4$ and $NaGdF_4$. [28]

Ln^{3+} ions employed as dopants are divided into two classes: donors and acceptors. In the ETU pathway, the donor (typically Yb^{3+} ca. mol 20%, Fig. 5) absorbs 980 nm photons and sequentially transfers energy to the long lifetime excited levels (hundreds of microseconds or more) of the acceptor (Er^{3+}, Tm^{3+}, Ho^{3+}, Eu^{3+}, Tb^{3+} ca. mol <5%), which should have suitable electronic energy level. Once the higher electron states of the acceptors are populated, the release of UV-vis photons takes place.

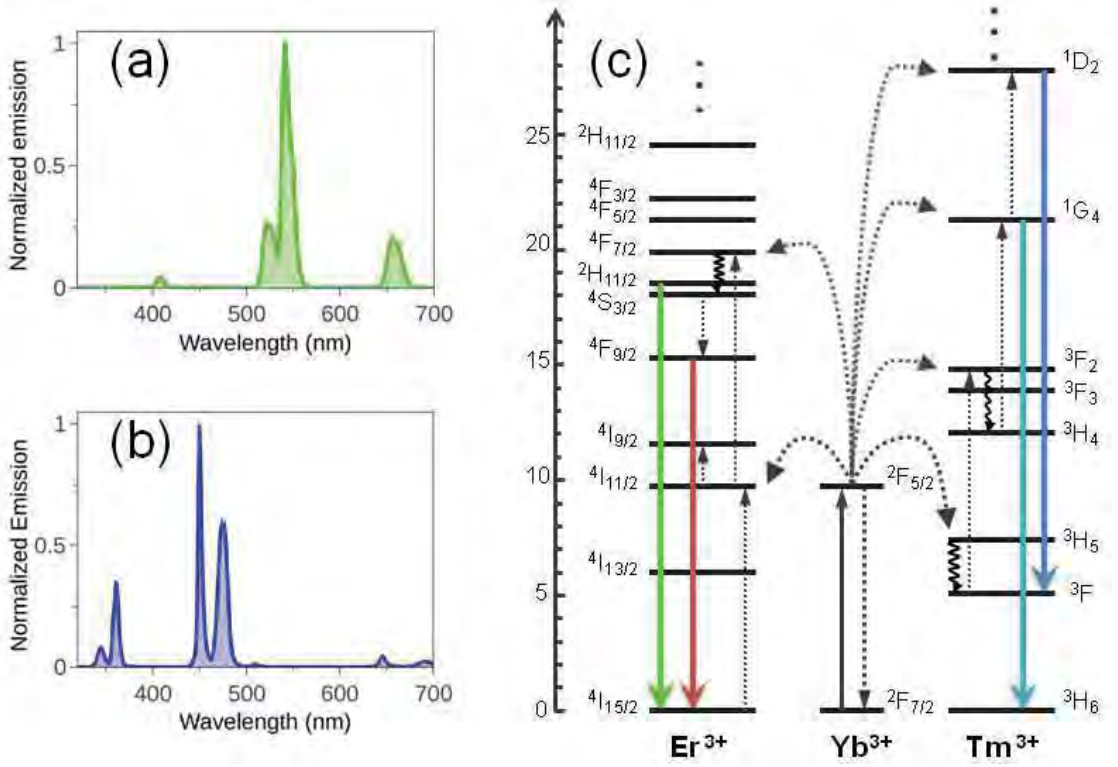

Fig. 5. Emission spectrum under 980 nm excitation of a solution of (a) $NaYF_4$:Yb/Er (20/2%) UCNPs and (b) $NaYF_4$:Yb/Tm (30/0.5%) UCNPs. (c) Energy-level diagram schemes for the Yb^{3+}-donor and Er^{3+}/Tm^{3+}-acceptors in upconverting systems.

As shown in Fig. 5, the emission profile depends on the lanthanide composition and can be easily tuned. Doping UCNPs with more than one Ln^{3+} acceptor leads to multicolor emission spectra with new emission bands arising via donor-acceptor energy transfer or multiphoton cross-relaxation acceptor-acceptor mechanisms. [28] Recently, new $NaYF_4$ nanoparticles triply doped with Nd^{3+}/Yb^{3+}/Tm^{3+} or Nd^{3+}/Yb^{3+}/Er^{3+} ions showed very promising optical properties. The absorption profile of Nd^{3+} and its interplay with Yb^{3+} energy levels allow excitation at 800 nm to achieve the typically

Tm/Er upconverted emissions. [29] This is a remarkable discovery since water absorption at 800 nm and heating effect are minimized, improving the applicability of these Nd-containing nanomaterials.

$NaREF_4$ UCNPs present two distinct crystal structures cubic (α-$NaREF_4$) and hexagonal (β-$NaREF_4$). These two crystal phases display a diverse arrangement of the rare-earth elements inside the nanocrystal. Coordination number and spatial distance vary in the two crystal lattices, thus affecting upconversion efficiency. The strongest upconverting emission occurs in the case of β-phase hexagonal $NaYF_4$ (codoped with Yb^{3+}/Er^{3+} or Yb^{3+}/Tm^{3+}). [28] Generally, upconversion emission of β-$NaYF_4$ crystals is up to two orders of magnitude more intense than in the case of α-$NaYF_4$. [34]

Although a complete characterization of the luminescence properties is crucial to compare among upconverting nanomaterials, only few publications have reported so far, the quantum yields (QYs) of upconversion. This lack of information is due to the multi-photonic nature of the upconversion process, the need of sophisticated experimental setups and challenging measurement protocols.

Van Veggel was the first to report the determination of absolute efficiencies of UCNPs at 980 nm in solution. [35]. QY values for $NaYF_4$:Yb/Er (20%/2%) with different diameter (from 10 to 100 nm) span from 0.005% to 0.3%. Upconversion luminescence increases with the size of UCNPs. The enhancement in quantum yield with size is attributed to the reduction in surface area for larger NPs which lowers the percentage of the optically active Ln^{3+} closer to the surface. This effect contains non-radiative relaxations in lanthanide ions due to solvent molecules. In the solid phase, an upconverting material is more efficient than in solution. In fact, Van Veggel reported a QY of 3% for $NaYF_4$:Yb/Er (20%/2%) as powder samples.

2.4 Synthesis of UCNPs

The two principal approaches employed to fabricate UCNPs are the hydro(solvo)thermal and the thermal decomposition methods. [36] Both strategies allow the production of NPs with controlled composition, crystalline phase and size.

Under milder heating conditions, the hydro(solvo)thermal method affords water-dispersible NPs in one-step. A typical synthesis requires that the mixture of rare earth and fluorine precursors are sealed and heated in special reaction vessels such as Teflon-lined autoclave. High pressure is crucial to increase the solubility of inorganic reactants. Surfactants and coating polymers (e.g. PEI, EDTA, PEG) are employed in order to regulate distribution and size as well as for obtaining water soluble nanoparticles. [36]

On the other hand, in a typical thermal decomposition procedure, rare-earth acetate and fluorine precursors are decomposed in high boiling-point organic solvents to give the nanomaterials. Solvents are classified into coordinating (e.g. oleic acid, oleylamine, triocylphosphine oxide) and non-coordinating (e.g. 1-octadecene) and the thermal decomposition method typically adopts a mixture of both. Post synthetic surface engineering is however required to achieve water soluble nanomaterials.

The group of Haase studied meticulously the mechanism through which this method works. [37] During the first step of the synthesis, very small nanocrystals of both α-phase and β-phase are formed. Afterwards, the less stable α-particles in solution dissolve and their constituents are re-deposit on the β-$NaREF_4$ nanoparticles, affording thermodynamically stable nanomaterials, where the surface-to-volume ratio is minimized. This kind of process is called Ostwald-ripening.

Notably, the thermal decomposition method can be repeated on synthesized UCNPs more than once to grow shells with different thickness and composition. In such a way, it is possible to modulate and/or improve the optical properties of UCNPs. [38]

Shell passivation reduces surface defects in nanocrystals and protects optically active Ln^{3+} ions from non-radiative deactivation by solvents and capping ligands. The core@shell nanoparticles are generally the brightest, with an increase in upconverted luminescence up to 10–20 times with respect to core-only nanoparticles. [39,40]

Up to now, thermal decomposition is the only method that provides core@shell UCNPs, making this synthetic procedure the preferred approach for the preparation of bright upconverting nanomaterials.

2.5 Multimodal imaging with UCNPs

Initially, UCNPs have attracted great attention for their use as inorganic probes in upconversion luminescence (UCL) imaging. UCNPs offer several benefits in comparison of other luminescence dyes, e.g. high photostability, lack of autofluorescence, high penetration depth and nonblinking emissions.

Huang and coworkers demonstrated the superior luminescence properties of these nanomaterials by performing *in vitro* microscopy experiments where organic and inorganic dyes were employed simultaneously. [41] In particular, they irradiated $NaYF_4$:Yb/Er UCNPs, 4,6-diamidino-2-phenylindole and indocarbocyanine DiI dye together, showing that only luminescence from UCNPs was preserved after prolonged light exposure. Furthermore, upconverting luminescence did not give autofluorescence from biological samples, since these could not be excited under NIR irradiation. The group of Han demonstrated that UCL signals were detectable even through a 3.2 cm thick pork tissue. Compared to QDs, UCNPs were nonblinking emitters under NIR excitation, since they presented a great amount of emission centers in one nanoparticle. [42]

These outstanding optical qualities were fundamental for the group of Li who employed $NaYF_4$:Yb/Er NPs as UCL imaging agents in one of the first *in vivo* studies (Fig. 6, [43]).

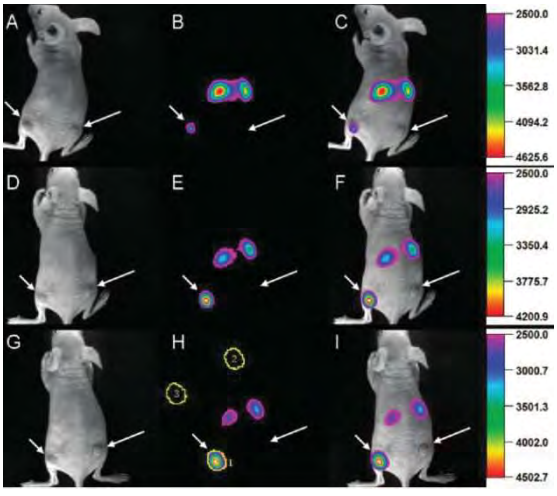

Fig. 6. *In vivo* upconverting luminescence imaging of subcutaneous U87MG cancer (left hind leg, marked by short arrows) and MCF-7 cancer (right hind leg, marked by long arrows) after UCNP intravenous injection over a 24 h period. The figure is reproduced from reference [43].

UCNPs functionalized with RGD peptide allowed targeting cancers in mice. Fig. 6 shows the high contrast images of tumor areas (U87MG and MCF-7 tumor) obtained by Li group under NIR irradiation.

Besides to their use as luminescence probes, these nanomaterials have also offered outstanding features for others imaging modalities. Their composition and structure made UCNPs suitable for magnetic resonance imaging (MRI), computed tomography (CT), positron emission tomography (PET), single-photon emission computed tomography (SPECT). [44] Often these modalities have been exploited simultaneously in one UCNP.

In MRI UCNPs were generally used for T1 weighted images (bright contrast) exploiting the well-known relaxation properties of Gd^{III} ions. In these nanomaterials, gadolinium can be employed through two approaches, e.g. as host material $NaGdF_4$ or as a free ion or Gd-complex on surface of UCNPs. The first approach is the most commonly adopted and avoids subsequent surface functionalizations which are used to attach other ligands (e.g. targeting moieties).

Gd-containing NPs showed appreciable, and in many cases, better relaxivity values than the ones displayed by clinically used agents such as Gd-DPTA (Magnevist r_1 = 3.7 mM^{-1} s^{-1} at 1.5 T). [45] Van Veggel and coworkers evaluated $NaGdF_4$ nanoparticles of different sizes and found that the relaxivity values spanned from a minimum of 3.0 mM^{-1} s^{-1} to a maximum of 7.2 mM^{-1} s^{-1} with decreasing nanoparticle diameter (from 8 nm to 2.5 nm). Increase in relaxivity with decreasing nanoparticle size followed the increase in the nanoparticle surface-to-volume ratio of smaller UCNPs. The experimental evidence was consistent with the observation that the superficial Gd^{III} ions are the mayor contributors to the relaxivity property. Remarkably, these nanomaterials had a strong relaxivity value normalized per contrast agent, which was 200–3000 times higher than the clinical agent, displaying great potentials as local contrast enhancement probe.

Another advantage of Gd-UCNPs is that they can increase the targeting capability of MRI probes through ligand-NP functionalization. The group of Mingyuan reported three UCNPs with different size (diameter = 5, 10 and 20 nm) functionalized with anti-

EGFR antibody (mAb) for tumor MRI targeting (Fig. 7). [46] The antibody selectively binds epidermal growth factor receptor, which is overexpressed in tumor cells, allowing accumulation of these UCNPs in the tumor. [47]

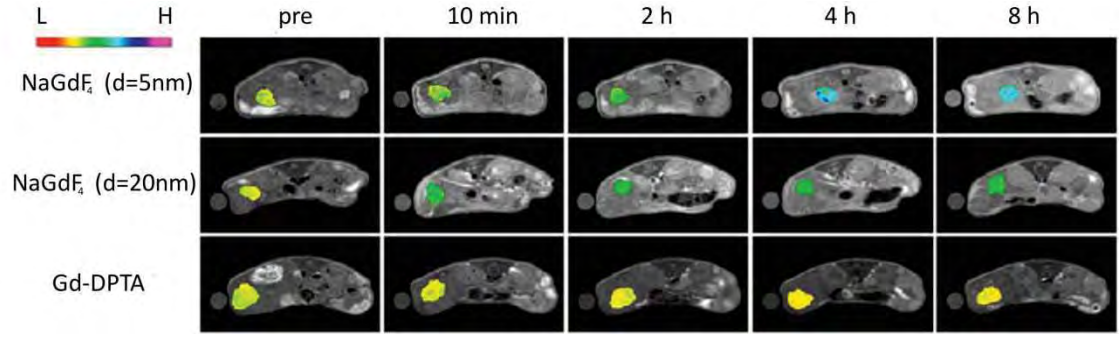

Fig. 7. T1-weighted MR images of tumor-bearing mice acquired at different time points before and after the intravenous injections of PEG-$NaGdF_4$ UCNPs d = 5 nm (top row), d = 20 nm (middle row) and Gd-DPTA. Figure is adapted from reference [46].

The relaxivity values of the three $NaGdF_4$ UCNPs (5, 10, 20 nm) were quite similar, 6.2 mM^{-1} s^{-1}, 5.7 mM^{-1} s^{-1}, and 8.8 mM^{-1} s^{-1}, respectively and all of them displayed a higher r1 value than clinically used Gd-DPTA. Surprisingly, the largest $NaGdF_4$ nanoparticles had the best value among all the MRI probes. The authors justified the result to the strong decrease in the nanoparticle tumbling time due to their large size. In fact, relaxivity of water protons is strongly dependent on the tumbling time of the contrast agent, lowering the tumbling rate of Gd^{III} ions in the NPs leads to higher r1 relaxivity.

The smallest and biggest Gd-UCNPs were both employed for targeting studies in mice bearing LS180 tumor xenografts. As show in Fig. 7, both UCNPs greatly enhanced the contrast of the tumor area in comparison to Gd-DTPA.

At the same time, lanthanides (e.g. La, Gd, Yb, Lu) also provide attractive X-ray attenuation properties, as they have high atomic number and electron density, which can block X-ray photons. For this reason, UCNPs were exploited as radiocontrasts in X-ray computed tomography to improve the imaging quality.

The group of Lu compared the X-ray absorption in solution of $NaYbF_4$:Er UCNPs to that of iobitridol, which is widely used in the clinic as a CT contrast agent (Fig. 8a). [48]

They showed that at equivalent concentrations, the X-ray absorption of UCNPs was much higher than that of iobitridol. When, a solution of $NaYbF_4$:Er nanoparticles was intravenously administered in a rat, the distribution of the particles could be effectively tracked by X-ray CT imaging at timed intervals (Fig. 8b). A clear enhancement of the signal in the heart, great vessels, liver, spleen and kidney was observed.

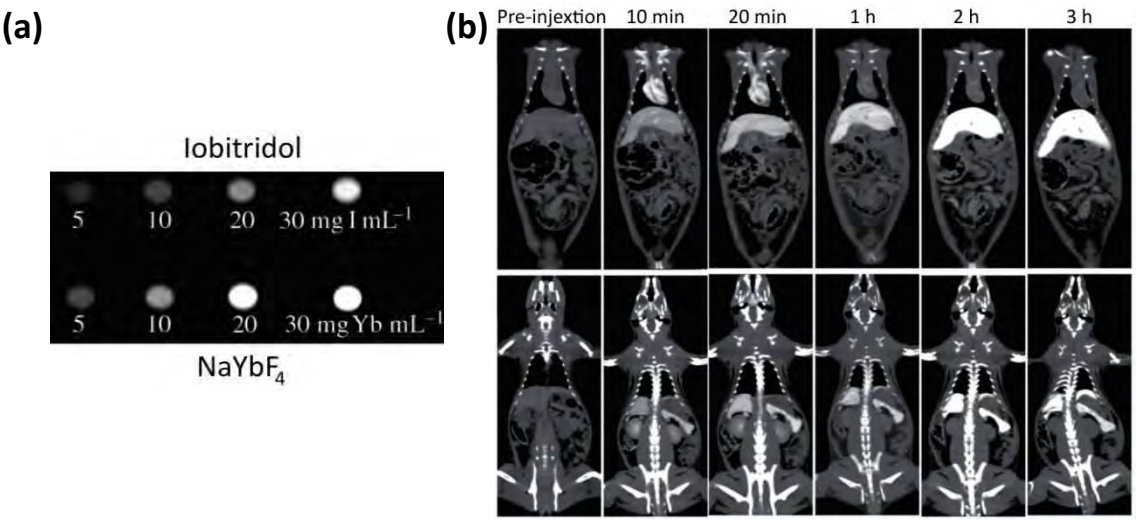

Fig. 8. (a) CT images of solutions of UCNPs and iobitridol with different concentrations of Yb and I, respectively (b) *In vivo* CT coronal view images of a rat after intravenous injection of Yb-UCNPs at different time points. (top) Heart and liver. (bottom) Spleen and kidney. Figures are adapted from reference [48].

Importantly, UCNPs can also be tracked by PET and SPECT imaging by labeling UCNPs with radioactive isotopes such as ^{18}F and ^{153}Sm.

The group of Li pioneered this field, developing a straightforward approach to functionalize $NaYF_4$ and $NaGdF_4$ particles with ^{18}F. [49,50] Using the high affinity between fluoride and cationic lanthanide ions, $^{18}F^-$ ions ($t_{1/2}$ 110 min) were trapped on the surface of UCNPs, simply by mixing nanoparticle suspension with water solution of $^{18}F^-$ for few minutes. Li group exploited this method to fabricate a variety of radiolabelled UCNPs for PET imaging of small animals (Fig. 9a) [49]

The group developed the UCNP-labeling methodologies for ^{153}Sm ($t_{1/2}$ 46.3 hours) as SPECT agent. In this case, radioactive $^{153}Sm^{3+}$ ions were directly incorporated as dopant element into the shell during the nanomaterial synthesis, obtaining

core@shell-^{153}Sm UCNPs. The resulting radio nanoagent was employed successfully in a number of *in vivo* imaging experiments (Fig 9b). [51]

Both approaches produced nanoprobes with high stability and radiochemical purity.

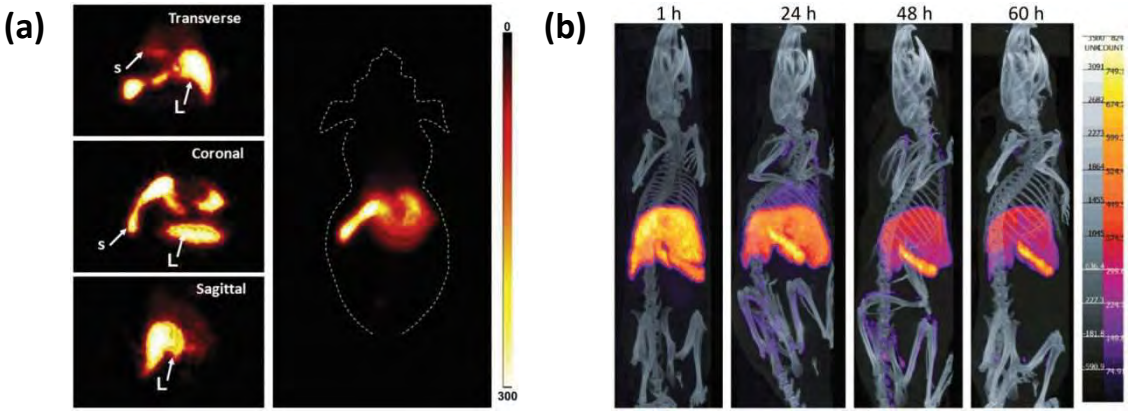

Fig. 9. (a) *In vivo* PET images of mouse acquired at 5 min after intravenous injection of UCNP-^{18}F. (b) SPECT/CT imaging of a mouse following intravenous injection of UCNP-^{153}Sm at various time points (1, 24, 48, 60 h). Figures are taken from reference [49,51].

Although UCNPs have demonstrated to be convenient nanomaterials in all these imaging techniques, their major appeal is related to their use as multimodal agents.

The development of multimodal imaging agent is a very active research area. Each imaging modality has strengths and restrictions in their different aspects, e.g. resolution, specificity and sensitivity. For example, nuclear imaging provides physiologic information (blood and lymphatic flow) or metabolic information (phosphate, sugar, nucleic acid, and some amino acids), but does not give good quality anatomical and spatial information. For this reason, PET and SPECT imaging were coupled with CT and MR imaging, which have high spatial resolution. [52] Ideally imaging probes should provide more than one modality at the same time to overcome these limitations.

Li reported $NaLuF_4$:Yb/Tm@$NaGdF_4$-^{153}Sm NPs capable of exploiting the advantages of four imaging modalities (UCL, CT, MRI and SPECT) in one nanoprobe. [51]

In these UCNPs, combination of the different imaging modalities did not affect their single performance and were optimized in such a way that:

(a) The UCL quantum yield at 800 nm was 1%, one of the best published;

(b) The X-ray attenuation of CT imaging was higher than the clinical Iopromide agent;

(c) The r1 relaxivity parameter was 18.1 s^{-1} M^{-1} at 3T scanner, amongst the highest reported;

(d) The ^{153}Sm labeling was stable and with high specific activity (740 MBq/mg).

The exceptional features of $NaLuF_4$:Yb/Tm@$NaGdF_4$^{153}Sm UCNPs were fundamental for investigating tumor angiogenesis in a mice with four imaging techniques (Fig. 10). [51]

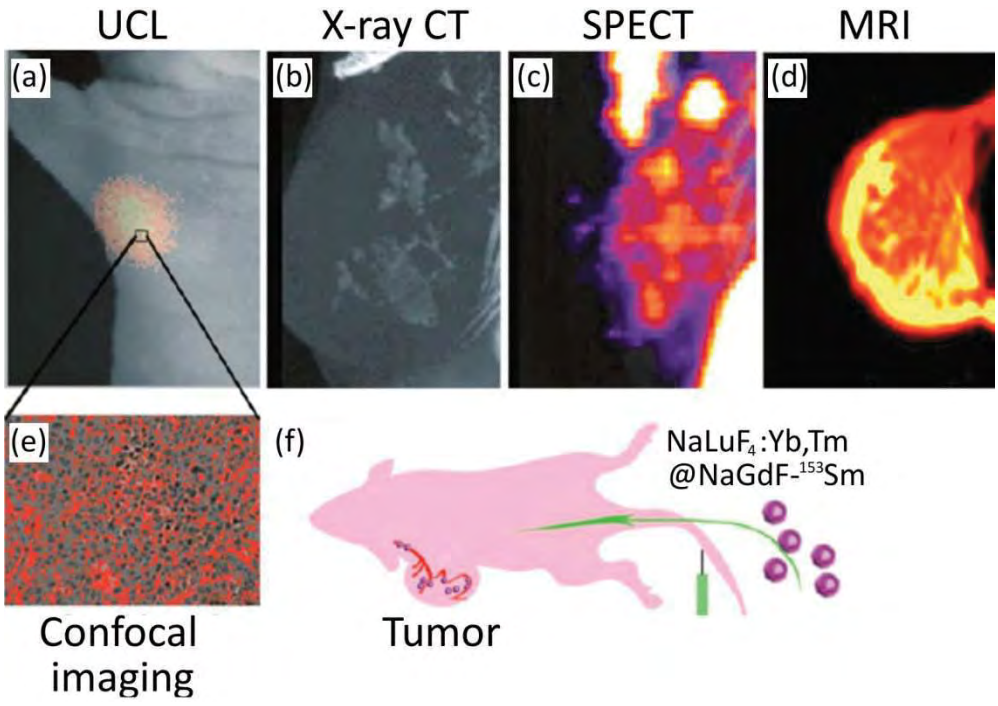

Fig. 10. Four-modal imaging of the focused cancer from the tumor-bearing nude mouse 1 h after intravenous injection of $NaLuF_4$:Yb,Tm@$NaGdF_4$-^{153}Sm. (a) *In vivo* UCL image, (b) X-ray CT image, (c) SPECT image, (d) MR imaging of tumor, (e) UCL confocal image of the paraffin section of tumor tissue. (f) Schematic illustration of tumor angiogenesis imaging using UCNPs as the probe. The figure is reproduced and adapted from reference [51].

In summary, the imaging potentials of UCNPs, in combination with their surface chemistry, make them ideal candidates for theranostic applications (the combination of therapy and diagnosis). UCNPs can be employed simultaneously as nanoplatforms for multimodal imaging and for the delivery of metal-based drugs. Theranostic is a

relevant topic in nanomedicine research, its appeal originates in the possibility of performing real-time examination of drug distribution and effects, potentially allowing clinicians to provide feedback on the treatment at earlier stages and improve therapy accuracy.

2.6 NIR activation of metal complexes by UCNPs

The interest of inorganic medicinal chemistry for upconverting nanoparticles began around four years ago motivated by the uniqueness of upconversion optical properties. UCNP-emission in the UV-vis, upon NIR excitation, can potentially activate transition metal complexes adsorbed or anchored to their surface. So far, only few examples have been published on the use of UCNPs (Er^{3+} or Tm^{3+} doped) for the near-infrared photoactivation of metal complexes, involving four metals: Mn, Fe, Ru and Pt. In this section a summary of all the systems reported to date will be presented, excluding those developed during this project which are the subject of Chapters 3–5.

All the reactions reported involve the photolysis of one or more ligands from the metal centre. The strategies adopted can be divided into three categories:

(a) The liberation of small bioactive molecules (NO, CO) from the metal coordination sphere; [53,54,55]

(b) The transformation of metal-prodrugs into biologically active metal fragments; [56,57,58,59,60,61]

(c) The controlled release of organic drugs. [62]

2.6.1 NIR-release of small bioactive molecules (NO, CO)

Ford and Zhang, in a joint article were the first to report in 2012 the NIR activation of an inorganic compound, the Roussin's black salt $Na[Fe_4S_3(NO)_7]$ (RBS). [53] The salt has a broad absorption band in the visible (400–600 nm), and can be used as photoactivatable releasing moiety of nitric oxide (NO, Fig. 11a).

As described in Chapter 1, NO plays a key role in vasodilatation, immune response, tumor growth and suppression. [63,64] Core@shell Er^{3+}-doped UCNPs were selected to attempt NIR photostimulation of RBS. The surface of the nanomaterials was coated

with a mesoporous SiO_2 shell, the pores of this layer were saturated with RBS and covered with polyallylamine hydrochloride. NO sensitive electrode (Nitric Oxide Analyzer) confirmed that nanocomposite successfully generated NO upon NIR-light remote activation.

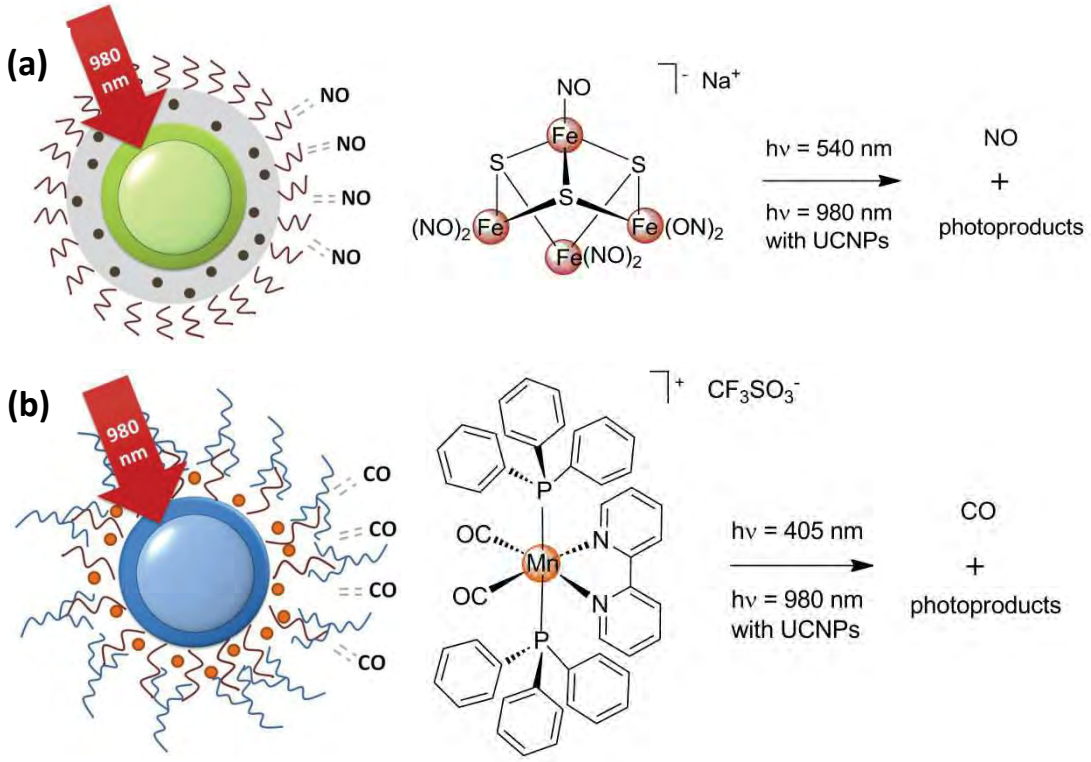

Fig. 11. Schematic representation of UCNP nanocarriers for the NIR-light photorelease of (a) NO from RBS (•) and (b) CO from the complex *cis,trans*-$[Mn(bpy)(CO)_2(PPh_3)_2][CF_3SO_3]$ (•).

In 2013, Ford implemented the same photochemical process in a more advanced system. UCNPs mixed with the RBS were encapsulated in a NIR transparent biocompatible polymer disk, as implant model for the controlled therapeutic release of NO (Fig. 12). [53] Such disk was made of a poly(dimethylsiloxane) matrix where RBS and Er- or Tm- doped core@shell $NaGdF_4$ particles were successfully trapped due to their affinity for the hydrophobic polymer. Notably, UCNPs with different acceptor element (Er^{3+}, Tm^{3+}) were able to photostimulate RBS, due to the optimized overlap between the different emission profiles of both UCNPs and the absorption property of RBS.

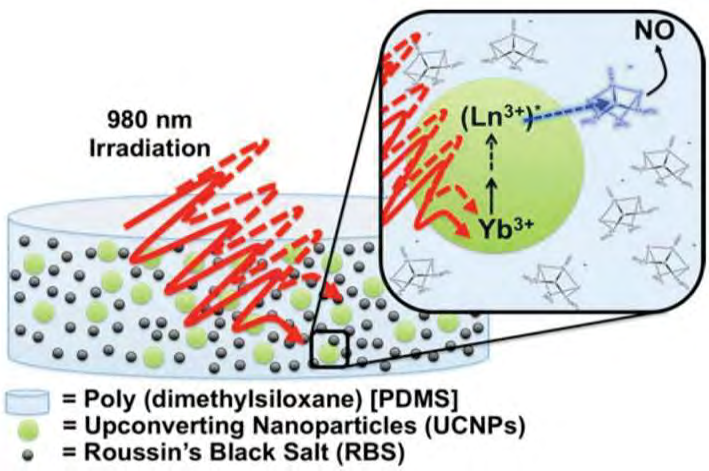

Fig. 12. Representation of a polymer disk for the NIR-light release of NO, containing UCNPs and RBS. The figure is reproduced from reference [53].

Moreover, in this case the capability of the system of NO delivery showed to be functioning also under NIR irradiation through tissues samples. Different porcine tissues (skin, muscle, fat) were employed as barrier in front of polymer disks in order to demonstrate the ability of NIR light to penetrate biological materials. Although in the presence of the tissues the amount of NO generated from the polymer disks was lower than in their absence, the quantity liberated was still biologically relevant.

Very recently, Ford and Zheng and their co-workers expanded the NIR-activation of inorganic compounds to another category of gasotransmitters using the photoCORM $[Mn(bpy)(CO)_2(PPh_3)_2][CF_3SO_3]$ (where PPh_3 = triphenylphosphine, Fig. 11b). [55] Under 470-nm excitation, the Mn complex released carbon monoxides, which is an attractive molecule for phototherapeutic applications due to its cytoprotective and anti-inflammatory properties, but it also displays antineoplastic activity.[65] In order to phototrigger the delivery of CO at longer wavelengths, a new water-soluble UCNP-system, carrying Mn complexes, was developed. The nanosystem consisted of $NaGdF_4$:Tm,Yb@$NaGdF_4$ particles functionalized with an amphiphilic PEG polymer, which provided a hydrophobic environment to entrap securely the water insoluble $[Mn(bpy)(CO)_2(PPh_3)_2][CF_3SO_3]$. Upon NIR irradiation, gas chromatography-thermal conductivity and myoglobin binding studies showed that the nanocarrier was a valid device for photochemical uncaging of CO.

2.6.2 NIR-activation of metal-prodrug candidates

In addition to the hybrid UCNP-metal complex systems which will be presented in this Ph.D. work (Chapters 3–5 [56,57,58]), three other articles have appeared in the years 2013–2016, addressing the activation of anticancer complexes with near-infrared light.

Few months ago, the group of Wang reported on the use of Tm-doped UCNPs to activate the Ru^{II} complex, $[Ru(bpy)_2(C_{18}H_{37}CN)_2]Cl_2$ by NIR light (Fig. 13). [59] Upon 400-nm irradiation, the isolated Ru complex released the two nitrile monodentate ligands, resulting in the formation of the bio-active specie $[Ru(bpy)_2(H_2O)_2]^{2+}$. As demonstrated earlier by Turro, this aqua product can potentially bind double stranded DNA and hence exert anticancer activity. [59]

The anchoring of the Ru^{II} complex on UCNPs was achieved, taking advantage of its structural features. The long aliphatic chain of the $C_{18}H_{37}CN$ ligand strongly interacted with the hydrophobic oleic acid ligands of the UCNPs, allowing the loading of the complex onto nanoparticles. Afterwards, the UCNPs were capped with PEG to improve their aqueous solubility. After demonstrating the light-triggered formation of $[Ru(bpy)_2(H_2O)_2]^{2+}$ by UV-vis (λ_{irr} = 400 nm), Wang and coworkers showed that the complex retained its DNA binding capability even after loading on UCNPs. In fact, electrophoresis demonstrated that under NIR excitation the UCNP-Ru assembly decreased the mobility of plasmid DNA, as result of DNA ruthenation, while no change was noted in dark conditions.

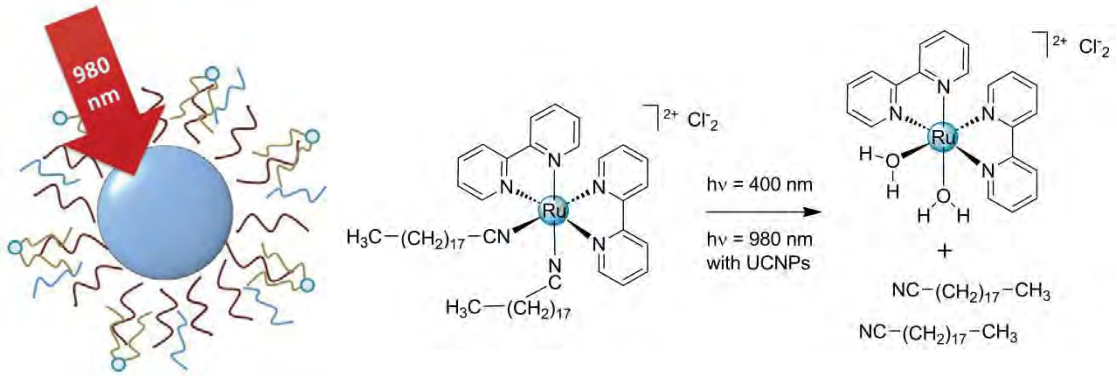

Fig. 13. Schematic representation of the NIR-light activation of the prodrug candidate $[Ru(bpy)_2(C_{18}H_{37}CN)_2][Cl]_2$ (•) mediated by UCNPs.

Expired on the success of Pt^{IV}-azido photoactivatable complexes developed by Sadler and coworkers [66], the group of Lin [60] and Xing [61] independently employed this family of compounds to investigate UCNPs as delivery platforms and light-activators. Unfortunately, the results and achievements described in their articles appear to be not sufficiently detailed on the basis of the expertise I have acquired on the subject in these three years.

The aforementioned research groups decorated the surface of UCNPs with PEI (polyethylenimine) or SiO_2 to attach *trans,trans,trans*-$[Pt(N_3)_2(NH_3)(py)(O_2CCH_2CH_2CO_2H)_2]$ and *trans,trans,trans*-$[Pt(N_3)_2(OH)(py)_2(O_2CCH_2CH_2CO_2H)]$, respectively (where py = pyridine, Fig. 14).

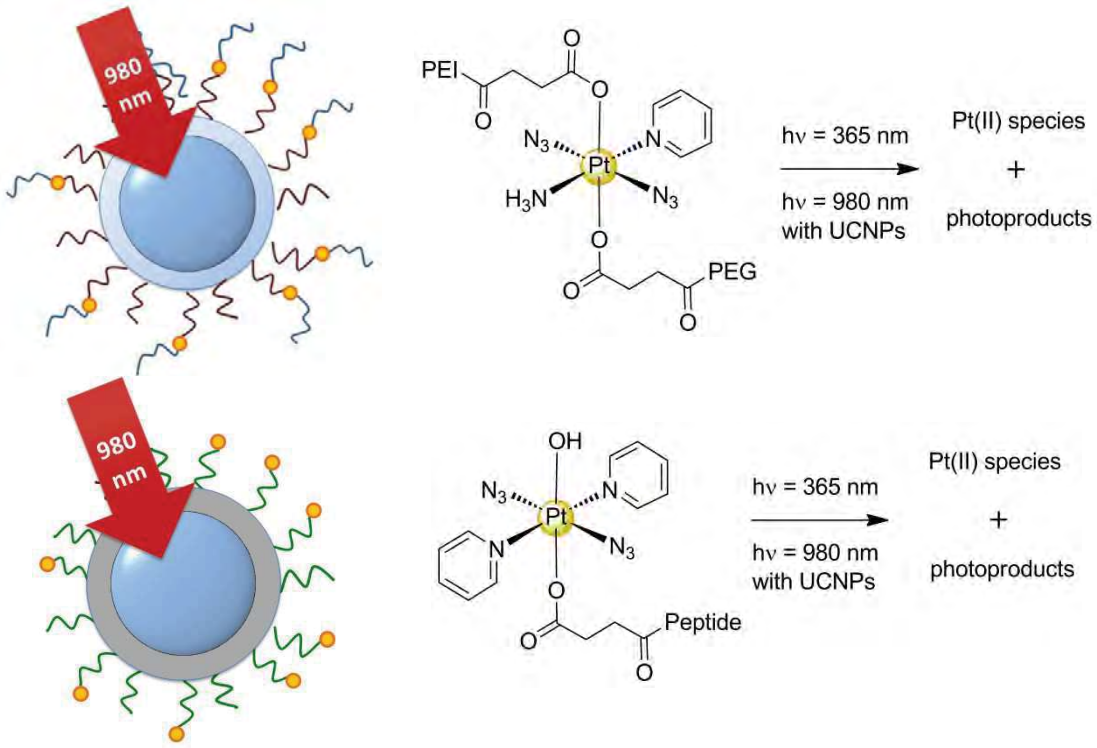

Fig. 14. Schematic representation of NIR-light generation of metal-drug candidates (a) *trans,trans,trans*-$[Pt(N_3)_2(NH_3)(py)(O_2CCH_2CH_2CO_2H)_2]$ (•) and (b) *trans,trans,trans*-$[Pt(N_3)_2(OH)(py)_2(O_2CCH_2CH_2CO_2H)]$ (•).

The photochemotherapeutic profile of these systems was then evaluated *in vitro* and *in vivo* under NIR light activation. Disappointingly, both articles did not provide any experimental evidence on the NIR activation of Pt^{IV}-azido prodrugs, despite clear

statements on their antineoplastic activities were being made. Indeed, the characterization of the Pt^{IV} photoactivation mechanism triggered by UCNPs was not reported. Although the authors proposed that a photogeneration of Pt^{II} species took place by the photolysis of two axial ligands, the mechanism of photoreaction was not confirmed by any exhaustive spectroscopic or analytical data. Both articles used changes in the absorbance spectrum of the Pt^{IV} complex as the only and decisive proof of NIR-induced Pt^{II} reduction. In the case of *trans,trans,trans*-$[Pt(N_3)_2(NH_3)(py)(O_2CCH_2CH_2CO_2H)_2]$ the observed variation in absorbance was extremely limited while for *trans,trans,trans*-$[Pt(N_3)_2(OH)(py)_2(O_2CCH_2CH_2CO_2H)]$ was not reported at all.

The poor characterization of these UCNP-Pt systems and the lack of crucial control experiments make their studies of the antineoplastic activity in cancer cells rather poor, and the results obtained *in vivo* unsatisfactory.

2.6.3 NIR-liberation of organic drugs

In 2014, the group of Wu reported a novel approach in the use of UCNPs and metal complexes for NIR-light responsive delivery systems. This approach exploited the photosensitive octahedral complex $[Ru(bpy)_2(PMe_3)((3\text{-aminopropyl})(EtO)_3Si)](PF_6)_2$ (Fig. 15) in which the silane group of the aminopropyl ligand served to covalently anchor the Ru compound on silica coated UCNPs. [62]

As in other Ru polypyridyl complexes, this ligand was effectively cleaved upon light excitation. Moreover, Wu did not use the Ru complex as prodrug or cage compound of a bioactive ligand, rather the complex acted as a photoactive molecular valve which permitted the controlled release of a chemically approved anticancer drug such as doxorubicin (Fig. 15).

Hence, the Wu group prepared $NaYF_4:Yb^{3+}/Tm^{3+}$@ $NaYF_4$ particles coated with mesoporous silica which encapsulated doxorubicin and the aforementioned silane-Ru complex. The authors suggested that the Ru complex was stably trapped behind the doxorubicin molecules inside the silica pores of NP-surface. Under NIR irradiation, the coordination bond between the metal centre and the silane-ligand broke and the

complex was liberated from the NPs, and induced consequently doxorubicin release, as demonstrated by fluorescence spectroscopy.

Upon 10–30 min of NIR excitation, Ru-UCNPs (300 µg/ml) decreased HeLa cell viability to a value of 30–40 %, while the system was nontoxic under dark conditions.

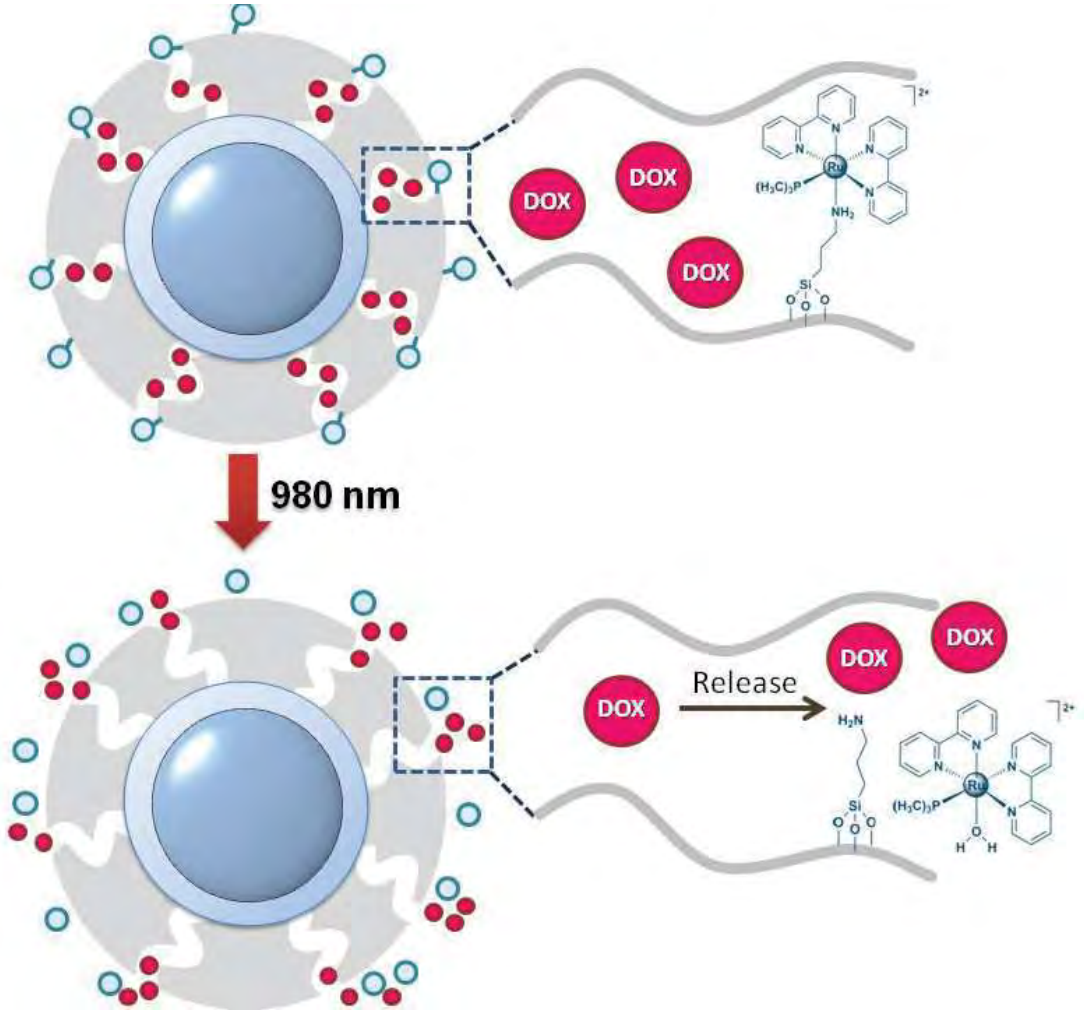

Fig. 15. Schematic representation of the nanocarrier developed by Wu and coworkers. Doxorubicin (DOX, •) is release by NIR-light activation of a $[Ru(bpy)_2(PMe_3)((3\text{-aminopropyl})(EtO)_3Si)](PF_6)_2$ (•) acting as valve. The figure is adapted from reference [62].

One of the most striking aspect of the system developed by Wu is the low power density that the system required for excitation, only 0.35 W cm^{-2}. To the best of our knowledge, such value is currently the lowest published for NIR activation of metal complexes by UCNPs. Typically, employed NIR power density ranges between few W

cm^{-2} up to hundreds W cm^{-2}. This is a key achievement considering the risks incurred upon prolonged NIR irradiation of biological issue with high power density. In 2015, Wu signaled that serious damages were noted on chicken tissues after 20 min of 974-nm irradiation at 35 W cm^{-2}. [67]

2.7 NIR-activatable chemical biological tools

In 2015, the Wu group employed again $[Ru(bpy)_2(PMe_3)((3\text{-aminopropyl})(EtO)_3Si)][PF_6]_2$ (Fig. 15) and a similar strategy in an analogous nano-system for photolithography of proteins. [68] Photolithography is a well-known process widely used in the fabrication of electronic devices (e.g. microchips). [69] This technique uses light to transfer a geometric pattern to a substrate from a photomask. The photomask is a stencil that allows the light to pass through only certain regions. The system normally contains light-sensitive compounds and mixture of polymers that become soluble or insoluble when irradiated to UV light, allowing to create a nanostructure. [70] Recently, photolithography has also been employed to pattern biomaterials e.g. proteins, cells, and extracellular matrices. [71,72,73,74,75,76] Indeed, light-induced pattering displays important advantages for the production of biotechnological and biomedical devices, such as a noncontact mode manipulation of biological systems with high spatial resolution, avoiding potential contamination. Up to now, photolithography operates with UV light, which is not optimal for biomaterials patterning (proteins, cells).

To address this issue, Wu and coworkers fabricated a self-assembled array of Ru complex-UCNPs for NIR-light protein-pattering. This nano-assembly was functionalized with bovine serum albumin as proof of concept.

Only in the exposed areas of the photomasked array, 974-nm light induced the dissociation of Ru complexes and proteins, generating a protein pattern (Fig. 16). Hence, NIR light allowed the selective protein desorption from the substrate, demonstrating the efficacy of UCNPs also as nano-agents for photolithography of biomaterials.

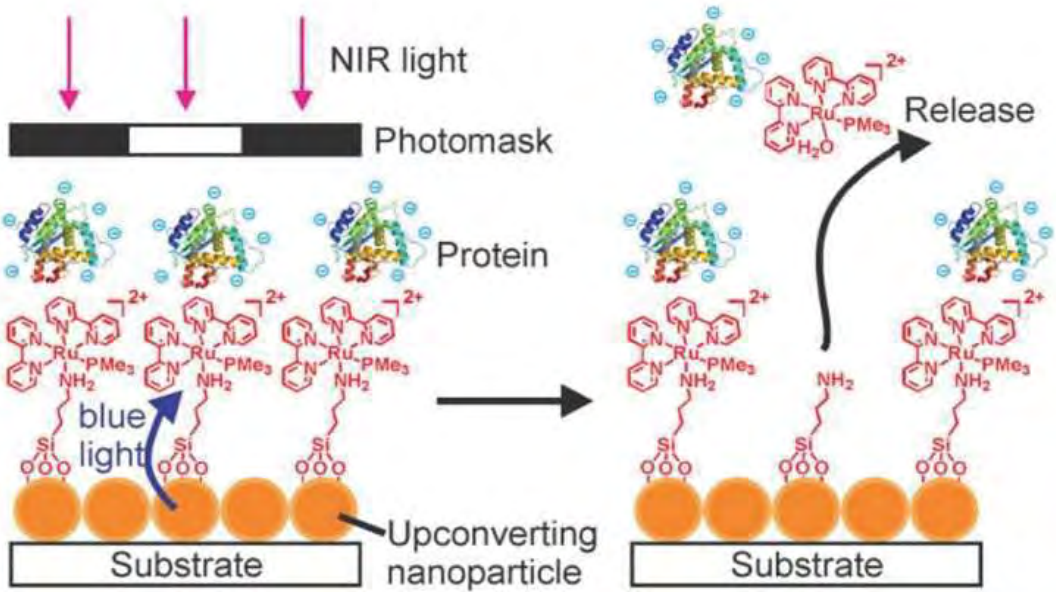

Fig. 16. Schematic representation of photon upconversion lithography. The figure is taken from [68].

2.8 Triplet-triplet annihilation upconversion (TTA-UC) as an alternative UC strategy for activating metal complexes

A different, yet attractive, photon upconversion process is triplet-triplet annihilation upconversion (TTA-UC). [77] This is a succession of different inter-molecular processes involving a sensitizer and two molecules of an annihilator. Specifically, TTA-UC populates high energy excited states of the annihilator molecule, which trigger the photochemistry of metal complexes by direct energy transfers.

In this context, Bonnet and co-workers designed a liposome delivery system, containing a porphyrin dye (1, sensitizer), a perylene moiety (2, annihilator), and the drug model $[Ru(tpy)(bpy)(S(Me)R)][PF_6]_2$ (where R is a cholesterol anchor, Fig. 17a). [78] As shown in Fig 17b, upon 630-nm light excitation, the porphyrin dye became excited and reached a triplet state via intersystem crossing (ISC). The energy was then transferred from the triplet excited porphyrin to the perylene moiety via triplet–triplet energy transfer (TTET). Afterwards, triplet–triplet annihilation (TTA) between two triplet excited perylene moieties led to a singlet excited state of one of them. The excited perylene moiety returned to the ground state, either emitting an upconverted

blue photon, or undergoing nonradiative energy transfer to prompt ligand photo-release of the Ru complex. After the cleavage of the ligand, the Ru compound was released from the liposome.

Although this liposome delivery system showed good TTA-UC quantum yield and it could be activated by low-intensity red light, it still suffered from degradation by singlet oxygen which was also produced during the TTA-UC process.

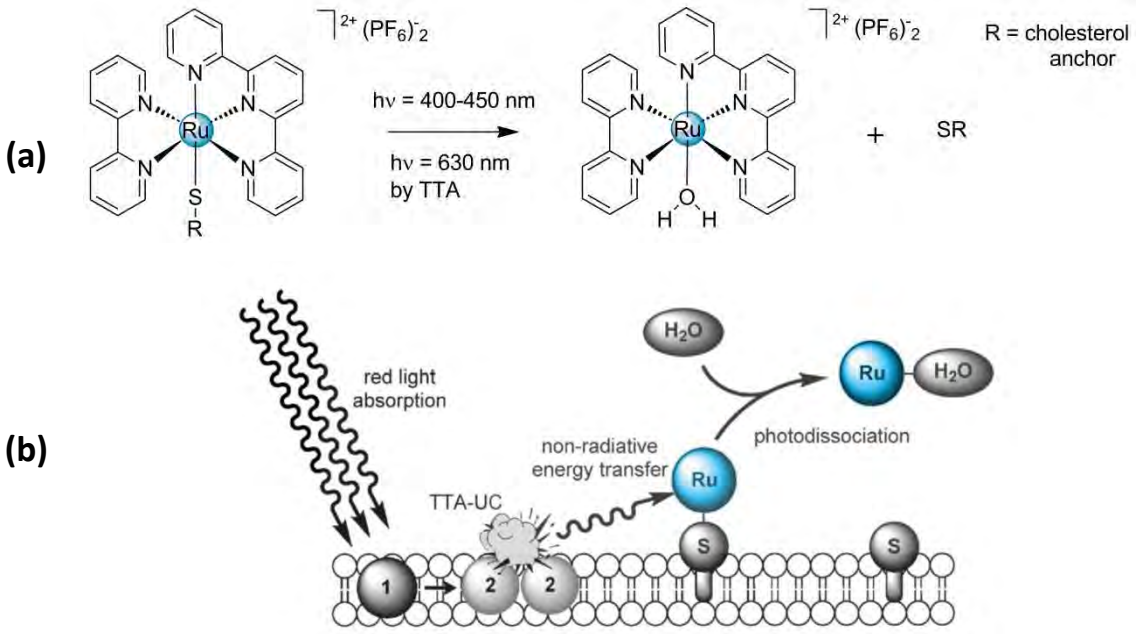

Fig. 17. Representation of the (a) light activation of $[Ru(tpy)(bpy)(S(Me)R)][PF_6]_2$ and of the (b) triplet–triplet annihilation upconversion (TTA-UC) where 1 is the sensitizer and 2 is the annihilator, followed by energy transfer to Ru complex (•) and its photodissociation. The latter figure is reproduced from reference [78].

2.9 Summary of Ph.D. research

After introducing the state of art and the advantages of combining UCNPs and metal complexes (Mn, Fe, Ru and Pt) to trigger their photochemistry in NIR range, the following three chapters will illustrate UCNP-assisted photoactivation of Ru and Pt anticancer prodrug candidates.

These chapters are the result of work published in international peer-reviewed journals.

Chapter 3: Herein the first NIR photoactivation of a metal complex *cis*-$[Ru^{II}(bpy)_2(py)_2]Cl_2$ through UCNP assistance will be presented (Fig. 18, [56]). Such complex was selected as good model for other well-known bioactive Ru polypyridyl complexes.

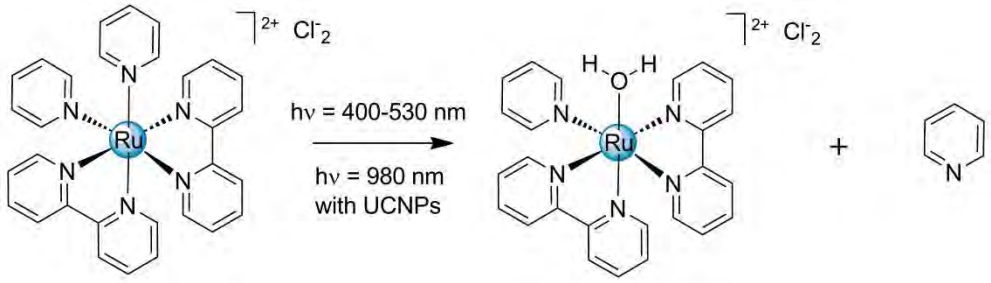

Fig. 18. Photoactivation of *cis*-$[Ru^{II}(bpy)_2(py)_2]Cl_2$ complex.

Chapter 4: This chapter describes the employ of UCNPs to photoreduce *cis,cis,trans*-$[Pt^{IV}(NH_3)_2(Cl)_2(O_2CCH_2CH_2CO_2H)_2]$ to Pt^{II} species (e.g. cisplatin) under NIR excitation (Fig. 19, [57]). The Pt^{IV} prodrug candidate was assembled with UCNPs through the functionalization of an amphiphilic PEG polymer.

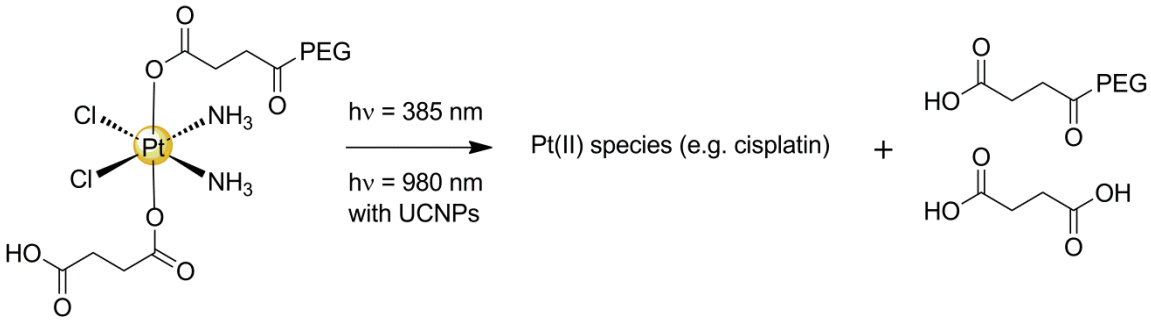

Fig. 19. Photoactivation of *cis,cis,trans*-$[Pt^{IV}(NH_3)_2(Cl)_2(O_2CCH_2CH_2CO_2H)_2]$ complex.

Chapter 5: The synthesis and full characterization of two new bioactive Ru^{II}-arene complexes, $[(\eta^6\text{-}p\text{-cym})Ru^{II}(bpy)(m\text{-CCH-Py})][PF_6]_2$ and $[(\eta^6\text{-}p\text{-cym})Ru^{II}(bpm)(m\text{-CCHPy})][PF_6]_2$ (where *p*-cym = *p*-cymene, bpm = 2,2'-bipyrimidine, and *m*-CCH-Py = 3-ethynylpyridine), is illustrated. Afterwards, the chapter reports the synthesis of a

water-soluble nanocarrier for the Ru^{II}-arene complexes which can be triggered with NIR excitation (Fig. 20, [58]).

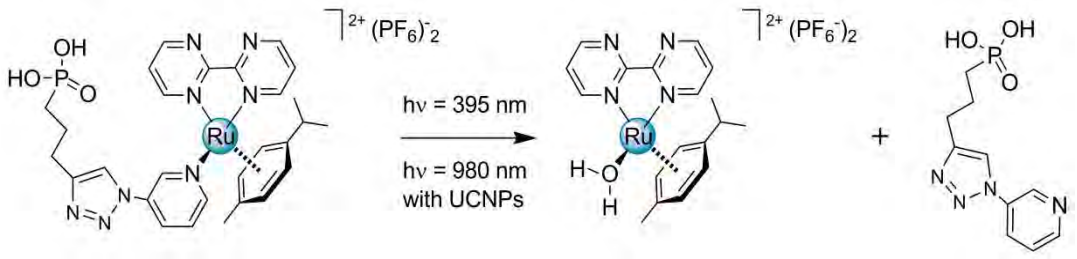

Fig. 20. Photoactivation of $[(\eta^6\text{-}p\text{-cym})Ru^{II}(bpm)(m\text{-CCHPy})][PF_6]_2$ complex.

2.10 References

[1] S. Stolik, J. A. Delgado, A. Perez, L. Anasagasti, *J. Photoch. Photobio. B*, **2000**, *57*, 90.

[2] Office for Research Safety, Northwestern University, Laser safety handbook, **2011**.

[3] E. Wachter, D. , B. S. Howerton, S. Parkin, E. C. Glazer, *Chem. Commun.*, **2012**, *48*, 9649.

[4] M. J. Rose, P. K. Mascharak, *Inorg. Chem.*, **2009**, *48*, 6904.

[5] M. J. Rose, N. L. Fry, L. Hinck, P. K. Mascharak, *J. Am.Chem. Soc.*, **2008**, *130*, 8834.

[6] C. R. Maldonado, L. Salassa, N. Gomez-Blanco, J. C. Mareque-Rivas, *Coord. Chem. Rev.*, **2013**, *257*, 2668.

[7] K. K Jain, Nanomedicine, **2012**, *7*, 1225.

[8] T. Sun, Y. S. Zhang, B. Pang, D. C. Hyun, M. Yang, Y. Xia, *Angew. Chem. Int. Ed.*, **2014**, *53*, 12320.

[9] Y. Matsamura, H. Maeda, *Cancer Res.*, **1986**, *46*, 6387.

[10] H. Maeda, *Bioconjug. Chem.*, **2010**, *21*, 797.

[11] Y. Zhong, F. Meng, C. Deng, Z. Zhong, *Biomacromolecules*, **2014**, *15*, 1955.

[12] F. Gu, L. Zhang, B. A. Teply, N. Mann, A. Wang, A. F. Radovic-Moreno, R. Langer, O. C. Farokhzad, *Proc. Natl. Acad. Sci. USA*, **2008**, *105*, 2586.

[13] D. Liu, F. Liu, Z. Liu, L. Wang, N. Zhang, *Mol. Pharmaceutics*, **2011**, *8*, 2291.

[14] S. Dong, H. Joon Cho, Y. W. Lee, M. Roman, B*iomacromolecules*, **2014**, *15*, 1560.

[15] M. Nahrendorf, H. Zhang, S. Hembrador, P. Panizzi, D. E. Sosnovik, E. Aikawa, P. Libby, F. K. Swirski, R. Weissleder, *Circulation*, **2008**, *117*, 379.

[16] M. J. Bruchez, M. Moronne, P. Gin, S. Weiss, A. P. Alivisatos, *Science*, **1998**, *281*, 2013.

[17] W. C. Chan, D. J. Maxwell, X. Gao, R. E. Bailey, M. Han, S. Nie, *Curr. Opin. Biotechnol.*, **2002**, *13*, 40.

[18] P. T. Burksa, P. C. Ford, *Dalton Trans.*, **2012**, *41*, 13030.

[19] D. Neuman, A. D. Ostrowski, R. O. Absalonson, G. F. Strouse, P. C. Ford, J. *Am. Chem. Soc.*, **2007**, *129*, 4146.

[20] L. P. Franco, S. A. Cicillini, J. C. Biazzotto, M. A. Schiavon, A. Mikhailovsky, P. Burks, J. Garcia, P. C. Ford, R. Santana da Silva, *J. Phys. Chem. A*, **2014**, *118*, 12184.

[21] N. J. Farrer, J. A. Woods, L. Salassa, Y. Zhao, K. S. Robinson, G. Clarkson, F. S. Mackay, P. J. Sadler, *Angew. Chem. Int. Ed.*, **2010**, *49*, 8905.

[22] N. Gómez-Blanco, C. R. Maldonado, J. C. Mareque-Rivas, *Chem. Commun.*, **2009**, 5257.

[23] C. R. Maldonado, N. Gómez-Blanco, M. Jauregui-Osoro, V. G. Brunton, L. Yate, J. C. Mareque-Rivas, *Chem. Commun.*, **2013**, *49*, 3985.

[24] I. Infante, J. M. Azpiroz, N. Gómez-Blanco, E. Ruggiero, J. M. Ugalde, J. C. Mareque-Rivas, L. Salassa, *J. Phys. Chem. C*, **2014**, *118*, 8712.

[25] A. M. Derfus , W. C. W. Chan, S. N. Bhatia, *Nano Letters*, **2004**, *4*, 11.

[26] S. Bellucci, Nanoparticles and Nanodevices in Biological Applications, Springer, 1, **2009**.

[27] J. Zhou, Z. Liub, F. Li, *Chem. Soc. Rev.*, **2012**, *41*, 1323.

[28] M. Haase, H. Schäfer, *Angew. Chem. Int. Ed.*, **2011**, *50*, 5808.

[29] J. Shen, G. Chen, A.-M. Vu, W. Fan, O. S. Bilsel, C.-C. Chang, G. Han, *Adv. Opt. Mater.*, **2013**, *1*, 644.

[30] Y. Sun, W. Feng, P. Yang, C. Huang, F. Li, *Chem. Soc. Rev.*, **2015**, *44*, 1509.

[31] G. H. Jang, M.P Hwang, S. Y. Kim, H. S. Jang, K. H. Lee, *Biomaterials*, **2014**, *35*, 440.

[32] H. Dong, L.-D. Sun, C.-H. Yan, *Chem. Soc. Rev.*, **2015**, *44*, 1608.

[33] N. A. Smith, P. J. Sadler, *Phil. Trans. R. Soc. A*, **2013**, *371*, 20120519.

[34] K. W Krämer, D. Biner, G. Frei, H. U Güdel, M. P Hehlen, S. R Lüthi, *Chem. Mater.*, **2004**, *16*, 1244.

[35] J.-C. Boyer, F. C. J. M. van Veggel., *Nanoscale*, **2010**, *2*, 1417.

[36] G. Chen, H. Qiu, P. N. Prasad, X. Chen, *Chem. Rev.*, **2014**, *114*, 5161.

[37] T. Rinkel, J. Nordmann, A. N. Raj, M. Haase, *Nanoscale*, **2014**, *6*, 14523.

[38] F. Vetrone, R. Naccache, V. Mahalingam, C. G. Morgan, J. A. Capobianco, *Adv. Funct. Mater.*, **2009**, *19*, 2924.

[39] F. Vetrone, R. Naccache, V. Mahalingam, C. G. Morgan, J. A. Capobianco, *Adv. Funct. Mater.*, **2009**, *19*, 2924.

[40] D. Chen, P. Huang, *Dalton. Trans.*, **2014**, *43*, 11299.

[41] M. Yu, F. Li, Z. Chen, H. Hu, C. Zhan, H. Yang, C. H. Huang, *Anal. Chem.*, **2009**, *81*, 930.

[42] A. D. Ostrowski, E. M. Chan, D. J. Gargas, E. M. Katz, G. Han, P. J. Schuck, D. J. Milliron, B. E. Cohen, *ACS Nano*, **2012**, *6*, 2686.

[43] L. Xiong, Z. Chen, Q. Tian, T. Cao, C. Xu, F. Li, *Anal. Chem.*, **2009**, *81*, 8687.

[44] J. Zhou, Z. Liub, F. Li, *Chem. Soc. Rev.*, **2012**, *41*, 1323.

[45] N. J. J. Johnson, W. Oakden, G. J. Stanisz, R. S. Prosser, F. C. J. M. van Veggel, *Chem. Mater.*, **2011**, *23*, 3714.

[46] Y. Hou, R. Qiao, F. Fang, X. Wang, C. Dong, K. Liu, C. Liu, Z. Liu, H. Lei, F. Wang, M. Gao, *ACS Nano*, **2013**, *7*, 330.

[47] W. Cai, K. Chen, L. He, A. Koong, X. Chen, *Eur. J. Med. Mol. Imaging*, **2007**, *34*, 850.

[48] Y. Liu, K. Ai, J. Liu, Q. Yuan, Y. He, L. Lu, *Angew. Chem. Int. Ed.*, **2012**, *51*, 1437.

[49] Q. Liu, M. Chen, Y. Sun, G. Chen, T. Yang, Y. Gao, X. Zhang, F. Li, *Biomaterials*, **2011**, *32*, 8243.

[50] Q. Liu, M. Chen, Y. Sun, G. Y. Chen, T. S. Yang, Y. Gao,X. Z. Zhang, F. Y. Li, *Biomaterials*, **2011**, *32*, 8243.

[51] Y. Sun, X. Zhu, J. Peng, F. Li, *ACS Nano*, **2013**, *7*, 11290.

[52] H. Kobayashi, M. R. Longmire, M. Ogawa, P. L. Choyke, *Chem. Soc. Rev.*, **2011**, *40*, 4626.

[53] J. V. Garcia, J. P. Yang, D. K. Shen, C. Yao, X. M. Li, R. Wang, G. D. Stucky, D. Y. Zhao, P. C. Ford, F. Zhang, *Small*, **2012**, *8*, 3800.

[54] P. T. Burks, J. V. Garcia, R. GonzalezIrias, J. T. Tillman, M. T. Niu, A. A. Mikhailovsky, J. P. Zhang, F. Zhang, P. C. Ford, *J. Am. Chem. Soc.*, **2013**, *135*, 18145.

[55] A. E. Pierri, P. J. Huang, J. V. Garcia, J. G. Stanfill, M. Chui, G. Wu, N. Zheng, P. C. Ford, *Chem. Commun*,. **2015**, *51*, 2072.

[56] E. Ruggiero, A. Habtemariam, L. Yate, J. C. Mareque-Rivas, L. Salassa, *Chem. Commun.*, **2014**, *50* , 1715 .

[57] E. Ruggiero, J. Hernández-Gil, J. C. Mareque-Rivas, L. Salassa, *Chem. Commun.*, **2015**, *51*, 2091.

[58] E. Ruggiero, C. Garino, J. C. Mareque-Rivas, A. Habtemariam, L. Salassa, *Chem. Eur. J.*, **2016**, *22*, 2801.

[59] Y. Chen, G. Jiang, Q. Zhou, Y. Zhang, K. Li, Y. Zheng, B. Zhang, X. Wang, *RSC Adv.*, **2016**, *6*, 23804.

[60] Y. L. Dai, H. H. Xiao, J. H. Liu, Q. H. Yuan, P. A. Ma, D. M. Yang, C. X. Li, Z. Y. Cheng, Z. Y. Hou, P. P. Yang, J. Lin, *J. Am. Chem. Soc.*, **2013**, *135*, 18920.

[61] Y. Z. Min, J. M. Li, F. Liu, E. K. L. Yeow, B. G. Xing, *Angew. Chem. Int. Ed.*, **2014**, *53*, 1012 .

[62] S. He, K. Krippes, S. Ritz, Z. Chen, A. Best, H.-J. Butt, V. Mailänder, S. Wu, *Chem. Commun.*, **2015**, *51*, 431.

[63] L. J. Ignarro, Nitric Oxide: Biology and Pathobiology, Elsevier Inc., Second Edition, **2010**.

[64] K. D. Bloch, F. Ichinose, J. D. Roberts, W. M. Zapol, *Cardiovasc. Res.*, **2007**, *75*, 339.

[65] R. Motterlini, L. E. Otterbein, *Nat. Rev. Drug. Discov.*, **2010**, *9*, 728.

[66] P. J. Bednarski, F. S. Mackay, P. J. Sadler, *Anticancer Agents Med. Chem.*, **2007**, *7*, 75.

[67] Z. Chen, W. Sun, H.-J. Butt, S. Wu, *Chem. Eur. J.*, **2015**, *21* , 9165.

[68] Z. Chen, S. He, H.-J. Butt, S. Wu, *Adv. Mater.*, **2015**, *27*, 2203.

[69] Y. Chen, A. Pépin, *Electrophoresis*, **2001**, *22*, 187.

[70] K. L. Berkowski, K. N. Plunkett, Q. Yu, J. S. Moore, *J. Chem. Educ.*, **2005**, *82*, 1365.

[71] A. M. Kloxin , A. M. Kasko , C. N. Salinas , K. S. Anseth , *Science*, **2009**, *324* , 59.

[72] J. Robertus, W. R. Browne, B. L. Feringa, *Chem. Soc. Rev.*, **2010**, *39*, 354.

[73] C. Rodriguez-Emmenegger, C. M. Preuss, B. Yameen, O. Pop-Georgievski, M. Bachmann, J. O. Mueller, M. Bruns, A. S. Goldmann, M. Bastmeyer, C. Barner-Kowollik, *Adv. Mater.*, **2013**, *25*, 6123.

[74] M. J. Salierno, A. J. García, A. del Campo, *Adv. Funct. Mater.*, **2013**, *23*, 5974.

[75] N. R. Gandavarapu, M. A. Azagarsamy, K. S. Anseth, *Adv. Mater.*, **2014**, *26*, 2521.

[76] T. Tischer, C. Rodriguez-Emmenegger, V. Trouillet, A. Welle, V. Schueler, J. O. Mueller, A. S. Goldmann, E. Brynda, C. Barner-Kowollik, *Adv. Mater.*, **2014**, *26*, 4087.

[77] J. Zhao, S. Ji, H. Guo, *RSC Advances*, **2011**, *1*, 937.

[78] S. H. C. Askes, M. Kloz, G. Bruylants, J. T. M. Kennis, S. Bonnet, *Phys. Chem. Chem. Phys.*, **2015**, *17*, 27380.

3

Near-Infrared Photolysis of a Ru Polypyridyl Complex by Upconverting Nanoparticles

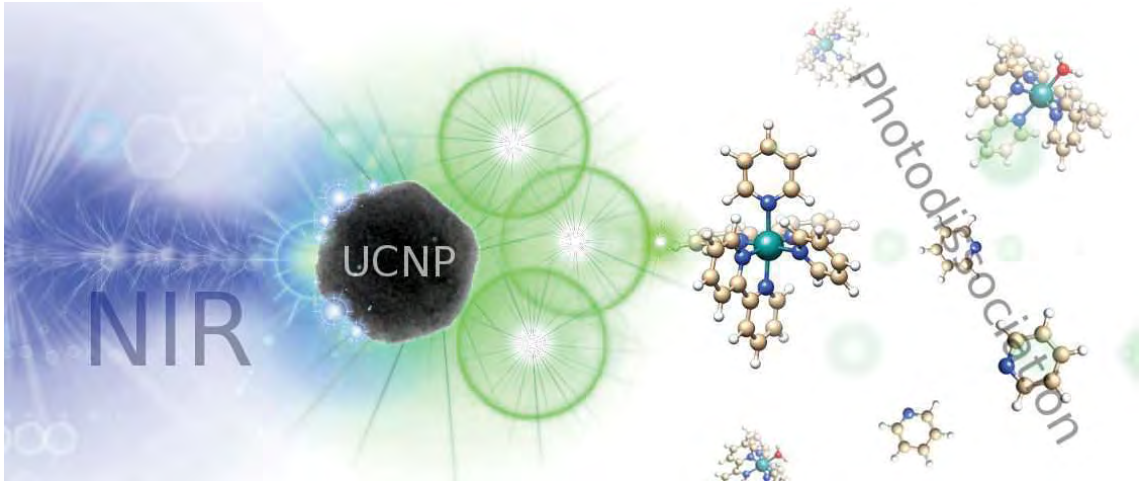

$NaYF_4:Yb^{3+}/Er^{3+}$ nanocrystals upconvert near-infrared light (980 nm) into higher energy visible photons capable of effecting the photodissociation of the monodentate pyridyl ligand in cis-$[Ru(bpy)_2(py)_2]Cl_2$: opening an opportunity for advancing the use of photoactivatable metal complexes in medicine and biology.

The work presented in this chapter was previously published: E. Ruggiero, A. Habtemariam, L. Yate, J.C. Mareque-Rivas, L. Salassa, Chem. Commun., 2014, 50, 1715.

3.1 Introduction

There is growing interest in utilizing transition metal complexes as light-activatable drugs for application in photochemotherapy and as tools for the controlled release of biologically active ligands (e.g. NO, CO, and neurochemicals). [1,2] To advance this class of compounds towards clinical use, it is imperative that their excitation wavelength should ideally emanate from the near-infrared (NIR) region, at which higher penetration and lower tissue damage occurs. However, there is a limit to the extent this could be achieved through ligand design and structural modification in the coordination compounds. In addition, any increment in red shift would invariably result in reduced photoactivity. [3] There are inevitably only a few examples reported in this field, [4] reflecting the inherent challenges that exist in metal based compounds.

An intriguing and new approach that is currently gaining momentum to overcome such limitations of metal complexes is the exploitation of the unique and superior optical properties of nanoparticles, [5,6] which can be used effectively to trigger the photochemistry of transition metal complexes, also offering the capability to act as delivery platforms and imaging agents. [7]

Rare-earth upconversion nanoparticles (UCNPs) are novel materials possessing optical properties particularly appropriate for such a strategy. In fact, UCNPs can efficiently convert highly tissue penetrating near-infrared (NIR) light into visible light via a nonlinear multiphoton process. [8] For example, $NaYF_4$ nanocrystals doped with Yb^{3+}, Tm^{3+} and/or Er^{3+} ions are able to emit blue and green light, respectively, when excited at 980 nm, a feature that has been successfully exploited for optical imaging purposes *in vitro* and *in vivo*. [9] Furthermore, UCNPs have been employed as multimodal optical/MRI/PET imaging agents due to the possibility of using Gd^{3+} ions in the composition (for MRI) or labeling with ^{18}F (for PET). [10] Coupling of UCNPs with photoactivatable metal complexes endowed with biological activity holds an enormous potential for applications in medicine. UCNPs can improve the biological impact of photoactivatable metal complexes by rendering them amenable to the design of theranostic systems, where the metal complex acts as a therapeutic prodrug and the nanoparticles as a NIR source as well as a delivery and multimodal imaging platform. Despite the promising photophysical properties of UCNPs, there are so far only very

few reports on their use as NIR triggers for photochemically active molecules. The Branda group has developed several UCNP-based photosensitive materials using organic scaffolds such as dithienylethenes [11] and 30,50-di(carboxymethoxy)benzoin, [12] while Ford and collaborators have reported the UCNP-mediated NO release from the inorganic salt $Na[Fe_4S_3(NO)_7]$ (Roussin's black). [13]

3.2 Results and Discussion

In this study we describe how UCNPs can be exploited to photoactivate the complex *cis*-$[Ru(bpy)_2(py)_2][Cl]_2$ (**1**) by NIR excitation, where bpy = 2,2'-bipyridine and py = pyridine. This complex was selected for its well-understood ability to efficiently release one pyridyl ligand and afford, in aqueous solution, the aqua adduct *cis*-$[Ru(bpy)_2(py)(H_2O)][Cl]_2$ (**2**) upon visible light (λ_{irr} = 400–530 nm) excitation (Scheme 1). [14] The photochemistry of **1** originates from the population of (d–d) ligand field dissociative states. [15,16]

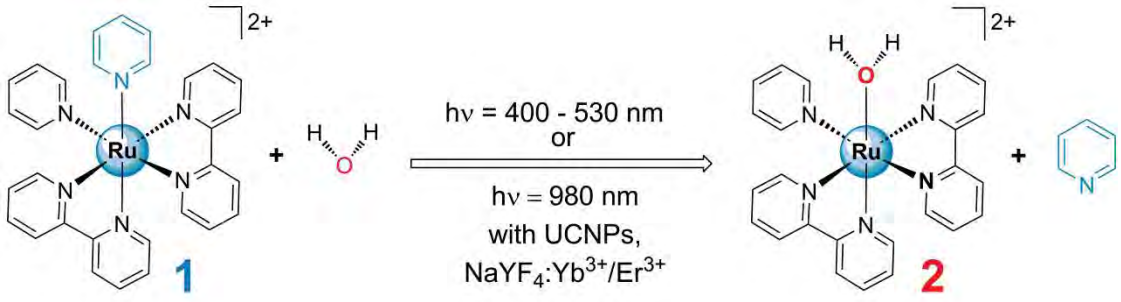

Scheme 1

Notably, **1** serves as a model for biologically active ruthenium polypyridyl complexes since systems based on the same *cis*-$[Ru(bpy)_2(L)_2]^{2+}$ scaffold and on other closely related structures are becoming promising cage compounds for the release of neurochemicals and other bioactive ligands with applications in neuronal stimulation, [17] protein inhibition [18] and cancer therapy. [19] To probe the feasibility of a UCNP as a NIR photoactivation agent for **1**, green light emitting $NaYF_4:Yb^{3+}/Er^{3+}$ (20/2mol%) nanocrystals were prepared. A previously reported synthetic procedure was adopted to afford oleate-capped hexagon-shaped nanoparticles of approximately 80 nm. [20]

Using the method described by Bogdan et al., [21] a portion of these nanoparticles were treated with aqueous HCl (pH = 4) to obtain oleate-free nanoparticles with higher water dispersibility. Suspensions of oleate free UCNPs in water resulted in significantly clearer solutions. The improved water solubility of these nanoparticles is an advantage for their use in biological environments and for bioconjugation with biocompatible molecules. Furthermore, it was previously reported that ligand-free UCNPs show increased brightness in D_2O [21] which would be an advantage for NMR photolysis studies.

The hydrophobic and hydrophilic UCNPs were characterized using TEM, IR analysis and XPS (Fig. 1 and 2).

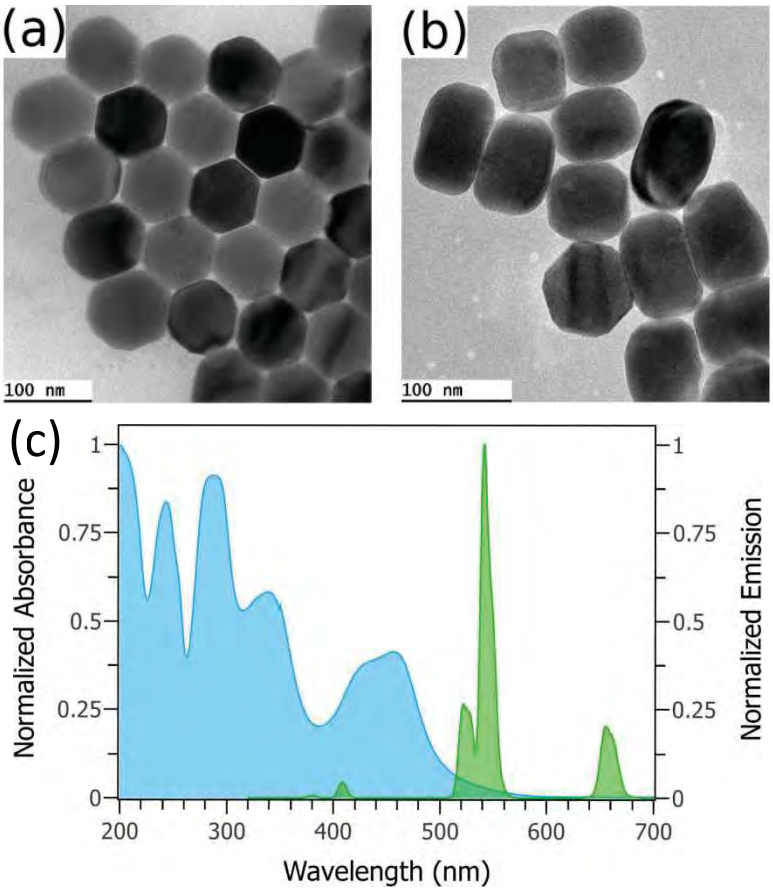

Fig. 1. TEM images of $NaYF_4:Yb^{3+}/Er^{3+}$ (20/2mol%) nanocrystals (a) capped with oleic acid and (b) oleate free; (c) overlap between the UV-Vis spectrum of 1 (blue) and the upconverted emission of the oleate-free $NaYF_4:Yb^{3+}/Er^{3+}$ UCNPs in aqueous solution (λ_{irr} = 980 nm, 4.2 W cm^{-2}) (green).

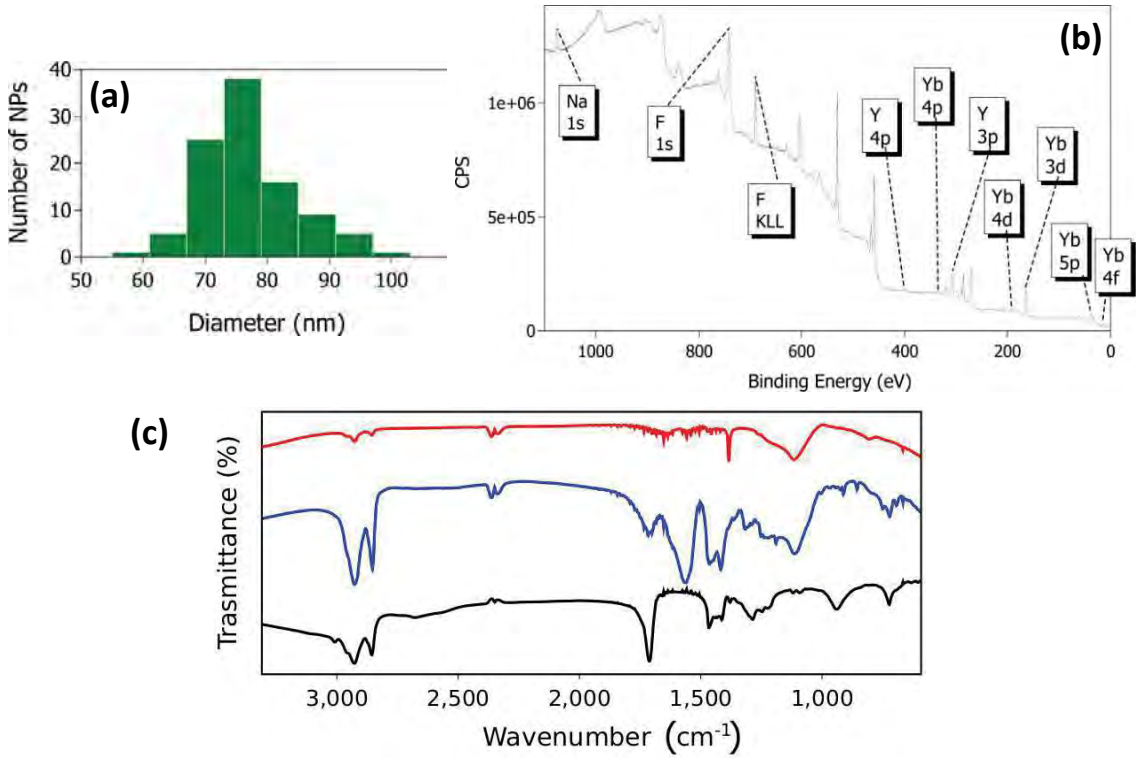

Fig 2. (a) Size distribution of $NaYF_4:Yb^{3+}/Er^{3+}$ average diameter = 80 ± 9 nm. (b) XPS spectrum of $NaYF_4:Yb^{3+}/Er^{3+}$ nanoparticles. Displayed peaks are assigned to the 1s level of Na, 1s level of F, 4p 3p 3d of Y, 4p 4d 5p 4f of Yb. (c) FT-IR spectra of $NaYF_4:Yb^{3+}/Er^{3+}$ nanoparticles colour code: black = oleic acid, blue = oleic acid capped NPs and red = oleate-free NPs.

In the case of the hydrophilic particles, removal of the oleate from their surfaces was confirmed by the disappearance of the ligand characteristic stretching frequencies in the IR spectrum. In the same solvent (THF), the two types of UCNPs have almost identical emission spectra (λ_{irr} = 980 nm) with intense maxima at 520, 541 and 654 nm, corresponding to $^2H_{11/2}\rightarrow{}^4I_{15/2}$, $^4S_{3/2}\rightarrow{}^4I_{15/2}$ and $^4F_{9/2}\rightarrow{}^4I_{15/2}$ electronic transitions, respectively. A multiphoton power dependence of the upconversion emission intensity was observed for the $^2H_{11/2}\rightarrow{}^4I_{15/2}$ and $^4S_{3/2}\rightarrow{}^4I_{15/2}$ emissions at low energy densities (Fig. 3). When dissolved in water, oleate-free UCNPs show different ratios of the bands at 541 and 654 nm compared to their hydrophobic analogues, with the latter band displaying increased intensity (Fig. 4).

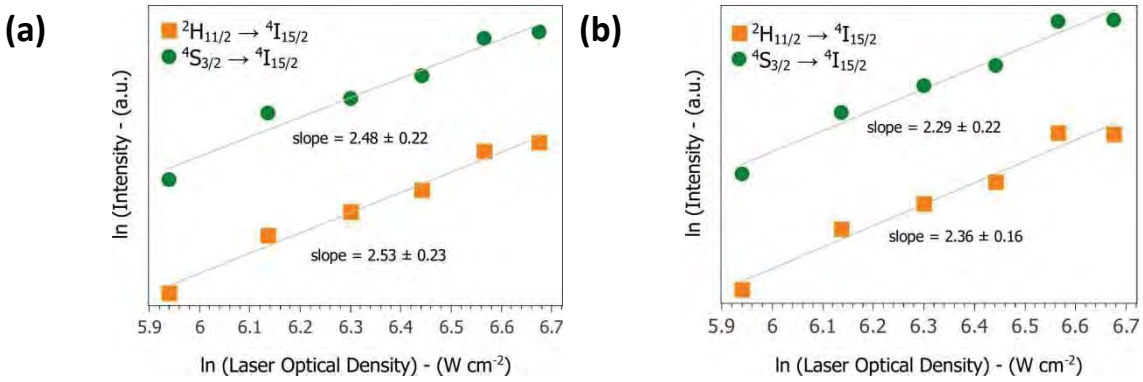

Fig 3. Power dependence of the upconverted emissions of (a) oleate-capped $NaYF_4:Yb^{3+}/Er^{3+}$ and (b) oleate-free $NaYF_4:Yb^{3+}/Er^{3+}$ nanocrystals in THF (0.4 mg/ml) excited at 980 nm.

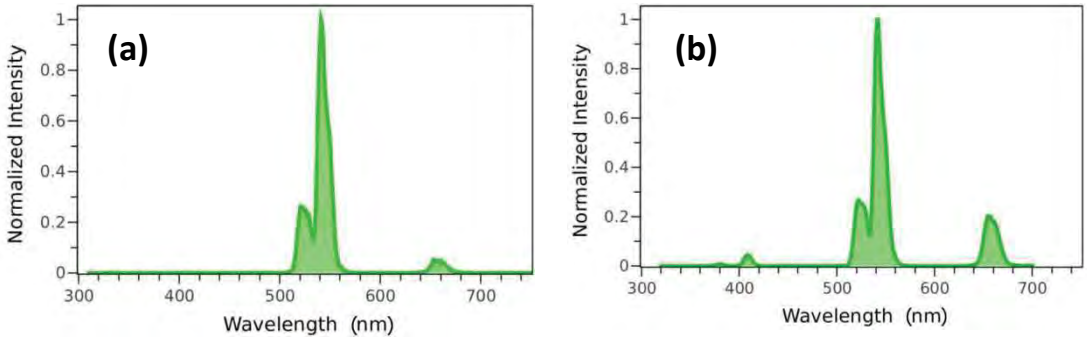

Fig 4. Upconversion emission spectra of (a) oleate-capped $NaYF_4:Yb^{3+}/Er^{3+}$ (2 mg/ml in THF) and (b) oleate-free $NaYF_4:Yb^{3+}/Er^{3+}$ (2 mg/ml in H_2O) upon NIR excitation (λ_{irr} = 980 nm, P = 4.2 W·cm^{-2}).

Fig. 1c shows the overlap between the absorption spectrum of **1** and the UCNP luminescence profile, highlighting the suitability of the upconverted emission for prompting the photochemistry of the complex.

In separate experiments oleate-capped or oleate-free $NaYF_4:Yb^{3+}/ Er^{3+}$ UCNPs (15 mg ml^{-1}) were suspended in an aqueous solution of **1** and the photolysis of the complex upon 980 nm excitation was monitored by UV-visible ([**1**] = 50 mM, Fig. 5) and NMR ([**1**] = 150 mM, Fig. 6) spectroscopes. The laser source employed was a 980 nm continuous-wave diode laser with power density set at 25 W cm^{-2}. For each time point, the solution containing **1** and the UCNPs was centrifuged and the supernatant was used for recording the UV-Vis and NMR spectra in order to minimize light scattering and the presence of paramagnetic nanoparticles. Experiments using UCNPs as the light

source were compared to the photolysis of **1** by direct excitation with visible light (λ_{irr} = 520 nm, 2–6 mW cm^{-2}). As expected, excitation of **1** with 520 nm light induces the dissociation of one pyridine ligand to afford the aqua adduct **2**. This is evident in the UV-visible spectrum in Fig. 5a in which a red shift of the metal-to-ligand charge transfer (MLCT) absorption band is observed (λ_{max} = 455→470 nm) and the presence of an isosbestic point confirms the clean conversion of **1** into **2**.

Comparable results were obtained in the presence of both oleate-capped (Fig. 5) and oleate-free (Appendix Chapter 2, Fig. A1) UCNPs under NIR irradiation (λ_{irr} = 980 nm, 25 W cm^{-2}). The red-shift corresponding to the formation of **2** was clearly evident even though no apparent isosbestic point seems to be present. In addition, a slight reduction in the intensity of the MLCT band was observed.

These variations are presumably due to the presence of residual nanoparticles in the supernatant and/or to a partial loss of complex during the centrifugation protocol (*vide experimental part*).

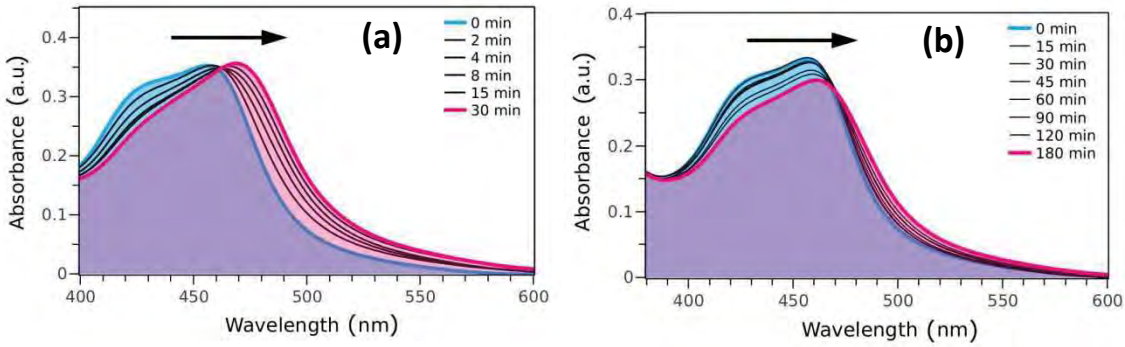

Fig. 5. Changes in the electronic absorption spectrum of **1** in aqueous solution (50 mM) upon (a) visible light excitation (λ_{irr} = 520 nm, 2 mW·cm^{-2}) and (b) NIR excitation (λ_{irr} = 980 nm, 25 Wcm^{-2}) in the presence of oleate-capped $NaYF_4$:Yb^{3+}/Er^{3+} UCNPs (15 mg ml^{-1}).

Significantly, no changes in the UV-Vis profile of **1** were observed when it was irradiated at 980 nm the absence of UCNPs, even for prolonged times (up to 4h). In fact, the only change observed was a slight loss in intensity due to solvent evaporation as a result of laser heating (Fig. 6).

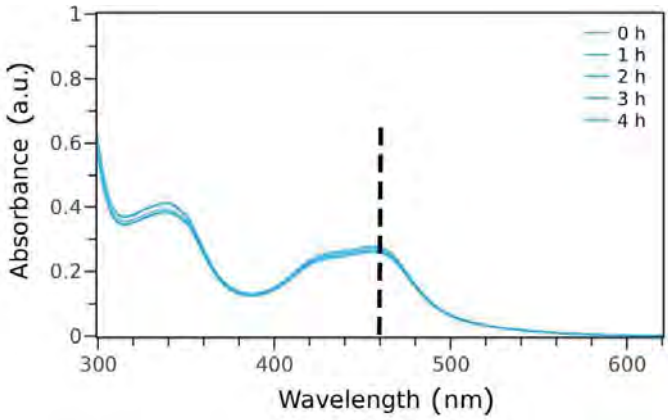

Fig. 6. NIR irradiation (λ_{irr} = 980 nm, laser power = 30 W cm^{-2}) of *cis*-[Ru(bpy)$_2$(py)$_2$]Cl$_2$ (**1**) (50 µM) in aqueous solution followed by UV-vis. The dotted line is put in correspondence of the MLCT maximum of **1** to highlight the absence of any shift in the absorption band under NIR irradiation.

The NMR studies unequivocally confirmed the capability of NaYF$_4$:Yb^{3+}/Er^{3+} UCNPs to photoactivate complex **1** with NIR light. As in the case of direct 520 nm excitation of complex solutions (Fig. 7a), light irradiation of **1** (150 mM) with 980 nm light in the presence of oleate-free UCNPs shows the formation of new peaks due to the presence of free py and generation of **2** (Fig. 7b).

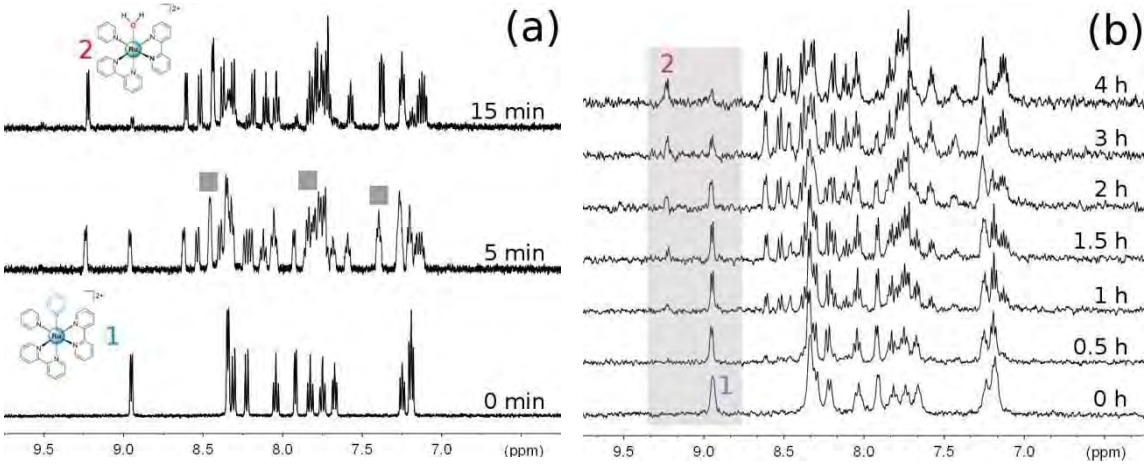

Fig. 7. Changes in ^{1}H NMR spectrum of **1** in D$_2$O (150 mM) upon (a) visible light excitation (λ_{irr} = 520 nm, 6 mW cm^{-2}) and (b) NIR excitation (λ_{irr} = 980 nm, 25 W cm^{-2}) in the presence of oleate-capped NaYF$_4$:Yb^{3+}/Er^{3+} UCNPs. (a) The free pyridine is indicated with grey ■; (b) the grey panel highlights the disappearance of the bpy signal relative to the proton in position 6 for **1** and the appearance of the analogue signal for **2**.

The resonance peaks in Fig. 7b are broader, which confirm the presence of some residual paramagnetic UCNPs in the supernatant. The course of the reaction can be easily monitored by following the signals under the grey panel, which correspond to the bpy protons in position 6 for **1** (8.96 ppm) and for **2** (9.23 ppm).

Both UV-vis and NMR spectroscopy studies clearly demonstrate that 980 nm excitation can trigger photolysis to afford the aqua adduct **2**. The use of the nanoparticles requires longer irradiation times compared to the direct visible-light photolysis. The mechanism of activation of **1** may involve (i) radiative emission from UCNPs and subsequent absorption by metal complex molecules in solution and/or (ii) energy transfer from the UCNPs to molecules of **1** which weakly interact with its surface. In the latter case, the hydrophobic interactions between the pyridine moieties of **1** and the oleate in the hydrophobic UCNPs, as well as the electrostatic interactions between the negatively charged 'naked' UCNPs and the positively charged complex, would provide enough confinement for the process to occur.

XPS studies revealed that indeed ruthenium is adsorbed onto the surface of nanoparticles for both types of UCNPs when pre-incubated in aqueous solutions (150 mM) of **1**. Extensive washing of the nanoparticles resulted in reducing the amount of ruthenium adsorbed, but still left the ruthenium clearly detectable by XPS (Fig. 8–9).

Blue emitting and smaller $NaYF_4$:Yb^{3+}/Tm^{3+} UCNPs (22 nm) were also synthesized to investigate the NIR photoactivation of **1** (Appendix Chapter 2, Fig. A2–A6) as well as to qualitatively gauge the role of upconversion quantum yield. As expected, [22] such UCNPs appeared significantly less bright and no photoactivation of **1** was achieved within 4 h of irradiation at 980 nm, even at increased laser powers (37.5 W cm^{-2}).

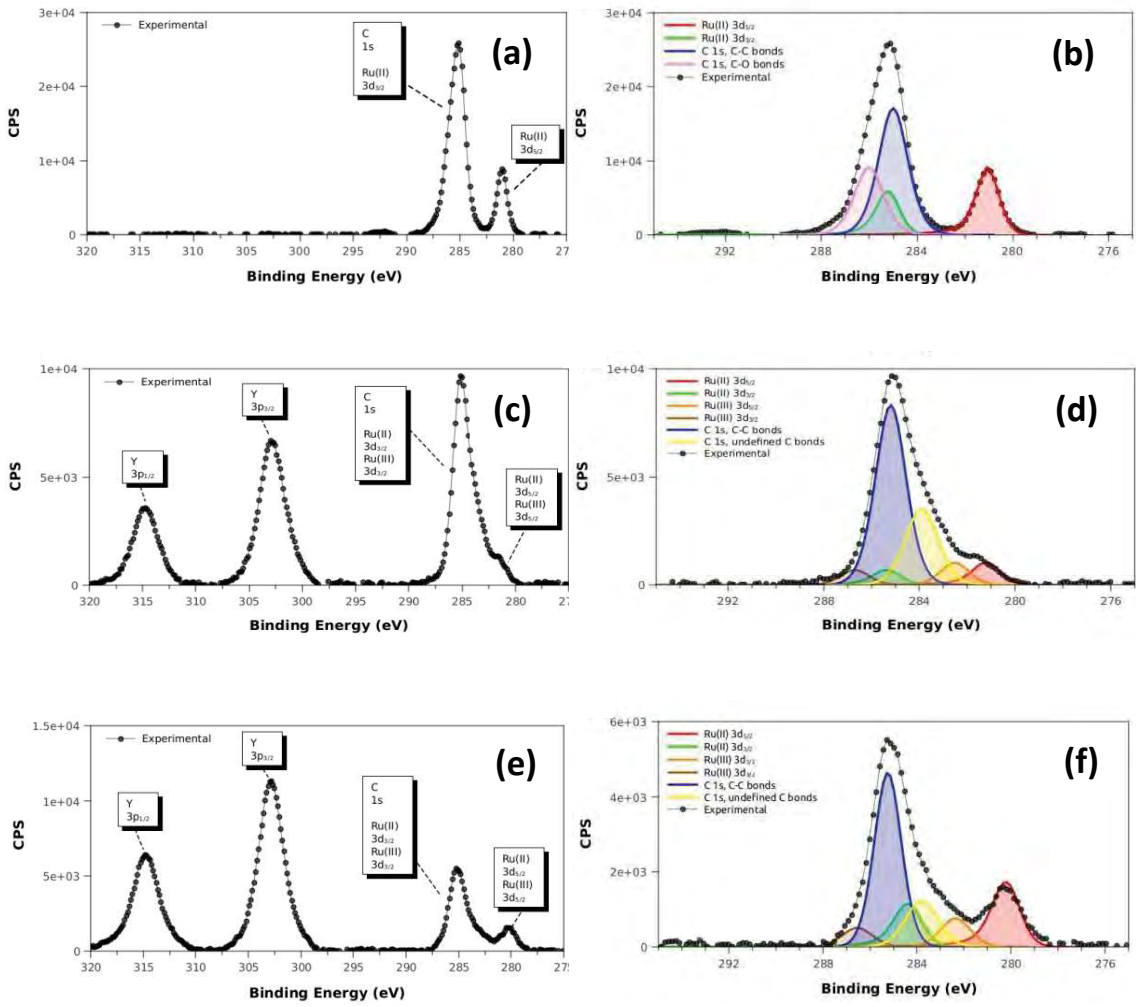

Fig. 8. (a) XPS C 1s and Ru 3d spectra and (b) fitted spectra for *cis*-$[Ru(bpy)_2(py)_2][Cl]_2$ (**1**). The Ru $3d_{3/2}$ peak overlaps with the C 1s peak. (c) XPS Y 3d, C 1s and Ru 3d spectra for the oleate-capped Er-doped UCNP-**1** sample together with corresponding C 1s and Ru 3d fitted spectra (d). The Ru $3d_{3/2}$ peaks overlap with the C 1s peak. Based on peak areas, Ru/Y for the sample is 0.087. (e) XPS Y 3d, C 1s and Ru 3d spectra for the oleate-capped Er-doped UCNP-**1** sample after washing in water together with corresponding C 1s and Ru 3d fitted spectra (f). The Ru $3d_{3/2}$ peaks overlap with the C 1s peak. Based on peak areas, Ru/Y for the sample is 0.063.

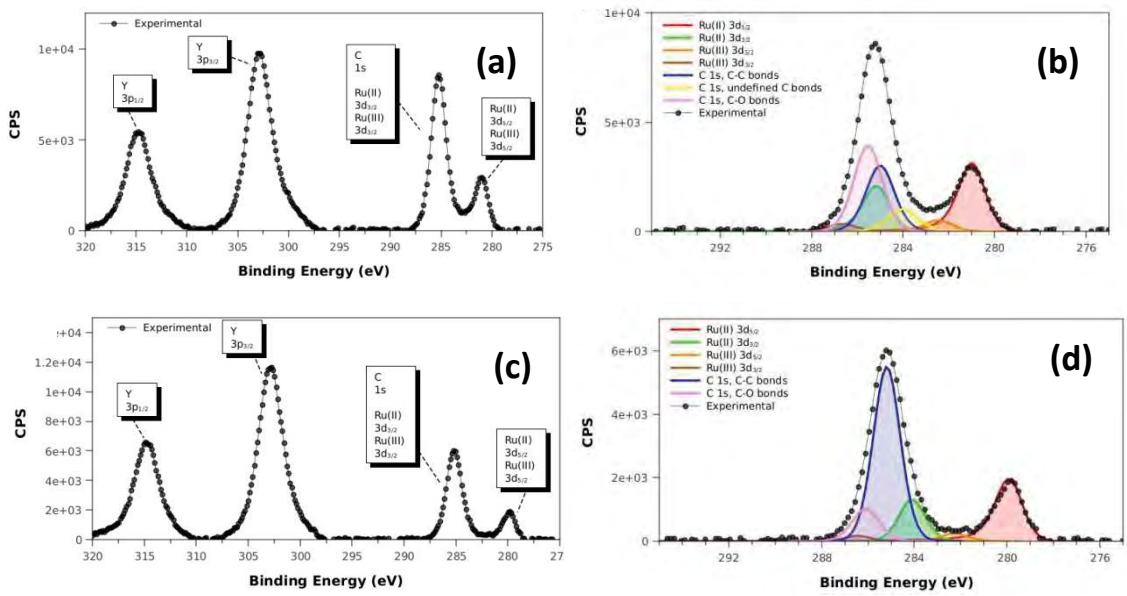

Fig. 9. (a) XPS Y 3d, C 1s and Ru 3d spectra for the oleate-free Er-doped UCNP-**1** sample together with corresponding C 1s and Ru 3d fitted spectra (b). The Ru $3d_{3/2}$ peaks overlap with the C 1s peak. Based on peak areas, Ru/Y for the sample is 0.098. (c) XPS Y 3d, C 1s and Ru 3d spectra for the oleate-free Er-doped UCNP-**1** sample after washing in water (d) together with corresponding C 1s and Ru 3d fitted spectra (B). The Ru $3d_{3/2}$ peaks overlap with the C 1s peak. Based on peak areas, Ru/Y for the sample is 0.050.

In conclusion, we have demonstrated here that photolysis of **1** which resulted in the release of pyridine and formation of the aqua adduct **2** can be achieved by exploiting the emission properties of $NaYF_4:Yb^{3+}/Er^{3+}$ UCNPs. To the best of our knowledge, this is the first example of UCNP-mediated photoactivation of a metal complex. The significance of these findings is worth noting, as the polypyridyl Ru complex studied in this work belongs to a class of derivatives with unique photochemical properties, which have shown great promise for the development of photoactivatable prodrugs.

3.3 Conclusions

This contribution clearly highlights that UCNPs offer a viable strategy for activating metal complexes at wavelengths more suitable for in vivo applications, although the

consequences of laser heating on biological tissues will need to be considered carefully. The upconversion efficiency is a key factor to target for future developments. UCNPs rely on energy transfer for activating metal complexes, hence the overlap between the emission of the donor and the absorption of the acceptor as well as their proximity to each other are important parameters for consideration. Covalent assembly of metal complexes on the UCNP surface (although not strictly needed) is likely to enhance the photolysis rate because of the possibility of a more efficient non-radiative energy transfer. Optimization of the aforementioned aspects offer the potential to lead to advances which will pave the way to the design of photoactivatable materials for theranostics based on metal complexes and UCNPs.

3.4 Experimental Section

3.4.1 Materials

All chemical reagents, yttrium(III) acetate hydrate (99.9%), ytterbium(III) acetate tetrahydrate (99.9%), erbium(III) chloride hexahydrate (99,9%), thulium(III) acetate hydrate (99.9%), 1-octadecene (technical grade, 90%), oleic acid (technical grade, 90%), sodium hydroxide (≥ 97%), ammonium fluoride (98%) and solvents were purchased from Sigma-Aldrich. Nanopure water was obtained using the Barnstead Nanopure Ultrapure Water Purification System.

3.4.2. Synthesis of oleate-capped $NaYF_4:Yb^{3+}/Er^{3+}$

The synthesis of oleate-capped $NaYF_4:Yb^{3+}/Er^{3+}$ UCNPs was achieved by using a slightly modified version of the protocol reported by Boyer et al. [20]. The ratio of rare earth elements used during the synthesis was the following: Y/Yb/Er 78/20/2 mol%. The scale of the synthesis was 1.5 mmol.

In a 100 ml three-neck round-bottom flask equipped with a water-cooled condenser, yttrium(III) acetate hydrate (312 mg, 1.17 mmol), ytterbium(III) acetate tetrahydrate (127 mg, 0.30 mmol), erbium(III) chloride hexahydrate (11 mg, 0.03 mmol) were dissolved in 1-octadecene (22.5 ml) and oleic acid (14.0 ml). The reaction mixture was stirred and heated slowly to 120 °C under vacuum. By maintaining such

conditions for 30 min, the lanthanide oleate complexes were formed and residual water and oxygen were removed by evaporation, observing a change in the solution, from turbid to transparent. The temperature was then lowered to 50 °C and the reaction flask placed under a gentle flow of nitrogen gas. Successively, a solution of sodium hydroxide (150 mg, 3.75 mmol) and ammonium fluoride (222 mg, 6.0 mmol) in methanol (5 ml) was prepared and was added to the reaction flask, drop wise (1 ml/min). The mixture was initially stirred for 30 min at 50 °C followed by stirring for a further 30 min at 70 °C in order to eliminate completely the excess methanol from the reaction vessel. The methanol-free reaction mixture was then heated up to 295 °C and maintained at this temperature for 90 min. During this period the solution became progressively clearer eventually forming a clear transparent solution at which point the reaction mixture was allowed to cool to ambient temperature.

The nanoparticles were obtained from the reaction mixtures via centrifugation at 4500 rpm at 20 °C for 15 minutes as a pellet. The pellet was dispersed in ethanol (30 ml) and centrifuged again. The new pellet was finally dispersed in THF (5 ml) and ethanol (25 ml) and collected via centrifugation. The resulting nanoparticles were dried under ambient conditions. In a typical preparation about 280 mg of product is obtained.

3.4.3. Synthesis of oleate-capped $NaYF_4:Yb^{3+}/Tm^{3+}$

The same protocol described above for oleate-capped Er-doped UCNPs was employed for $NaYF_4:Yb^{3+}/Tm^{3+}$nanocrystals. In the latter case, the reaction mixture was maintained at 295 °C for 60 min instead of 90 min to obtain NPs of smaller size. The ratio of rare earth elements used was Y/Yb/Tm 69.5/30/0.5 mol%. The scale of the synthesis was 1.5 mmol.

3.4.4. Synthesis of oleate-free $NaYF_4$: Yb^{3+}/Er^{3+} and oleate-free $NaYF_4$: Yb^{3+}/Tm^{3+}

The oleate-free nanoparticles were obtained using the procedure reported by N. Bogdan et al. [21].

3.4.5. Synthesis of cis-$[Ru(bpy)_2(py)_2]^{2+}$ (1)

The complex cis-$[Ru(bpy)_2(py)_2]^{2+}$ was synthesized as a ClO4 salt following the method of Dwyer et al. [Aust. J. Chem. 1963, 16, 544–548] and then as chloride derivative following the procedure published by Borfecchia et al. [23].

3.4.6. Photolysis of cis-$[Ru(bpy)_2(py)_2][Cl]_2$ (1) with and without UCNPs

Aqueous solutions of 1 were photoirradiated under visible (450 nm and 520 nm) and near-infrared (980 nm) light. A KiloArc light source was employed in the case of visible light irradiation, providing 1.5 $mW \cdot cm^{-2}$ for 450 nm excitation or 2 or 6 $mW \cdot cm^{-2}$ for 520 nm excitation. Aqueous solution of 1 (50 µM for UV-Vis and 150 µM for NMR) were placed in a cuvette under constant stirring and the evolution of the photoreaction was followed by UV-Vis or NMR.

For NIR photolysis experiments, a 980 nm laser diode (CNI, MDL-N-980) was used to irradiate (25–37.5 $W \cdot cm^{-2}$) aqueous solutions of 1 (50 µM for UV-Vis and 150 µM for NMR) in the presence of UCNPs (15 mg/ml). Typically suspensions containing 1 and UCNPs were placed in a cuvette under constant stirring and the irradiation of 1 was followed by UV-Vis and NMR. Before acquisition of spectra, the suspension was centrifuged for 5 min at 12500 rpm to remove NPs and improve the quality of measurements. The surnatant was used to record UV-Vis or NMR spectra and afterwards was used to re-dissolve the UNCP pellet to obtain the initial suspension used for irradiation experiments.

3.5 References

[1] N. J. Farrer, L. Salassa, P. J. Sadler, *Dalton Trans.*, **2009**, 10690.

[2] U. Schatzschneider, *Eur. J. Inorg. Chem.*, **2010**, 1451.

[3] J. N. Demas, B. A. DeGraff, *Anal. Chem.*, **1991**, *63*, A829.

[4] M. J. Rose, P. K. Mascharak, *Inorg. Chem.*, **2009**, *48*, 6904.

[5] D. Neuman, A. D. Ostrowski, A. A. Mikhailovsky, R. O. Absalonson, G. F. Strouse, P. C. Ford, *J. Am. Chem. Soc.*, **2008**, *130*, 168.

[6] C. R. Maldonado, N. Gomez-Blanco, M. Jauregui-Osoro, V. G. Brunton, L. Yate, J. C. Mareque-Rivas, *Chem. Commun.*, **2013**, *49*, 3985.

[7] C. R. Maldonado, L. Salassa, N. Gomez-Blanco, J. C. Mareque-Rivas, *Coord. Chem. Rev.*, **2013**, *257*, 2668.

[8] A. Gnach, A. Bednarkiewicz, *Nano Today*, **2012**, *7*, 532.

[9] J. Zhou, Z. Liu, F. Li, *Chem. Soc. Rev.*, **2012**, *41*, 1323.

[10] J. Zhou, M. Yu, Y. Sun, X. Zhang, X. Zhu, Z. Wu, D. Wu, F. Li, *Biomaterials*, **2011**, *32*, 1148.

[11] C.-J. Carling, J.-C. Boyer, N. R. Branda, *Org. Biomol. Chem.*, **2012**, *10*, 6159.

[12] C.-J. Carling, F. Nourmohammadian, J.-C. Boyer, N. R. Branda, *Angew. Chem., Int. Ed.*, **2010**, *49*, 3782.

[13] J. V. Garcia, J. Yang, D. Shen, C. Yao, X. Li, R. Wang, G. D. Stucky, D. Zhao, P. C. Ford, F. Zhang, *Small*, **2012**, *8*, 3800.

[14] D. V. Pinnick, B. Durham, *Inorg. Chem.*, **1984**, *23*, 1440.

[15] L. Salassa, C. Garino, G. Salassa, R. Gobetto, C. Nervi, *J. Am. Chem. Soc.*, **2008**, *130*, 9590.

[16] E. Borfecchia, C. Garino, L. Salassa, T. Ruiu, D. Gianolio, X. Zhang, K. Attenkofer, L. X. Chen, R. Gobetto, P. J. Sadler, C. Lamberti, *Dalton Trans.*, **2013**, *42*, 6564.

[17] E. Fino, R. Araya, D. S. Peterka, M. Salierno, R. Etchenique, R. Yuste, *Front. Neural Circuits*, **2009**, *3*, 1.

[18] T. Respondek, R. N. Garner, M. K. Herroon, I. Podgorski, C. Turro, J. J. Kodanko, *J. Am. Chem. Soc.*, **2011**, *133*, 17164.

[19] M. A. Sgambellone, A. David, R. N. Garner, K. R. Dunbar, C. Turro, *J. Am. Chem. Soc.*, **2013**, *135*, 11274.

[20] J.-C. Boyer, C.-J. Carling, S. Y. Chua, D. Wilson, B. Johnsen, D. Baillie, N. R. Branda, *Chem. Eur. J.*, **2012**, *18*, 3122.

[21] N. Bogdan, F. Vetrone, G. A. Ozin, J. A. Capobianco, *Nano Lett.*, **2011**, *11*, 835.

[22] J.-C. Boyer, F. C. J. M. Veggel, *Nanoscale*, **2010**, *2*, 1417.

[23] E. Borfecchia, C. Garino, L. Salassa, T. Ruiu, D. Gianolio, X. Zhang, K. Attenkofer, L.-X. Chen, R. Gobetto, P. J. Sadler, C. Lamberti, *Dalton Trans.*, **2013**, *42*, 6564.

4

Near-Infrared Activation of an Anticancer Pt^{IV} Complex by Tm-Doped Upconversion Nanoparticles

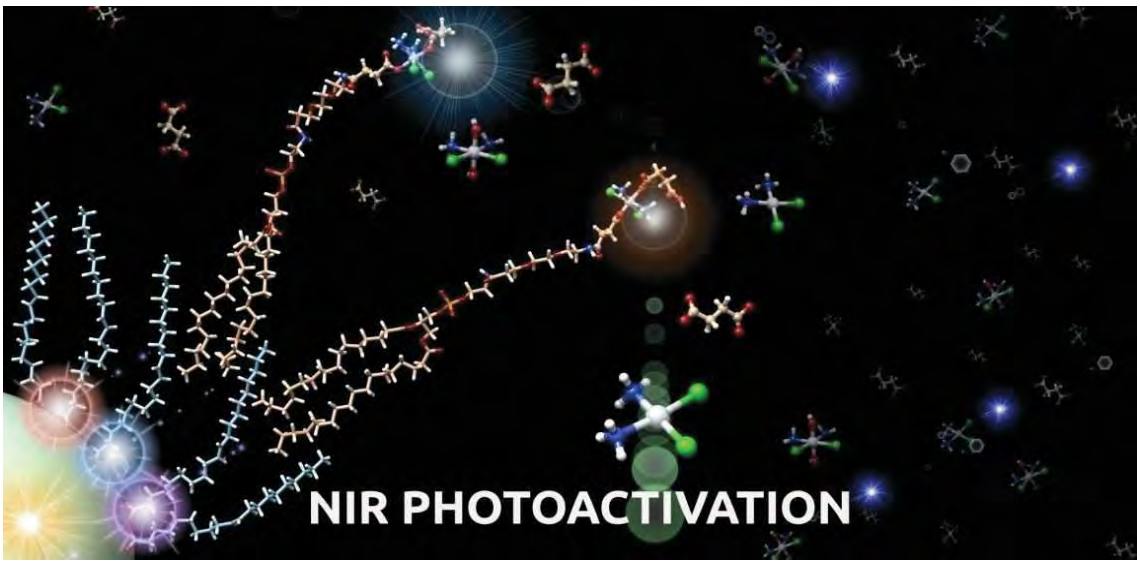

The Pt^{IV} complex cis,cis,trans-[$Pt(NH_3)_2(Cl)_2(O_2CCH_2CH_2CO_2H)_2$] is photoactivated by near-infrared light (980 nm) using $NaYF_4:Yb^{3+}/Tm^{3+}$@$NaYF_4$ core–shell upconversion nanoparticles. Coupling of this cisplatin precursor with the biocompatible PEGylated phospholipid DSPE-PEG(2000)-NH_2 affords a valuable approach to decorate the surface of the nanoparticles, providing novel photoactivatable nanomaterials capable of releasing Pt^{II} species upon NIR light excitation.

The work presented in this chapter was previously published: E. Ruggiero, J. Hernández-Gil, J.C. Mareque-Rivas, L. Salassa, Chem. Commun., 2015, 51, 2091.

4.1 Introduction

Light-induced activation of transition metal complexes acting as anticancer prodrugs has been proven to be a promising approach to induce novel modes of actions and to localize toxicity to irradiated tissue areas, hence potentially limiting unwanted side effects associated with cancer treatment. [1,2] Although encouraging in vivo activity has been recently demonstrated in the case of photoactivatable Pt and Rh complexes, [3,4] a major limitation for the progression of this class of anticancer agents towards preclinical and clinical stages is related to their poor absorption properties in the therapeutic window, i.e. 650–1000 nm, where tissue penetration is higher and direct damaging of cellular components lower. [5]

Upconversion nanoparticles (UCNPs) are innovative materials which have the capability to overcome such fundamental drawbacks of transition metal complexes. They have unique optical features allowing efficient conversion of near-infrared (NIR) photons into visible and UV light via multiphotonic energy transfer processes. [6,7] Potentially, light emitted by UCNPs can be used to excite metal complexes and prompt their photochemistry upon 980 nm excitation. In addition to upconverted luminescence, magnetic resonance relaxivity (Gd-containing UCNPs) and ease of radiolabeling (e.g. ^{18}F) have also made UCNPs excellent new probes for multimodal (optical/MRI/PET-SPECT) imaging. [6] Such promising features combined with the low toxicity of UCNPs *in vitro* and *in vivo* [6] suggest that these materials are ideal candidates for applications in nanomedicine and photochemotherapy.

Although a number of reports have shown how UCNPs can be integrated into porphyrin-like photosensitizers or caged compounds to afford novel NIR-activatable nanomaterials for therapy and imaging, [8–10] very little has been done to develop UCNPs as phototriggers capable of promoting functional structural changes in metal complexes (or chromophores [11, 12] in general). Following the pioneering work by the groups of Fuyou Li and Branda on photoswitchable UCNP systems based on organic dyes (e.g. dithienylethene), [13–15] Ford and collaborators showed photorelease of NO from Roussin's black salt embedded in UCNP composites upon 980 nm excitation, [16, 17] and we recently reported on the NIR-activated pyridine release in the Ru polypyridyl complex *cis*-$[Ru(bpy)_2(py)_2][Cl]_2$. [18]

4.2 Results and Discussion

In this communication, we expand the potentially broad application of these nanomaterials by demonstrating that UCNPs can mediate the NIR-photoactivation of the Pt^{IV} complex *cis,cis,trans*-$[Pt(NH_3)_2(Cl)_2(O_2CCH_2CH_2CO_2H)_2]$ (**1**, Scheme 1).

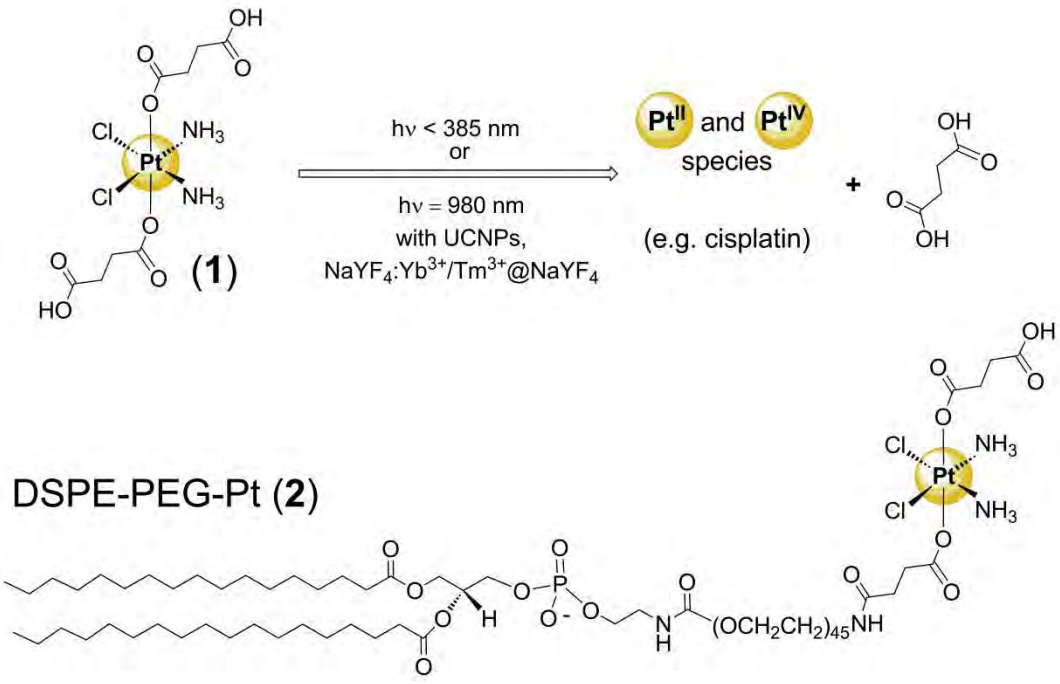

Scheme 1

This compound is representative of a class of anticancer prodrug candidates [19] that has shown significant promise and reached advanced stages in clinical trials. [20] Notably, complex **1** has a high reduction potential compared to other Pt(IV) analogues, [21] a fundamental requirement to exhibit dark stability (i.e. low toxicity) in the cellular environment. Moreover, we show that functionalization of **1** with the biocompatible PEGylated phospholipid DSPE-PEG(2000)-NH_2 [22] to afford **2** (Scheme 1) offers a viable strategy to decorate UCNPs and obtain nanomaterials capable of releasing Pt^{II} species upon NIR remote control.

Using a two-step procedure previously reported, [14,18] we prepared core–shell $NaYF_4:Yb^{3+}/Tm^{3+}@NaYF_4$ UCNPs. Firstly, $NaYF_4:Yb^{3+}/Tm^{3+}$ (69.5/30/0.5 mol%) nanocrystals with an average size of ca. 30 nm (Fig. 1) were synthesized by thermal

decomposition in the presence of oleic acid and octadecene and next used as seeds for growing a protective $NaYF_4$ shell.

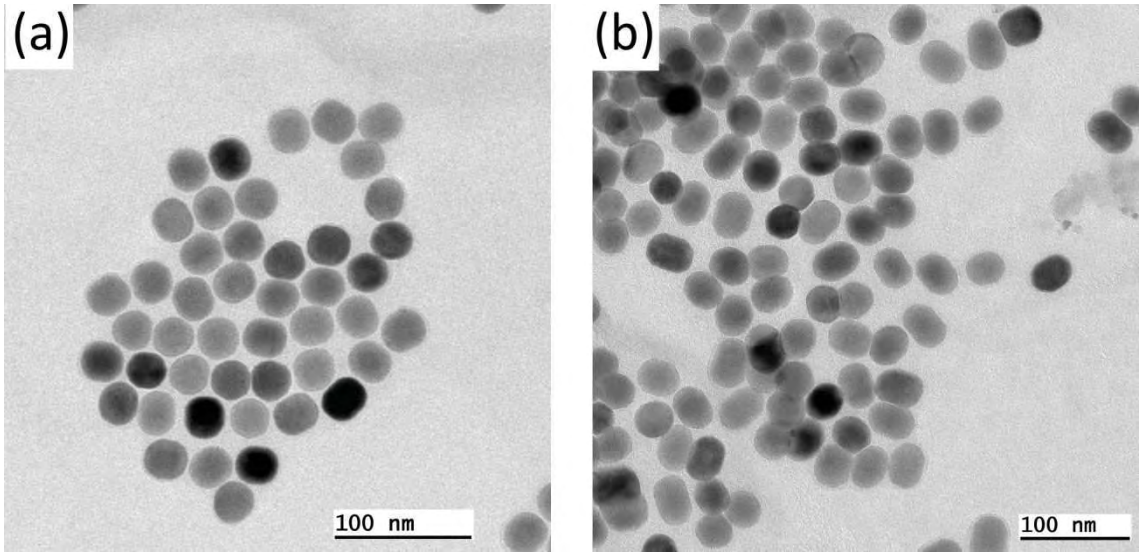

Fig. 1. TEM images of oleate-capped (a) core $NaYF_4:Yb^{3+}/Tm^{3+}$ and (b) core-shell $NaYF_4:Yb^{3+}/Tm^{3+}@NaYF_4$ UCNPs.

The TEM image shows that resulting core–shell $NaYF_4:Yb^{3+}/Tm^{3+}@NaYF_4$ UCNPs are uniform and have an average diameter of ca. 37 nm (Fig. 2). Characterization of both types of UCNPs was completed by IR, XPS and emission spectroscopy (Fig. 3–5).

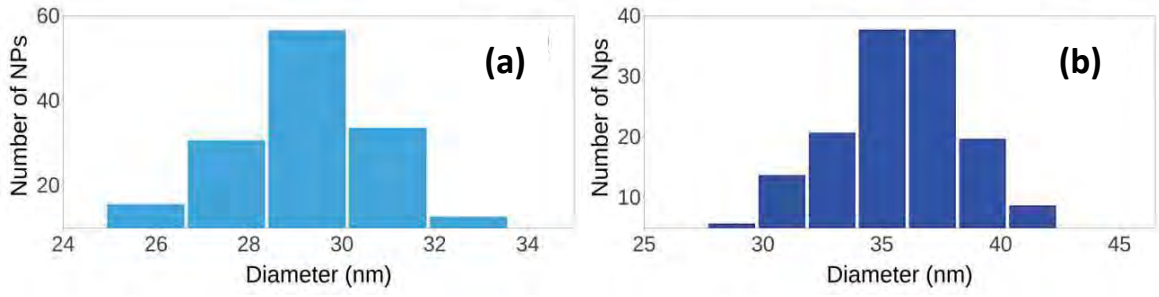

Fig. 2. Size distribution histograms of (a) $NaYF_4:Yb^{3+}/Tm^{3+}$ and (b) $NaYF_4:Yb^{3+}/Tm^{3+}@NaYF_4$ nanoparticles. Average diameter of $NaYF_4:Yb^{3+}/Tm^{3+}$ is 30 ± 2 nm. Average diameter of $NaYF_4:Yb^{3+}/Tm^{3+}@NaYF_4$ is 37 ± 3 nm.

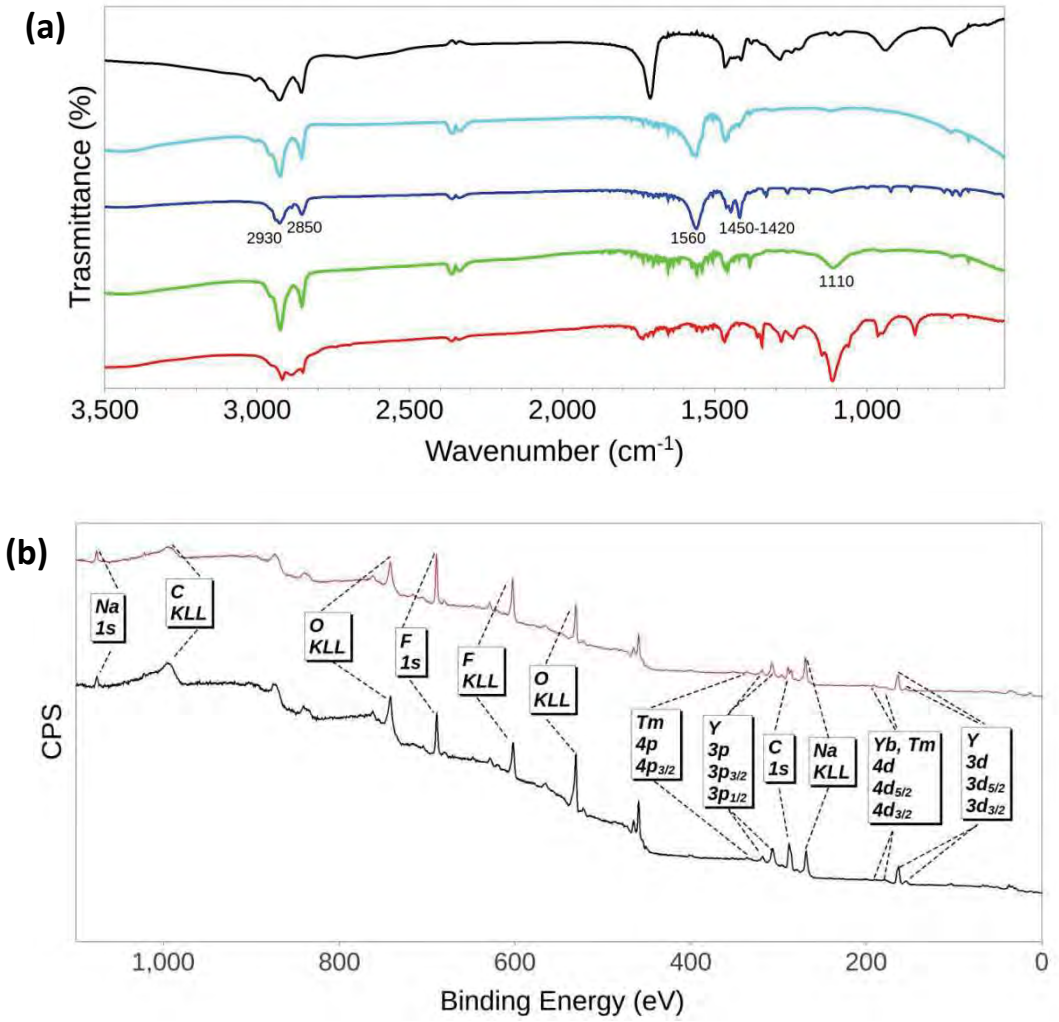

Fig. 3. (a) FT-IR spectra of (black) pure oleic acid, (light blue) $NaYF_4:Yb^{3+}/Tm^{3+}$, (blue) $NaYF_4:Yb^{3+}/Tm^{3+}@NaYF_4$, (green) **2**, $NaYF_4:Yb^{3+}/Tm^{3+}@NaYF_4$@**2**, (red) **2**. (b) XPS spectra of (black) $NaYF_4:Yb^{3+}/Tm^{3+}$ and (red) $NaYF_4:Yb^{3+}/Tm^{3+}@NaYF_4$ nanoparticles confirming the presence of C, O, F, Na, Y, Tm and Yb as assigned by core level and Auger electrons.

As previously demonstrated, [23] passivation of UCNPs with un-doped $NaYF_4$ considerably increases the upconversion efficiency compared to the corresponding core-only nanocrystals. In THF (λ_{irr} = 980 nm, Fig. 4), $NaYF_4:Yb^{3+}/Tm^{3+}@NaYF_4$ UCNPs display multiple emission maxima which are typical of Tm^{3+} electronic transitions and fall at 345 and 360 nm ($^3P_0 \rightarrow {}^3F_4$ and $^1D_2 \rightarrow {}^3H_6$), 450 and 475 nm ($^1D_2 \rightarrow {}^3F_4$ and $^1G_4 \rightarrow {}^3H_6$), 645, 690 and 720 nm ($^1G_4 \rightarrow {}^3F_4$ and $^3F_3 \rightarrow {}^3H_6$) and at 800 nm ($^3H_4 \rightarrow {}^3H_6$). [24] Upconversion of NIR light occurs through a non-linear multiphoton process and, as

expected, changes in the excitation power density alter the relative intensities of the emission bands (Fig. 4–5). [24]

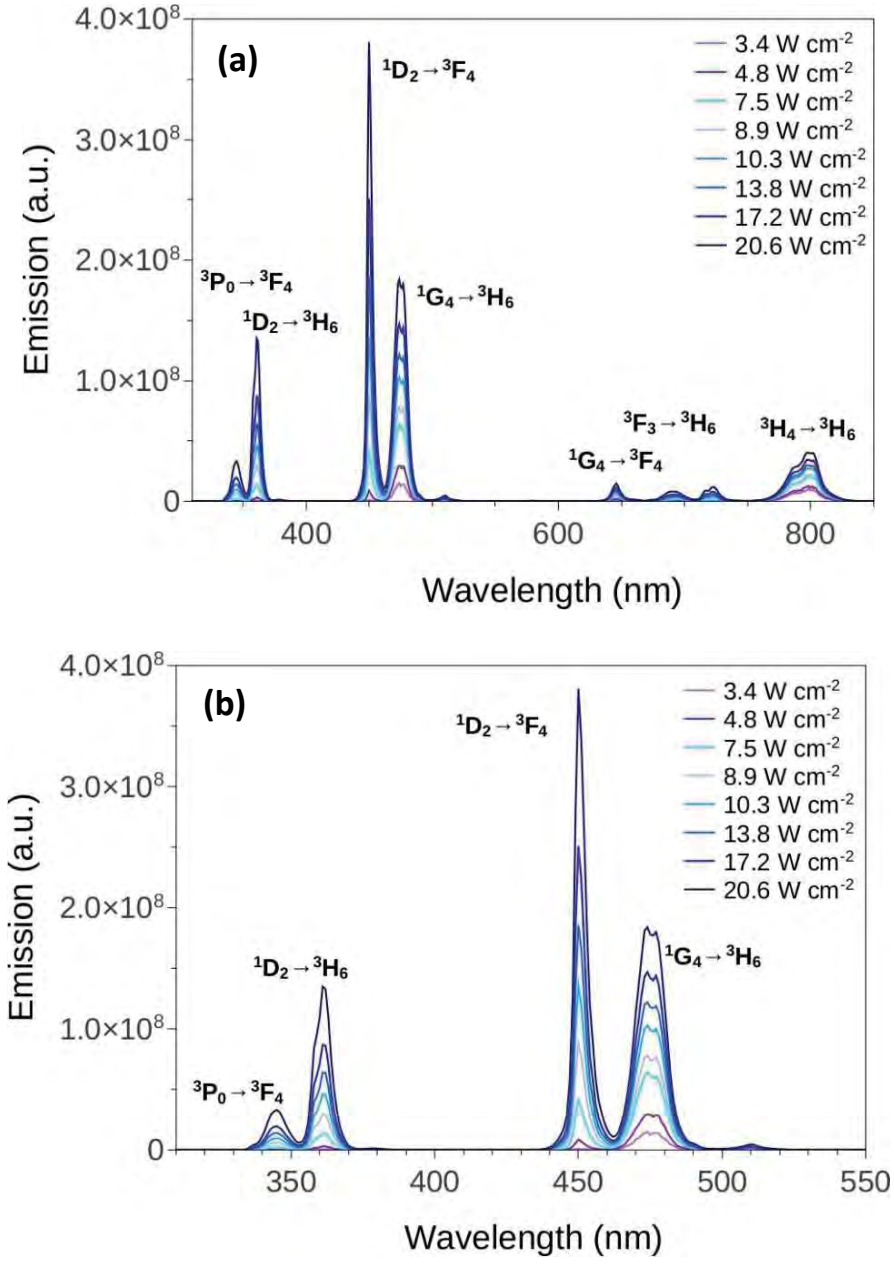

Fig. 4. Upconversion luminescence spectra of (a) $NaYF_4$:Yb^{3+}/Tm^{3+}@$NaYF_4$ (0.5 mg·ml^{-1} in THF) and (b) its magnification upon 980 nm excitation at different powers (3.4–20.6 W cm^{-2}).

Crucially, emission bands at 345 nm, 360 nm and 450 nm significantly rise with respect to the emission band at 475 nm in the case of Yb^{3+}/Tm^{3+}-doped core–shell UCNPs.

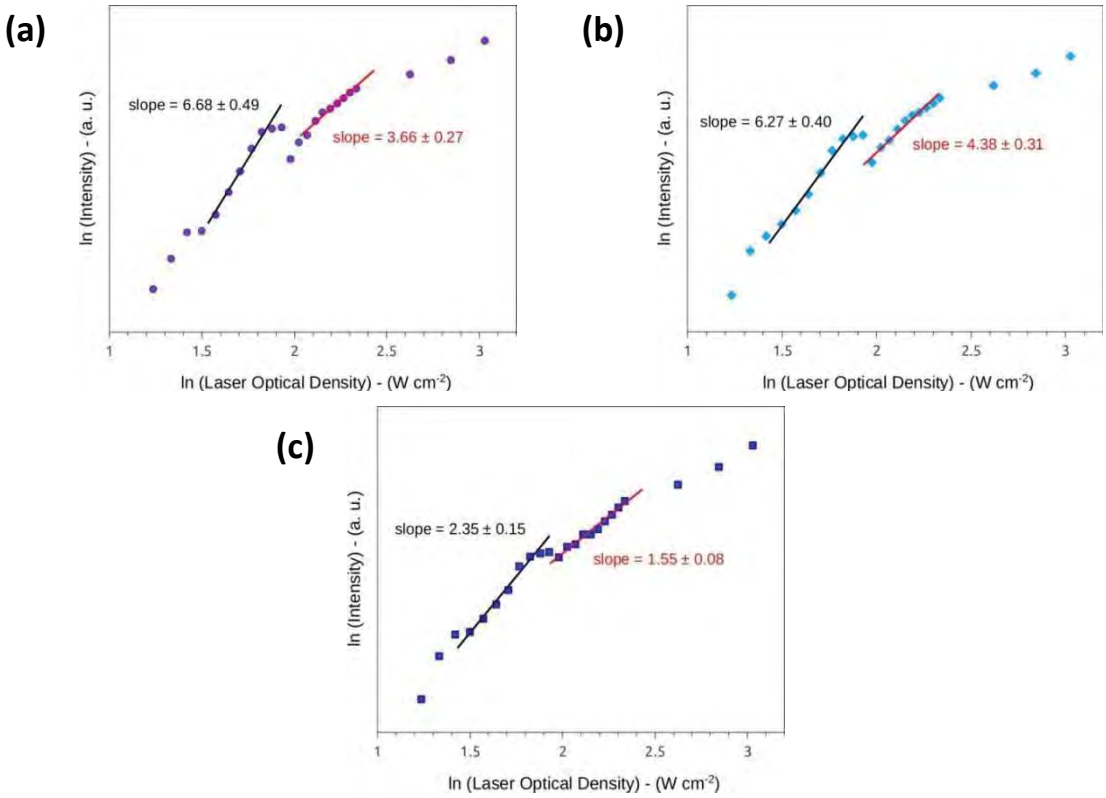

Fig. 5. Power dependence of the emission at 360 nm (a), 450 nm (b) and 475 nm (c) of $NaYF_4:Yb^{3+}/Tm^{3+}@NaYF_4$ upon NIR irradiation.

Indeed, such improvement in emission properties of UCNPs is key since complex **1** only absorbs in the UV region of the spectrum, up to 390 nm (Fig. 6).

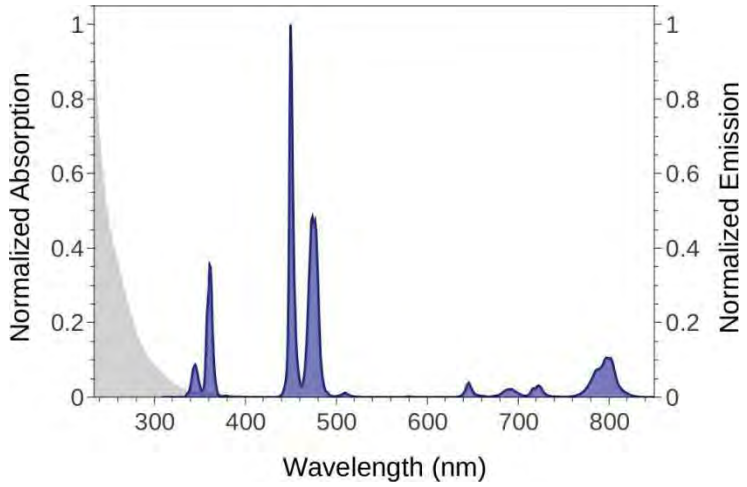

Fig. 6. Overlap between the UV-Vis spectrum (normalized) of **1** and the upconverted emission spectrum (normalized) of core-shell $NaYF_4:Yb^{3+}/Tm^{3+}@NaYF_4$ UCNPs (THF, λ_{irr} = 980 nm).

To test whether the overlap between the absorption of **1** and the emission of $NaYF_4:Yb^{3+}/Tm^{3+}@NaYF_4$ UCNPs is suitable for NIR-light photoactivation of the complex, we prepared a suspension containing oleate-capped core–shell UCNPs (5 mg ml^{-1}) and **1** (150 mM) in buffer (PBS/D_2O, pH = 7.3, 0.4 ml) and investigated the photolysis of the complex upon 980 nm excitation by NMR. For each time point, the sample was centrifuged and the supernatant used for collecting NMR spectra, a necessary procedure to minimize signal broadening due to the paramagnetic nanoparticles and obtain good quality data. The ^1H NMR spectrum of **1** in the dark displays two diagnostic pseudo-triplets between 2.30 and 2.60 ppm, corresponding to the two non-equivalent CH_2 protons of the coordinated succinates. NIR irradiation of the reaction mixture using a 980 nm continuous-wave laser (4.9 W cm^{-2}) causes succinate dissociation, as clearly observed by the appearance of the singlet at 2.33 ppm (Fig. 7, red circle).

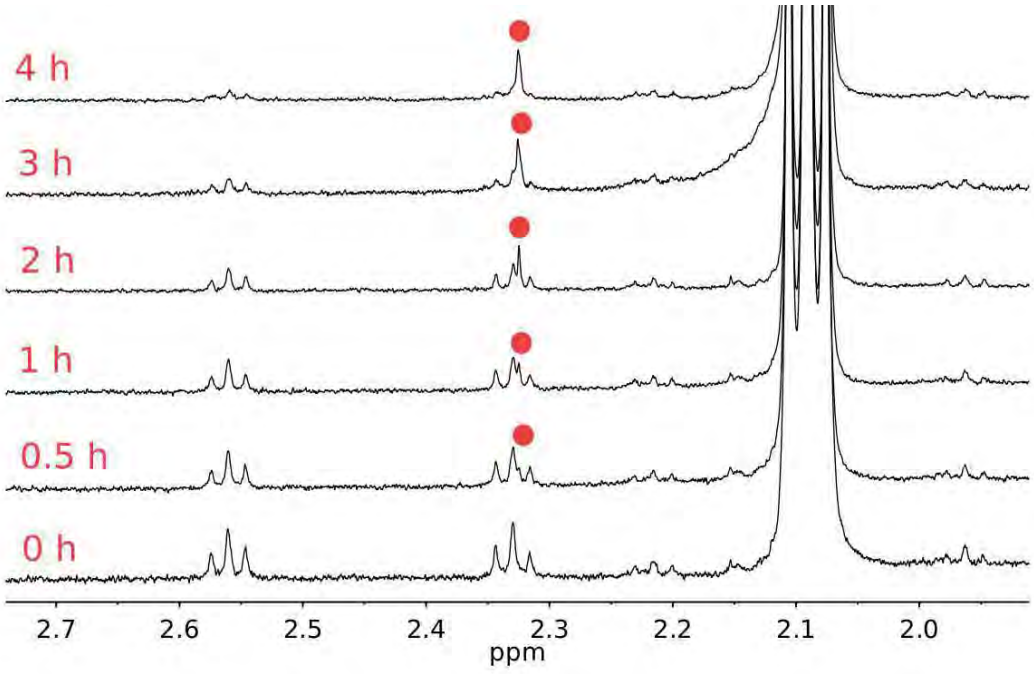

Fig. 7. Near-infrared (λ_{irr} = 980 nm, 4.9 W·cm^{-2}) photolysis of **1** in the presence of core-shell $NaYF_4:Yb^{3+}/Tm^{3+}@NaYF_4$ UCNPs followed by ^1H NMR (PBS/D_2O, pH = 7.3, 0.4 ml); the signal relative to photoreleased succinate is labelled with a red circle (●). In addition, NMR spectra show a triplet at 2.10 ppm corresponding to the protons of oleic acid associated with the UCNPs.

The photoreaction is practically complete after 4 h under the chosen conditions and control experiments confirm that direct excitation of **1** at 385 nm (40 mW cm^{-2}, 15 min) similarly promotes the release of the axial ligands, whereas in the absence of UCNPs no changes in the ^{1}H NMR of **1** are observed after 7 h of irradiation at 980 nm (Fig. 8). Besides free succinate, **1** is known to simultaneously generate Pt^{IV} and Pt^{II} photoproducts upon light activation. [25,26] Recently, we showed how the high concentration of **1** and a low UVA light dose (ca. 4.8 J cm^{-2}) resulted prevalently in the formation of a range of Pt^{IV} species, including the cytotoxic dihydroxido complex *cis,cis,trans*-$[Pt^{IV}(NH_3)_2(Cl)_2(OH)_2]$. [26]

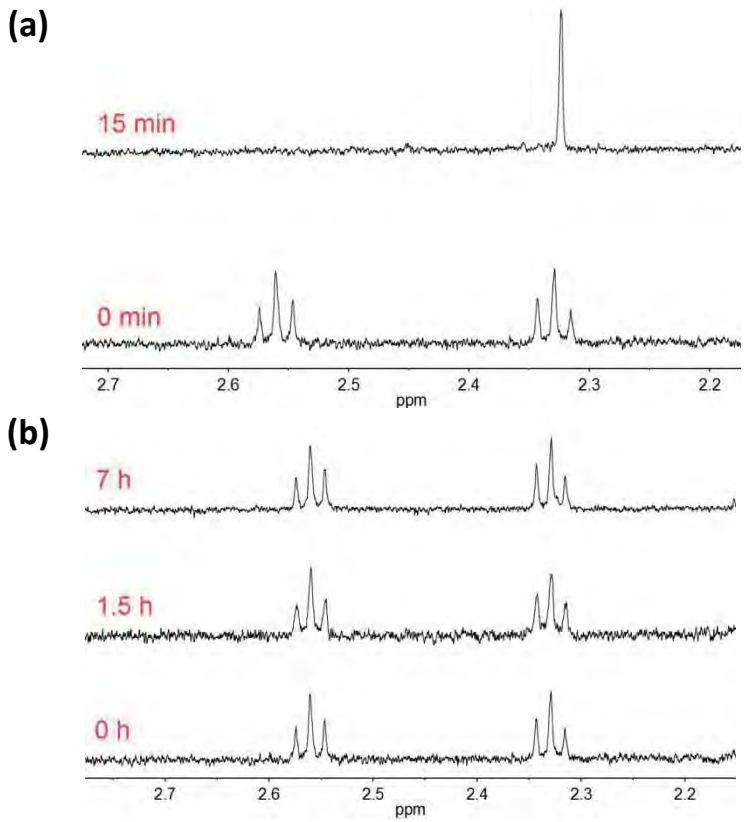

Fig. 8. (a) ^{1}H NMR spectra of **1** in PBS/D_2O buffer (10 mM, pH = 7.3) before and after it was exposed to 385 nm light for 15 min (40 mW cm^{-2}). (b) ^{1}H NMR spectra of 1 in PBS/D2O buffer (10 mM, pH = 7.3) before and after irradiation at 980 nm light for 7 hours (6.5 W cm^{-2}).

Some of these Pt^{IV} photoproducts reasonably evolve to cytotoxic species in the cellular environment; however, it is desired that Pt^{IV} prodrugs such as **1** could undergo efficient $Pt^{IV} \rightarrow Pt^{II}$ photoreduction (in irradiated areas) and generate cisplatin-like

species, since these have typically superior and better understood antiproliferative activity.

For this reason, we employed X-ray photoelectron spectroscopy (XPS) to assess the oxidation state of the Pt-containing photoproducts obtained from the various photoreactions. XPS allowed determining the Pt^{II}:Pt^{IV} ratio of samples, although partial X-ray-induced reduction should always be taken into account as previously reported for other systems. [27] Results indicate partial formation of Pt^{II} species (Pt^{II}:Pt^{IV} = 30:70) in the Pt $4f_{7/2}$ and $4f_{5/2}$ XPS spectrum of the supernatant solution obtained by NIR excitation of **1** in the presence of UCNPs (Fig. 9a). In contrast, no trace of Pt is obtained for the UCNP pellet precipitated from the reaction mixture, suggesting that **1** and its photoproducts do not adsorb on the surface of UCNPs after photoactivation (Appendix Chapter 3, Fig. A1). [18] A similar finding is obtained for the complex under direct UVA irradiation (ca. 36 J cm^{-2}, Pt^{II}:Pt^{IV} = 56:44, Fig. 9b). Consistently, **1** retains the Pt^{IV} oxidation state in the dark (Pt^{IV} = 100%) and after 7 h of irradiation at 980 nm in the absence of UCNPs (Fig. 9c).

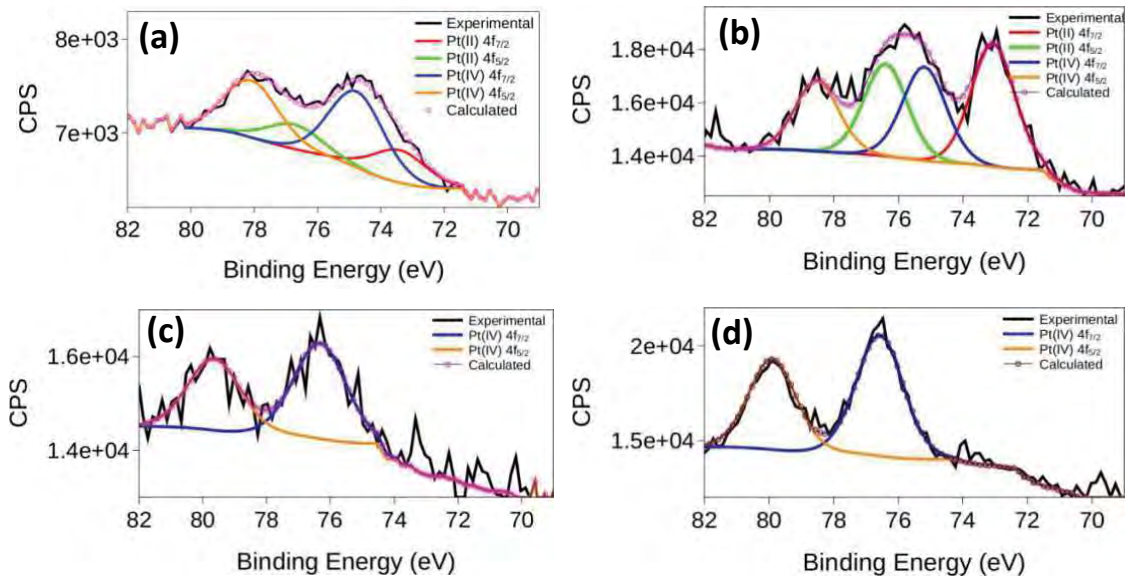

Fig. 9. Pt 4f XPS spectra of **1** (150 µM) (a) (supernatant) after irradiation at 980 nm (4.9 $W \cdot cm^{-2}$, 4h) in the presence of core-shell $NaYF_4$:Yb^{3+}/Tm^{3+}@$NaYF_4$ UCNPs. (b) after 15 min of irradiation at 385 nm (40 mW cm^{-2}) (c) after 7h of irradiation at 980 nm (6.5 W cm^{-2}), (d) without irradiation. Based on fit peak areas, the ratio Pt^{II}:Pt^{IV} in the spectra are (a) 30:70 (b) 56:44, (c) 0:100 and (d) 0:100.

After demonstrating that $NaYF_4:Yb^{3+}/Tm^{3+}@NaYF_4$ UCNPs have the capability of functioning as NIR phototriggers for the activation of Pt^{IV} complexes, we explored the surface functionalization of the nanoparticles for the loading of **1**. The carboxylic groups of the complex were exploited for its coupling with the PEGylated-phospholipid DSPE-PEG(2000)-NH_2 via an EDC-based conjugation method (*vide experimental part*). [28] The resulting water dispersible DSPE-PEG-Pt^{IV} adduct (**2**, Scheme 1) can interact with the oleate chains covering the UCNPs by means of the phospholipidic tails, while the hydrophilic PEG units of the polymer are exposed towards the solvent, further stabilizing the nanoparticles and improving their water solubility. [29] Characterization of $NaYF_4:Yb^{3+}/Tm^{3+}@NaYF_4@$**2** nanoparticles was achieved by different techniques (Fig. 3, 10–12).

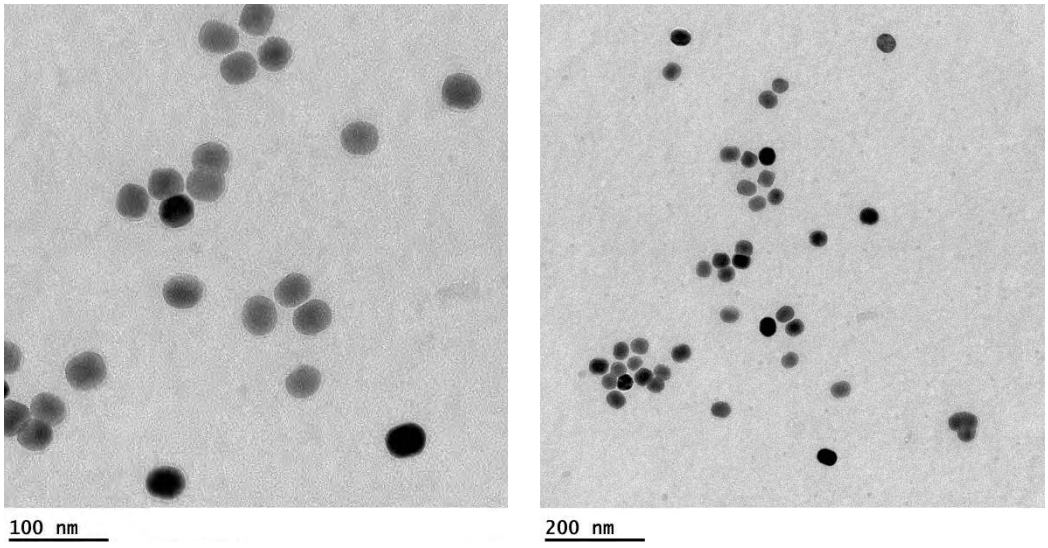

Fig. 10. TEM images of $NaYF_4:Yb^{3+}/Tm^{3+}@NaYF4@$**2** nanoparticles (1 mg·ml^{-1} in H_2O).

TEM indicates that nanoparticles are rather uniform and monodisperse and that no significant changes in the morphology occurred upon functionalization (Fig. 10), while XPS measurements unequivocally confirm the presence of Pt^{IV} (100%) on the surface of UCNPs (Fig. 11). Under the preparation conditions chosen for $NaYF_4:Yb^{3+}/Tm^{3+}@NaYF_4@$**2**, some degree of aggregation possibly occurs as DLS provides a hydrodynamic radius of ca. 157 nm for the system in water (Fig. 12).

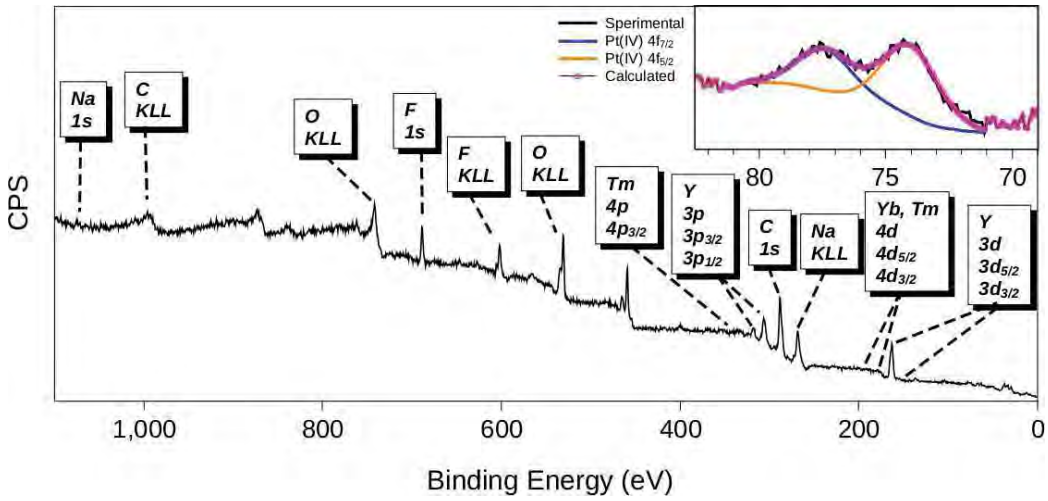

Fig. 11. XPS spectrum of $NaYF_4:Yb^{3+}/Tm^{3+}$@$NaYF_4$@**2** with assignment for C, O, F, Na, Y, Tm and Yb by core level and Auger electrons. Inset: zoomed spectrum in the 69–82 eV energy range confirming the presence of Pt^{IV} on the surface of $NaYF_4:Yb^{3+}/Tm^{3+}$@$NaYF_4$@**2**.

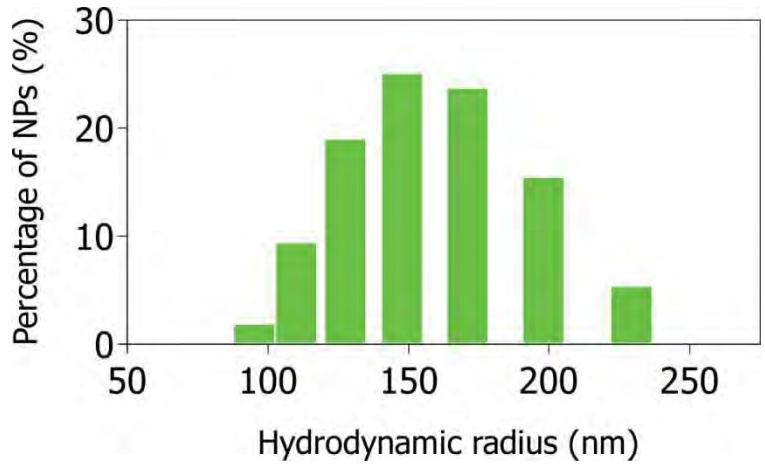

Fig. 12. Histogram illustrating hydrodynamic size distributions of $NaYF_4:Yb^{3+}/Tm^{3+}$@$NaYF_4$@**2** (0.5 mg·ml^{-1} in H_2O) measured by Z-sizer. The hydrodynamic radius was determined to be equal to 157 ± 32 nm.

Nevertheless, such dimensions are appropriate for passive targeting via the enhanced permeation effect (EPR). [30] Besides the typical oleic acid stretching bands at 2930 and 2850 cm^{-1}, IR spectroscopy displays a new band characteristic of the PEGC–O–C stretching mode at 1110 cm^{-1} (Fig. 3). [31] Furthermore, the absorption spectrum of $NaYF_4:Yb^{3+}/Tm^{3+}$@$NaYF_4$@**2** in aqueous solution shows the Yb^{3+} band at

ca. 980 nm together with features in the UV region which are consistent with the presence of oleate and **2** on the surface of UCNPs (Appendix Chapter 3, Fig. A2). Importantly, decoration of UCNPs with **2** does not seem to affect their upconversion properties, as also confirmed in the case of analogue NH_2-free PEGylated-phospholipid UCNPs (Appendix Chapter 3, Fig. A3). Indeed, no significant quenching of the UCNP emission bands at 345 and 360 nm is apparent in both cases. However, occurrence of a FRET process may still be plausible in the case of the Pt^{IV} loaded system, considering the limited spectral overlap between **1** and UCNPs.

^{1}H NMR photolysis experiments on $NaYF_4$:Yb^{3+}/Tm^{3+}@$NaYF_4$@**2** were performed in order to establish whether the material was capable of photoreleasing biologically active Pt^{II}/Pt^{IV} upon NIR light excitation. Fig. 13 compares the photochemical behavior of **2** alone upon 385 nm excitation (40 mW cm^{-2}, grey panel) and $NaYF_4$:Yb^{3+}/Tm^{3+}@$NaYF_4$@**2** (5 mg ml^{-1}) under NIR irradiation (λ_{irr} = 980 nm, 7.3 W cm^{-2}). The ^{1}H NMR spectrum of **2** in buffer shows four pseudo triplets between 2.30 and 2.65 ppm (grey panel), corresponding to its four non-equivalent protons.

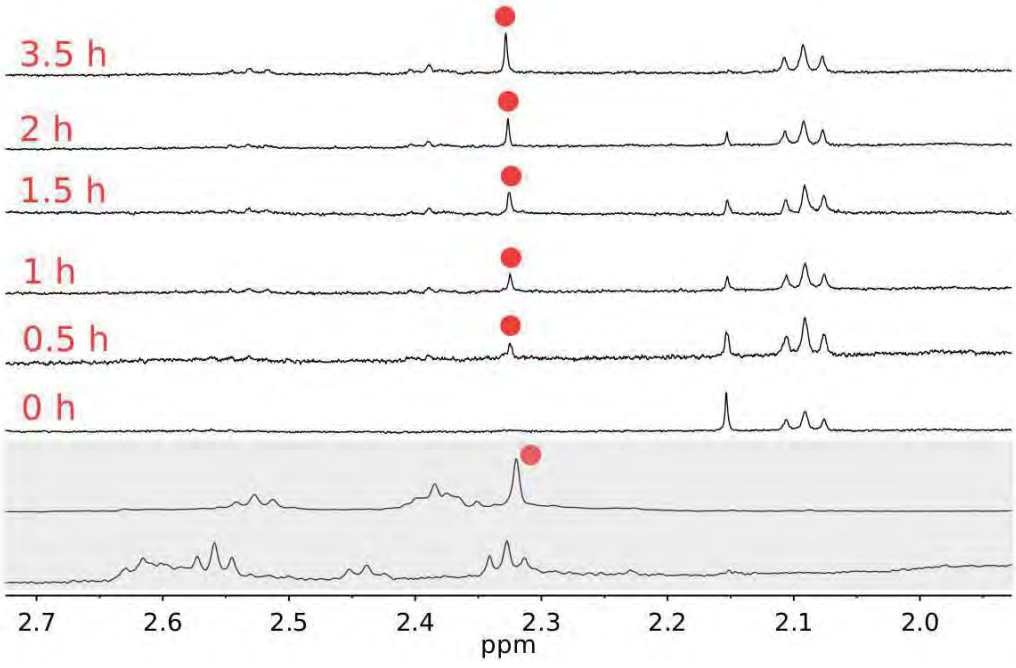

Fig. 13. Near-infrared (λ_{irr} = 980 nm, 7.3 W cm^{-2}) photolysis of $NaYF_4$:Yb^{3+}/Tm^{3+}@$NaYF_4$@**2** UCNPs followed by ^{1}H NMR (PBS/D_2O buffer, pH = 7.3, 0.4 ml); the signal relative to photoreleased succinate is labeled with a red circle (●); the grey panel shows the photolysis of **2** upon UVA excitation (λ_{irr} = 385 nm, 40 mW cm^{-2}, 10 min) followed by ^{1}H NMR (PBS/ D_2O buffer, pH = 7.3).

Two of these signals disappear upon UV irradiation (10 min), while the singlet relative to free succinate and two pseudo-triplets relative to the PEG anchored succinate appear alongside (Appendix Chapter 3, Fig. A4–5). Differently, when $NaYF_4:Yb^{3+}/Tm^{3+}@NaYF_4@$**2** is suspended in PBS/D_2O buffer and the solution is then centrifuged to extract the supernatant, signals corresponding to **2** cannot practically be detected in the ^1H NMR spectrum of this fraction.

These results are in agreement with the absence of Pt in the supernatant and demonstrates the good stability of the adduct. Yet, NIR irradiation of the $NaYF_4:Yb^{3+}/Tm^{3+}@NaYF_4@$**2** solution clearly leads to the appearance of free succinate in the ^1H NMR spectrum (Fig. 13, red circle ●). The photoreaction is completed in 3.5 h and control experiments at 980 nm in the absence of UCNPs show that **2** cannot be photoactivated at this wavelength (Appendix Chapter 3, Fig. A6).

XPS was also employed in the case of $NaYF_4:Yb^{3+}/Tm^{3+}@NaYF_4@$**2** to understand the nature of the Pt^{II}/Pt^{IV} photoproducts generated by its photolysis at 980 nm (Fig. 14a).

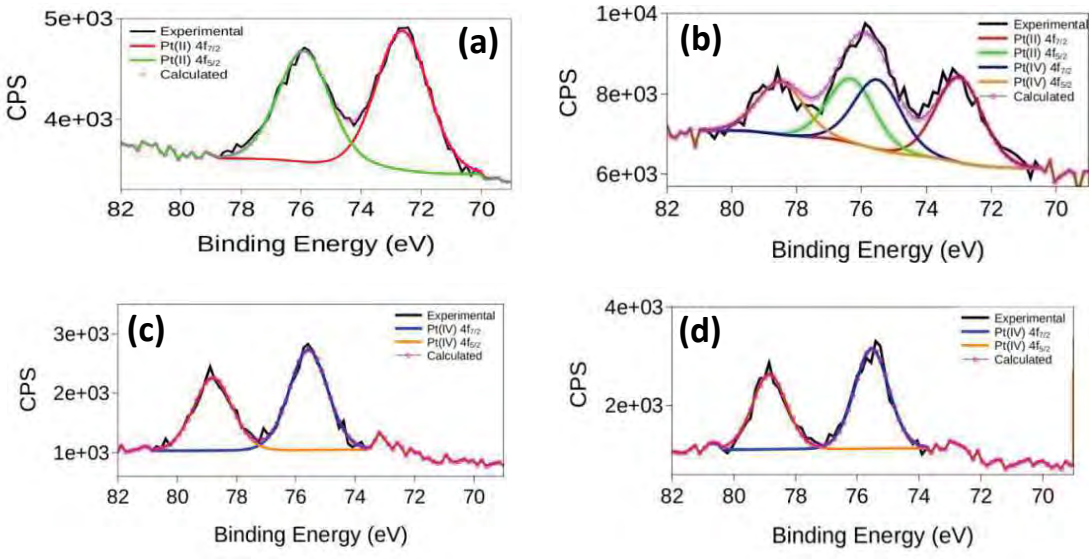

Fig. 14. Pt $4f_{7/2}$ and $4f_{5/2}$ XPS spectra of **2** (a) supernatant of $NaYF_4:Yb^{3+}/Tm^{3+}@NaYF_4@$**2** after irradiation at 980 nm (7.3 W cm^{-2}, 3.5 h), (b) **2** (150 µM) after 10 min of irradiation at 385 nm (40 mW cm^{-2}), (c) **2** (150 µM) after 5 h of irradiation at 980 nm (8.8 W cm^{-2}) and (d) **2** (150 µM) without irradiation. Based on fit peak areas, the ratio $Pt^{II}:Pt^{IV}$ in the spectra are (a) 100:0, (b) 55:45 (c) 0:100 and (d) 0:100.

The supernatant solution analyzed by XPS indicates that Pt^{IV} is fully converted into Pt^{II} at the end of the photoreaction. Also in this case, no trace of Pt species is found by XPS in the pellet separated from the photolysis reaction of the nanomaterials (Appendix Chapter 3, Fig. A7) and control experiments (dark and **2** at 980 nm without UCNPs, Fig. 14) confirming that platinum is in the Pt^{IV} oxidation state.

4.3 Conclusions

In summary, we provided in this work clear spectroscopic evidence that UCNPs can be employed to photoactivate Pt^{IV} anticancer complexes with NIR light, a remarkable result considering the poor absorption properties of this class of derivatives in the visible and near-infrared region of the spectrum. Furthermore, decoration of nanoparticles with a biocompatible (FDA-approved [22]) PEGylated phospholipid functionalized with **1** appears to be a valuable strategy to develop photoactivatable nanomaterials capable of releasing active Pt^{II} species upon NIR light excitation. More studies are needed to thoroughly evaluate the effect of the excitation power over cellular environments and to improve the efficacy of UCNPs as phototriggers by increasing their upconversion yield and optimize surface functionalization. However, activating Pt^{IV} precursors of anticancer agents, such as cisplatin, carboplatin or oxaliplatin, with NIR light is indeed an attractive prospect as these Pt^{IV} complexes have extensively been studied in the last few years and some of them have even reached clinical trials (e.g. iproplatin). [20] In particular, the low toxicity (both in vitro and in vivo) of UCNPs with respect to other nanomaterials and their multimodal imaging capability are key advantages to exploit for novel applications in nanomedicine.

4.4 Experimental Section

4.4.1 Materials

All chemical reagents, yttrium(III) acetatehydrate (99.9%), ytterbium(III) acetate tetrahydrate (99.9%), thulium(III) acetate hydrate (99.9%), 1-octadecene (technical grade, 90%), oleic acid (technical grade, 90%), sodium hydroxide (≥ 97%), ammonium

fluoride (98%), potassium iodide (99%), potassium hydroxide (90%), silver nitrate (≥ 99%), sodium chloride (99%), succinic anhydride (≥ 99%), hydrogen peroxide solution (30 wt. % in H_2O), N,N'-dicyclohexyl carbodiimide (99%), N,N-Dimethylpyridin-4-amine (≥ 99%), and solvents were purchased from Sigma-Aldrich. The amphiphilic polymerDSPE-PEG(2000) amine, 1,2-distearoyl-sn-glycero-3-phosphoethanolamine-N-[amino(polyethyleneglycol)-2000] (ammonium salt), was purchased from Avanti Polar Lipids, Inc. The precursor of the metal complex potassium tetrachloroplatinate(II) (99%) was purchased from Precious Metals OnlinePMO Pty Ltd. Nanopure water was obtained using the Barnstead Nanopure Ultrapure Water Purification System.

4.4.2 Synthesis of core-$NaYF_4$:Yb^{3+}/Tm^{3+}

The *core*-$NaYF_4$:Yb^{3+}/Tm^{3+} (rare earth element ratio 78/20/2mol%) synthesis was carried out following a slightly modified literature procedure. [18]

In a typical synthesis (total rare earth amount, 3 mmol),yttrium(III) acetate hydrate (555 mg, 2.1 mmol), ytterbium(III) acetate tetrahydrate (380 mg, 0.90 mmol) and thulium(III) acetate hydrate (5.2 mg, 0.015 mmol) were dissolved in 1-octadecene (25 ml) and oleic acid (15 ml) in a 100 ml three-neck round-bottom flask with coil condenser. The suspension was heated up to 120 °C with a slow temperature ramp of 3.2 °C/min under stirring and vacuum. Once reaction mixture reached such temperature, it was kept in these conditions for 30 min in order to form a clear solution and eliminate residual water and oxygen. The system was then allowed to cool to 50 ºC under a flow of nitrogen gas.

A solution of sodium hydroxide (300 mg, 7.5 mmol) and ammonium fluoride (444 mg, 12.0 mmol) in methanol (8 ml) was added to the reaction flask drop wise in 10 min. The subsequent cloudy solution was stirred for 30 min at 50 °C and for 30 min at 70 °C under nitrogen to evaporate the entire amount of methanol from the solution. Successively, the system was heated up to 300 °C with a fast temperature ramp of 13.5 ºC/min under stirring and nitrogen and maintained in such conditions for 90 min. The reaction mixture progressively changed from turbid to yellow and transparent.

Next, the flask was left cooling to room temperature, and nanoparticles were purified by centrifugation (4500 rpm at 20 °C for 15 min) to remove any excess of

reagents and solvents. The white pellet was washed once with of ethanol (40 ml) and once with THF/ethanol (5/35 ml) and recollected by centrifugation. Upconversion nanoparticles were dried at room temperature overnight. Typically, ca. 600 mg of $NaYF_4:Yb^{3+}/Tm^{3+}$ nanoparticles are obtained employing the reaction conditions described.

4.4.3 Synthesis of core-shell $NaYF_4:Yb^{3+}/Tm^{3+}@NaYF_4$

Synthesis of core-shell $NaYF_4:Yb^{3+}/Tm^{3+}@NaYF_4$ nanoparticles was realized by employing a slightly modified version of the procedure published by J-C. Boyer *et al*. [14] The previously-obtained $NaYF_4:Yb^{3+}/Tm^{3+}$nanoparticles were used as seeds to grow a $NaYF_4$ shell.

In a typical synthesis (total rare earth amount, 0.9 mmol), yttrium (III) acetate hydrate (240 mg, 0.9 mmol) was dissolved in 1-octadecene (15 ml) and oleic acid (6 ml) in a 100 ml three-neck round-bottom flask with coil condenser.

As for core nanoparticles, the suspension was heated up to 120 °C with a slow temperature ramp of 3.2 °C /min under constant stirring and vacuum, and maintained in such conditions for 30 min. Afterwards, the solution was cooled down to 80 °C and placed under a flow of nitrogen gas.

In the same time, a suspension of $NaYF_4:Yb^{3+}/Tm^{3+}$ (260 mg) in hexane (10 ml) was prepared via sonication and added to the reaction flask drop by drop (10 min). The resulting turbid solution was heated up to 110 ºC (3.2 °C/min) under vacuum to eliminate the hexane. After 30 min the solution was again cooled down to 50 °C and a methanolic (5 ml) solution of sodium hydroxide (88 mg, 2.2 mmol) and ammonium fluoride (130 mg, 3.5 mmol) was added to the system drop wise over 5 min. The flask was maintained for 30 min at 50 °C and for 30 min at 70 °C under nitrogen to evaporate the entire amount of methanol from the reaction mixture. Afterwards, the reaction flask was heated up at 300 °C with a fast temperature ramp of 13.5 °C/min and heating was kept for 90 min. During the nucleation process the solution switches from cloudy to slightly yellow and transparent.

The solution was then cooled down to room temperature, and formation of a white precipitated is observed on the bottom of the flask. The so-obtained core-shell

nanoparticles were purified by centrifugation (4500 rpm at 20 °C for 15 min). The pellet was washed with ethanol and THF and dried overnight. Typically, ca.500 mg of core-shell $NaYF_4$:Yb^{3+}/Tm^{3+}@$NaYF_4$ NPs are obtained.

4.4.4 Synthesis of cis,cis,trans-[Pt(NH$_3$)$_2$(Cl)$_2$(O$_2$CCH$_2$CH$_2$CO$_2$H)$_2$] (1)

The Pt prodrug was synthesized by complying the procedure described by M. Reithofer *et al*. [32]

4.4.5 Synthesis of DSPE-PEG-Pt^{IV} (2)

The amphiphilic polymer 1,2-distearoyl-sn-glycero-3-phosphoethanolamine-N-[amino(polyethyleneglycol)-2000] (ammonium salt, DSPE-PEG(2000) amine) was functionalized with **1** using the protocol reported by J. Hernández-Gil *et al.* [28]

Briefly, *cis,cis,trans*-[$Pt(NH_3)_2(Cl)_2(O_2CCH_2CH_2CO_2H)_2$] (**1**) (9.6 mg, 18.0 µmol), dicyclohexyl carbodiimide (3.7 mg, 18.0 µmol) and 4-(dimethylamino)pyridine (1.0 mg, 7.2 µmol) were dissolved in DMSO (130 µL). After 10 minutes, the solution containing the activated Pt^{IV} complex was added to a DMSO solution of DSPE-PEG(2000)-NH_2 (10 mg, 3.6 µmol, 170 µL). The resulting mixture was allowed to react at room temperature for 72 h under continuous stirring. Water was then added to the reaction mixture. The solution was centrifuged and the supernatant was passed through a 0.45 µm filter to remove insoluble traces. Then, the supernatant was dialyzed in a Slide-A-Lyzer Dialysis Cassete (Thermo Scientific) (MW cutoff of 2,000) against water (3 x 500 ml). The dyalizate, containing the pure product was lyophilized and the residue dried in vacuo over P_2O_5 (10.86 mg, 90%). ^{1}H NMR (500 MHz, $CDCl_3$) for **2**: δ 0.88 (t, CH_3, 6H), 1.25 (s, CH_2, 56H), 1.61 (m, CH_2CH_2CO, 4H), 2.32 (m, CH_2CH_2CO, 4H), 2.60 (m, CH_2-succinic, 8H), 3.44 (m, CH_2CH_2N, 2H), 3.64 (s, PEG ~ 180 H), 3.96 (m, CH_2CH_2NH, 2H), 4.22 (m, trans-PO_4CH_2CH, 1H), 4.32 (m, $COOCH_2COH$, 2H), 4.40 (m, *cis*-PO_4CH_2CH, 1H), 5.26 (m, PO_4CH_2CH, 1H), 6.25 (bs, NH_3, 6H), 6.68 (bs, $NHCOCH_2$), 6.82 (bs, $NHCOOCH_2$). UPLC/MS τ_r = 11.38 min; m/z for $[C1_{40}H_{289}N_7O_{61}PPtCl_2]^{3+}$ expected = 1114.28, found = 1114.17 (ESI+).

4.4.6 Synthesis of $NaYF_4:Yb^{3+}/Tm^{3+}$@$NaYF_4$@2

Nanoparticle surface functionalization with DSPE-PEG-Pt^{IV}(**2**) was obtained following previous work by some of us with few adjustments (Gomez Blanco *et al.*, [33]). $NaYF_4:Yb^{3+}/Tm^{3+}$@$NaYF_4$ nanocrystals (12 mg) and **2** (4 mg) were solubilised in a glass flask containing 6 ml of $CHCl_3$. The solvent was left to evaporate overnight at room temperature under stirring. The flask was placed into an water bath at 80 °C for 30 s, then the nanoparticles were solubilised with 1.5 ml of H_2O obtaining a pearly solution. The solution was purified from the excess of polymer by centrifugation (8000 rpm at room temperature for 5 min), and the resulting white nanoparticle pellet was resuspended with 1.5 ml of H_2O. Later, the product was freeze-dried overnight and 8 mg of $NaYF_4:Yb^{3+}/Tm^{3+}$@$NaYF_4$@**2** NPs were collected.

4.4.7 Synthesis of $NaYF_4:Yb^{3+}/Tm^{3+}$@$NaYF_4$@DSPE-PEG(2000)-NH_2

The same method illustrated above was used to prepare$NaYF_4:Yb^{3+}/Tm^{3+}$@$NaYF_4$@DSPE-PEG(2000)-NH_2 nanomaterials.

4.4.8 Photolysis experiments

Inside a 1 ml glass vial PBS/D_2O buffer solutions (10 mM, pH = 7.3) of **1** and **2** were irradiated with UVA (λ_{irr} = 385 nm) and NIR light (λ_{irr} = 980 nm) in the presence or absence of UCNPs. A Prizmatix LED Multi-Wavelength MWLLS-11 and a BWT diode laser DS3-11312-110 were employed for UVA and NIR irradiation experiments respectively.

At 385 nm, solutions of **1** (150 μM) and **2** (150 μM) were irradiated with a power density of 40 mW cm^{-2} and formation of photoproducts was monitored by ^1H NMR.

In the case of UCNP-mediated photolysis, a power density of 4.9 and 7.3 W cm^{-2} was employed for 980-nm excitation of **1** (150 μM) with $NaYF_4:Yb^{3+}/Tm^{3+}$@$NaYF_4$ (5 mg), and for $NaYF_4:Yb^{3+}/Tm^{3+}$@$NaYF_4$@**2** (5 mg) respectively. After irradiation, the nanoparticle solutions were centrifuged (5000 rpm, 5 min) and the supernatants were analysed by ^1H NMR. After each measurement, supernatants were combined again with the pellet, obtaining the initial solution used in the photoreaction. Such procedure was employed to improve the quality of NMR spectra. Control experiments

consisted of exciting directly (no UCNPs) at 980 nm **1** (150 μM) and **2** (150 μM) in buffer using a power density of 6.5 and 8.8 W cm^{-2} respectively.

4.5 References

[1] U. Schatzschneider, *Eur. J. Inorg. Chem.*, **2010**, 1451.

[2] N. J. Farrer, L. Salassa, P. J. Sadler, *Dalton Trans.*, **2009**, 10690.

[3] A. F. Westendorf, J. A. Woods, K. Korpis, N. J. Farrer, L. Salassa, K. Robinson, V. Appleyard, K. Murray, R. Grunert, A. M. Thompson, P. J. Sadler, P. J. Bednarski, *Mol. Cancer Ther.*, **2012**, *11*, 1894.

[4] M. R. Kima, H. Morrison, S. I. Mohammed, *Anti-Cancer Drugs*, **2011**, *22*, 896.

[5] D. Barolet, *Semin. Cutaneous Med. Surg.*, **2008**, *27*, 227.

[6] J. Zhou, Z. Liu, F. Li, *Chem. Soc. Rev.*, **2012**, *41*, 1323.

[7] A. G. Arguinzoniz, E. Ruggiero, A. Habtemariam, J. Hernández-Gil, L. Salassa, J. C. Mareque-Rivas, *Part. Part. Syst. Charact.*, **2014**, *31*, 46.

[8] L. Zhao, J. Peng, Q. Huang, C. Li, M. Chen, Y. Sun, Q. Lin, L. Zhu, F. Li, *Adv. Funct. Mater.*, **2014**, *24*, 363.

[9] N. M. Idris, M. K. Gnanasammandhan, J. Zhang, P. C. Ho, R. Mahendran, Y. Zhang, *Nat. Med.*, **2012**, *18*, 1580.

[10] Y. Yang, Q. Shao, R. Deng, C. Wang, X. Teng, K. Cheng, Z. Cheng, L. Huang, Z. Liu, X. Liu, B. Xing, *Angew. Chem. Int. Ed.*, **2012**, *51*, 3125.

[11] W. Wu, L. Yao, T. Yang, R. Yin, F. Li, Y. Yu, *J. Am. Chem. Soc.*, **2011**, *133*, 15810.

[12] J. Mendez-Ramos, P. Acosta-Mora, J. C. Ruiz-Morales, T. Hernández, M. E. Borges, P. Esparza, *RSC Adv.*, **2013**, *3*, 23028.

[13] Z. Zhou, H. Hu, H. Yang, T. Yi, K. Huang, M. Yu, F. Li, C. Huang, *Chem. Commun.*, **2008**, 4786.

[14] J.-C. Boyer, C.-J. Carling, B. D. Gates, N. R. Branda, *J. Am. Chem. Soc.*, **2010**, *132*, 15766.

[15] J.-C. Boyer, C.-J. Carling, S. Y. Chua, D. Wilson, B. Johnsen, D. Baillie, N. R. Branda, *Chem. Eur. J.*, **2012**, *18*, 3122.

[16] J. V. Garcia, J. Yang, D. Shen, C. Yao, X. Li, R. Wang, G. D. Stucky, D. Zhao, P. C. Ford, F. Zhang, *Small*, **2012**, *8*, 3800.

[17] P. T. Burks, J. V. Garcia, R. GonzalezIrias, J. T. Tillman, M. Niu, A. A. Mikhailovsky, J. Zhang, F. Zhang, P. C. Ford, *J. Am. Chem. Soc.*, **2013**, *135*, 18145.

[18] E. Ruggiero, A. Habtemariam, L. Yate, J. C. Mareque-Rivas, L. Salassa, *Chem. Commun.*, **2014**, *50*, 1715.

[19] H. P. Varbanov, M. A. Jakupec, A. Roller, F. Jensen, M. Galanski, B. K. Keppler, *J. Med. Chem.*, **2013**, *56*, 330.

[20] N. J. Wheate, S. Walker, G. E. Craig, R. Oun, *Dalton Trans.*, **2010**, *39*, 8113.

[21] P. Gramatica, E. Papa, M. Luini, E. Monti, M. B. Gariboldi, M. Ravera, E. Gabano, L. Gaviglio, D. Osella, *J. Biol. Inorg. Chem.*, **2010**, *15*, 1157.

[22] K. Knop, R. Hoogenboom, D. Fischer, U. S. Schubert, *Angew. Chem. Int. Ed.*, **2010**, *49*, 6288.

[23] F. Vetrone, R. Naccache, V. Mahalingam, C. G. Morgan, J. A. Capobianco, *Adv. Funct. Mater.*, **2009**, *19*, 2924.

[24] J.-C. Boyer, L. A. Cuccia, J. A. Capobianco, *Nano Lett.*, **2007**, *7*, 847.

[25] C. R. Maldonado, N. Gomez-Blanco, M. Jauregui-Osoro, V. G. Brunton, L. Yate, J. C. Mareque-Rivas, *Chem. Commun.*, **2013**, *49*, 3985.

[26] I. Infante, J. M. Azpiroz, N. Gomez-Blanco, E. Ruggiero, J. M. Ugalde, J. C. Mareque-Rivas, L. Salassa, *J. Phys. Chem. C*, **2014**, *118*, 8712.

[27] E. Ozkaraoglu, I. Tunc, S. Suzer, Surf. Coat. Technol., **2007**, *201*, 8202.

[28] J. Hernández-Gil, M. Cobaleda-Siles, A. Zabaleta Azpiroz, L. Salassa, J. Calvo, J. C. Mareque-Rivas, *Adv. Healthc. Mater.*, **2015**, *4*, 1034.

[29] M. Moros, B. Pelaz, P. Lopez-Larrubia, M. L. Garcıa-Martin, V. Grazu, J. M. de la Fuente, *Nanoscale*, **2010**, *2*, 1746.

[30] M. K. Danquah, X. A. Zhang, R. I. Mahato, *Adv. Drug Delivery Rev.*, **2011**, *63*, 623.

[31] M. B. Ahmad, M. Y. Tay, K. Shameli, M. Z. Hussein, J. J. Lim, *Int. J. Mol. Sci.*, **2011**, *12*, 4872.

[32] M. Reithofer, M. Galanski, A. Roller, B. K. Keppler, *Eur. J. Inorg. Chem.*, **2006**, *13*, 2612.

[33] N. Gomez Blanco, M. Jauregui-Osoro, M. Cobaleda-Siles, C. R. Maldonado, M. Henriksen-Lacey, D. Padro, S. Clark, J. C. Mareque-Rivas., *Chem. Commun.*, **2012**, *48*, 4211.

5

Upconverting Nanoparticles Prompt Remote Near-Infrared Photoactivation of Ru^{II}-Arene Complexes

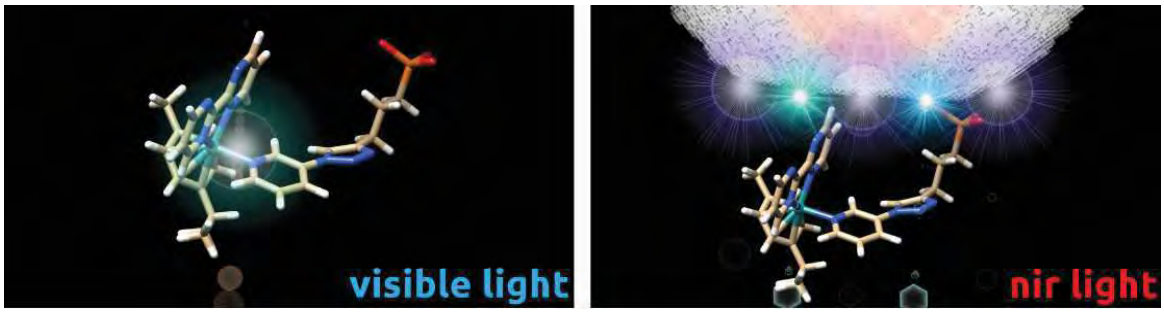

*The synthesis and full characterization (including X-ray diffraction studies and DFT calculations) of two new piano-stool Ru^{II}-arene complexes, namely $[(\eta^6$-p-cym)Ru(bpy)(m-CCH-Py)$][PF_6]_2$ (**1**) $[(\eta^6$-p-cym)Ru(bpm)(m-CCH-Py)$][PF_6]_2$ (**2**) (p-cym = p-cymene, bpy = 2,2'-bipyridine, bpm = 2,2'-bipyrimidine, and m-CCH-Py = 3-ethynylpyridine), is described and discussed. The reaction of the m-CCH-Py ligand of **1** and **2** with diethyl-3-azidopropyl phosphonate by Cu-catalyzed click chemistry affords $[(\eta^6$-p-cym)Ru(bpy)(P-Trz-Py)$][(PF)_6]_2$ (**3**) and $[(\eta^6$-p-cym)Ru(bpm)(P-Trz-Py)$][(PF)_6]_2$ (**4**) (P-Trz-Py = [3-(1-Pyridin-3-yl-[1,2,3]triazol-4-yl)-propyl]-phosphonic acid diethyl ester). Upon light excitation at λ_{irr} = 395 nm, complexes **1**–**4** photodissociate the monodentate pyridyl ligand and form the aqua adduct ions $[(\eta^6$-p-cym)Ru(bpy)$(H_2O)]^{2+}$ and $[(\eta^6$-p-cym)Ru(bpm)$(H_2O)]^{2+}$. Thulium-doped upconverting nanoparticles (UCNPs) are functionalized with **4**, thus exploiting their surface affinity for the phosphonate group in the complex. The so-obtained nanosystem **UCNP@4** undergoes near-infrared (NIR) photoactivation at λ_{irr} = 980 nm, thus producing the corresponding reactive aqua species that binds the DNA-model base guanosine 5'-monophosphate.*

The work presented in this chapter was previously published: E. Ruggiero, C. Garino, J.C. Mareque-Rivas, A. Habtemariam, L. Salassa, Chem. Eur. J., 2016, 22, 2801.

5.1 Introduction

Encouraged by the clinical success of photodynamic therapy (PDT), [1] light-activatable molecules and nanomaterials are being increasingly investigated for their capacity to generate biologically active species in situ with high spatiotemporal control. In principle, such an attractive strategy allows the biological effects of drugs to be localized, thus potentially reducing their therapeutic drawbacks. For this reason, light activation has found application in a number of fields and diverse systems have been designed as neuroscience tools, [2] drug delivery platforms, [3, 4] and anticancer prodrugs. [5, 6]

Promising metal-based photo-chemotherapeutics have been developed that exploit the unique photochemical and antitumor properties of transition-metal complexes. Several research groups worldwide have demonstrated that light-activatable complexes of various transition metals (e.g., Pt, Ru, Rh, and Ir) show encouraging antineoplastic profiles and unconventional mechanisms of action relative to their ground-state analogues. [4–7]

Nevertheless, the poor absorption properties of metal complexes in the therapeutic window of the red and near-infrared (NIR) spectrum (λ_{irr} = 650–1000 nm) pose a serious limitation to advancing their use toward preclinical and clinical studies because maximal light penetration into tissues is achieved in this wavelength range and damage to biological components is minimized. [8, 9] Relative to PDT photosensitizers, photoactivatable anticancer metal complexes generally display low-energy absorption bands that rarely extend over λ_{irr} = 550 nm and have modest extinction coefficients. Although a few exceptions have been reported, [10–12] it is extremely challenging to improve absorption features without altering the ground-state stability and photoreactivity of the metal complexes.

For this reason, we and other groups have recently started to explore the use of upconversion nanoparticles (UCNPs) as phototriggers for the NIR photoactivation of (anticancer) metal complexes. [9, 13–20] UCNPs are typically $NaYF_4$ or $NaGdF_4$ nanocrystals doped with lanthanide ions, such as Yb^{3+}:Tm^{3+} or Yb^{3+}:Er^{3+}, which convert NIR light (λ_{irr} = 980 nm) into UV-vis light through multiphotonic processes. [21, 22] Conveniently, UV-vis photons emitted by UCNPs upon NIR-light excitation can promote

photochemical reactions in metal complexes and potentially switch on their biological effects. Ford and co-workers showed that the NIR irradiation of UCNPs loaded with either the Roussin black salt anion or the photoactivated CO-releasing moiety (photoCORM) trans-[Mn(2,2'-bipyridine)(PPh_3)$_2$(CO)$_2$] results in the release of NO and CO, respectively. [13, 14] Similarly, we have demonstrated that related upconversion nanosystems promoted the release of pyridine from a Ru–polypyridyl complex [16] and the generation of a Pt^{II} species from a Pt^{IV} prodrug candidate. [17] Alternatively, He et al. designed an UCNP system capable of releasing doxorubicin in a controlled fashion by taking advantage of a photoactivatable Ru complex that acts as a valve. [20] Conversely, Bonnet and co-workers also reported a promising system for activation at λ_{irr} = 630 nm of a model Ru–polypyridyl complex by using triplet-triplet annihilation upconversion. [23]

The unique optical (upconversion emission) and chemical (e.g., Gd^{3+} and $^{18}F^{-}$ ions on the surface) features of UCNPs are also exploited for multimodal imaging (e.g., single-photon emission computed tomography/positron emission tomography (SPECT/PET), [24, 25] computed tomography (CT), [26] magnetic resonance imaging (MRI), [27] optical, [28] and photoacustic, [29] as demonstrated by numerous studies *in vivo*, which have appeared in the last few years. These properties and the low toxicity of UCNPs [30] make hybrid nanomaterials based on UCNPs and metal complexes suitable for application in theranostics. [31]

Herein, we devise a new approach to demonstrate the usefulness of UCNPs in the photoactivation of Ru^{II}–arene complexes, an attractive class of metal complex with remarkable anticancer activity *in vitro* [32, 33] and *in vivo*. [34]

Pyridinato Ru^{II}–arene derivatives display dark-stability and selectively release pyridinato ligands upon visible-light excitation, thus generating highly reactive aqua species. [35–37] Controlling such a reaction is key for activating the biological activity of Ru^{II}–arene derivatives. For this purpose, we prepared two new Ru–pyridinato derivatives, namely [(η^6-*p*-cym)Ru(bpy)(*m*-CCH-Py)][PF_6]$_2$ (**1**) and [(η^6-*p*-cym)Ru(bpm)(*m*-CCH-Py)][PF_6]$_2$ (**2**; *p*-cym=*p*-cymene, bpy=2,2'-bipyridine, bpm=2,2'-bipyrimidine, and *m*-CCH-Py=3-ethynylpyridine) and exploited a click-chemistry strategy to derivatize the monodentate 3-ethynylpyridine pendant arm with a phosphonate group, which has high affinity for the UCNP surface. [38] The

functionalized complexes **3** and **4** and their precursors were characterized and their photochemistry studied in detail by using different methods, including DFT calculations.

On the basis of its photoreactivity, complex 4 was selected to anchor onto the core@shell $NaYF_4$:Yb(30%)/Tm(0.5%)@$NaYF_4$ nanoparticles and perform NIR photochemistry experiments. Results proved the obtained **UCNP@4** nanoconstruct is activated at λ_{irr} = 980 nm, thus generating the reactive aqua photoproduct $[(\eta^6\text{-}p\text{-cym})Ru(bpm)(H_2O)]^{2+}$, which binds the DNA-model base guanosine 5'-monophosphate (GMP). The synthetic strategy and NIR photoactivation reported herein may offer new intriguing opportunities for the design of innovative prodrug nanosystems that rely on the rich anticancer properties of metallo–arene complexes.

5.2 Results and Discussion

5.2.1 Synthesis of complexes 1–4 and UCNP@4

Complexes $[(\eta^6\text{-}p\text{-cym})Ru(bpy)(m\text{-CCH-Py})][PF_6]_2$ (**1**) and $[(\eta^6\text{-}p\text{-cym})Ru(bpm)(m\text{-CCH-Py})][PF_6]_2$ (**2**) were synthesized in moderate yields (ca. 35%) by treating the precursors $[(\eta^6\text{-}p\text{-cym})Ru(bpy)Cl][PF_6]$ and $[(\eta^6\text{-}p\text{-cym})Ru(bpm)Cl][PF_6]$ with $AgNO_3$ and subsequently performing ligand-exchange reactions with 3-ethynylpyridine in $MeOH/H_2O$ (Scheme 1a). [39–42] A range of techniques was used to characterize both complexes, including X-ray, multinuclear NMR, mass-spectrometry, and elemental analysis.

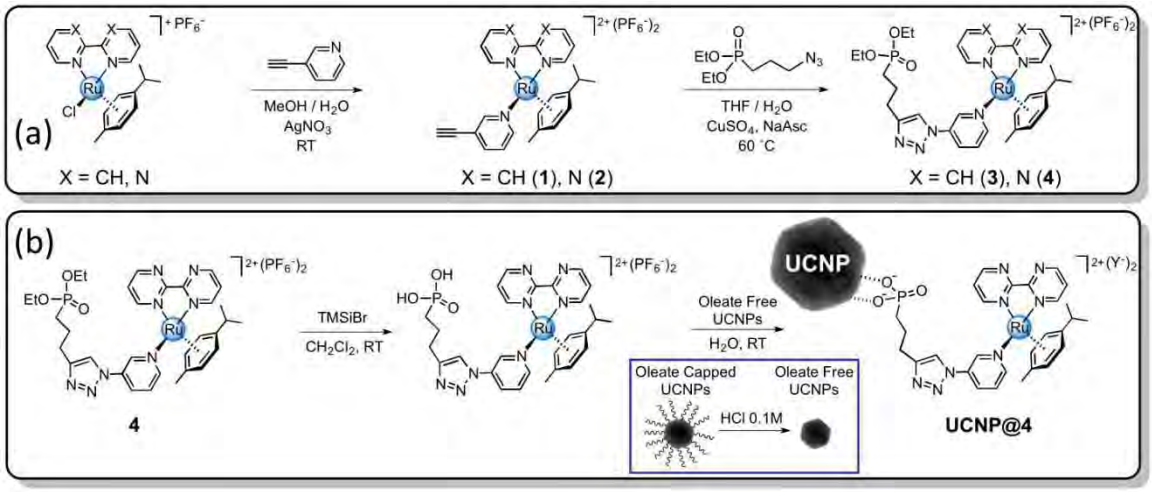

Scheme 1

We employed 3-ethynylpyridine because pyridyl ligands are known to render Ru–arene complexes hydrolytically stable in the dark. [35–37] Moreover, the presence of an alkyne group on the ligand allowed us to adopt click chemistry for the functionalization of **1** and **2** and anchoring onto UCNPs. Click chemistry is a convenient strategy for ligand design in inorganic chemistry and has attracted significant attention in recent years. [43] Such an approach affords (bio)orthogonal reactions that are high yielding, selective, and robust under mild conditions. [44]

Inspired by the work of Branda and co-workers, [45] we employed diethyl-3-azidopropyl phosphonate and its azido function to incorporate the phosphonate group into **1** and **2** by using click chemistry. Phosphonates have good affinity for the $NaYF_4$ surface of UCNPs, as demonstrated by various groups. [38, 46] Diethyl-3-azidopropyl phosphonate was obtained reacting (3-bromopropyl)phosphonic acid with sodium azide in acetone. [47] Clicked complexes $[(\eta^6\text{-}p\text{-cym})Ru(bpy)(P\text{-}Trz\text{-}Py)][PF_6]_2$ (**3**) and $[(\eta^6\text{-}p\text{-cym})Ru(bpm)(P\text{-}Trz\text{-}Py)][PF_6]_2$ (**4**; P-Trz-Py = [3-(1-pyridin-3-yl-[1,2,3]triazol-4-yl)-propyl]phosphonic acid diethyl ester) were prepared by treating **1** and **2** with diethyl-3-azidopropyl phosphonate in THF/water at 60 °C for 72 hours in the presence of $CuSO_4$ and sodium ascorbate (Scheme 1a).

Complexes **3** and **4** were obtained in good yields and purity and were characterized by ^{1}H, ^{13}C, and ^{31}P NMR spectroscopic and mass-spectrometric analysis. Although the photochemical behavior of the complexes is rather similar (see below), complex **4** was selected for loading onto the core@shell $NaYF_4$:Yb^{3+}/Tm^{3+}@$NaYF_4$ UCNPs on the basis of the higher reactivity of its bpm analogue 2 relative to 1 (e.g., with the bpy ligand). For this reason, we first activated the phosphonate group of **4** into the acid form by de-esterification with tribromo(methyl)silane (TMSBr) in CH_2Cl_2. The so-obtained complex was stirred overnight with oleate-free core@shell UCNPs in H_2O, and an orange pellet corresponding to **UCNP@4** was collected after several washing and centrifugation steps (Scheme 1b). Characterization of the hybrid material was achieved by using a combination of different techniques (see below).

5.2.2 Characterization of 1 and 2: X-ray and DFT structures

The crystal structure of the hexafluorophosphate salts of **1** and **2** were determined by means of X-ray diffraction studies (Fig. 1). These structures are fairly similar, and the

first-coordination spheres of both Ru complexes display comparable bond lengths and angles (Table 1). Complexes **1** and **2** present the typical piano-stool geometry of related Ru^{II}-arene complexes with N,N' ancillary ligands. [41] Crystal packing and experimental details, including the X-ray diffraction data, are reported in Appendix Chapter 5 (Table A1 and Fig. A1 and A2). DFT-optimized ground state geometries (Table 1, B3LYP/LanL2DZ/6-31G**) for **1** and **2** describe the structure of the complexes satisfactorily. The calculated and experimental Ru-N bond lengths differ only by less than 0.02 Å. However, the Ru-*p*-cym(centroid) distances are approximately 0.15 Å longer in the DFT calculations relative to the X-ray determinations.

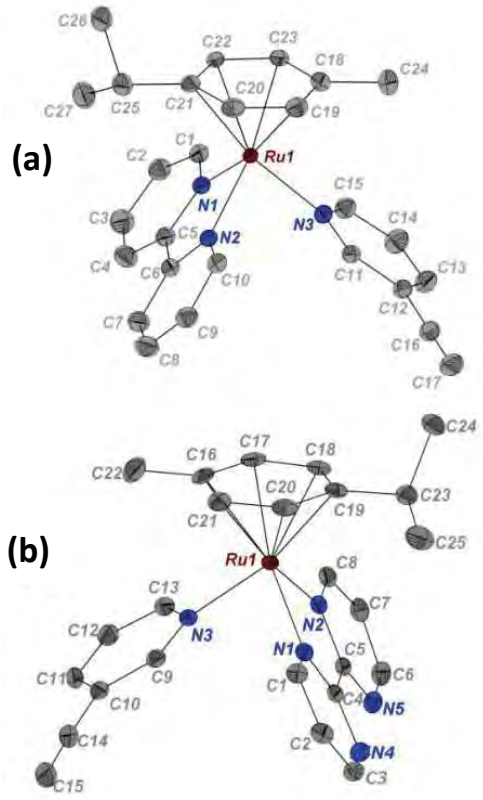

Fig. 1. Crystal structures of (a) **1** and (b) **2**. Thermal ellipsoids are depicted at the 50% probability level. Counter ions (PF_6^-) and H atoms are omitted for clarity.

Two triplet excited-state structures were also DFT-minimized for **1** and **2** (Table 1) because triplet states are likely to be involved in the photochemistry of the complexes. The lowest-lying triplet state (T0) for both compounds has a distorted structure with one Ru-N(N,N') bond strongly elongated (>2.40 Å). However, the higher-energy triplet

geometries (T1) for both compounds display elongated Ru-N(*m*-CCH-Py) distances (>2.51 Å).

Table 1. Selected X-ray and DFT-calculated bond distances (Å) for **1** and **2** in the ground-state (S0) and in two triplet-state (T0 and T1) geometries.

Compd.	Ru–N(*m*-CCH-Py)	Ru–N(N,N')	Ru–N(N,N')	Ru–*p*-cym$_{(centroid)}$
X-Ray				
1	2.125(2)	2.085(2)	2.084(2)	1.701
2	2.1241(17)	2.0995(16)	2.0873(16)	1.704
Ground State (S0)				
1	2.159	2.103	2.095	1.848
2	2.158	2.111	2.106	1.850
Lowest-lying Triplet State (T0)				
1	2.164	2.404	2.113	2.079
2	2.143	2.457	2.131	2.082
Triplet State (T1)				
1	2.556	2.087	2.082	2.157
2	2.511	2.093	2.113	2.140

5.2.3 Photophysical and photochemical properties of 1 and 2

The UV-vis spectrum (Fig. 2a) of **1** exhibits five distinct bands at λ = 245, 269, 305, 317, and 370 nm (ε = 7600, 6400, 5400, 5700, and 1300 $M^{-1}cm^{-1}$, respectively), whereas **2** (Fig. 2b) displays two major bands and one shoulder, respectively at λ = 246, 370, and 291 nm (ε = 3700, 1200, and 3200 $M^{-1}cm^{-1}$, respectively).

Time dependent (TD)-DFT is a valuable tool to assign the character of the absorption bands. Calculation of singlet–singlet transitions and analysis of their orbital composition (Appendix Chapter 5, Table A2 and A3, and Fig. A3) provide information on the nature of the singlet-excited states, which can be conveniently visualized by using electron-density difference maps (EDDMs, Appendix Chapter 5, Fig. A4 and A5).

In agreement with related complexes, the high-energy bands of **1** and **2** have mixed metal-to-ligand charge transfer (MLCT) and intra-ligand character (< 325 nm).

Conversely the lowest-energy bands have mainly MLCT character. Furthermore, transitions of weak intensity with mixed MLCT/MC (metal-centred) character are present in their tail. These latter transitions have a significant contribution from σ-antibonding orbitals, which confer a dissociative nature (Appendix Chapter 5, Fig. A3). Through generation of these dissociative singlet states and subsequent intersystem-crossing, the low-energy triplet states T0 and T1 (Fig. 3) can be populated.

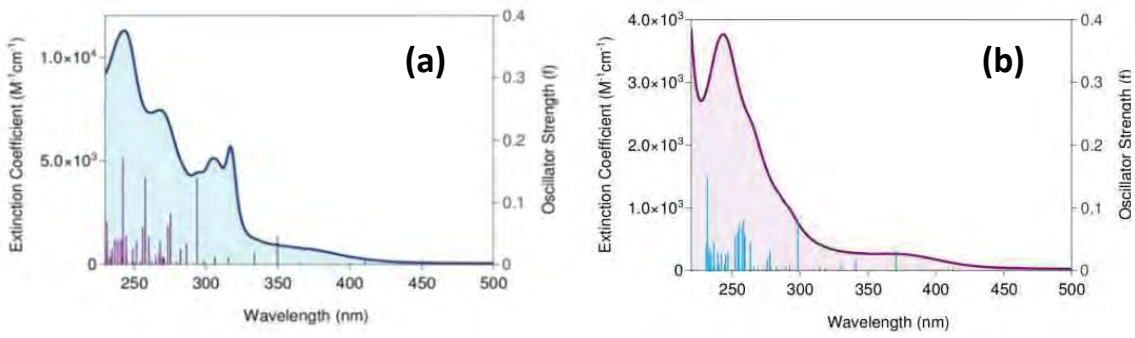

Fig. 2. UV-vis absorption spectrum of **1** (a) and **2** (b) in aqueous solution (95:5 H_2O:DMSO); vertical bars represent singlet-singlet TD-DFT transitions (Appendix Chapter 5,Table A2 and A3).

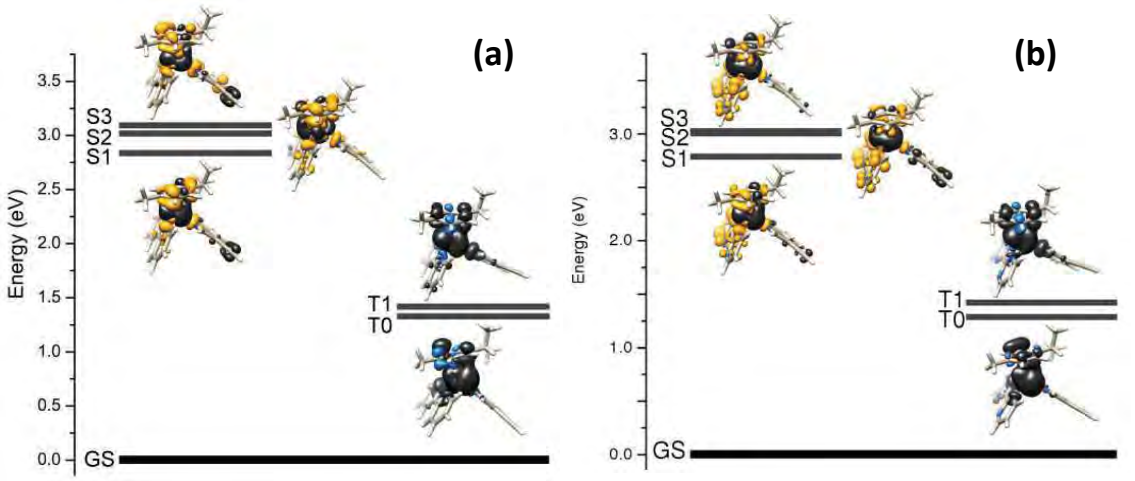

Fig. 3. Singlet and triplet energy level diagram with EDDMs (singlets) and spin density surfaces (triplets) for **1** (a) and **2** (b). In the EDDMs, black indicates a decrease in electron density while yellow indicates and increase.

T1 is dissociative toward the 3-ethynylpyridine ligand, whereas T0 might promote the partial dissociation of a pyridyl ring of the bpy/bmp ligand (Appendix Chapter 5,

Fig. A6–A8). Nevertheless, release of the chelating ligands is prevented by the strong coordination of the second ring. For this reason, light excitation of **1** and **2** results in selective photodissociation of the monodentate 3-ethynylpyridine ligand. Fig. 3 reports the energy level of selected singlet and triplet states for **1** and **2** and their corresponding EDDMs (singlet states) and spin densities (triplet states). The low energy of the T0 state (1.33 and 1.29 eV for **1** and **2**, respectively) calculated by DFT calculations and the small energy difference between this state and T1 are consistent with the lack of emission from the two complexes, which tend to relax to the ground state by non-radiative pathways, and with their modest photodissociation quantum yields of less than 1%, as determined by using actinometry methods [48] $\Phi_{\mathbf{1}}$ = 0.003 and $\Phi_{\mathbf{2}}$ = 0.008, Table 2 and Fig. 4).

Table 2. Functions describing the temporal evolution of the absorbance of **1** and **2** and starting rate of absorbance decreasing used to calculate the reaction rate.

Compound	$A = f(t)$	$\left.\frac{dA}{dt}\right\|_{t=0}$	Φ
1	$A_{317\,nm} = 0.00105 + 0.70544 \cdot e^{-\frac{t}{94.9943}}$	$\left.\frac{dA_{317nm}}{dt}\right\|_{t=0} = -7.4 \cdot 10^{-3} s^{-1}$	0.003
2	$A_{291nm} = -0.00714 + 0.23187 \cdot e^{-\frac{t}{23.2838}}$	$\left.\frac{dA_{291nm}}{dt}\right\|_{t=0} = -9.9 \cdot 10^{-3} s^{-1}$	0.008

Fig. 4b and 5b show the photolysis of **2** (D_2O:DMSO-d_6, 95:5%) upon 395-nm light irradiation (15 mW·cm^{-2}) followed by UV-vis and ^{1}H NMR spectroscopic analysis. Light irradiation induces variations in the UV-vis absorption profile of **2**, with a decrease at 370 nm and an increase in the 260−320 nm region of the bands. The presence of isosbestic points at 230 and 315 nm reveals the formation of a single photoproduct. Furthermore, diagnostic changes in the ^{1}H NMR spectra of **2** and ultraperformance (UP)LC-MS analysis (Appendix Chapter 5, Fig. A9) clearly confirm the release of 3-ethynylpyridine and the formation of the aqua $[(\eta^6\text{-}p\text{-cym})Ru(bpm)(H_2O)]^{2+}$ ionic species. [35–37] A control experiment indicates **2** is stable in the dark up to at least 24 hours (Fig. A11). Analogue results were observed for **1** and are summarized in Fig. 4a, 5a, A10 and A11 of the Appendix Chapter 5.

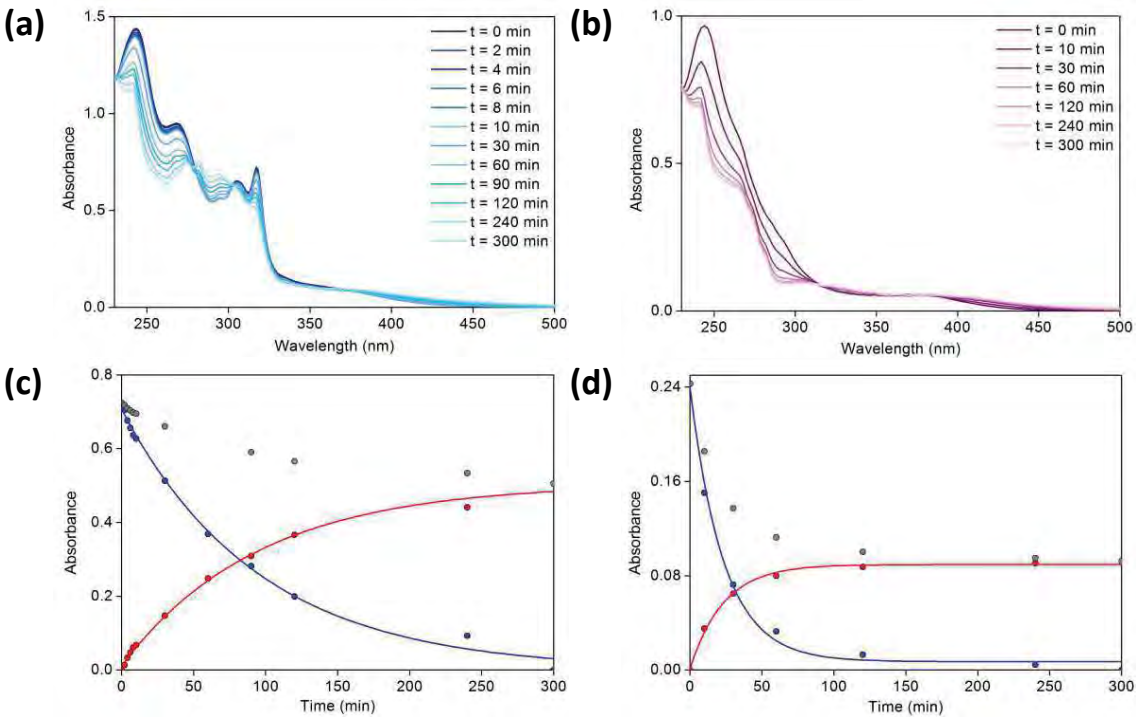

Fig. 4. Time course of photolysis for **1** (a) and **2** (b) in aqueous solution (95:5 H_2O:DMSO) upon 395 nm (15 mW·cm^{-2}) followed by electronic absorption spectroscopy. Temporal evolution of the absorbance of an aqueous solution of **1** (c) and **2** (d) irradiated at 395 nm (15 mW·cm^{-2}) and monitored at 317 nm (gray), together with the contributions of **1** (blue) (or **2**) and [(η^6-*p*-cym)Ru(bpy)(H_2O)]$^{2+}$ (red) (or [(η^6-*p*-cym)Ru(bpm)(H_2O)]$^{2+}$).

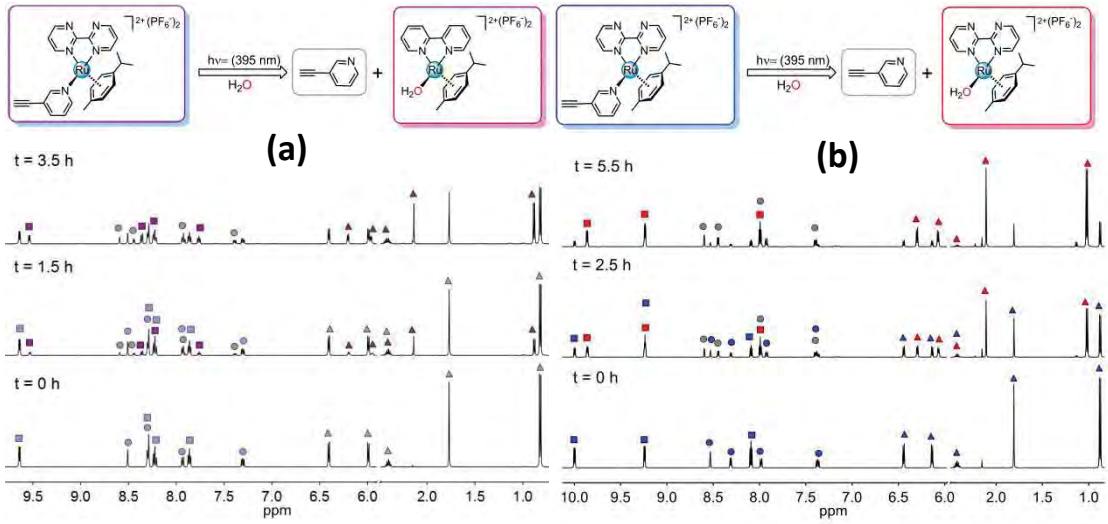

Fig. 5. Time course of photolysis of **1** and **2** upon 395 nm irradiation (15 mW·cm^{-2}) followed by ^{1}H NMR. **1** (a) is indicated with violet and [(η^6-*p*-cym)Ru(bpy)(H_2O)]$^{2+}$ with purple. **2** (b) is indicated with blue and [(η^6-*p*-cym)Ru(bpm)(H_2O)]$^{2+}$ with red. Free 3-ethynylpyridine is colored in grey.■ = bpy or bpm, ▲= *p*-cym, ● = 3-ethynylpyridine.

5.2.4 Photochemistry of 3, 4 and UCNP@4 under visible and NIR light excitation

Initially, the behavior of clicked complexes **3** and **4** was verified and compared with their analogues **1** and **2** in the dark and under visible-light conditions. Analysis by NMR spectroscopy and UPLC-MS (Fig. 6, Appendix Chapter 5, Fig. A12–14) shows that **3** and **4** indeed react as the precursors **1** and **2**; namely, **3** and **4** undergo photodissociation of the P-Trz-Py ligand upon excitation at λ_{irr} = 395 nm. The addition of excess GMP to irradiated solutions of **3** and **4** results in the formation of the adducts $[(\eta^6\text{-}p\text{-cym})Ru(bpy)(GMP)]^{2+}$ and $[(\eta^6\text{-}p\text{-cym})Ru(bpm)(GMP)]^{2+}$ after 12 hours of incubation at ambient temperature (Appendix Chapter 5, Fig. A15–18). Next, we selected **4** to perform decoration of UCNPs because of the slightly higher photodissociation yield of bpm complexes with respect to their bpy analogues.

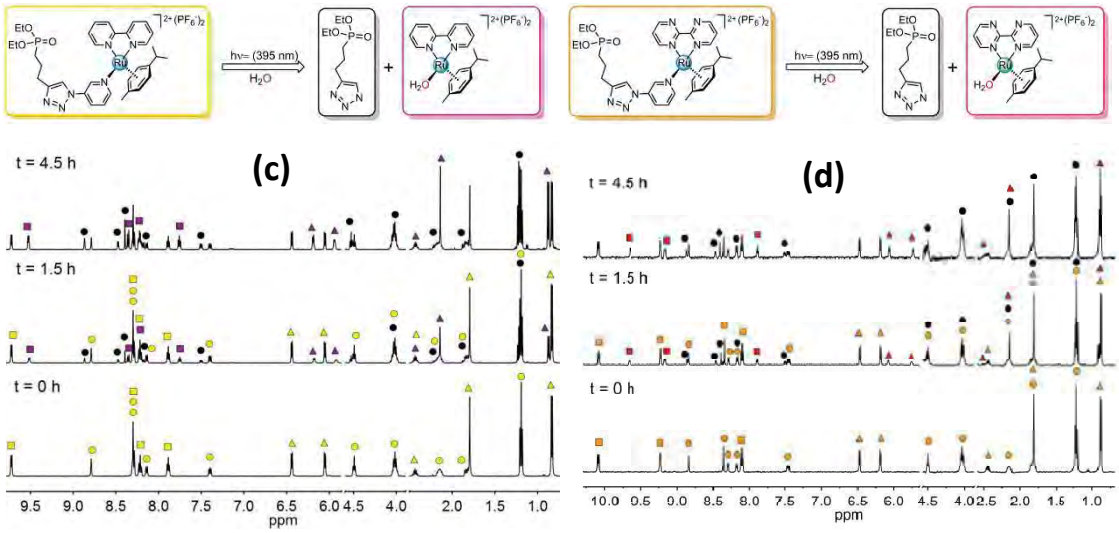

Fig. 6. Time course of photolysis of **3** and **4** upon 395 nm irradiation (15 $mW \cdot cm^{-2}$) followed by ^1H NMR. Complex **3** (a) is indicated with yellow and $[(\eta^6\text{-}p\text{-cym})Ru(bpy)(H_2O)]^{2+}$ with violet. Complex **4** (b) is indicated with orange and $[(\eta^6\text{-}p\text{-cym})Ru(bpm)(H_2O)]^{2+}$ with red. Free P-Trz-Pyligand is colored with black. ■ = bpy or bpm, ▲= *p*-cym, ● = P-Trz-Py

For anchoring of **4** to UCNPs, we first synthesized core@shell $NaYF_4$:Yb^{3+}/Tm^{3+}(30/0.5%)@$NaYF_4$ nanoparticles by thermal decomposition as previously described by several groups. [17, 49, 50] UCNPs were thoroughly characterized by TEM, X-ray photoelectron spectroscopy (XPS), and FTIR and emission

spectroscopy (Fig. 7, 8 and Appendix Chapter 5, A19). TEM images of the core@shell UCNPs show uniform size and shape (diameter = 37 nm; Figure 7b).

Functionalization with **4** was achieved as described in Scheme 1b and did not cause any observable change to the nanoparticles, rather TEM images of aqueous solutions of **UCNP@4** showed improved dispersion and lower aggregation relative to the core-only and core@shell UCNPs capped with oleic acid. We obtained a rough estimate of the complex-grafting density onto UCNPs by UV-vis spectroscopic analysis following the procedure of Branda and co-workers.[51] By assuming a particle density of 4.2 $g \cdot cm^{-3}$ and a diameter of 36.9 nm, the **4**/UCNP ratio was calculated to be approximately 3000:1 (3.5% wt).

The UCNPs display a typical upconversion emission in THF of Tm^{3+} ions (Fig. 9b) with peaks at λ = 345 and 360 nm ($^3P_0 \rightarrow {}^3F_4$ and $^1D_2 \rightarrow {}^3H_6$), λ = 450 and 475 nm ($^1D_2 \rightarrow {}^3F_4$ and $^1G_4 \rightarrow {}^3H_6$), λ = 645, 690 and 720 nm ($^1G_4 \rightarrow {}^3F_4$ and $^3F_3 \rightarrow {}^3H_6$) and at λ = 800 nm ($^3H_4 \rightarrow {}^3H_6$). Photoluminescence studies confirm that core@shell NPs present more intense emissions relative to their core counterparts, especially in the blue region of the UV spectrum (Appendix Chapter 5, Fig. A19). The undoped $NaYF_4$ shell is essential to improve the efficiency of the upconversion process as it decreases non-radiative decay due to the solvent and capping ligands. [49] As we demonstrated previously, [17] such an improvement is key to take full advantage of the overlap between the emission spectrum of UCNPs and the absorption spectrum of metal complexes (Fig.9b).

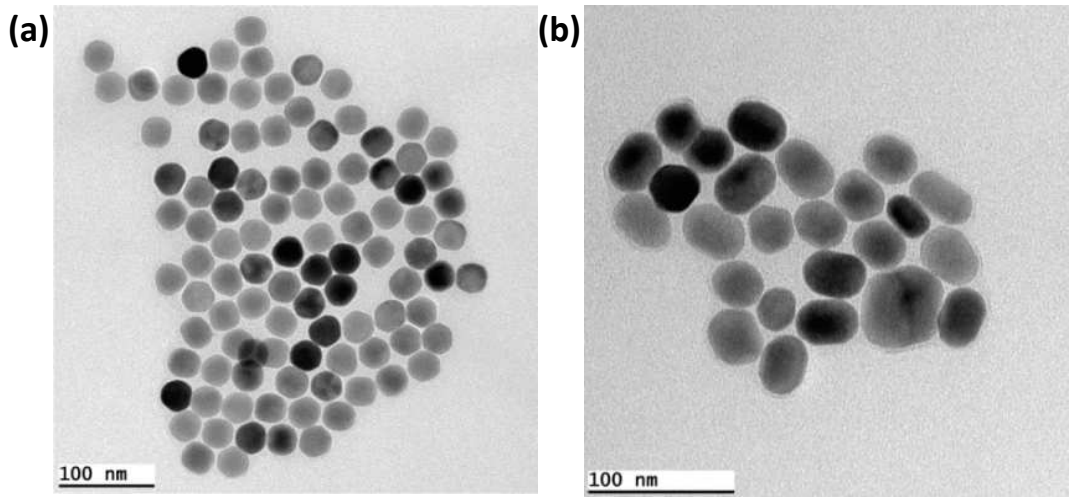

Fig. 7. TEM images of core-$NaYF_4$:Yb(30%)/Tm(0.5%) (a), core@shell $NaYF_4$:Yb(30%)/Tm(0.5%)@$NaYF_4$ (b).

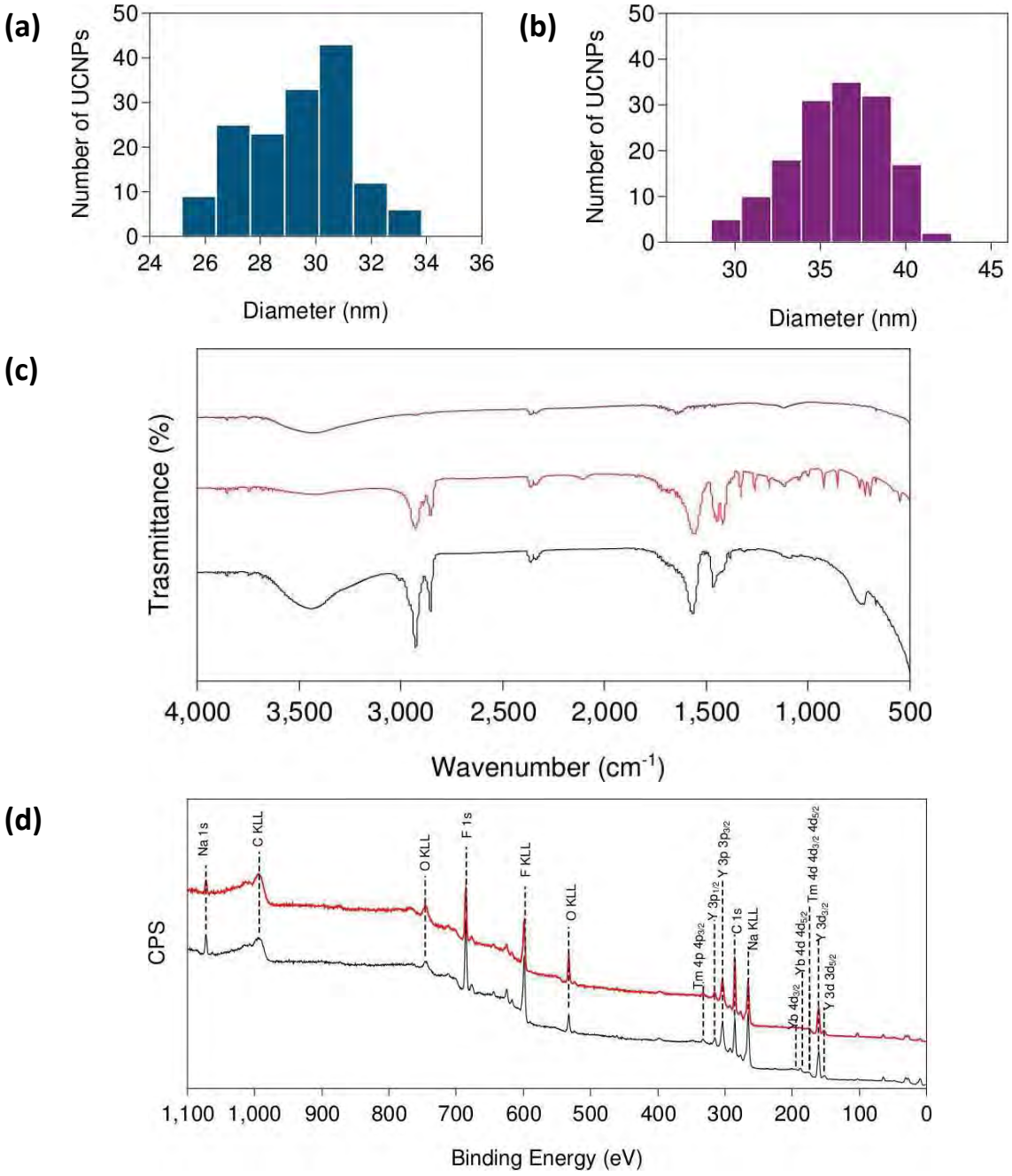

Fig. 8. Histograms of diameter distribution for core (a) and core@shell (b) UCNPsobtained by TEM. Averageparticle sizesof core and core@shell UCNPs are respectively 30.0 ± 1.9 nm and 36.9 ± 2.8 nm. The size was determined counting 150 particles. (c) FT-IR spectra of (black) oleate-coated core UCNPs, (red) oleate-coated core@shell UCNPs and (purple) oleate-free core@shell UCNPs. The two oleate-coated NPs show the characteristic oleic acid bands at 2930, 2850, 1560, 1450 cm^{-1},while the oleate-free NPs exhibit the complete disappearance of such stretching bands. (d) XPS spectra of (black) core UCNPs and (red) core@shell UCNPs with peak assignment to C, O, F, Na, Y, Tm and Yb.

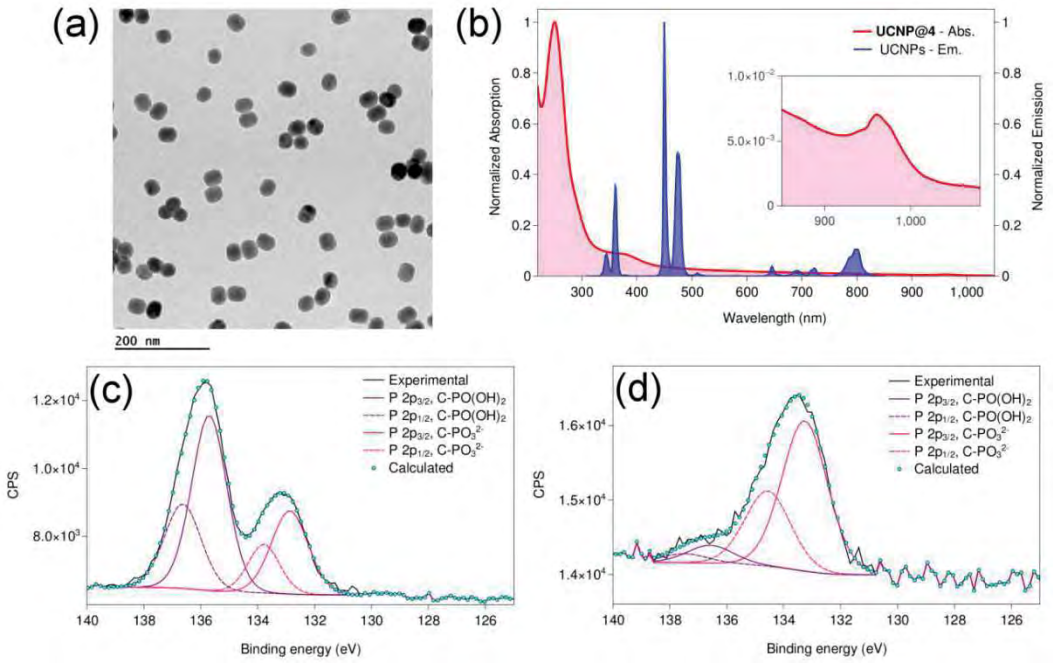

Fig. 9. (a) TEM image of **UCNP@4** . (b) Overlap between the normalized absorption (violet) and emission (blue) spectrum of **UCNP@4** of core@shell UCNPs (THF) upon excitation at 980 nm (15 $W \cdot cm^{-2}$); Inset: zoom in the 900–1000 nm range of the absorption of **UCNP@4** in aqueous solution. P $2p_{3/2}$, $2p_{1/2}$ XPS spectra of (c) **4** and (d) **UCNP@4**.

No significant changes in UCNP luminescence was detected once the particles were treated with hydrochloric acid to remove the oleic acid, thus favoring the interaction with the phosphonic acid group of (activated) **4**. Surface modification was confirmed first by the color of the UCNPs, which became pale orange, and then by UV-vis spectroscopic analysis of **UCNP@4** suspended in aqueous solution and by XPS. The UV-vis spectrum of **UCNP@4** (Fig. 9b) exhibits the absorption profile of the complex with bands at λ = 261 and 370 nm. Notably, the spectrum shows the characteristic band of the dopant Yb^{3+} ion at λ =980 nm.

Aqueous solutions of **4** and **UCNP@4** were deposited onto titanium supports for XPS measurements (Fig. 9C and 9D and Appendix Chapter 5, Fig. A20 and A21). The expected Ru and P peaks for the Ru^{2+} ion and the phosphonic group of the ligand, respectively, were observed in both samples; however, a dramatic difference appeared in the P $2p_{3/2}$ and $2p_{1/2}$ region. In particular, the protonation state of the phosphonic group was clearly different in the case of **UCNP@4** relative to **4**. The former showed a

much greater proportion of R-PO_3^{2-} *versus* R-$PO(OH)_2$ groups (90:10 for **UCNP@4** and 33:67 for **4**, respectively) in agreement with the formation of electrostatic interactions between the phosphonic group of the complex and the surface of the UCNPs.

Therefore, we investigated the effects of NIR light on **UCNP@4** in aqueous solution by irradiating at λ_{irr} = 980 nm and monitoring the course of photoreaction by ^{1}H NMR spectroscopic analysis, which was possible despite the decreased resolution of the ^{1}H NMR spectrum of **UCNP@4** due to the intrinsic paramagnetism of UCNPs. Remarkably, the NMR spectra of the NIR-irradiated **UCNP@4** display changes in the signal pattern (Fig. 10), thus resembling the spectra observed for **4** under excitation at λ_{irr} = 395 nm and ultimately confirming the formation of the [(η^6-*p*-cym)Ru(bpm)(H_2O)]$^{2+}$ specie.

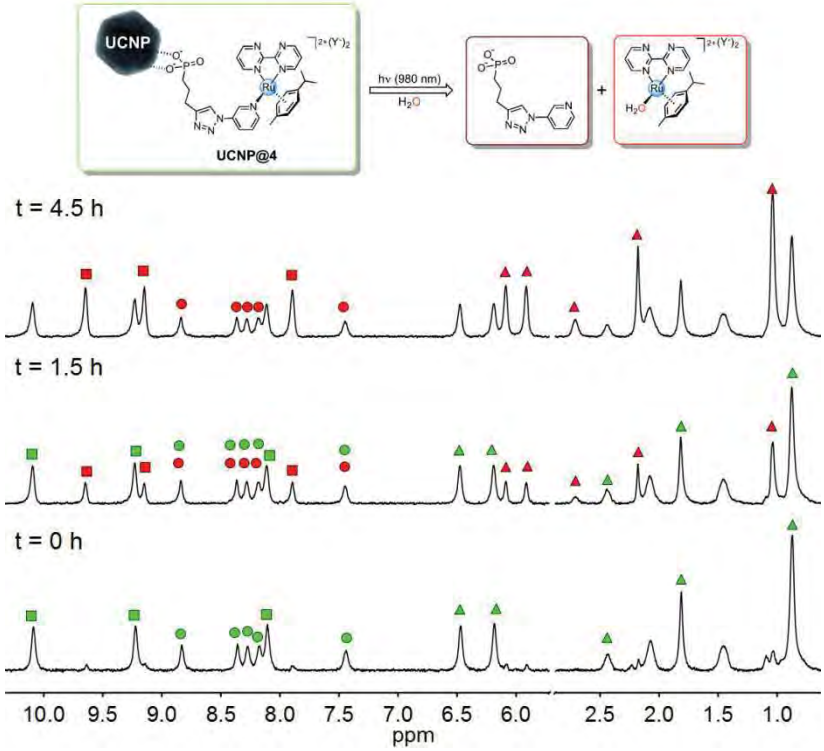

Fig. 10. Photolysis time course for **UCNP@4** in aqueous solution upon 980-nm excitation (8.1 W·cm^{-2}) followed by ^{1}H NMR. ^{1}H NMR: **UCNP@4** (green) and [(η^6-*p*-cym)Ru(bpm)(H_2O)]$^{2+}$ (red); ■ = bpm, ▲= *p*-cym, ● = P-Trz-Py.

Moreover, UPLC-MS experiments consistently show an optimal agreement in retention time and m/z values for irradiated solutions of **4** and **UCNP@4** (at λ_{irr} = 395 and 980 nm; Appendix Chapter 5, Fig. A12 and A22). The aqua photoproduct generated by NIR light at the UCNP surface reacts with GMP to afford the adduct [(η^6-

p-cym)Ru(bpm)(GMP)]$^{2+}$ (as confirmed by using NMR spectroscopy and UPLC-MS; Appendix Chapter 5, Fig. A23 and A24), hence demonstrating that the reactivity of Ru^{II} complexes toward biological targets can be triggered by low energy photons.

Control experiments indicate that **UCNP@4** is stable and does not undergo ligand dissociation in the dark, whereas **4** (and **2**) does not photoreact when irradiated by NIR light for several hours (Appendix Chapter 5, Fig. A25 and A26).

The photochemical efficiency of these hybrid systems still needs to be improved for more advanced applications; however, the combination of UCNP optical features with their multimodal-imaging capability can open new intriguing opportunities for innovative application in theranostics.

5.3 Conclusions

Herein, we have reported the synthesis of two new photoactivatable Ru‑arene complexes **1** and **2** and the thorough characterization of their structural and photochemical proprieties. In addition, we have demonstrated that click chemistry is a valuable strategy to introduce a phosphonate group directly on complexes **1** and **2** by exploiting the alkyne function on the 3-ethynylpyridyl ligand coordinated to their Ru centers. As in the case of their precursors, the so-obtained derivatives **3** and **4** selectively release the pyridyl ligand under direct light excitation of their lowest-energy absorption band. Moreover, phosphonate groups on **3** and **4** confer these complexes high affinity for the surface of core@shell $NaYF_4$:Yb/Tm@$NaYF_4$ upconverting nanoparticles.

Notably, ligand photodissociation and GMP coordination is triggered under excitation at λ_{irr} = 980 nm when **4** is anchored on UCNPs (**UCNP@4**), thus providing, to the best our knowledge, the first example of remote near-infrared photoactivation of a Ru^{II}-arene model prodrug.

Although UCNPs have been intensively investigated for medical applications, research into their combination with coordination compounds is still very limited. The approach that we proposed herein is of general applicability in terms of synthetic and photoactivation strategies. The 3-ethynylpyridyl ligand is indeed a convenient

candidate on which to perform click chemistry reactions in the proximity of transition-metal centers. Furthermore, the aliphatic arm of the azido-phosphonate ligand can be opportunely changed to modify the distance between the UCNPs and photoactivatable complexes and perhaps modulate their photochemistry.

Our proof of concept study demonstrates that UCNPs are convenient platforms for the use of deep-penetrating NIR light in the activation of anticancer metal complexes and the generation of active species in situ.

5.4 Experimental Section

5.4.1 Materials

$RuCl_3 \cdot 3H_2O$ (99%) was purchased from Precious Metals Online (PMO Pty Ltd) and used as received. 2,2'-bipyrimidine (bpm) (97%), 2,2'-bipyridine (bpy) (≥ 99%), silver nitrate ($AgNO_3$) (≥ 99%), potassium hexafluorophosphate (KPF_6) (98%), 3-ethynylpyridine (98%), yttrium(III) acetate hydrate (99.9%), ytterbium(III) acetate tetrahydrate (99.9%), thulium(III) acetate hydrate (99.9%), 1-octadecene (technical grade, 90%), oleic acid (technical grade, 90%), sodium hydroxide (≥ 97%), ammonium fluoride (98%), iron(III) chloride (97%), potassium oxalate monohydrate (99%), sodium azide (≥ 95%), guanosine 5'-monophosphate disodium salt hydrate(≥ 99%). All solvents were obtained from Sigma-Aldrich and used as received.

5.4.2 Synthesis of Ruthenium Complexes

The dimer $[(\eta^6\text{-}p\text{-cym})RuCl_2]_2$ and the Ru^{II} complexes $[(\eta^6\text{-}p\text{-cym})Ru(bpy)Cl][PF_6]$ and $[(\eta^6\text{-}p\text{-cym})Ru(bpm)Cl][PF_6]$ were prepared based on literature methods. [39–41] The Ru^{II} pyridinato complexes **1–4** were prepared based on previously reported methodology with some modifications. [42]

$[(\eta^6\text{-}p\text{-cym})Ru(bpy)(m\text{-CCH-Py})][PF_6]_2$ (1). $AgNO_3$ (0.2 g, 1.17 mmol) was added to an aluminium-foil-covered round bottom flask charged with $[(\eta^6\text{-}p\text{-cym})Ru(bpy)Cl][PF_6]$ (500 mg, 1.2 mmol), in a 1:1 mixture of $MeOH/H_2O$ (50 ml). The reaction mixture was stirred at ambient temperature for 18 h. The solution turned to light yellow and the off-white AgCl precipitate was filtered off. To the clear yellow solution of $[(\eta^6\text{-}p\text{-}$

cym)Ru(bpy)(H_2O)]$^{2+}$, 3-ethynylpyridine (620 mg, 6 mmol) was added to give a dark red solution. The reaction mixture was heated at 40 °C for 18 hours and KPF_6 (1.3 g, 7.2 mmol) was added after cooling. The precipitate that formed was dissolved by the addition of acetone to give a clear solution, which was filtered. The solution was reduced in volume until the onset of precipitation on the rotary evaporator and left to evaporate slowly at ambient temperature to afford yellowish flakes, which were collected by filtration, washed with methanol and diethyl ether, and dried in air (330 mg, 35%). ^{1}H NMR (D_2O, 500 MHz) δ_H: 0.82 (d, ^3J(H,H) = 6.9 Hz, 6H), 1.77 (s, 3H), 2.41 (spt, ^3J(H,H) = 7.0 Hz, 1H), 5.99 (d, ^3J(H,H) = 6.4 Hz, 2H), 6.40 (d, ^3J(H,H) = 6.5 Hz, 2H), 7.30 (dd, ^3J(H,H) = 8.0, 5.9 Hz, 1H), 7.86 (td, ^3J(H,H) = 7.3, 5.7, 2H), 7.93 (dt, ^3J(H,H) = 8.1, 1.5 Hz, 1H), 8.22 (td, ^3J(H,H) = 7.9, 1.4 Hz, 2H), 8.30 (m, 3H), 8.51 (s, 1H), 9.64 (d, ^3J(H,H) = 5.0 Hz, 2H); the proton of the alkyn group overlaps the residual water signal, wherease this proton resonates at 4.73 (s, 1H) in DMSO-d_6; ^{13}C NMR (DMSO-d_6, 500 MHz) δ_C:17.89, 22.17, 30.56, 78.51, 84.94, 87.51, 92.48, 103.68, 108.76, 122.04, 125.15, 127.09, 129.47, 141.80, 143.29, 152.84, 155.07, 155.38, 156.69. FTIR (KBr pellet) ν_{max} (cm^{-1}): 3300, 1580, 1410, 840, 560. Anal. Calcd for $C_{27}H_{27}F_{12}N_3P_2Ru$: C, 41.34; H, 3.47; N, 5.36%. Found: C, 40.94; H, 3.12; N, 5.08%. ESI-MS (m/z) (H_2O/MeOH), [$C_{27}H_{27}N_3RuPF_6$]$^+$ expected = 640.09 , found = 640.30

[(η^6-*p*-cym)Ru(bpm)(*m*-CCH-Py)][PF_6]$_2$ (2). Complex **2** was synthesized using the procedure described above for **1**, using the [(η^6-*p*-cym)Ru(bpm)Cl][PF_6] precursor (200 mg, 0.48 mmol). Yield: (120 mg, 32%);^{1}H NMR (D_2O, 500 MHz) δ_H: 0.88 (d, ^3J(H,H) = 6.9 Hz, 6H), 1.81 (s, 3H), 2.43 (spt, ^3J(H,H) = 7.0 Hz, 1H), 6.14 (d, ^3J(H,H) = 6.5 Hz, 2H), 6.44 (d, ^3J(H,H) = 6.5 Hz, 2H), 7.37 (dd, ^3J(H,H) = 8.0, 5.8 Hz, 1H), 7.98 (dt, ^3J(H,H) = 8.0, 1.5 Hz, 1H), 8.09 (dd, ^3J(H,H) = 5.8, 4.9 Hz, 2H), 8.31 (d, ^3J(H,H) = 5.8 Hz, 1H), 8.53 (s, 1H), 9.24 (dd, ^3J(H,H) = 4.8, 1.9 Hz, 2H), 10.00 (dd, ^3J(H,H) = 5.8, 1.9 Hz, 2H); the proton of the alkyn group overlaps the residual water signal, wherease this proton resonates at 4.72 (s, 1H) in DMSO-d_6; ^{13}C NMR (DMSO-d_6, 500 MHz) δ_C: 17.74, 22.18, 30.41,78.79, 86.07, 87.28, 90.77, 106.33, 107.61, 122.01, 126.01, 126.91, 143.04, 153.44, 155.97, 160.84, 161.47, 164.10. FTIR (KBr pellet) ν_{max} (cm^{-1}): 3300, 1580, 1410, 840, 560. Anal. Calcd for $C_{25}H_{25}F_{12}N_5P_2Ru$: C, 38.18; H, 3.20; N, 8.90%. Found: C, 37.59; H, 3.04; N, 8.71%. ESI-MS (m/z) (H_2O/MeOH), [$C_{25}H_{25}N_5RuPF_6$]$^+$ expected = 642.08 , found = 642.28 .

Diethyl-3-azidopropyl phosphonate. The preparation of the azido-ligand for click chemistry is based on the procedure reported by A. K. Garrell and coworkers. [47] The (3-bromopropyl) phosphonic acid diethyl ether (5 ml, 26.02 mmol) was dissolved in acetone (25 ml) dried by passing through neutral alumina. To this, NaN_3 (2.6 g, 40.4 mmol) was added and the reaction mixture heated under reflux for 18 h. The reaction mixture was then cooled and was filtered through celite and washed several times with acetone. The solvent was taken off under rotary evaporation to leave a clear yellowish oil (5.81 g, quantitative yield). ^{1}H NMR (DMSO-d_6, 500 MHz) δ_H: 1.24 (t, ^3J(H,H) = 7.1 Hz, 6H), 1.78 (m, 4H), 3.41 (t, ^3J(H,H) = 6.6 Hz, 2H), 4.00 (m, 4H). ^{31}P NMR (DMSO-d_6, 500 MHz) δ_P: 30.9. FTIR (KBr pellet) ν_{max} = 3400, 3000, 2100, 1240, 1050, 960 cm^{-1}.

[(η^6-*p*-cym)Ru(bpy)(P-Trz-Py)][PF_6]$_2$ (3) (P-Trz-Py = [3-(1-Pyridin-3-yl-[1,2,3]triazol-4-yl)-propyl]-phosphonic acid diethyl ester). $CuSO_4$ (8 mg, 0.032 mmol), sodium ascorbate (6.3 mg, 0.032 mmol), and diethyl-3-azidopropyl phosphonate (14.4 mg, 0.064 mmol) were added to a solution of [(h6-p-cym)Ru(bpy)(*m*-CCH-Py)][PF_6]$_2$ (**1**; 50 mg, 0.064 mmol) in THF/H_2O (4:1, 5 mL). The reaction mixture was heated at 60 °C for 72 h. KF_6 (9.5 g, 52 mmol) in H_2O (30 mL) was then added to the reaction mixture, which was placed in a separating funnel and extracted with dichloromethane (3 x 10 mL) to give a reddish solution. This mixture was dried over $MgSO_4$, and the solvent was removed by rotary evaporation to give an oily product, which was dissolved in methanol. KPF_6 (2 g) was added to the solution and the product was precipitated by the addition of diethyl ether. The solid was collected by decanting the diethyl ether, the residue was redissolved in dichloromethane, and the precipitated salt was filtered off to obtain a red solid, which was dried in air (25 mg, 41%). ^{1}H NMR (D_2O, 500 MHz) δ_H: 0.83 (d, ^3J(H,H) = 6.9 Hz, 6H), 1.19 (t, ^3J(H,H) = 7.1 Hz, 6H), 1.82 (m, 5H), 2.15 (m, 2H), 2.44 (stp, ^3J(H,H) = 6.8 Hz, 1H), 4.02 (m, 4H), 4.49 (t, ^3J(H,H) = 6.7 Hz, 2H), 6.05 (d, ^3J(H,H) = 6.3 Hz, 2H), 6.44 (d, ^3J(H,H) = 6.3 Hz, 2H), 7.40 (dd, ^3J(H,H) = 8.1, 5.8 Hz, 1H), 7.89 (t, ^3J(H,H) = 7.2 Hz, 2H), 8.14 (d, ^3J(H,H) = 8.0 Hz, 1H), 8.22 (t, ^3J(H,H) = 7.9 Hz, 2H), 8.29 (m, 4H), 8.79 (s, 1H), 9.72 (d, ^3J(H,H) = 6.0 Hz, 2H). ^{13}C NMR (DMSO-d_6, 500 MHz) δ_C: 16.73, 17.94, 21.54, 22.21, 23.77, 30.61, 50.21, 61.59, 85.06, 92.33, 104.02, 108.57, 124.05, 125.15, 127.61, 129.51, 130.03, 136.78, 141.74, 141.80, 148.54, 152.37,

155.27, 156.71. ^{31}P NMR (DMSO-d_6, 500 MHz) δ_P: 30.4. ESI-MS (m/z) (H_2O/MeOH), $[C_{34}H_{43}O_3N_6PRuPF_6]^+$ expected = 861.18 , found = 861.45 .

[(η^6-*p*-cym)Ru(bpm)(P-Trz-Py)] $[PF_6]_2$ (4) (P-Trz-Py = [3-(1-Pyridin-3-yl-[1,2,3]triazol-4-yl)-propyl]-phosphonic acid diethyl ester). Complex **4** was synthesized using the procedure described above for **3**, starting with [(η^6-*p*-cym)Ru(bpm)(*m*-CCH-Py)][PF_6]$_2$ (50 mg, 0.06 mmol)). Yield: (15mg, 23%); ^{1}H NMR (D_2O, 500 MHz) δ_H: 0.89 (d, ^3J(H,H) = 6.9 Hz, 6H), 1.21 (t, ^3J(H,H) = 7.1 Hz, 6H), 1.82 (m, 5H), 2.16 (m, 2H),2.45 (stp, ^3J(H,H) = 6.8 Hz, 1H), 4.03 (m, 4H), 4.50 (t, ^3J(H,H) = 6.8 Hz, 2H), 6.19 (d, ^3J(H,H) = 6.4 Hz, 2H), 6.48 (d, ^3J(H,H) = 6.4 Hz, 2H), 7.46 (dd, ^3J(H,H) = 8.1, 5.8 Hz, 1H), 8.11 (dd, ^3J(H,H) = 5.9, 4.8 Hz, 2H), 8.18 (dt, ^3J(H,H) = 8.1, 1.6 Hz, 1H), 8.30 (d, ^3J(H,H) = 5.7 Hz, 1H), 8.36 (s, 1H), 8.84 (s, 1H), 9.23 (dd, ^3J(H,H) = 4.9, 1.9 Hz, 2H), 10.09 (dd, ^3J(H,H) = 5.9, 1.9 Hz, 2H). ^{13}C NMR (DMSO-d6, 500 MHz) δ_C: 16.73, 17.80, 22.24, 22.66, 23.80, 30.48, 50.35, 61.62, 86.19, 90.64, 106.66, 107.47, 123.96, 126.05, 127.53, 130.07, 137.58, 141.97, 149.52, 152.92, 160.78, 161.54, 164.13. ^{31}P NMR (DMSO-d_6, 500 MHz) δ_P: 30.4. ESI-MS (m/z) (H_2O/MeOH), $[C_{32}H_{41}O_3N_8PRuPF_6]^+$ expected = 863.17 , found = 863.42

5.4.3 Synthesis of UCNPS

Synthesis of core-$NaYF_4$:Yb(30%)/Tm(0.5%). In a 100 ml three-neck round-bottom flask, with a water condenser coil, 15 ml oleic acid (OA), 25 ml octadecene, yttrium(III) acetate hydrate (555 mg, 2.1 mmol), ytterbium(III) acetate tetrahydrate (380 mg, 0.90 mmol) and thulium(III) acetate hydrate (5.2 mg, 0.015 mmol) were mixed together under agitation. The mixture was slowly heated (3.2 °C/min) to form a homogeneous and clear solution at 120 °C under vacuum. The round-bottom flask was kept in these conditions for 30 min to remove all oxygen and water traces. After 30 min the system was allowed to cool naturally to 50 °C under Ar flux. In the meantime, a solution of sodium hydroxide (300 mg, 7.5 mmol) and ammonium fluoride (444 mg, 12.0 mmol) was prepared in methanol (8 ml). The methanol solution was added (drop by drop in 10 min) into the round-bottom flask. Immediately the reaction solution changed from colorless and transparent to cloudy and pearly. The system was heated at 50 °C for 30 min and at 70 °C for other 30 min under Ar flux in order to eliminate the methanol

from the reaction mixture. Afterwards, the system was heated up quickly to 300 °C (13.5°C/min) under Ar flux. On the heating the aspect of the solution changes to transparentand subsequently slightly yellow. Such reaction conditions were maintained for 90 min. Finallythe system was cooled naturally to room temperature. The final product was separated by centrifugationat 4500 rpm for 15 minutes.The white precipitates were washed with ethanol and THF, and the UCNPs(ca. 600 mg) were dried at room temperature overnight.

Synthesis of core@shell $NaYF_4$:Yb(30%)/Tm(0.5%)@$NaYF_4$. In the second step, yttrium(III) acetate hydrate (240 mg, 0.9 mmol) was mixed in a 100 ml three-neck round-bottom flask, equipped with a water condenser coil, with octadecene (15 ml) and oleic acid (6 ml). As the first step, the system was heated up slowly (3.2 °C/min) at 120 °C under vacuum and kept in these conditions for 30 min in order to obtain a deoxygenated and anhydrous yttrium oil. Simultaneously, the core precursors (260 mg) were dissolved in hexane (10 ml) through sonication. Subsequently, the mixture reaction was cooled down at 80 °C under Ar, and then the UCNP suspension was added dropwisely (10 min) to the round-bottom flask. The aspect of the oil changes to cloudy. Afterwards the temperature of reaction was increased at 110 °C (3.2 °C/min) maintained under vacuum for 30 min to remove the hexane. On a separate flask, 2.2 mmol of sodium hydroxide (88 mg) and 3.5 mmol of ammonium fluoride (130 mg) were solubilized with a small amount of methanol (5ml). The reaction flask was once more cooled down to 50 °C under nitrogen and the methanolic solution (1ml/min) was added drop by drop inside. Following the addition, the solution was heated under Ar flux at 50 °C for 30 min and at 70 °C for other 30 min to evaporate the methanol. After, the temperature of the system was quickly raised at to 300 °C with rate of approximately 13.5 °C/min. The system was maintained at this temperature for 90min to form the core@shell UCNPs. During this period the solution turned to yellow. At last, the solution was cooled to room temperature, and the product was obtained via centrifugation as in the first step. Routinely around 500 mg of core@shell UCNPs were obtained.

5.4.4 Synthesis of the adduct UCNP@4

Both **3** and **4** selectively photodissociate the P-Trz-Py ligand upon irradiation at λ_{irr} = 400 nm. However, **4** was selected for the functionalization of UCNPs (Scheme 1b) and NIR photolysis studies because its analogue bpm derivative **2** displayed slight higher photodissociation yield compared to the bpy derivative **1**.

Deprotection of [(η^6-*p*-cym)Ru(bpm)(P-Trz-Py)][PF_6]$_2$ (4). We followed a similar procedure to the reported one for the deprotection of diethyl-3-azidopropyl phosphonate to 3-azido propyl phosphoric acid. [47] An aluminium-foil-covered round-bottom flask was charged with 2.5 mg of [(η^6-*p*-cym)Ru(bpm)(P-Trz-Py)][PF_6]$_2$ (**4**) in CH_2Cl_2 (anhydrous, 1 ml) to obtain a yellow solution. Trimethylsilyl bromide (TMSBr) was added (c.a. 10 drops) to the flask. Instantaneously the reaction solution changed from transparent to cloudy. After the end of the addition, the reaction mixture was maintained under stirring overnight at ambient temperature. Afterwards, the solvent was removed under gentle nitrogen flow to give a yellow precipitate.

Preparation of oleate-free UCNPs. The preparation was performed following literature procedure reported by N. Bogdan et al. [52] Briefly, in round-bottom flask 50 mg of core@shell $NaYF_4$:Yb(30%)/Tm(0.5%)@$NaYF_4$ were suspended in H_2O (5 ml). The pH of the mixture was adjusted to **4** using 0.1 M HCl solution and the suspension was then stirred for 2 h at ambient temperature. Afterwards, the oleate-free UCNPs were purified from the released oleic acid *via* extraction with diethyl ether (3 X 5 ml). The product (ca. 30 mg) was dried at ambient temperature overnight.

Functionalization of oleate-free UCNPs with 4. Deprotected complex **4** (2.5 mg) was mixed with oleate-free core@shell $NaYF_4$:Yb/Tm@$NaYF_4$ (10 mg) and suspended in H_2O (1.5 mL) in an aluminium-foil-covered round-bottom flask. The suspension was stirred overnight at ambient temperature. The reaction mixture was then lyophilized. The yellow powder obtained was washed several times with ethanol and precipitated by centrifugation (10000 rpm for 5 min) to remove excess of Ru complex. **UCNP@4** (ca. 6 mg) was dried at ambient temperature overnight. ^{1}H NMR (D_2O, 500 MHz) δ_H: 0.87 (6H), 1.81 (3H), 2.16 (2H), 2.43 (1H), 4.47 (2H), 6.18 (2H), 6.47 (2H), 7.44 (1H), 8.11 (2H), 8.18 (1H), 8.27 (1H), 8.36 (1H), 8.83 (1H), 9.22 (2H), 10.09 (2H). Note: All the proton signals of **UCNP@4** were broader than those of **4**, loss of multiplicity is due to the paramagnetic nature of the UCNPs, and four aliphatic protons relative to the propyl chain of the phosphonic acid group gave signals too broad to be observed

(previously falling in at δ_H 4.03 in complex **4**), due to their proximity to the surface of UCNPs.

5.4.5 Photolysis experiments

Photoirradiation of Ru complexes at 395 nm. Aqueous solutions of **1–4** were irradiated at 395 nm with the Prizmatix LED Multi-Wavelength MWLLS-11 source (15 $mW \cdot cm^{-2}$) at ambient temperature. The progress of the photoreaction was followed by either ^1H NMR or UV-vis spectroscopies. Finally, the nature of the photoproducts was also analyzed by UPLC-MS.

Photoirradiation of 4 and UCNP@4 at 980 nm. Aqueous solutions of **4** and **UCNP@4** were irradiated under 980 nm light using a BWT diode laser DS3-11312-110. Complex **4** (150 µM, 400 µL) and **UCNP@4** (10 mg/ml, 400 µL) solutions were irradiated for 7 h (8.8 $W \cdot cm^{-2}$) and 5.5 h (8.1 $W \cdot cm^{-2}$), respectively. The progress of photoreaction was followed by ^1H NMR measurements. Before ^1H NMR measurements, solutions of **UCNP@4** were centrifuged (6000 rpm, 5 min) to improve the quality of the NMR spectra. Finally, the nature of the photoproducts was also analyzed by UPLC-MS. The output power density of all light sources employed was measured by an optical power meter (Ophir Photonics PD300-3W).

5.4.6 NMR Spectroscopy

^1H, ^{13}C, ^{31}P NMR spectra of the various samples in deuterated solvents (D_2O or DMSO-d_6) were acquired using standard pulse programson an AVANCE III Bruker 500 NMR spectrometer. Chemical shifts were reported in parts-per-million (δ, ppm) and referenced to the residual solvent peak.

5.4.7 X-ray Crystallography

Diffraction data for **1** and **2** was obtained using an Agilent Super Nova Mo-diffractometer coupled with CCD area detector. All work was conducted at 100 K using an Agilent 700 Cryosystem Cooler fed with liquid nitrogen. Full-matrix least-squares refinements based on F2 were performed using SHELXL-97 and the structures were solved by direct methods. The rest of the hydrogen atoms were located by riding

model. The crystallographic details of **1** and **2** have been deposited in the Cambridge Crystallographic Data Centre under the accession numbers 1055609 and 1055610, respectively.

5.4.8 Fourier-transform Infrared (FTIR) Spectroscopy

FTIR spectra of **1**, **2**, core-$NaYF_4$:Yb/Tm, core@shell-$NaYF_4$:Yb/Tm@$NaYF_4$ and oleate-free core@shell-$NaYF_4$:Yb/Tm@$NaYF_4$ were recorded on a Nicolet FTIR 6700 spectrometer as KBr disk.

5.4.9 UV-vis Absorption Spectroscopy

UV-vis experiments of Ru complexes and **UCNP@4** were performed in H_2O using a Varian Cary 5000 spectrophotometer.

5.4.10 Emission Spectroscopy

The emission spectra of UCNPs dispersions (in THF or H_2O) were obtained under 980 nm excitation (15 $W \cdot cm^{-2}$) with a 980 nm laser diode (CNI, MDL-N-980) coupled with a Fluorometer Fluorolog (Horiba). The laser power density was measured as described above.

5.4.11 Transmission Electron Microscopy (TEM)

TEM images were collected for core-$NaYF_4$:Yb/Tm, core@shell-$NaYF_4$:Yb/Tm@$NaYF_4$, and **UCNP@4** samples on a JEOL JEM-1400 PLUS-HC microscope that operated at 120 kV. A small amount of the sample was dispersed in H_2O or THF (1 mL) as the solvent to give an approximate 0.5 mg mL^{-1} solution. One drop (3 mL) of the resulting solution was allowed to evaporate on a carbon film supported on a 300 mesh copper grid (diameter=3 mm).

5.4.12 X-Ray Photoelectron Spectroscopy (XPS)

XPS data of **4** and **UCNP@4** were acquired employing a SPECS Sage HR 100 spectrometer with a non-monochromatic X-ray source Magnesium Kα line of 1253.6 eV energy and a power applied of 250 W and calibrated using the $3d_{5/2}$ line of Ag with a full width at half maximum (FWHM) of 1.1 eV. All measurements were made in an ultra high vacuum (UHV) chamber at a pressure below $8 \cdot 10^{-8}$ mbar. Samples were measured on titanium surfaces.

5.4.13 UPLC-MS

UPLC-MS measurements on **1–4** were performed by positive-ion electrospray ionization mass spectrometry (ESI-MS) LCT Premier XE from Waters (10000 FWHM) coupled to an Ultra Performance Liquid Chromatograph (UPLC). Samples were prepared in a H_2O/DMSO (95/5%) mixture. The analysis was achieved on an ACQUITY UPLC BEH C18 column (50 X 2.1 mm) using H_2O (0.1% formic acid)/MeOH as the mobile phase with a flow rate of 0.3 ml min^{-1}. The injection volume was 5 µL. The ESI source was employed in W-optics positive ionization scan mode with the capillary voltage at 2.5 kV. The temperatures of the source and desolvation were 120 °C. The cone and desolvation gas flows were 50 and 600 l h^{-1}. The collision gas flow was 0.2 ml min^{-1} and collision energy of 15–18 V was operated. In the case of **UCNP@4**, the sample was sonicated and ultracentrifugated (10^5 rpm, 45 min) in order to eliminate possible aggregates and nanoparticles before the injection in the UPLC-MS.

5.4.14 Ligand Photodissociation Quantum Yield

The quantum yields ($\Phi = \frac{\text{number of reacted molecules per time unit}}{\text{number of photons adsorbed per time unit}}$) of ligand photodissociation were determined for **1** and **2** in H_2O by irradiation with 395 nm light.

The ferrioxalate actinometer $K_3[Fe(C_2O_4)_3]$ was used to determine the photon flux ($5.77 \cdot 10^{-8}$mol s^{-1}) irradiating the samples in our experimental setup equipped with a Prizmatix LED Multi-Wavelength MWLLS-11. The colorimetric actinometry experiment was performed as described in Handbook of Photochemistry of Montalti et al. [48] and $K_3[Fe(C_2O_4)_3]$ was obtained following the procedure described by J. G. Carriazo [53].

Electronic absorption spectroscopy (Fig. 4a and 4b) was employed to quantitative the decrease of reactant as a function of irradiation time (nmol s^{-1}). Due to the low extinction coefficients and low solubility of the complexes, optically dense (A > 4) solutions could not be prepared for quantum yield determinations and a modified procedure was developed. The time course of the photoreaction was followed monitoring the absorbance of aqueous solutions of **1** and **2** respectively at 317 and 291 nm (Fig. 4).Solutions (800 μl, 95:5 H_2O:DMSO) were irradiated until the complete exhaustion of the starting complexes.

For each irradiation time, the contribution to absorbance due to the reagent and to the photoproduct was extracted and plotted. The data fitting provided functions ($A = A_0 + B \cdot e^{-\frac{t}{\tau}}$) describing the temporal evolution of the absorbance of each compound (Table S4).The derivative over the time of such functions, calculated for t = 0, provides the starting rate of absorbance increasing/decreasing that was used to calculate the reaction rate, employing the Lambert–Beer's law (**1**$\varepsilon_{317\ nm}$ = 5700 $M^{-1}cm^{-1}$,**2**$\varepsilon_{291\ nm}$ = 3200 $M^{-1}cm^{-1}$). For t = 0 the concentration of the photoproduct is negligible hence the mean fraction of light (F) absorbed by the solution can be ascribed to the reactant (**1**, $F_{395\ nm}$ = 0.12; **2**, $F_{395\ nm}$ = 0.09).

5.4.15 Computational Details

All calculations were performed with the Gaussian 09 (G09) program package, [54] employing the DFT and TD-DFT methods, [55,56] the Becke three-parameter hybrid functional, [57] and the Lee−Yang−Parr's gradient corrected correlation functional (B3LYP). [58] The solvent effect was included using the polarizable continuum model (PCM method) [59,60] with water as solvent. The LanL2DZ basis set [61] and effective core potential were used for the Ru atom and the 6-31G** basis set [62] was used for all the other atoms. The B3LYP/LanL2DZ/6-31G** combination was selected since it previously provided satisfactory results on similar ruthenium arene complexes. [35,36]

Geometry optimizations of ground states (S0) and lowest-lying triplet states (T0 and T1) for **1** and **2** were carried out without any symmetry constraints. The nature of all stationary points was verified via harmonic vibrational frequency calculations. No

imaginary frequencies were found, indicating we had located minima on potential energy surfaces.

The UV-vis electronic absorption spectra were simulated by TD-DFT, [55,56] computing a total of 50 singlet excited states. The electronic distribution and the localization of the singlet excited states were visualized using electron density difference maps (EDDMs).

GaussSum 2.2.5 [63] was used to simulate the theoretical UV–vis spectra and for extraction of EDDMs. [64,65] Molecular graphics images were produced using the UCSF Chimera package from the Resource for Biocomputing, Visualization, and Informatics at the University of California, San Francisco (supported by NIH P41 RR001081). [66]

5.5 References

[1] D. E. J. G. J. Dolmans, D. Fukumura, R. K. Jain, *Nat. Rev. Cancer*, **2003**, *3*, 380.

[2] E. Fino, R. Araya, D. S. Peterka, M. Salierno, R. Etchenique, R. Yuste, *Front. Neural Circuits*, **2009**, *3*, 2.

[3] M. A. Sgambellone, A. David, R. N. Garner, K. R. Dunbar, C. Turro, *J. Am. Chem. Soc.*, **2013**, *135*, 11274.

[4] U. Schatzschneider, *Eur. J. Inorg. Chem.*, **2010**, 1451.

[5] E. Ruggiero, S. Alonso-de Castro, A. Habtemariam, L. Salassa, *Struct. Bond.*, **2015**, *165*, 69.

[6] N. J. Farrer, L. Salassa, P. J. Sadler, *Dalton Trans.*, **2009**, 10690.

[7] E. C. Glazer, *Isr. J. Chem.*, **2013**, *53*, 391.

[8] D. Barolet, *Semin. Cutan. Med. Surg.*, **2008**, *27*, 227.

[9] Z. Chen, W. Sun, H. J. Butt, S. Wu, *Chem. Eur. J.*, **2015**, *15*, 9165.

[10] E. Wachter, D. K. Heidary, B. S. Howerton, S. Parkin, E. C. Glazer, *Chem. Commun.*, **2012**, *48*, 9649.

[11] M. J. Rose, P. K. Mascharak, *Inorg. Chem.*, **2009**, *48*, 6904.

[12] M. J. Rose, N. L. Fry, R. Marlow, L. Hinck, P. K. Mascharak, *J. Am. Chem. Soc.*, **2008**, *130*, 8834.

[13] J. V. Garcia, J. Yang, D. Shen, C. Yao, X. Li, R. Wang, G. D. Stucky, D. Zhao, P. C. Ford, F. Zhang, *Small*, **2012**, *8*, 3800.

[14] A. E. Pierri, P.-J. Huang, J. V. Garcia, J. G. Stanfill, M. Chui, G. Wu, N. Zheng, P. C. Ford, *Chem. Commun.*, **2015**, *51*, 2072.

[15] P. T. Burks, J. V. Garcia, R. GonzalezIrias, J. T. Tillman, M. Niu, A. A. Mikhailovsky, J. Zhang, F. Zhang, P. C. Ford, *J. Am. Chem. Soc.*, **2013**, *135*, 18145.

[16] E. Ruggiero, A. Habtemariam, L. Yate, J. C. Mareque-Rivas, L. Salassa, *Chem. Commun.*, **2014**, *50*, 1715.

[17] E. Ruggiero, J. Hernández-Gil, J. C. Mareque-Rivas, L. Salassa, *Chem. Commun.*, **2015**, *51*, 2091.

[18] S. Wu, H. J. Butt, *Adv. Mater.*, **2016**, *28*, 1208.

[19] Z. Chen, S. He, H. J. Butt, S. Wu, *Adv. Mater.*, **2015**, 27, 2203.

[20] S. He, K. Krippes, S. Ritz, Z. Chen, A. Best, H. J. Butt, V. Mailänder, S. Wu, *Chem. Commun.*, **2015**, *51*, 431.

[21] M. Haase, H. Schäfer, *Angew. Chem. Int. Ed.*, **2011**, *50*, 5808.

[22] J. Zhou, Q. Liu, W. Feng, Y. Sun, F. Li, *Chem. Rev.*, **2015**, *115*, 395.

[23] S. H. C. Askes, A. Bahreman, S. Bonnet, *Angew. Chem. Int. Ed.*, **2014**, *53*, 1029.

[24] Y. Sun, M. Yu, S. Liang, Y. Zhang, C. Li, T. Mou, W. Yang, X. Zhang, B. Li, C. Huang, F. Y. Li, *Biomaterials*, **2011**, *32*, 2999.

[25] T. Cao, Y. Yang, Y. Sun, Y. Wu, Y. Gao, W. Feng, F. Li, *Biomaterials*, **2013**, *34*, 7127.

[26] J.-W. Shen, C.-X. Yang, L.-X. Dong, H.-R. Sun, K. Gao, X.-P. Yan, *Anal. Chem.*, **2013**, *85*, 12166.

[27] J. Zhou, Y. Sun, X. Du, L. Xiong, H. Hu, F. Li, *Biomaterials*, **2010**, *31*, 3287.

[28] L. Xiong, Z. Chen, Q. Tian, T. Cao, C. Xu, F. Li, *Anal. Chem.*, **2009**, *81*, 8687.

[29] S. K. Maji, S. Sreejith, J. Joseph, M. Lin, T. He, Y. Tong, H. Sun, S. W.-K. Yu, Y. Zhao, *Adv. Mater.*, **2014**, *26*, 5632.

[30] Y. Sun, W. Feng, P. Yang, C. Huang, F. Li, *Chem. Soc. Rev.*, **2015**, *44*, 1509.

[31] J. Zhou, Z. Liu, F. Li, *Chem. Soc. Rev.*, **2012**, *41*, 1323.

[32] G. Gasser, I. Ott, N. Metzler-Nolte, *J. Med. Chem.*, **2011**, *54*, 3.

[33] Z. Adhireksan, G. E. Davey, P. Campomanes, M. Groessl, C. M. Clavel, H. Yu, A. A. Nazarov, C. H. F. Yeo, W. H. Ang, P. Dröge, U. Rothlisberger, P. J. Dyson, C. A. Davey, *Nat. Commun.*, **2014**, *5*, 3462.

[34] M. Frik, A. Martínez, B. T. Elie, O. Gonzalo, D. Ramírez de Mingo, M. Sanaú, R. Sánchez-Delgado, T. Sadhukha, S. Prabha, J. W. Ramos, I. Marzo, M. Contel, *J. Med. Chem.*, **2014**, *57*, 9995.

[35] S. Betanzos-Lara, L. Salassa, A. Habtemariam, O. Novakova, A. M. Pizarro, G. J. Clarkson, B. Liskova, V. Brabec, P. J. Sadler, *Organometallics*, **2012**, *31*, 3466.

[36] S. Betanzos-Lara, L. Salassa, A. Habtemariam, P. J. Sadler, *Chem. Commun.*, **2009**, 6622.

[37] G. Ragazzon, I. Bratsos, E. Alessio, L. Salassa, A. Habtemariam, R. J. McQuitty, G. J. Clarkson, P. J. Sadler, *Inorg. Chim. Acta*, **2012**, *393*, 230.

[38] J.-C. Boyer, M.-P. Manseau, J. I. Murray, F. C. J. M. van Veggel, *Langmuir*, **2010**, *26*, 1157.

[39] R. A. Zelonka, M. C. Baird, *Can. J. Chem.*, **1972**, *50*, 3063.

[40] M. A. Bennett, A. K. Smith, *Dalton Trans.*, **1974**, 233.

[41] A. Habtemariam, M. Melchart, R. Fernández, S. Parsons, I. D. H. Oswald, A. Parkin, F. P. A. Fabbiani, J. E. Davidson, A. Dawson, R. E. Aird, *J. Med. Chem.*, **2006**, *49*, 6858.

[42] F. Wang, A. Habtemariam, E. P. L. van der Geer, R. Fernández, M. Melchart, R. J. Deeth, R. Aird, S. Guichard, F. P. A. Fabbiani, P. Lozano-Casal, I. D. H. Oswald, D. I. Jodrell, S. Parsons, P. J. Sadler, *Proc. Natl. Acad. Sci. USA*, **2005**, *102*, 18269.

[43] B. S. Uppal, A. Zahid, P. I. P. Elliott, *Eur. J. Inorg. Chem.*, **2013**, 2571.

[44] B. C. Boren, S. Narayan, L. K. Rasmussen, L. Zhang, H. Zhao, Z. Lin, G. Jia, V. V. Fokin, *J. Am. Chem. Soc.*, **2008**, *130*, 8923.

[45] J.-C. Boyer, C.-J. Carling, S. Y. Chua, D. Wilson, B. Johnsen, D. Baillie, N. R. Branda, *Chem. Eur. J.*, **2012**, *18*, 3122.

[46] L.-L. Li, P. Wu, K. Hwang, Y. Lu, *J. Am. Chem. Soc.*, **2013**, *135*, 2411.

[47] A. K. Tucker-Schwartz, R. L. Garrell, *Chem. Eur. J.*, **2010**, *16*, 12718.

[48] M. Montalti, A Credi, L Prodi, M. T. Gandolfi, Handbook of Photochemistry, CRC press, Third Edition, **2006**.

[49] F. Vetrone, R. Naccache, V. Mahalingam, C. G. Morgan, J. A. Capobianco, *Adv. Funct. Mater.*, **2009**, *19*, 2924.

[50] J.-C. Boyer, C.-J. Carling, B. D. Gates, N. R. Branda, *J. Am. Chem. Soc.*, **2010**, *132*, 15766.

[51] C. J. Carling, F. Nourmohammadian, J. C. Boyer, N. R. Branda, *Angew. Chem. Int. Ed.*, **2010**, *17*, 3782.

[52] N. Bogdan, F. Vetrone, G. A. Ozin, J. A. Capobianco, *Nano Lett.*, **2011**, 11, 835.

[53] J. G. Carriazo, *Chemistry*, **2010**, *19*, 103.

[54] M. J. Frisch, G. W. Trucks, H. B. Schlegel, G. E. Scuseria, M. A. Robb, J. R. Cheeseman, G. Scalmani, V. Barone, B. Mennucci, G. A. Petersson, H. Nakatsuji, M. Caricato, X. Li, H. P. Hratchian, A. F. Izmaylov, J. Bloino, G. Zheng, J. L. Sonnenberg, M. Hada, M. Ehara, K. Toyota, R. Fukuda, J. Hasegawa, M. Ishida, T. Nakajima, Y. Honda, O. Kitao, H. Nakai, T. Vreven, J. A. Montgomery, Jr., J. E. Peralta, F. Ogliaro, M. Bearpark, J. J. Heyd, E. Brothers, K. N. Kudin, V. N. Staroverov, R. Kobayashi, J. Normand, K. Raghavachari, A. Rendell, J. C. Burant, S. S. Iyengar, J. Tomasi, M. Cossi, N. Rega, J. M. Millam, M. Klene, J. E. Knox, J. B. Cross, V. Bakken, C. Adamo, J. Jaramillo, R. Gomperts, R. E. Stratmann, O. Yazyev, A. J. Austin, R. Cammi, C. Pomelli, J. W. Ochterski, R. L. Martin, K. Morokuma, V. G. Zakrzewski, G. A. Voth, P. Salvador, J. J. Dannenberg, S. Dapprich, A. D. Daniels, Ö. Farkas, J. B. Foresman, J. V. Ortiz, J. Cioslowski, D. J. Fox, Gaussian 09, Revision C.01; Gaussian, Inc.: Wallingford, CT, **2009**.

[55] M. E. Casida, C. Jamorski, K. C. Casida, D. R. Salahub, *J. Chem. Phys.*, **1998**, *108*, 4439.

[56] R. E. Stratmann, G. E. Scuseria, M. J. Frisch, *J. Chem. Phys.*, **1998**, *109*, 8218.

[57] A. D. Becke, *J. Chem. Phys.*, **1993**, *98*, 5648.

[58] C. Lee, W. Yang, R. G. Parr, *Phys. Rev. B*, **1988**, *37*, 785.

[59] M. Cossi, G. Scalmani, N. Rega, V. Barone, *J. Chem. Phys.*, **2002**, *117*, 43.

[60] S. Miertuš, E. Scrocco, J. Tomasi, *Chem. Phys.*, **1981**, *55*, 117.

[61] P. J. Hay, W. R. Wadt, *J. Chem. Phys.*, **1985**, *82*, 270.

[62] A. D. McLean, G. S. Chandler, *J. Chem. Phys.*, **1980**, *72*, 5639.

[63] N. M. O'Boyle, A. L. Tenderholt, K. M. Langner, *J. Comput. Chem.*, **2008**, *29*, 839.

[64] W. R. Browne, N. M. O'Boyle, J. J. McGarvey, J. G. Vos, *Chem. Soc. Rev.*, **2005**, *34*, 641.

[65] M. Head-Gordon, A. M. Grana, D. Maurice, C. A. White, *J. Phys. Chem.*, **1995**, *99*, 14261.

[66] E. F. Pettersen, T. D. Goddard, C. C. Huang, G. S. Couch, D. M. Greenblatt, E. C. Meng, T. E. Ferrin, *J. Comput. Chem.*, **2004**, *25*, 1605.

Conclusions

Since its first approval in 1995 from FDA, photodynamic therapy (PDT) has demonstrated to be an attractive alternative to classical chemotherapy. PDT is a minimally invasive treatment, where red light is exploited for the stimulation of a photosensitizer to produce in situ cytotoxic reactive oxygen species with spatial and temporal selectivity. This clinical procedure is employed to treat nonmalignant diseases and various types of tumors. Nevertheless, PDT agents are still not integrated into the mainstream of cancer treatments, due to their oxygen-dependent cytotoxicity mechanism of action and others drawbacks. In fact, solid tumors are generally hypoxic which lowers the effectiveness of PDT.

To overcome this limitation, photochemotherapeutic metal complexes, which can photodamage cancer cells in an oxygen independent fashion, have been considered as alternative PDT agents. Under light irradiation, such metal-based agents can lead to cellular death by releasing cytotoxic drug fragments and/or binding DNA in an analogous way to cisplatin. Although, photosensitive metal-based prodrugs offer spatiotemporal control of the therapeutic effects, they suffer from their modest absorption properties and lack of photoreactivity in the red part of the visible spectrum. The majority of metal complexes needs UV-blue light to trigger their photochemistry, which is not optimal for biomedical application since such range of wavelengths shows high cellular photodamage and low tissue penetration. Indeed, wavelength-dependent penetration of light into tissue is a key factor to take into account for the development of new phototherapeutic agents. The best wavelength-range for light-based remedies is between 650–1000 nm, the so-called phototherapeutic window, where tissues are the most phototransparent.

At the beginning of this research project, the literature reported only limited results regarding the extension of excitation wavelengths of bioactive metal complexes into the phototherapeutic window range (e.g. functionalization with antenna chromophores or anchoring to quantum dots).

This Ph.D. work aimed at demonstrating a challenging and pioneeristic approach based on the use of upconverting nanoparticles (UCNPs) to enable the photoactivation of metal-based prodrugs upon near-infrared (NIR) excitation at 980 nm.

Upon NIR excitation, UCNPs emit UV-visible light that, reabsorbed by metal complexes, can trigger their photochemistry, red-shifting the wavelengths of photoactivation.

This Ph.D. thesis adopted a bottom-up approach, as it started with the synthesis and characterization of molecules and materials needed by the project (Er- and Tm-doped UCNPs, Pt and Ru metal complexes), and ended with the study of the properties of UCNP-based nanosystems carrying metal complexes. Due to its multidisciplinary and innovative nature, the project required the design of tailored experiments and their optimization (e.g. NIR light photolysis), as well as the use of a wide range of techniques; some of these suited for molecular chemistry (e.g. multinuclear NMR, UPLC-MS, UV-vis spectroscopy) and others for materials science (e.g. TEM, XPS, DLS).

The thesis achieved remarkable results, since all the metal complexes selected were successfully photoactivated at 980 nm, despite they lacked absorption features in the phototherapeutic window and were totally inert under red or near-infrared irradiation in absence of UCNPs. Furthermore, the oxygen independence of these UCNP mediated photochemical reactions increases their value for photochemotherapy. Indeed, structurally related derivatives of *cis*-$[Ru^{II}(bpy)_2(py)_2]Cl_2$ and $[(\eta^6\text{-}p\text{-cym})Ru^{II}(bpm)(P\text{-}Trz\text{-}Py)][PF_6]_2$ have displayed *in vivo* antitumor activity as classical chemotherapeutic agents. Concerning the photocytotoxic $[Pt^{IV}(NH_3)_2(Cl)_2(O_2CCH_2CH_2CO_2H)_2]$, several Pt^{IV} prodrugs are being assessed in clinical trials and a photoactivatable Pt^{IV} complex has given encouraging results *in vivo*.

This Ph.D. work also shows the designed photoactivation strategy is of general applicability. The photochemistry of different classes of metal complexes was triggered by adopting various UCNP-coupling schemes:

(a) A partial confinement of *cis*-$[Ru^{II}(bpy)_2(py)_2]Cl_2$ on the UCNP surface by direct electrostatic or hydrophobic interactions between them;

(b) An electrostatic anchoring of $[(\eta^6\text{-}p\text{-cym})Ru^{II}(bpm)(P\text{-}Trz\text{-}Py)][PF_6]_2$ on the surface of UCNPs by a phosphonic spacer arm;

(c) A hydrophobic assembling between the oleic acid ligands capping UCNPs and $[Pt^{IV}(NH_3)_2(Cl)_2(O_2CCH_2CH_2CO_2H)_2]$ functionalized with a PEGylated phospholipid.

These three approaches provided different architectures and distances between the acceptor metal agent and the emitting donor Ln^{3+} ions of the UCNPs.

An important implication of the results obtained in the thesis is related to the efficiency of the upconversion process. This is typically various orders of magnitude higher than that of 2-photons absorption, allowing the use of experimental setups with low-cost continuous-wave diode lasers instead of the ultra-short pulsed lasers for multiphoton excitation of metal compounds.

UCNPs can also offer considerable advantages for the delivery and targeting of anticancer drugs and, most importantly, they can be exploited as nanoprobe for multimodal imaging modalities (UCL, CT, MRI, PET and SPECT). The combination of the unique optical properties, the multimodal imaging capability and the biocompatibility of UCNPs make them promising candidates for theranostic applications.

Considering that this work is a starting point, there is need for improvement of the NIR irradiation conditions employed. In fact, before performing *in vitro* or *in vivo* studies is crucial to reduce the actual irradiation time (ca. 1–4 hours) and laser power density (approx. 5–10 W cm^{-2}). These are important factors to consider, since high-intensity and prolonged NIR irradiation can cause serious photodamage on biological components, reducing the utility of UCNPs. At this stage different strategies can be envisioned to address this issue and further advance towards biomedical applications:

(a) Improving the synthetic design of the UCNPs to obtain nanomaterials with higher upconversion efficiency (e.g. active shell, calibration of dopant concentrations, plasma enhancement);

(b) Adding Neodymium in the UCNP host matrix to shift the excitation wavelengths from 980 nm to 800 nm. Indeed, tissue irradiation at 800 nm is more biocompatible than 980 nm since it does not cause water excitation and heating, and allows using higher power density;

(c) Employing photochemical reactions of metal complexes with superior yield (e.g. radical reactions) in order to increase their activation.

Other fields where photochemistry plays a role could also be positively affected by some of the discoveries reported in this work. In the future, combination of UCNPs and inorganic photocatalysts (e.g. Ru and Co complexes) could introduce unexplored solutions for the exploitation of solar energy to produce green fuels (e.g. H_2 from water) or to degrade soil contaminants and air/water pollutants. This is a striking possibility considering that solar light displays about half of the total spectrum of emission in infrared range. Few pioneering examples on UNCP-TiO_2 assemblies have recently demonstrated that such option is more than a long term vision. In this scenario, the approach here successfully developed might lead to the next generation of hybrid nanomaterials for NIR photocatalyst.

Appendix

Chapter 3

Near-Infrared Photolysis of a Ru Polypyridyl Complex by Upconverting Nanoparticles

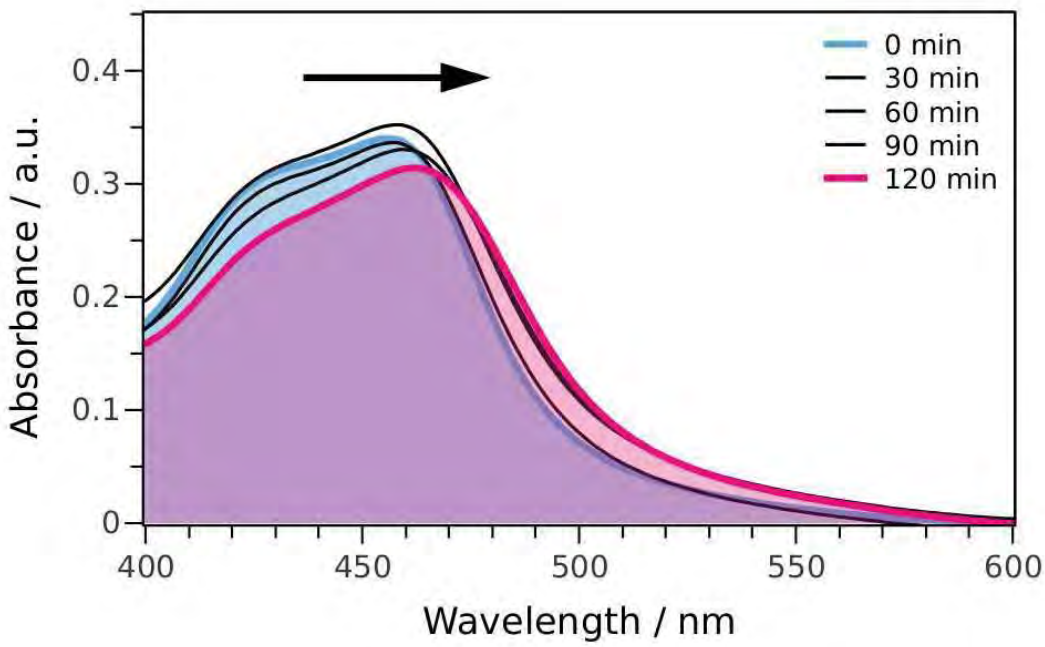

Fig. A1. Changes in the electronic absorption spectrum of *cis*-$[Ru(bpy)_2(py)_2]Cl_2$ (**1**) in aqueous solution (50 µM) upon NIR excitation (λ_{irr} = 980 nm, 25 $W \cdot cm^{-2}$) in the presence of oleate-free $NaYF_4:Yb^{3+}/Er^{3+}$ UCNPs (15 mg/ml).

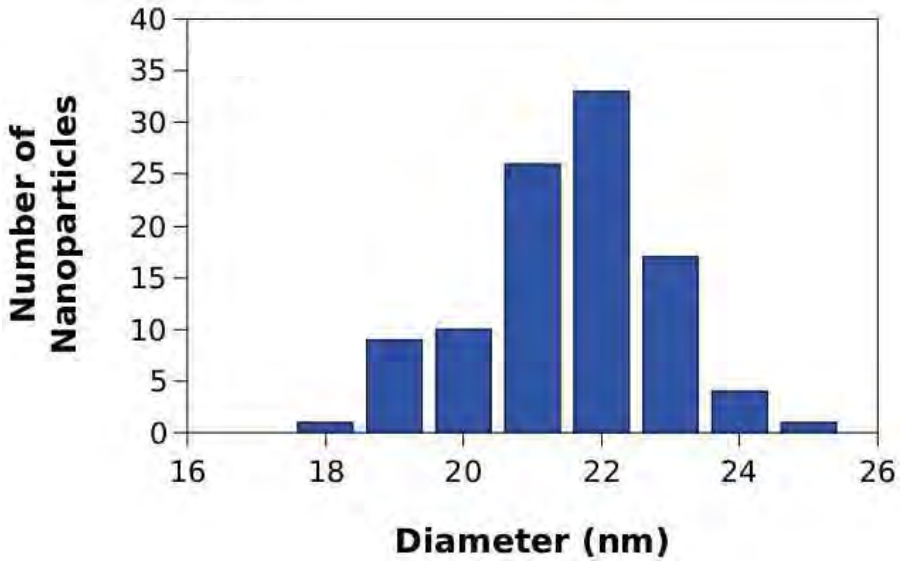

Fig. A2. Size distribution of $NaYF_4:Yb^{3+}/Tm^{3+}$ nanoparticles. Diameter of $NaYF_4:Yb^{3+}/Er^{3+}$= 80 ± 9 nm. Diameter of $NaYF_4:Yb^{3+}/Tm^{3+}$= 22 ± 1 nm.

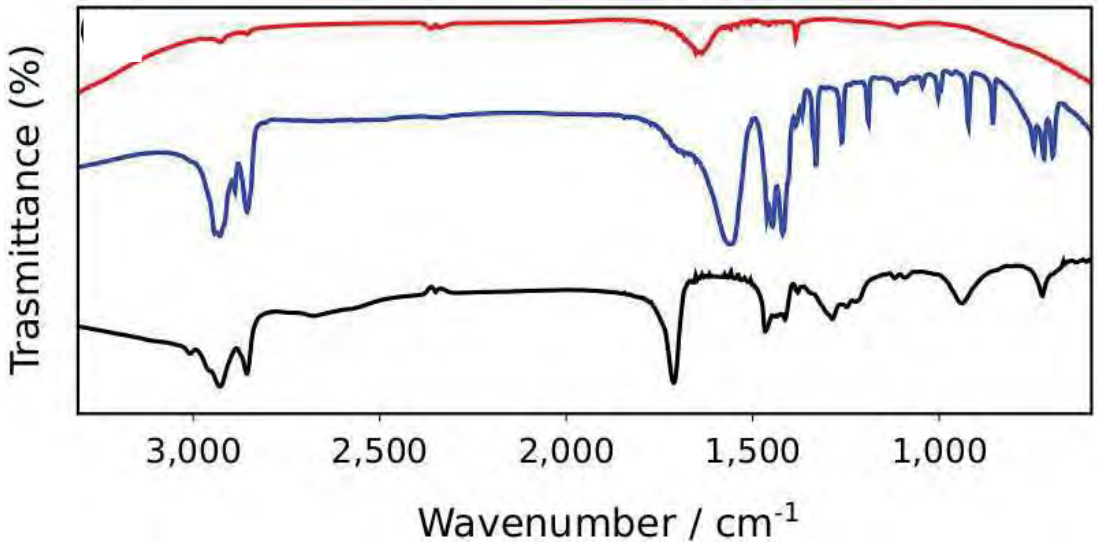

Fig. A3. FT-IR spectra of $NaYF_4:Yb^{3+}/Tm^{3+}$ nanoparticles. Top = oleic acid, middle = oleic acid capped NPs and bottom = oleate-free NPs.

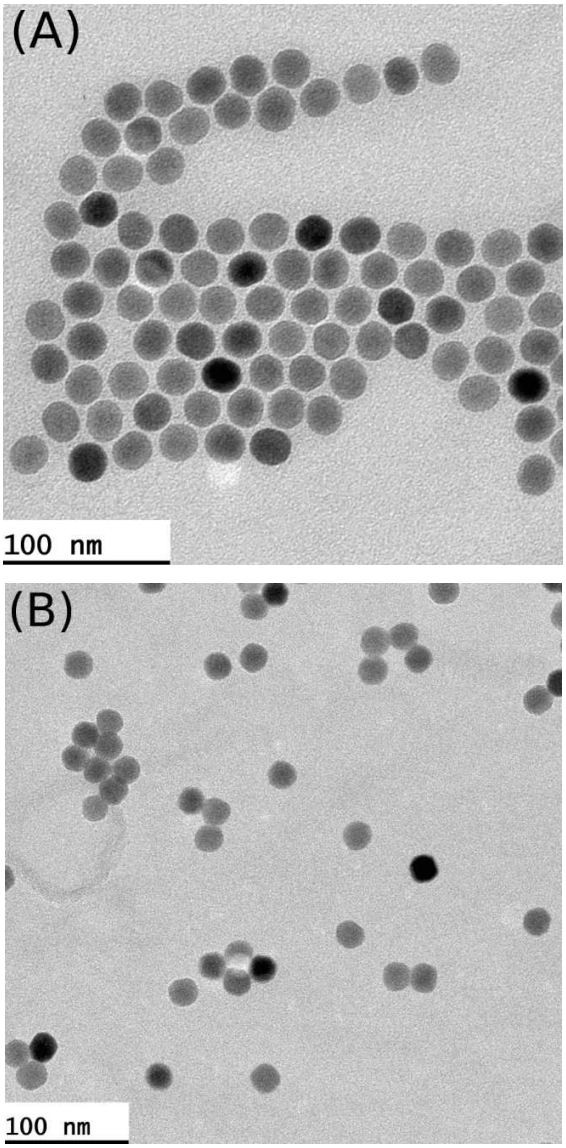

Fig. A4. Transmission electron microscopy (TEM) images of (a) oleic acid capped (0.1 mg/ml in THF) and (b) oleate-free (0.1 mg/ml in H_2O) $NaYF_4$:Yb^{3+}/Tm^{3+} nanoparticles.

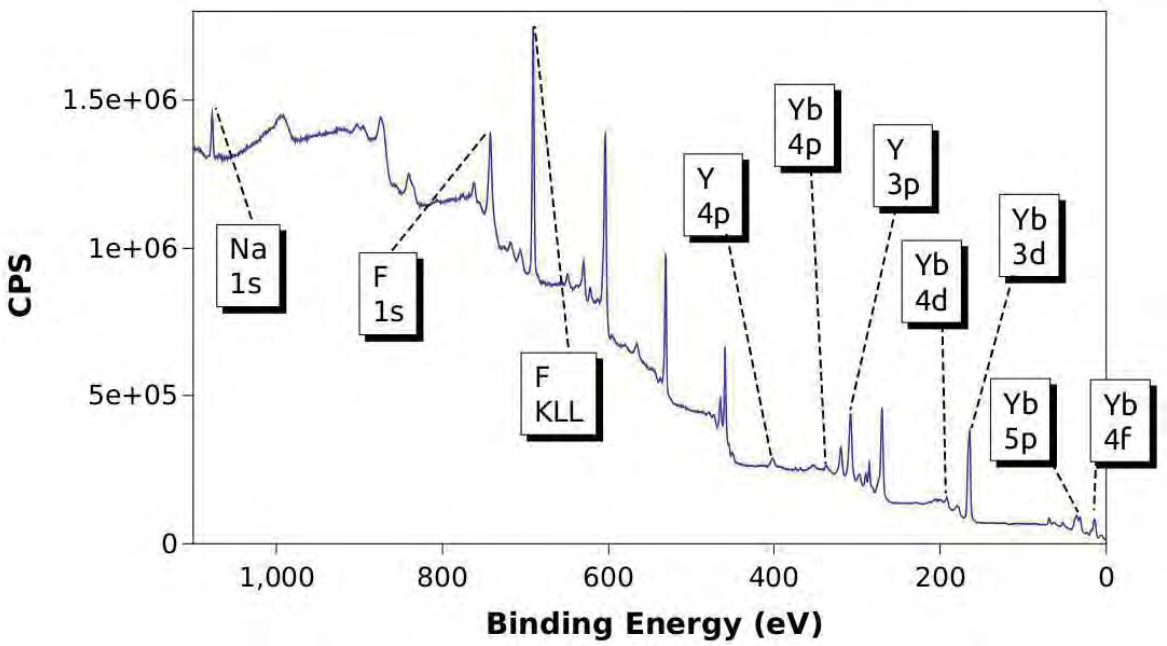

Fig. A5. XPS spectrum of $NaYF_4:Yb^{3+}/Tm^{3+}$ nanoparticles. Displayed peaks are assigned to the 1s level of Na, 1s level of F, 4p 3p 3d of Y, 4p 4d 5p 4f of Yb.

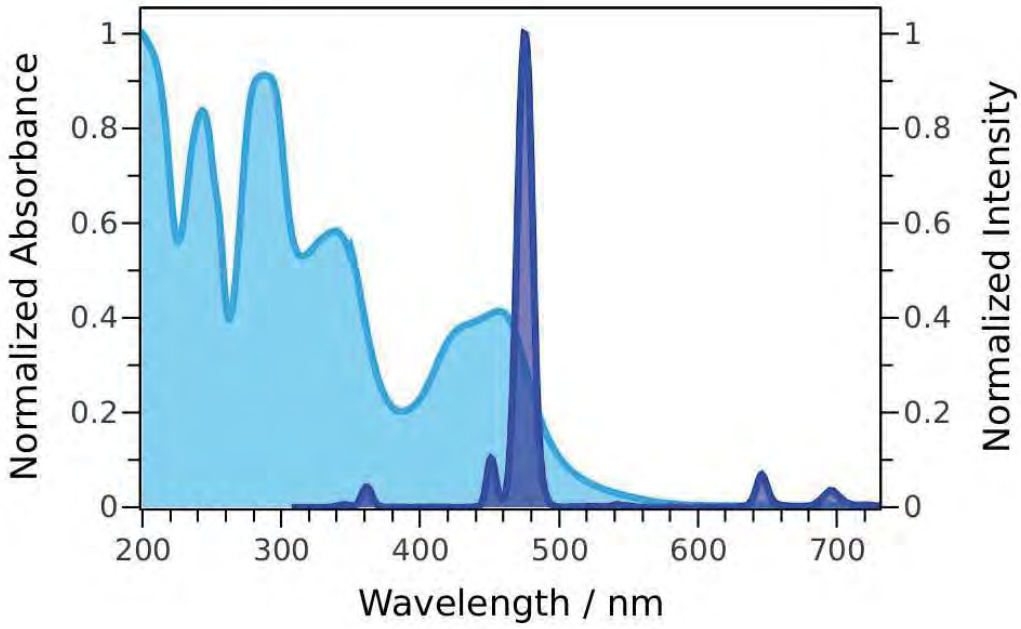

Fig. A6. Overlapped absorption spectrum of *cis*-$[Ru(bpy)_2(py)_2]Cl_2$ (**1**) (light grey) and upconversion emission (dark grey) of oleate-free (2 mg/ml in H_2O) $NaYF_4:Yb^{3+}/Tm^{3+}$ nanoparticles (λ_{irr} = 980 nm).

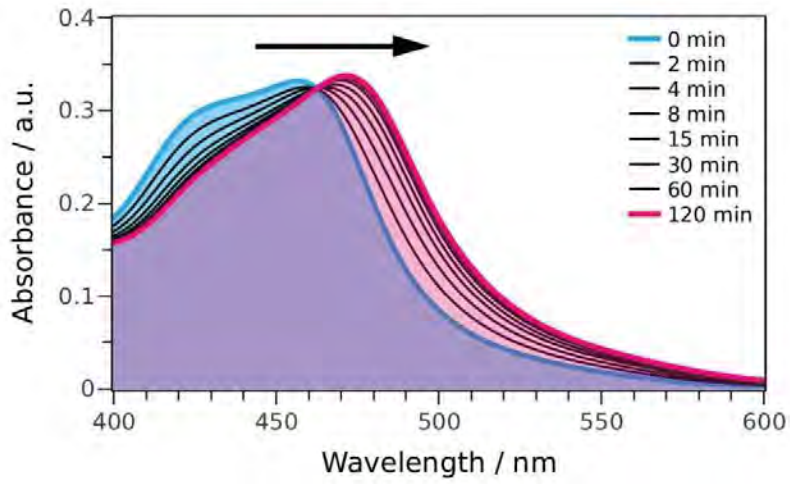

Fig. A7. Photolysis (λ_{irr} = 450 nm, *ca.* 1.5 mW·cm^{-2}) of *cis*-[Ru(bpy)$_2$(py)$_2$]Cl$_2$ (**1**) (50 µM) in aqueous solution followed by UV-Vis.

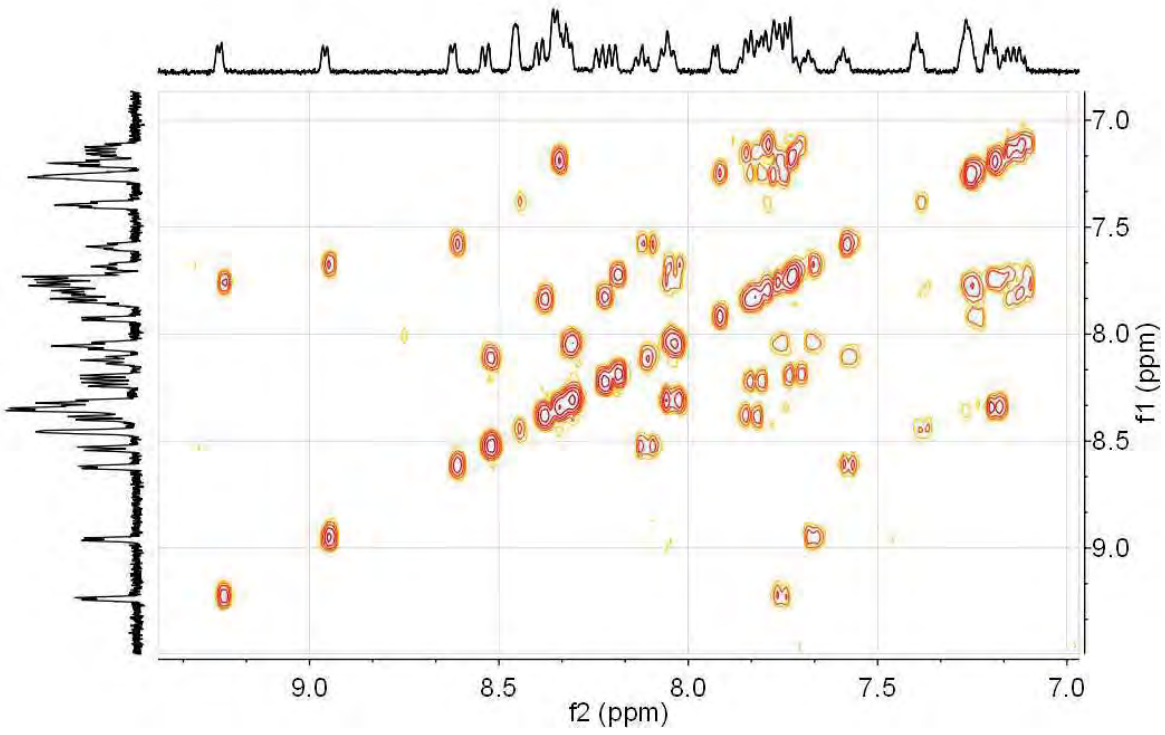

Fig. A8. ^{1}H-^{1}H COSY 2D NMR spectrum for an irradiated solution of *cis*-[Ru(bpy)$_2$(py)$_2$]Cl$_2$ (**1**) (150 µM) in D$_2$O (aromatic region). Irradiation details: λ_{irr} = 520 nm (*ca.* 6 mW·cm^{-2}) at 310 K for 5 min.

Appendix

Chapter 4

Near-Infrared Activation of an Anticancer Pt^{IV} Complex by Tm-Doped Upconversion Nanoparticles

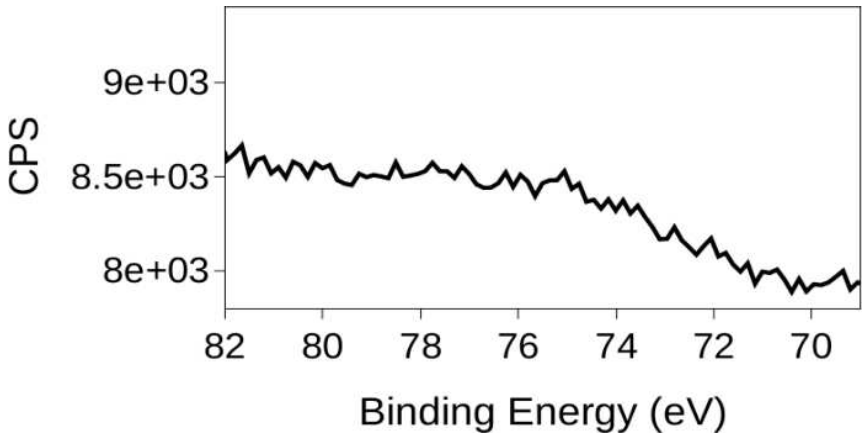

Fig. A1. Pt 4f XPS spectra for pellet of **1** (150 μM) with $NaYF_4:Yb^{3+}/Tm^{3+}@NaYF_4$ (5 mg) after 6 h NIR irradiation at 4.9 W cm^{-2}

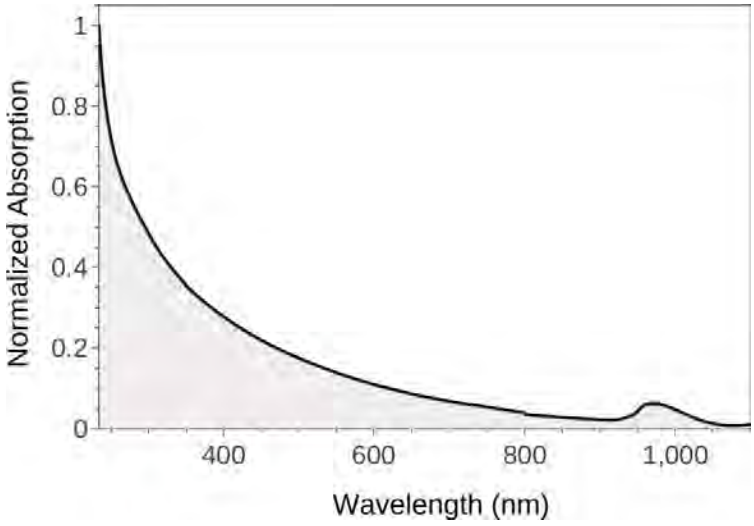

Fig. A2. UV-visible-NIR absorption spectrum of $NaYF_4:Yb^{3+}/Tm^{3+}@NaYF_4@$**2** (0.5 mg·$ml^{-1}$ in H_2O).

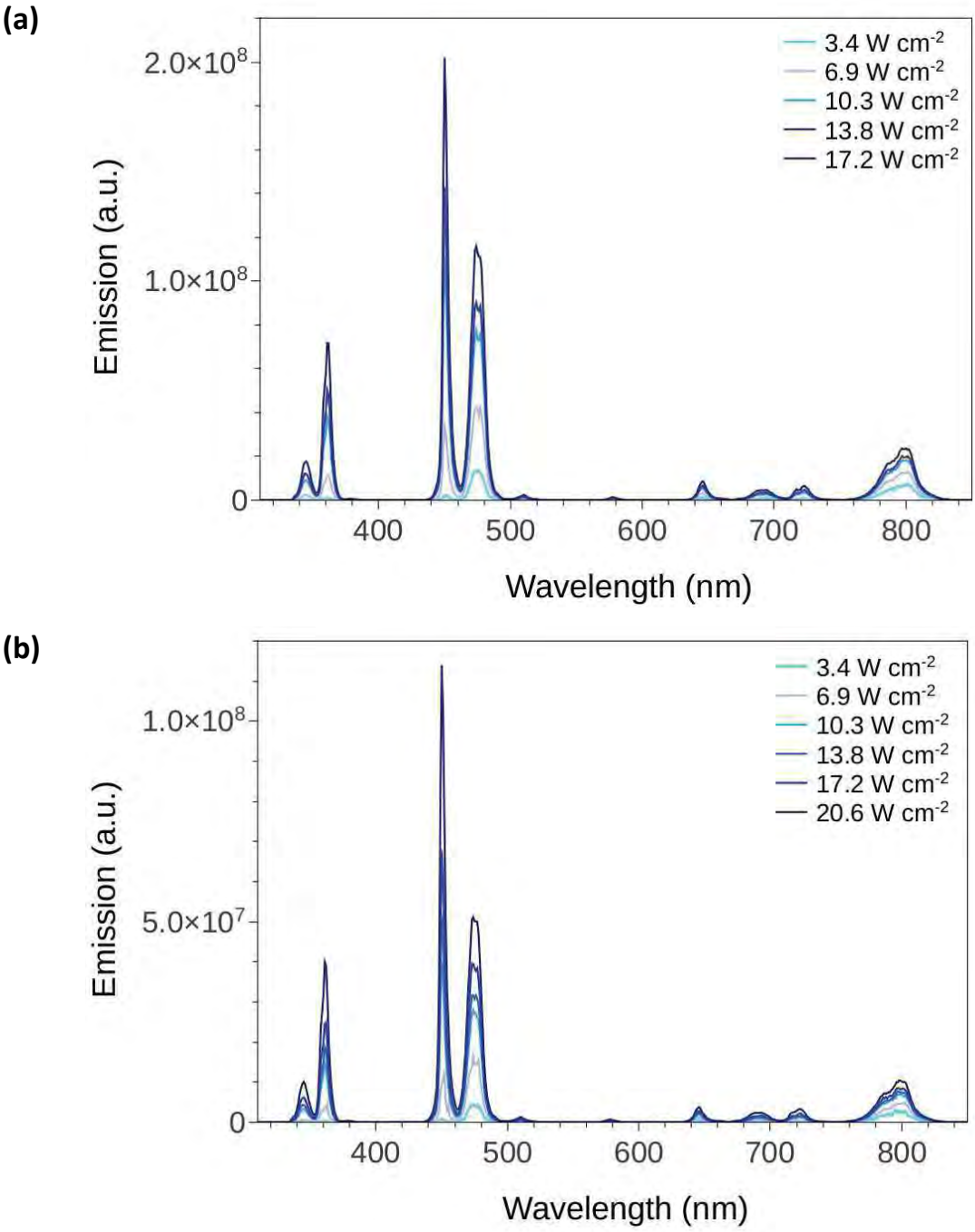

Fig. A3. Upconversion luminescence spectra of (a) $NaYF_4:Yb^{3+}/Tm^{3+}@NaYF_4@$**2** and (b) $NaYF_4:Yb^{3+}/Tm^{3+}@NaYF_4@$DSPE-PEG(2000)-$NH_2$, (0.5 mg·ml^{-1} in H_2O) upon 980-nm excitation at different powers (0.4–2.4 W cm^{-2}).

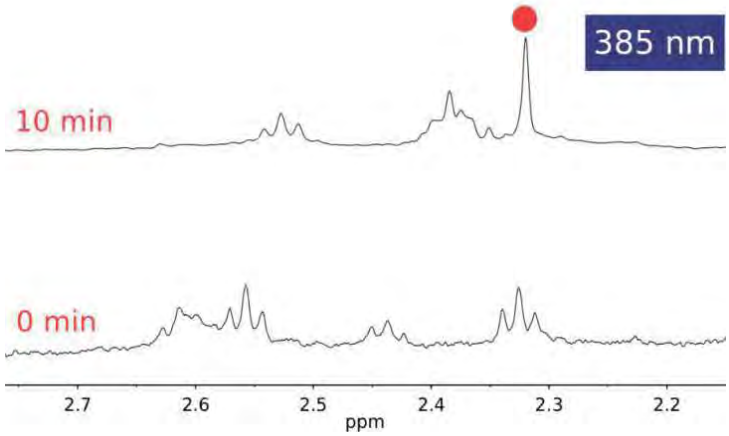

Fig. A4. ^{1}H NMR spectra of **2** in PBS/D_2O buffer (10 mM, pH = 7.3) before (bottom) and after (top) irradiation at 385 nm light for 10 min (40 mW cm^{-2}).

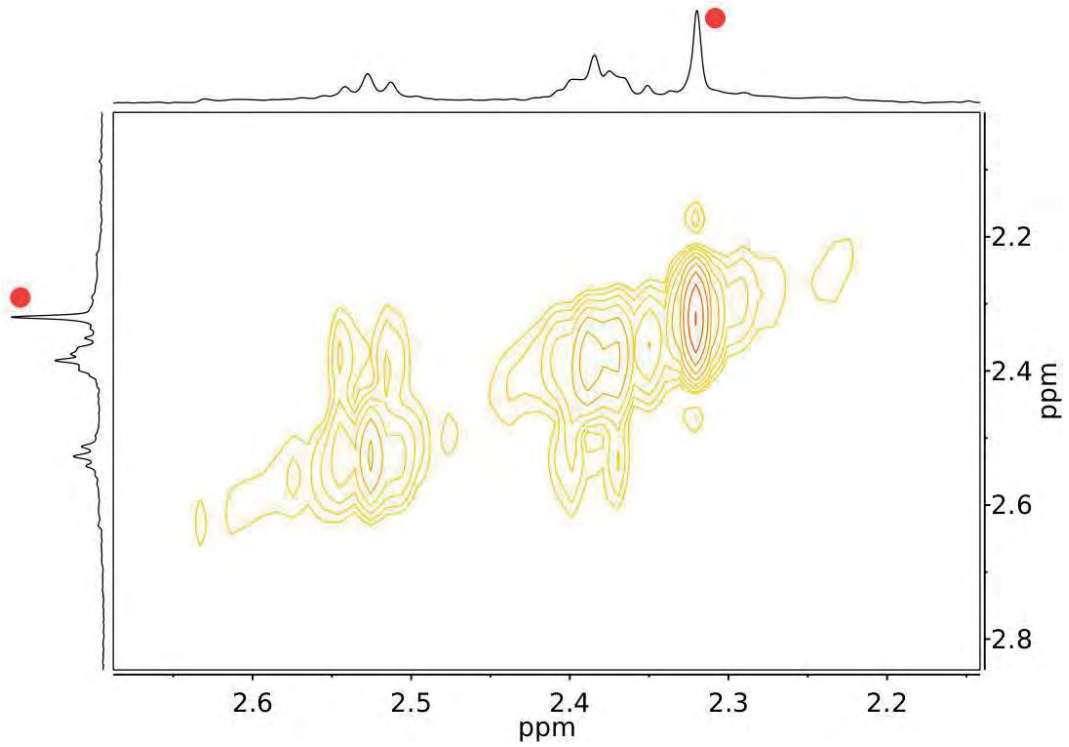

Fig. A5. ^{1}H-^{1}H COSY 2D NMR spectrum of **2** in PBS/D_2O buffer (10 mM, pH = 7.3) after irradiation at 385 nm light for 10 min (40 mW cm^{-2}).

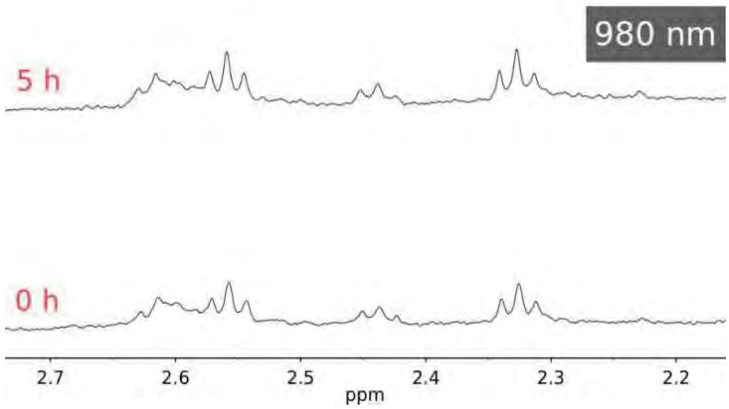

Fig. A6. ^{1}H NMR spectra of **2** in PBS/D_2O buffer (10 mM, pH = 7.3) before (bottom) and after (top) after irradiation at 980 nm light for 5 h (8.8 W cm^{-2}).

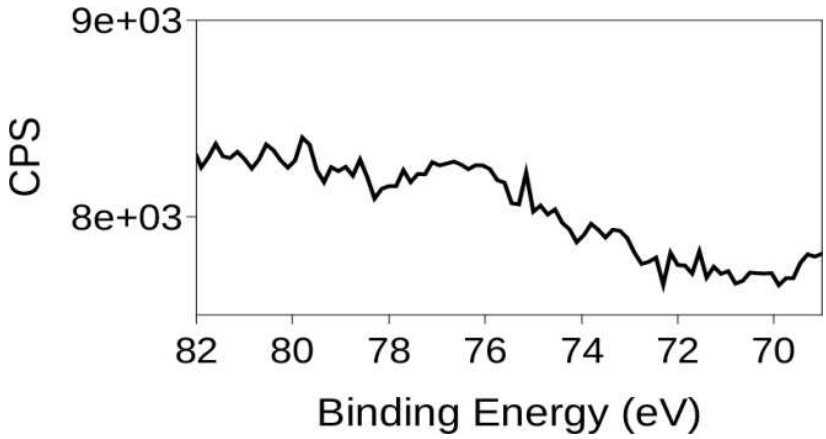

Fig. A7. Pt 4f XPS spectra for pellet of $NaYF_4$:Yb^{3+}/Tm^{3+}@$NaYF_4$@**2** (5 mg) after 3.5 h NIR irradiation at 7.3 W cm^{-2}.

Appendix

Chapter 5

Upconverting Nanoparticles Prompt Remote Near-Infrared Photoactivation of Ru^{II}-Arene Complexes

Compound	1 [2]
Empirical formula	C27H27F12N3P2Ru [C25H25F12N5P2Ru]
Formula weight	784.53 [786.51]g·mol^{-1}
Temperature	100 K
Wavelength	1.54184 Å
Crystal system	Orthorhombic[Triclinic]
Space group	$P2_12_12_1$[P-1]
Unit cell dimensions	a (Å)10.33000(10)[9.9041(5)] b (Å)12.55270(10)[11.0992(4)] c (Å)23.6885(2)[14.4409(7)] α (°) 90 [74.353(4)] β (°) 90 [69.956(4)] γ (°)90[81.961(4)]
Volume	3071.67(5)[1434.06(11)] Å^3
Z	4 (Z'=1)[2 (Z'=1)]
Density	1.696(1)[1.821(1)]g·cm^{-3}
μ (CuKα)	6.016[6.466](mm^{-1})
F (000)	1568[784]
Color	Yellow [Red]
Crystal size	0.06x0.14x0.24[0.18x0.19x0.38] mm
Theta range	3.73-69.99[3.35-71.00]θ (°)
Index rangesminimum(h, k, l)	(–12, –13, –28)[(–12, –13, –17)]
Index rangesmaximum(h, k, l)	(12, 15, 26)[(12, 11, 17)]
Reflections collected	24486[10168]
Independent reflections(R_{int}.)	5807(0.030)[5460(0.028)]
Observed reflections [I>2σ(I)]	5739[5342]
Refinement method	SHELXL97
Restraints/parameters	14/423 [0/409]
R(F) (I>2σ_I, all data)	0.0169, 0.0172[0.0243, 0.0249]
$R_w(F^2)$[a] (I>2σ_I ,all data)	0.0419, 0.0421[0.0626, 0.0630]
Δ/σmaximum	0.006[0.001]
Δ/σ medium	0.000[0.000]
Δρ maximum (eÅ^3)	0.231[0.635]
Δρ minimum (eÅ^{-3})	-0.253[-0.718]

Table A1. Crystal data and structure refinement for **1** and **2**.

(a)

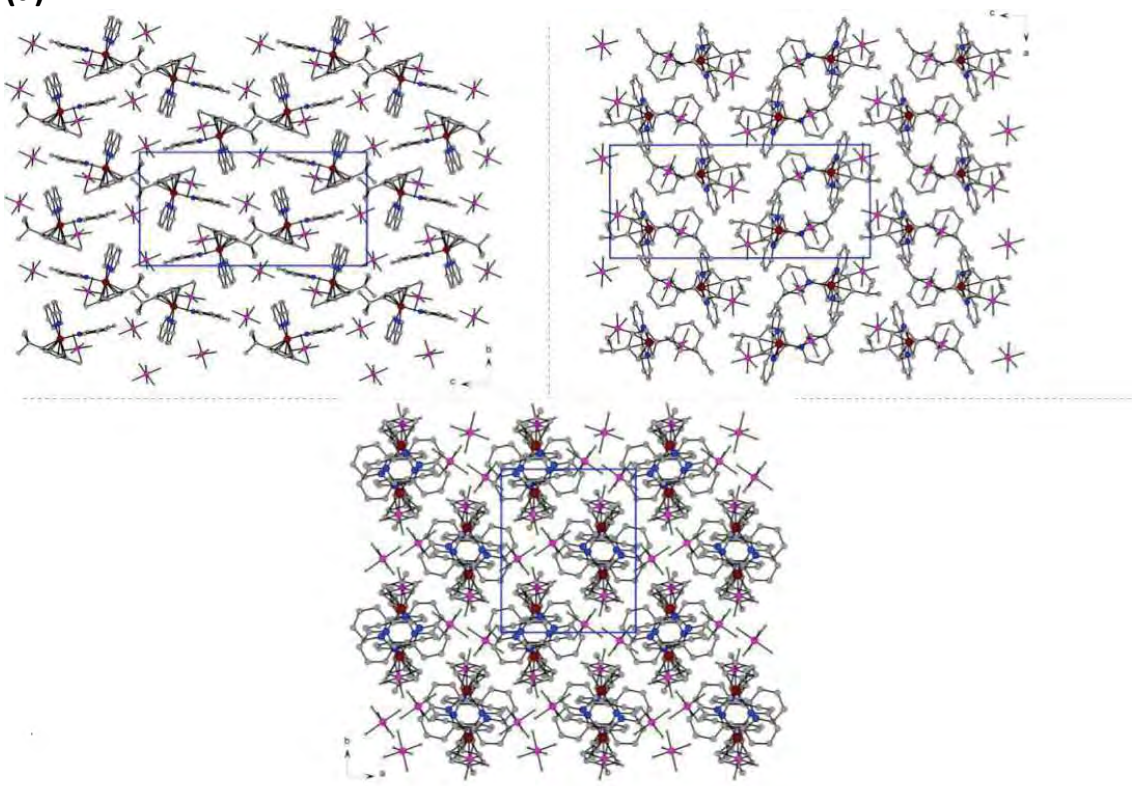

(b)

Fig. A1. (a) Crystal packing of **1** along the crystallographic axes a, b and c, respectively. Hydrogen atoms were removed for simplicity. (b) Single crystal of **1** used for the collection of X-ray data.

(a)

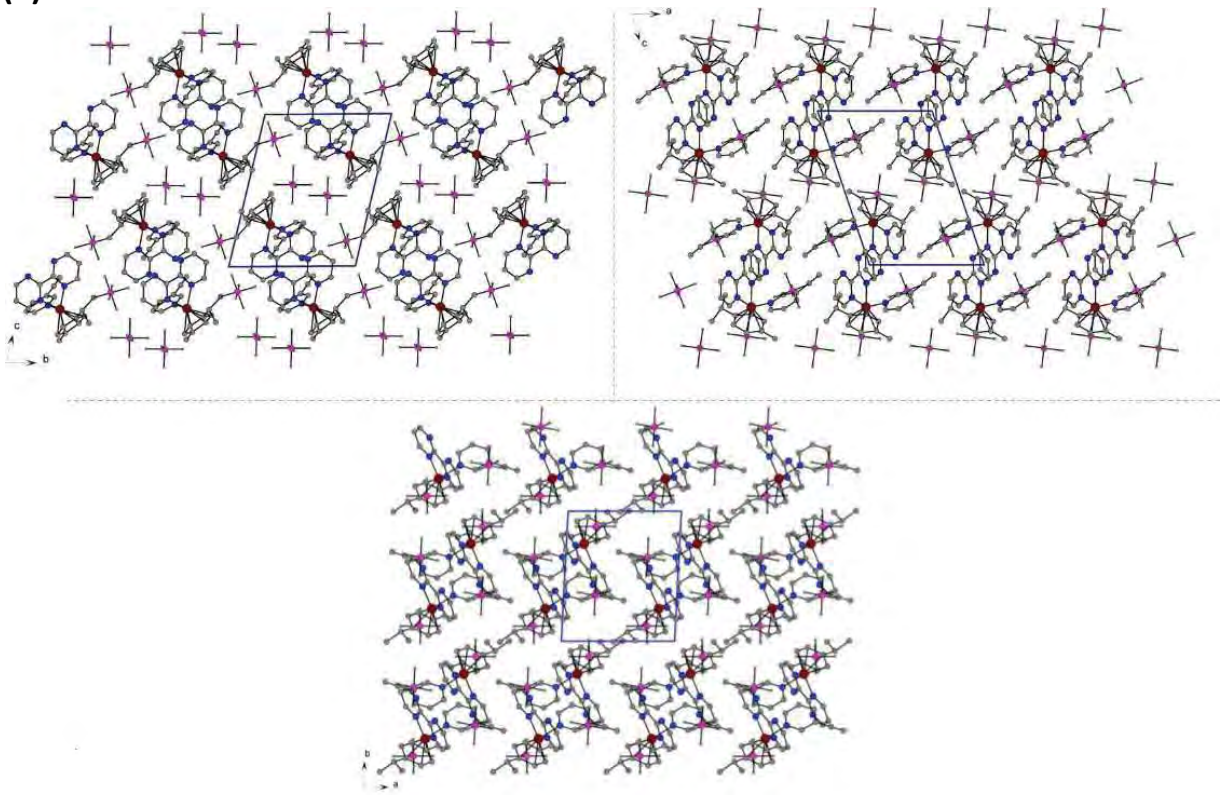

(b)

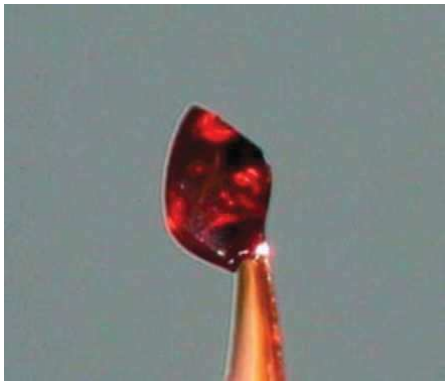

Fig. A2. (a) Crystal packing of **2** along the crystallographic axes a, b and c, respectively. Hydrogen atoms were removed for simplicity. (b) Single crystal of **2** used for the collection of X-ray data.

Complex	HOMO	LUMO	LUMO+1	LUMO+2	LUMO+8
1	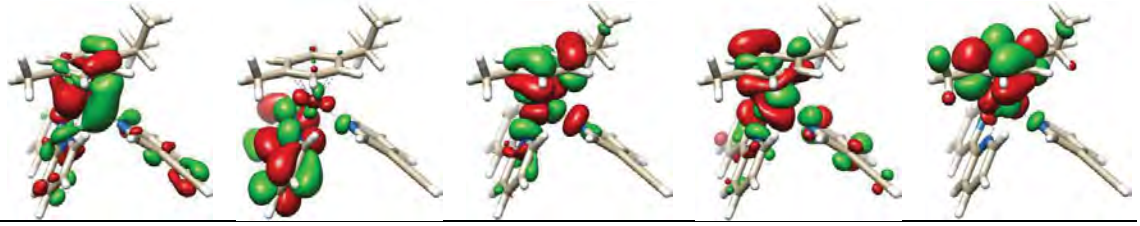				
	HOMO	LUMO	LUMO+1	LUMO+3	LUMO+8
2	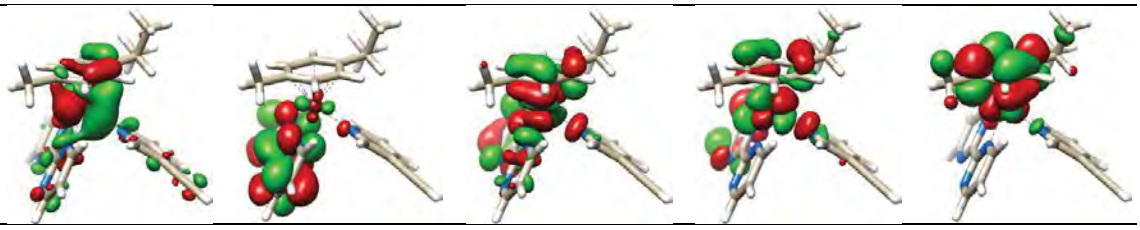				

Fig. A3. Selected frontier orbitals for complexes **1** and **2** in the ground state (S0) geometry.

Trans.	Energy (eV)	Wavelength (nm)	Oscillator Strength	Major contributions
1	2.84	437	0.002	H-1→L+2 (10%), HOMO→L+1 (63%), HOMO→LUMO (9%)
2	3.02	411	0.0061	H-4→L+1 (11%), H-1→LUMO (10%), H-1→L+1 (41%), H-1→L+2 (20%)
3	3.09	401	0.0005	H-1→L+1 (16%), HOMO→L+2 (47%)
4	3.18	390	0.0006	H-4→L+1 (15%), H-4→L+2 (34%), H-1→L+2 (9%)
5	3.39	366	0.0021	HOMO→LUMO (81%)
6	3.54	350	0.0438	H-1→LUMO (66%), H-4→LUMO (7%), H-4→L+1 (9%)
8	3.71	334	0.0195	H-4→L+1 (20%), H-4→L+2 (10%), H-1→LUMO (17%), H-1→L+1 (10%), H-4→LUMO (8%), H-1→L+2 (7%), HOMO→L+2 (8%)
9	3.92	316	0.0111	H-4→LUMO (24%), H-2→LUMO (52%), H-4→L+1 (9%)
10	4.05	306	0.0126	H-4→LUMO (50%), H-2→LUMO (40%)
12	4.22	294	0.1394	H-3→LUMO (68%), HOMO→L+4 (15%)
13	4.32	287	0.0333	H-1→L+2 (10%), H-1→L+3 (72%)
14	4.40	282	0.0249	HOMO→L+4 (21%), HOMO→L+5 (21%), HOMO→L+7 (17%), H-2→L+1 (8%)
17	4.52	274	0.0616	H-1→L+4 (61%), HOMO→L+5 (10%), H-1→L+5 (7%), H-1→L+7 (8%)
19	4.59	270	0.0102	H-2→L+2 (62%), H-4→L+2 (8%),
20	4.59	270	0.0121	H-1→L+4 (14%), H-1→L+5 (10%), HOMO→L+5 (23%), HOMO→L+7 (11%), H-3→L+1 (9%), HOMO→L+8 (9%)
21	4.63	268	0.0384	H-1→L+5 (19%), H-1→L+7 (10%), HOMO→L+8 (25%), H-2→L+2 (8%), H-1→L+4 (8%),
22	4.73	268	0.0164	HOMO→L+6 (66%), H-4→L+3 (6%), H-2→L+2 (4%), H-2→L+3 (7%)
24	4.68	265	0.0131	H-2→L+3 (30%), H-1→L+6 (28%), HOMO→L+6(14%)
25	4.73	262	0.0045	H-1→L+8 (31%), HOMO→L+5 (10%), HOMO→L+7 (18%), HOMO→L+8 (13%)
26	4.77	260	0.0432	H-4→L+2 (11%), H-4→L+3 (62%)
28	4.84	256	0.0598	H-2→L+3 (13%), H-1→L+6 (38%), H-5→LUMO (6%), H-1→L+7 (7%)
30	4.92	252	0.036	H-4→L+4 (26%), H-2→L+4 (23%), H-4→L+5 (9%), H-4→L+7 (9%)
32	4.98	249	0.026	H-4→L+5 (22%), H-4→L+7 (10%), H-2→L+4 (28%), H-2→L+5 (18%)
34	5.06	245	0.0123	H-6→LUMO (24%), H-4→L+4 (20%),

				H-2→L+4 (13%)
35	5.06	245	0.0456	H-6→LUMO (10%), H-4→L+4 (30%), H-2→L+4 (16%)
36	5.10	243	0.1697	H-2→L+5 (20%), H-2→L+6 (22%), H-4→L+6 (9%)

Table A2. Selected TDDFT singlet transitions for complex **1**.

Trans.	Energy (eV)	Wavelength (nm)	Oscillator Strength	Major contributions
1	2.79	445	0.0024	HOMO→L+1 (42%), HOMO→L+3 (22%), HOMO→LUMO (9%)
2	3.00	413	0.005	H-3→L+3 (14%), H-1→L+3 (23%), H-3→L+1 (7%), HOMO→L+1 (7%), HOMO→L+2 (7%), HOMO→L+3 (8%), HOMO→L+4 (8%)
3	3.03	409	0.0022	H-1→L+1 (23%), H-1→L+3 (24%), HOMO→L+3 (10%), HOMO→L+4 (12%), H-1→LUMO (7%), HOMO→L+1 (8%), HOMO→L+2 (8%)
4	3.11	399	0.001	H-3→L+1 (21%), H-3→L+2 (10%), H-3→L+4 (12%), H-1→L+1 (13%), HOMO→LUMO (12%)
5	3.18	390	0.0022	HOMO→LUMO (72%)
6	3.34	371	0.0305	H-1→LUMO (79%)
8	3.64	341	0.0149	H-3→LUMO (31%), H-3→L+3 (12%), H-2→LUMO (15%), H-1→L+3 (8%)
9	3.76	330	0.0086	H-3→LUMO (19%), H-3→L+3 (25%), H-2→LUMO (24%), H-3→L+1 (8%)
14	4.15	299	0.0816	H-1→L+2 (22%), HOMO→L+4 (41%), H-1→L+1 (7%), HOMO→L+2 (7%)
15	4.23	293	0.0085	H-1→L+3 (12%), H-1→L+4 (68%)
16	4.28	290	0.0062	HOMO→L+5 (92%)
19	4.46	278	0.0292	H-2→L+1 (27%), H-1→L+5 (52%)
20	4.49	276	0.0168	H-3→L+1 (17%), H-3→L+2 (21%), H-2→L+2 (28%), H-2→L+3 (10%), H-1→L+5 (12%)
27	4.71	263	0.044	H-6→LUMO (19%), H-5→L+1 (10%), H-5→L+2 (27%)
28	4.77	260	0.0555	H-6→LUMO (11%), H-1→L+6 (19%), H-1→L+8 (31%)

29	4.79	259	0.0101	H-2→L+4 (15%), H-2→L+5 (28%), H-6→LUMO (8%)
30	4.81	258	0.0791	H-6→LUMO (11%), HOMO→L+6 (26%), H-2→L+4 (8%), H-1→L+7 (7%)
31	4.82	257	0.0704	H-8→L+2 (12%), H-5→L+4 (16%), H-6→LUMO (8%), H-5→L+1 (9%)
33	4.86	255	0.0717	H-2→L+5 (25%), H-1→L+8 (19%), HOMO→L+6 (18%), H-3→L+5 (8%)
34	4.88	254	0.0594	H-7→LUMO (15%), H-3→L+4 (18%), H-2→L+4 (26%)
35	4.92	252	0.0544	H-3→L+5 (74%), HOMO→L+6 (9%)
36	5.02	247	0.0285	H-2→L+5 (10%), H-1→L+6 (47%), H-1→L+8 (11%)

Table A3. Selected TDDFT singlet transitions for complex **2**.

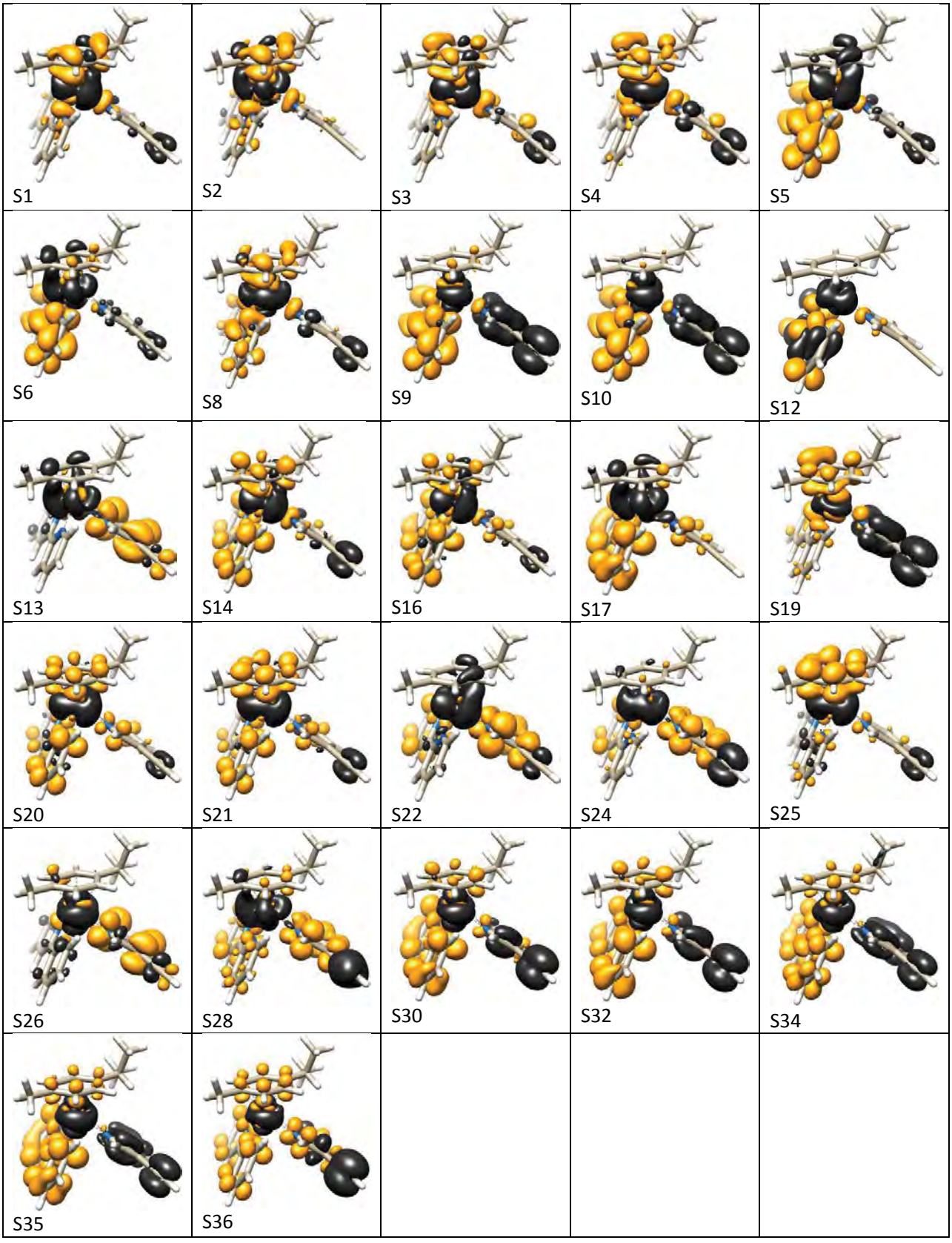

Fig. A4. Selected Electron Difference Density Maps (EDDMs) of singlet excited state transitions of **1** in H_2O (black indicates a decrease in electron density, while grey indicates an increase).

Fig. A5. Selected Electron Difference Density Maps (EDDMs) of singlet excited state transitions of **2** in H_2O (black indicates a decrease in electron density, while grey indicates an increase).

Complex	Lowest-SOMO	Highest-SOMO
1	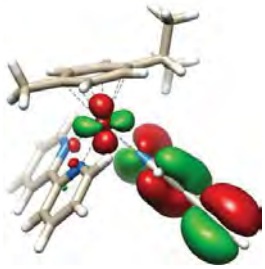	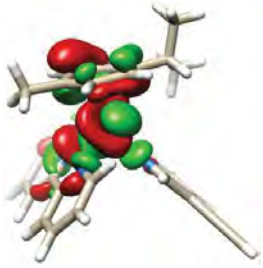
2	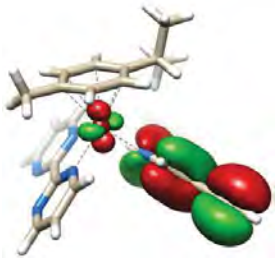	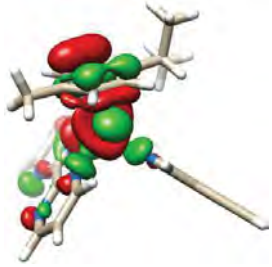

Fig. A6. Calculated lowest- and highest-Single Occupied Molecular Orbitals (h-SOMO and l-SOMO, respectively, isovalue 0.02), for **1** and **2** in the lowest-lying triplet (T0) optimized geometry.

Complex	Lowest-SOMO	Highest-SOMO
1	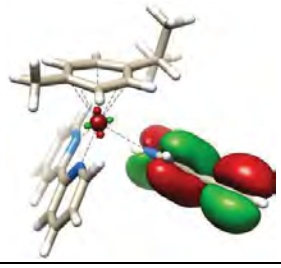	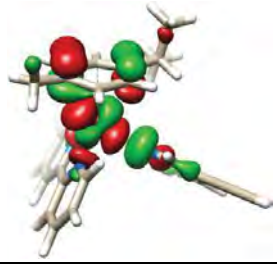
2	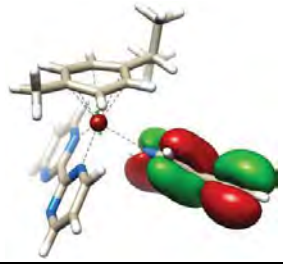	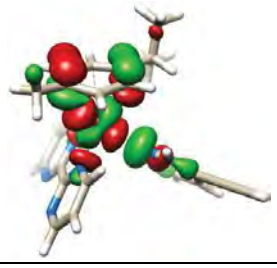

Fig. A7. Calculated lowest- and highest-Single Occupied Molecular Orbitals (h-SOMO and l-SOMO, respectively, isovalue 0.02), for **1** and **2** in the T1 optimized geometry.

Complex	T0	T1
1		
2		

Fig. A8. Calculated spin density surfaces for complexes **1** and **2** in the T0 and T1 triplet optimized geometries.

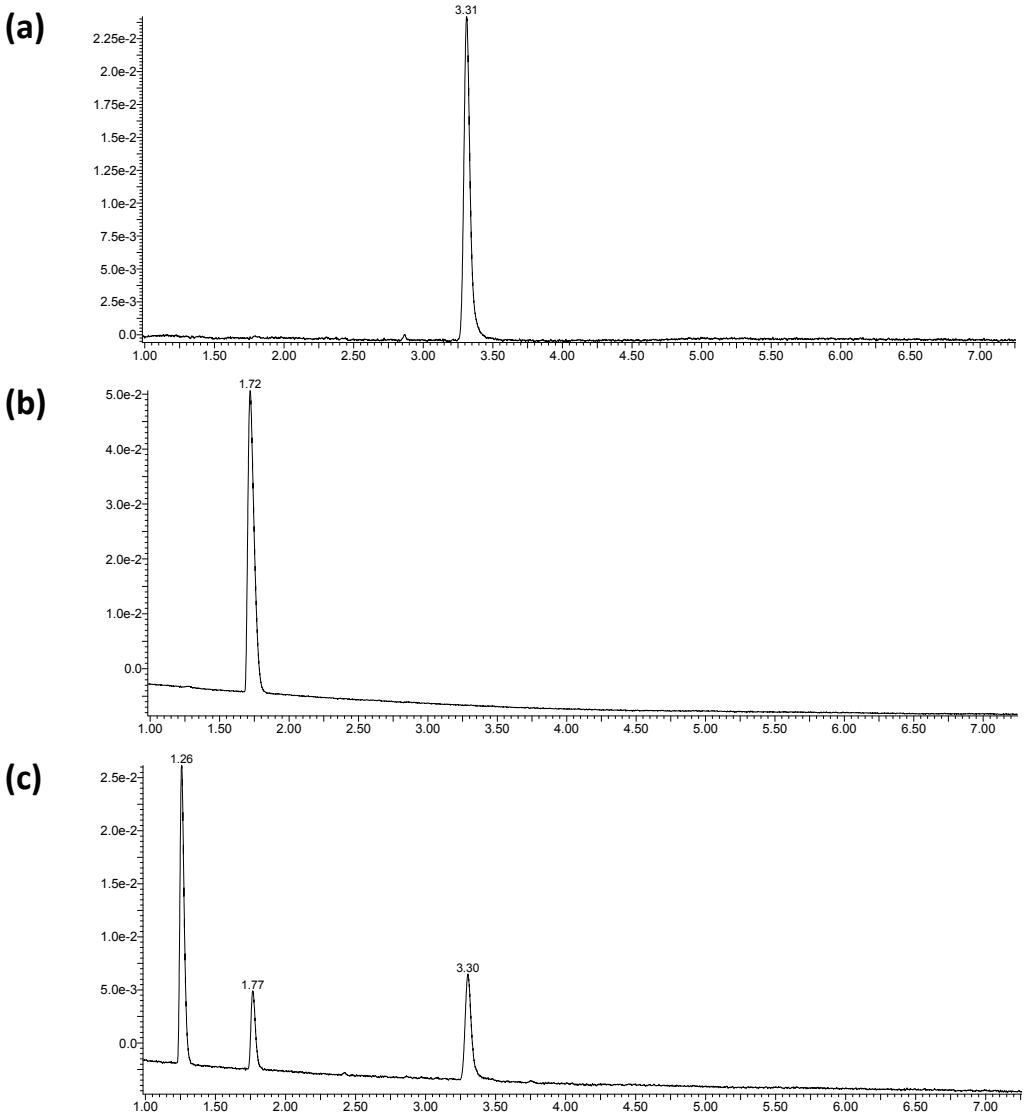

Fig. A9. (a) Chromatogram of 3-ethynylpyridine in water. (b) Chromatogram of **2** in aqueous solution (95:5 H_2O:DMSO). (c) Chromatogram of **2** in aqueous solution (95:5 H_2O:DMSO) after 395-nmexcitation (15 $mW \cdot cm^{-2}$).

Retention time (RT) of 3-ethynylpyridine is 3.3 min, RT of **2** is 1.7 min and RT of $[(\eta^6\text{-}p\text{-cym})Ru(bpm)(H_2O)]^{2+}$ is 1.3 min.

ESI-MS (m/z) of 3-ethynylpyridine $[C_7H_6N]^+$ expected = 104.05 found = 104.01, ESI-MS (m/z) of **2** $[C_{25}H_{25}N_5RuPF_6]^+$ expected = 642.08 found = 642.28, ESI-MS (m/z) of $[(\eta^6\text{-}p\text{-cym})Ru(bpm)(H_2O)]^{2+}$ $[C_{18}H_{21}N_4ORu]^+$expected = 411.08 found = 411.11.

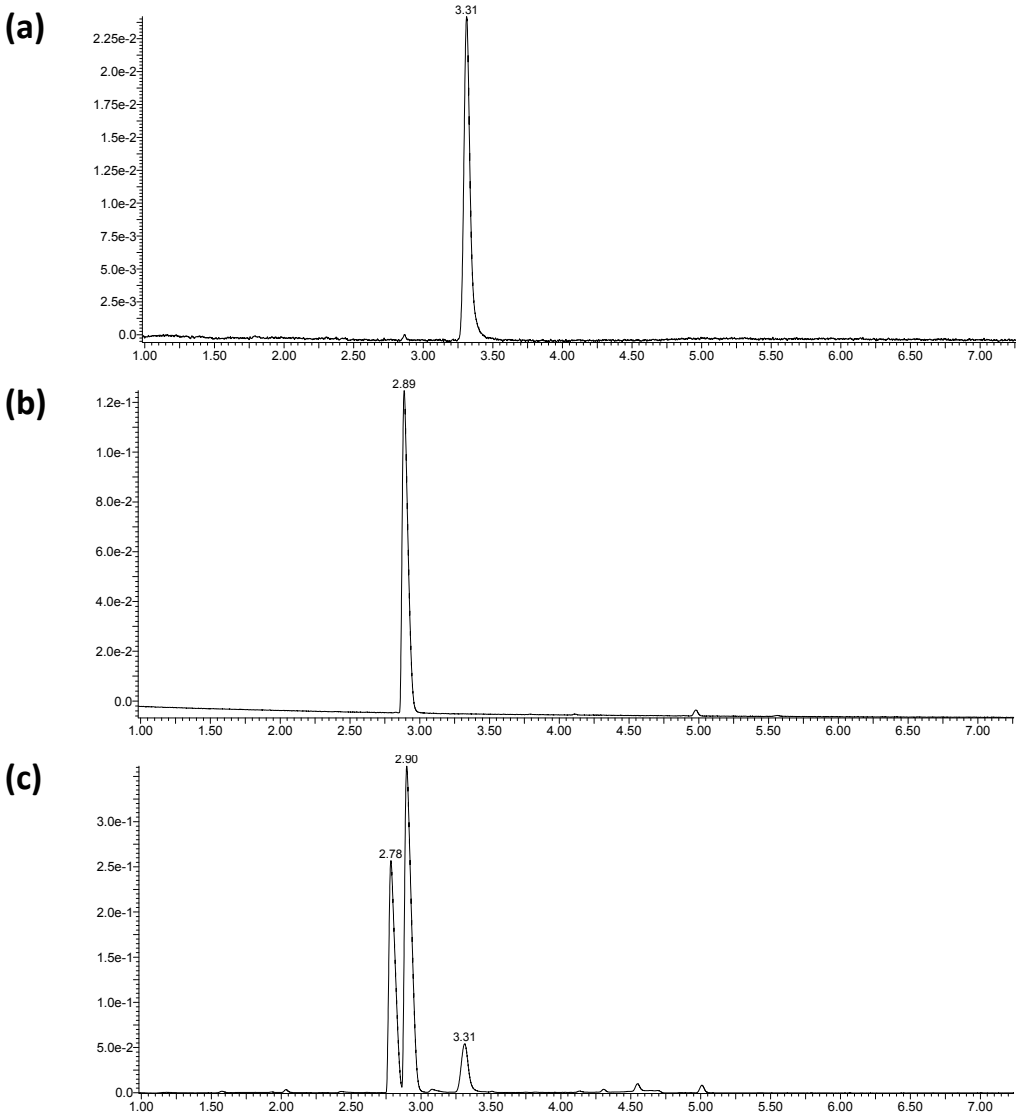

Fig. A10. (a) Chromatogram of 3-ethynylpyridine in water. (b) Chromatogram of **1** in aqueous solution (95:5 H_2O:DMSO). (c) Chromatogram of **1** in aqueous solution (95:5 H_2O:DMSO) after 395-nmexcitation (15 $mW \cdot cm^{-2}$).

Retention time (RT) of 3-ethynylpyridine is 3.3 min, RT of **1** is 2.9 min and RT of $[(\eta^6\text{-}p\text{-cym})Ru(bpy)(H_2O)]^{2+}$ is 2.8 min. ESI-MS (m/z) of 3-ethynylpyridine $[C_7H_6N]^+$ expected = 104.05 g/mol, found = 104.01.

ESI-MS (m/z) of 3-ethynylpyridine $[C_7H_6N]^+$ expected = 104.05 found = 104.01, ESI-MS (m/z) of **1** $[C_{27}H_{27}N_3RuPF_6]^+$ expected = 640.09 found = 640.30, ESI-MS (m/z) of $[(\eta^6\text{-}p\text{-cym})Ru(bpy)(H_2O)]^{2+}$ $[C_{20}H_{23}N_2ORu]^+$ expected = 409.09 found = 409.12.

(a)

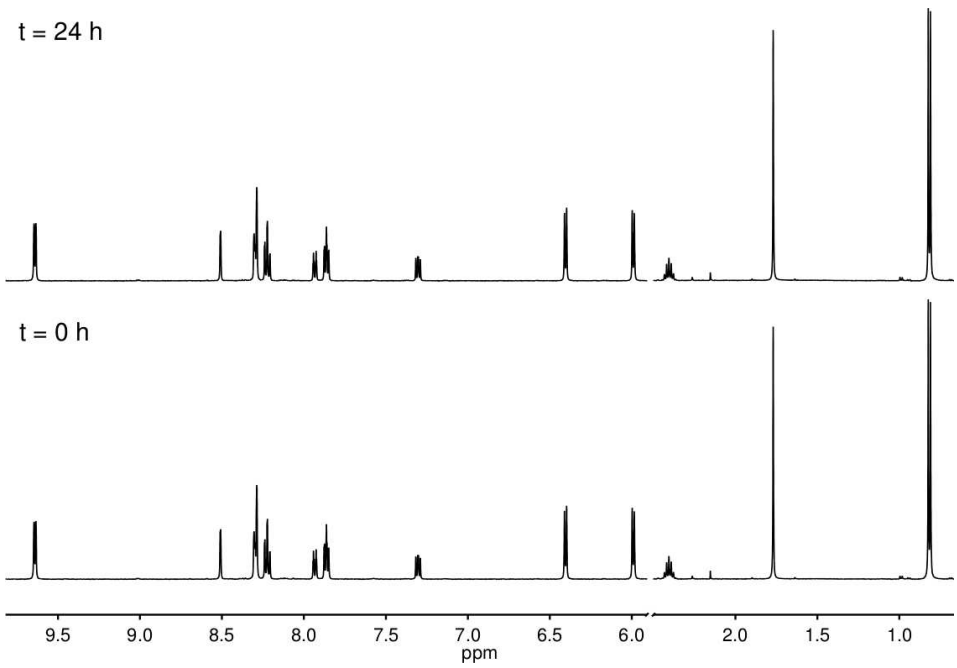

(b)

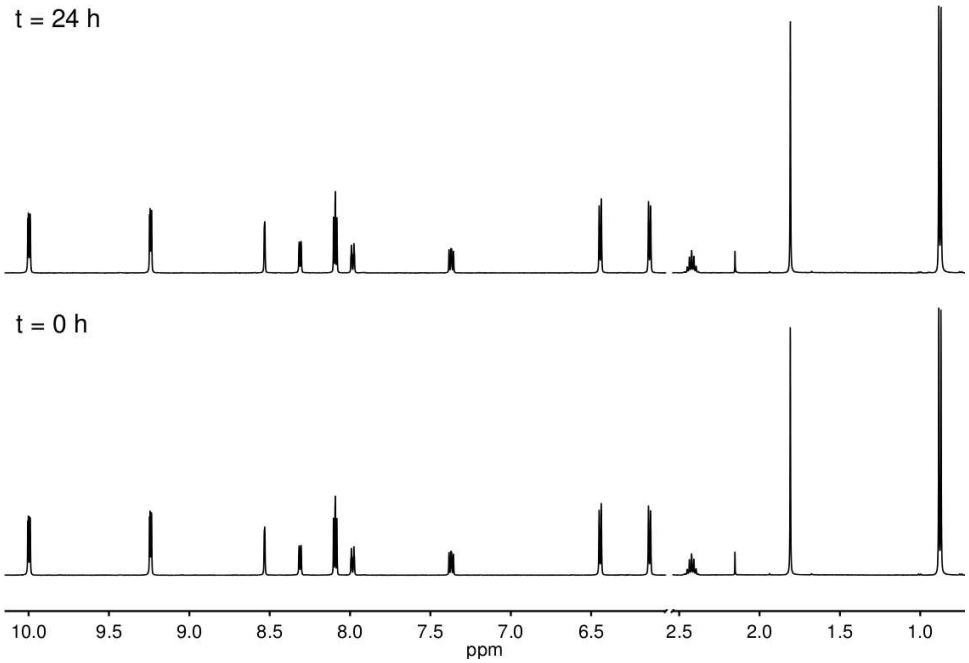

Fig. A11. ^{1}H NMR control spectra of aqueous solutions of **1** (a) and **2** (b) in the dark for 24 h

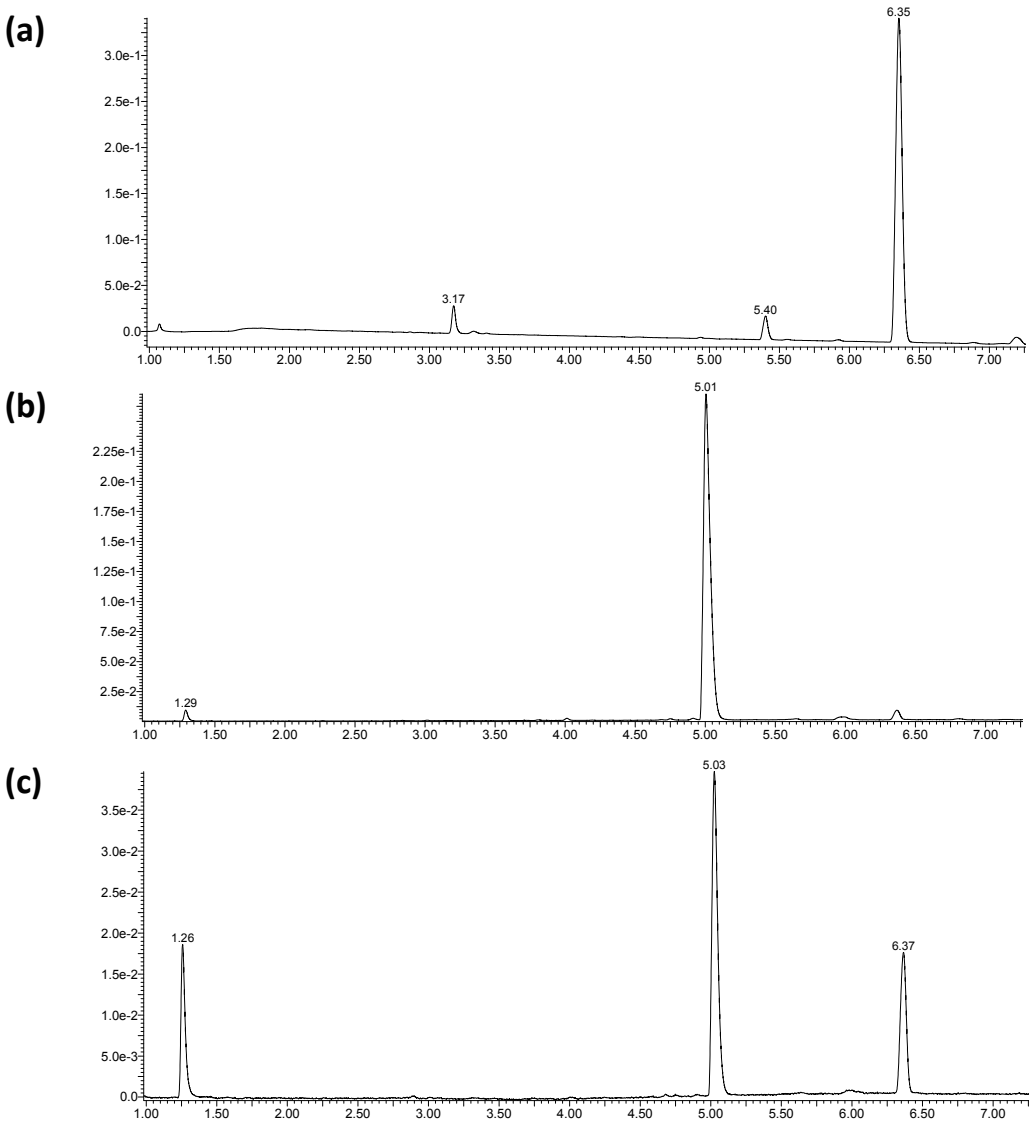

Fig. A12. (a) Chromatogram of P-Trz-Py in water. (b) Chromatogram of **4** in aqueous solution (95:5 H_2O:DMSO). (c) Chromatogram of **4** in aqueous solution (95:5 H_2O:DMSO) after 395-nmexcitation (15 $mW \cdot cm^{-2}$).

Retention time (RT) of P-Trz-Py is 6.4 min, RT of **4** is 5.0 min and RT of $[(\eta^6\text{-}p\text{-cym})Ru(bpm)(H_2O)]^{2+}$ is 1.3 min.

ESI-MS (m/z) of P-Trz-Py $[C_{14}H_{22}N_4O_3P]^+$ expected = 325.14 found = 325.16, ESI-MS (m/z) of **4** $[C_{32}H_{41}O_3N_8PRuPF_6]^+$ expected = 863.17 found = 863.42, ESI-MS (m/z) of $[(\eta^6\text{-}p\text{-cym})Ru(bpm)(H_2O)]^{2+}$ $[C_{18}H_{21}N_4ORu]^+$ expected = 411.08 found = 411.11.

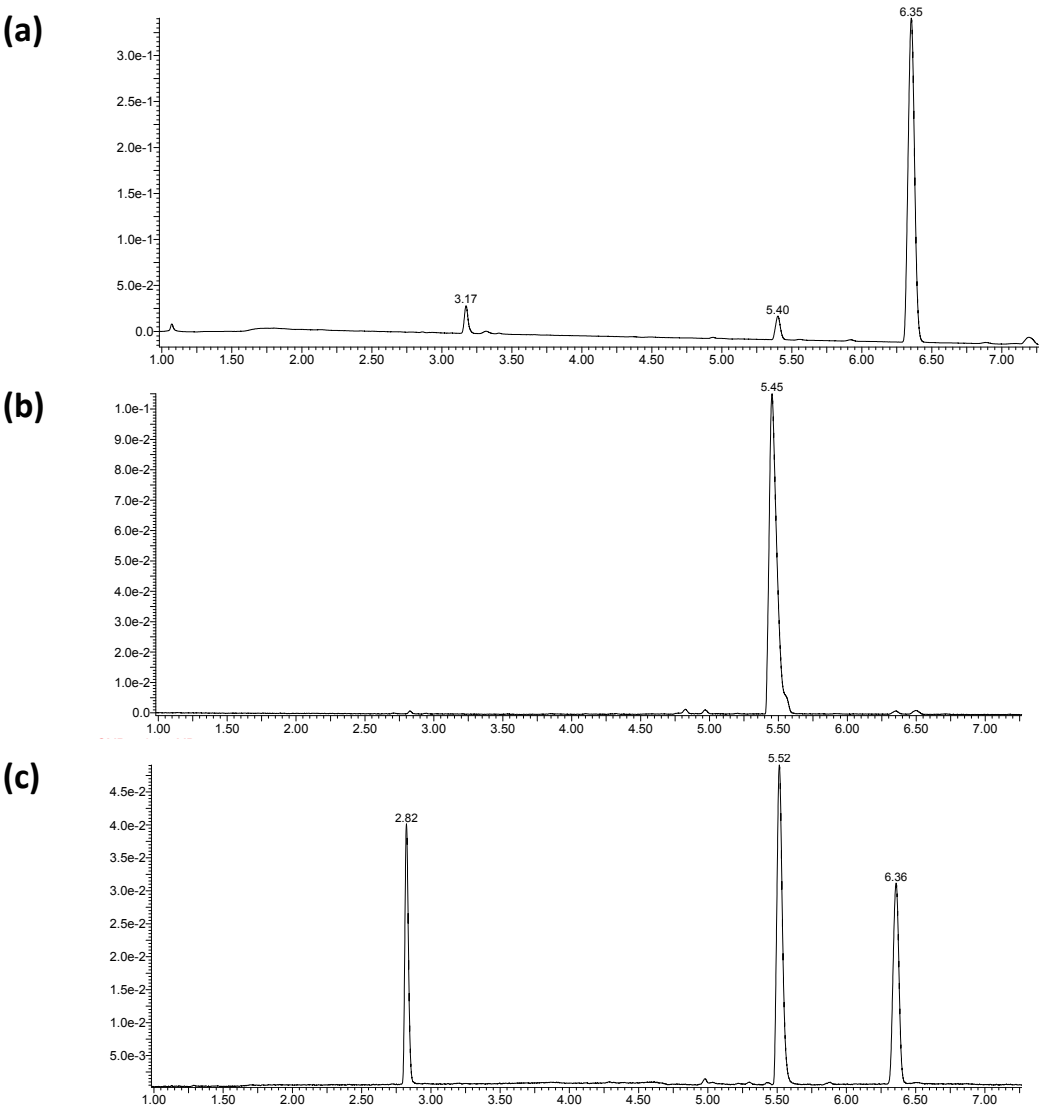

Fig. A13. (a) Chromatogram of P-Trz-Py in water. (b) Chromatogram of **3** in aqueous solution (95:5 H_2O:DMSO). (c) Chromatogram of **3** in aqueous solution (95:5 H_2O:DMSO) after 395-nmexcitation (15 $mW \cdot cm^{-2}$).

Retention time (RT) of P-Trz-Py is 6.4 min, RT of **3** is 5.5 min and RT of $[(\eta^6\text{-}p\text{-cym})Ru(bpy)(H_2O)]^{2+}$ is 2.8 min.

ESI-MS (m/z) of P-Trz-Py $[C_{14}H_{22}N_4O_3P]^+$ expected = 325.14 found = 325.16, ESI-MS (m/z) of **3** $[C_{34}H_{43}O_3N_6PRuPF_6]^+$ expected = 861.18 found = 861.45, ESI-MS (m/z) of $[(\eta^6\text{-}p\text{-cym})Ru(bpy)(H_2O)]^{2+}$ $[C_{20}H_{23}N_2ORu]^+$ expected = 409.09 found = 409.12.

(a)

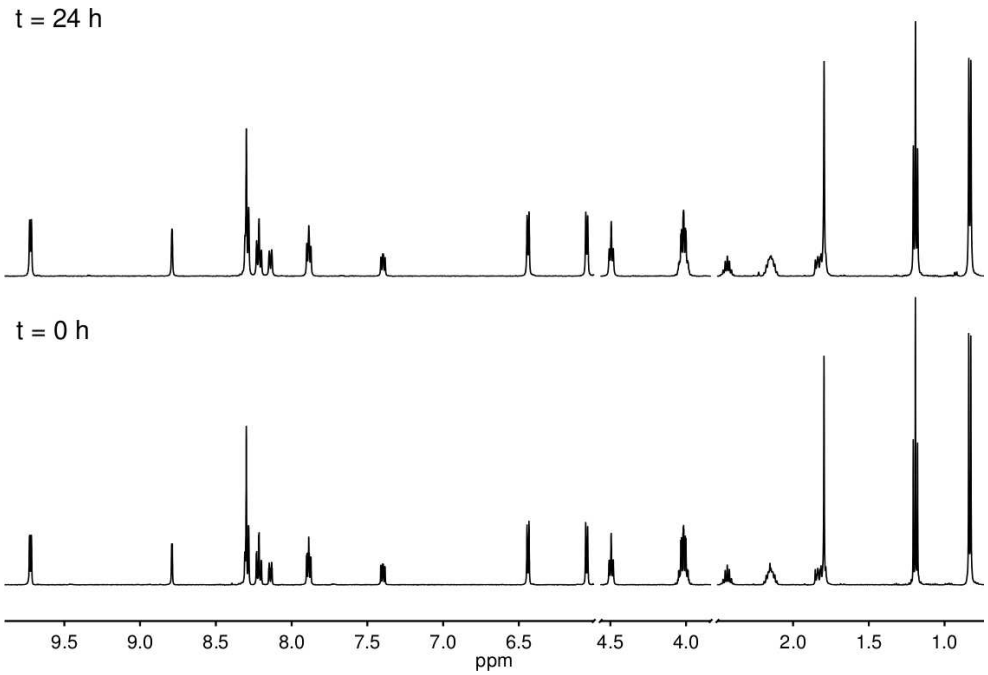

(b)

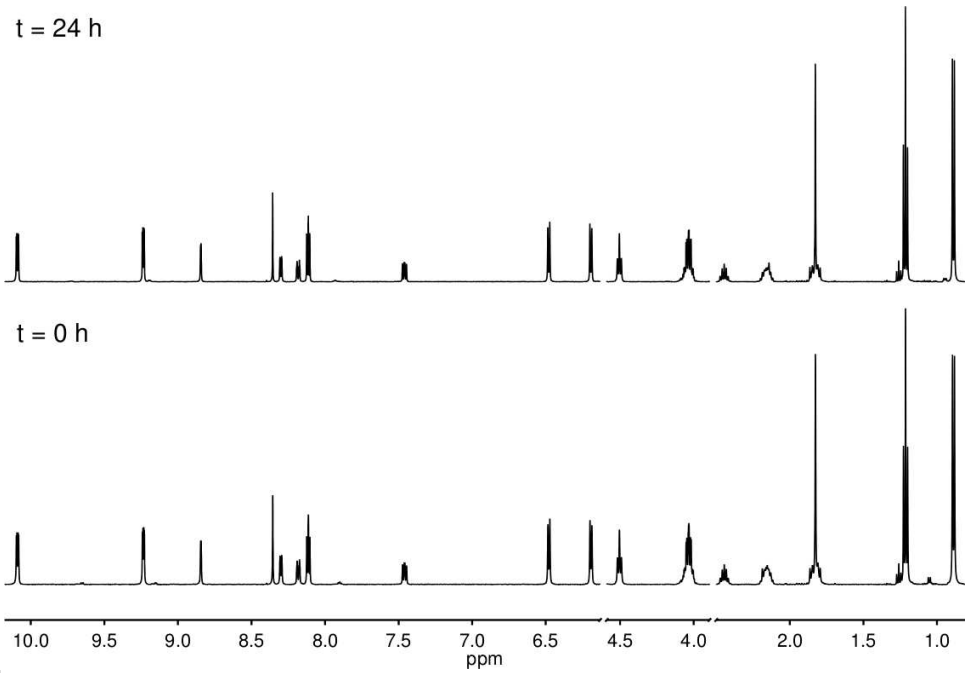

Fig. A14. ^{1}H NMR control spectra of aqueous solutions of **3** (a) and **4** (b) in the dark for 24 h.

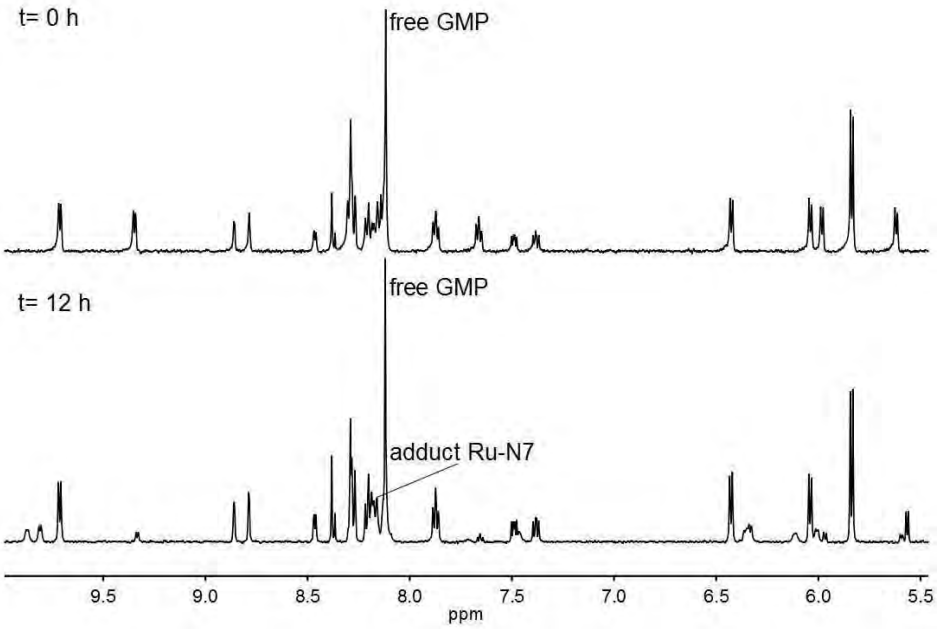

Fig. A15. ^{1}H NMR control spectra of **3** in aqueous solution (95:5 H_2O:DMSO) after irradiation at 395-nm in presence of GMP.

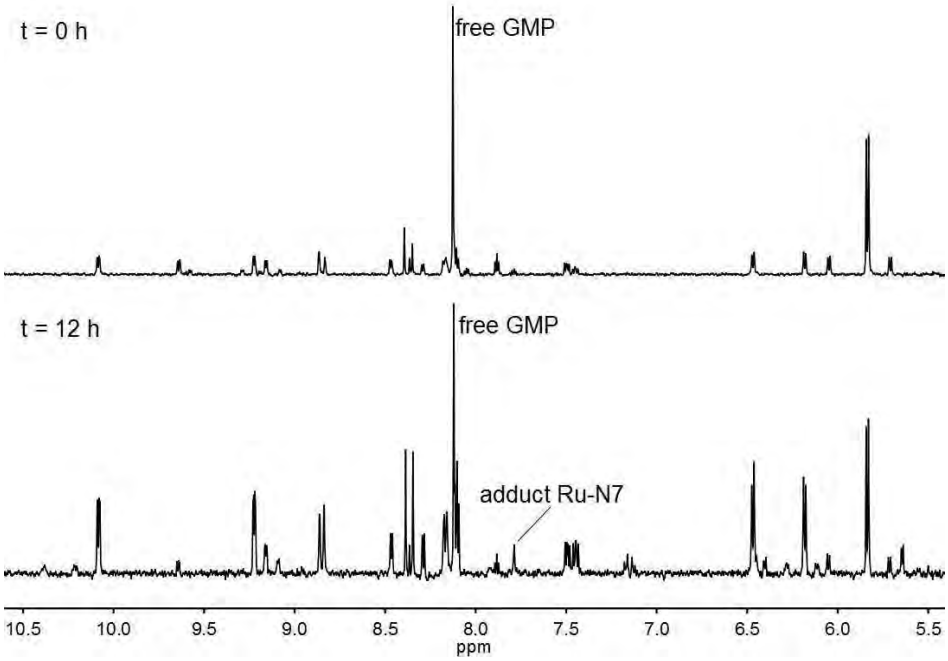

Fig. A16. ^{1}H NMR control spectra of **4** in aqueous solution (95:5 H_2O:DMSO) after irradiation at 395-nm in presence of GMP.

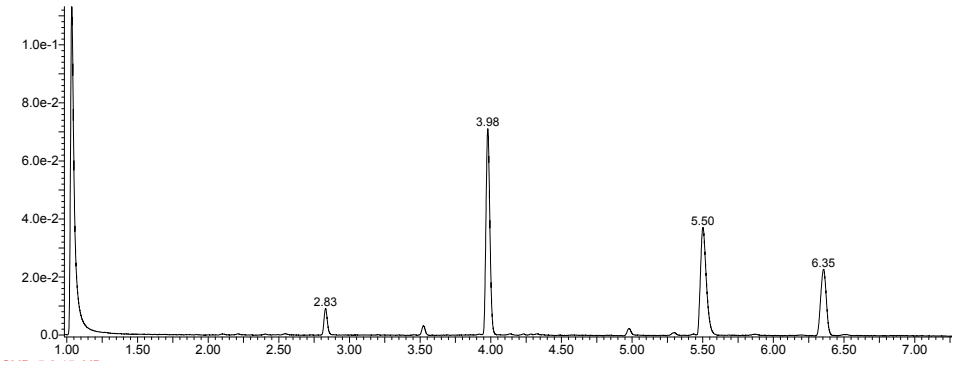

Fig. A17. Chromatogram of **3** in aqueous solution (95:5 H_2O:DMSO) after irradiation at 395-nm in presence of GMP.

Retention time (RT) of P-Trz-Py is 6.4 min, RT of **3** is 5.5 min, RT of adduct $[(\eta^6\text{-}p\text{-cym})Ru(bpy)(GMP)]^{2+}$ is 4.0 min, RT of $[(\eta^6\text{-}p\text{-cym})Ru(bpy)(H_2O)]^{2+}$ is 2.8 min and RT of GMP is 1.1 min.

ESI-MS (m/z) of P-Trz-Py $[C_{14}H_{22}N_4O_3P]^+$ expected = 325.14 found = 325.16, ESI-MS (m/z) of **3** $[C_{34}H_{43}O_3N_6PRuPF_6]^+$ expected = 861.18 found = 861.45, ESI-MS (m/z) of adduct $[(\eta^6\text{-}p\text{-cym})Ru(bpy)(GMP)]^{2+}$ $[C_{30}H_{35}O_8N_7PRu]^+$ expected = 754.13 found = 754.17, ESI-MS (m/z) of $[(\eta^6\text{-}p\text{-cym})Ru(bpy)(H_2O)]^{2+}$ $[C_{20}H_{23}N_2ORu]^+$expected = 409.09 found = 409.12, ESI-MS (m/z) of GMP $[C_{10}H_{15}N_5O_8P]^+$ expected = 364.07 found = 364.10.

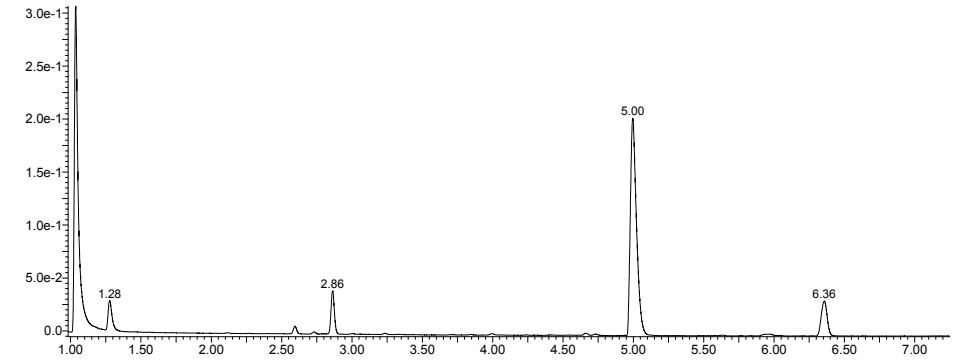

Fig. A18. Chromatogram of **4** in aqueous solution (95:5 H_2O:DMSO) after irradiation at 395-nm in presence of GMP.

Retention time (RT) of P-Trz-Py is 6.4 min, RT of **4** is 5.0 min, RT of adduct $[(\eta^6\text{-}p\text{-cym})Ru(bpm)(GMP)]^{2+}$is 2.9 min, RT of $[(\eta^6\text{-}p\text{-cym})Ru(bpm)(H_2O)]^{2+}$ is 1.3 min and RT of GMP is 1.1 min.

ESI-MS (m/z) of P-Trz-Py $[C_{14}H_{22}N_4O_3P]^+$ expected = 325.14 found = 325.16, ESI-MS (m/z) of **4** $[C_{32}H_{41}O_3N_8PRuPF_6]^+$ expected = 863.17 found = 863.42, ESI-MS (m/z) of adduct $[(\eta^6\text{-}p\text{-cym})Ru(bpm)(GMP)]^{2+}$ $[C_{28}H_{33}O_8N_9PRu]^+$ expected = 756.12 found = 756.16, ESI-MS (m/z) of $[(\eta^6\text{-}p\text{-cym})Ru(bpm)(H_2O)]^{2+}$ $[C_{18}H_{21}N_4ORu]^+$expected = 411.08 found = 411.11, ESI-MS (m/z) of GMP $[C_{10}H_{15}N_5O_8P]^+$ expected = 364.07 found = 364.10.

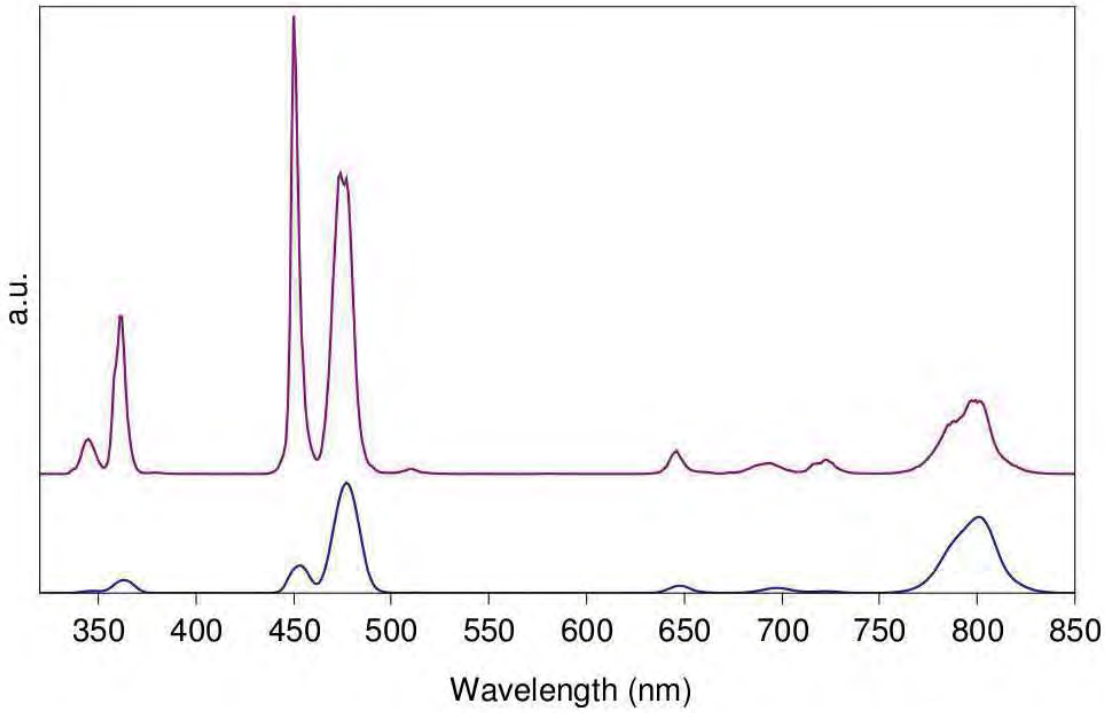

Fig. A19. Upconversion emission spectra normalized at 800 nm of (bottom) core and (top) core@shell UCNPs in THF solutions under 980-nm excitation (15 W·cm^{-2}).

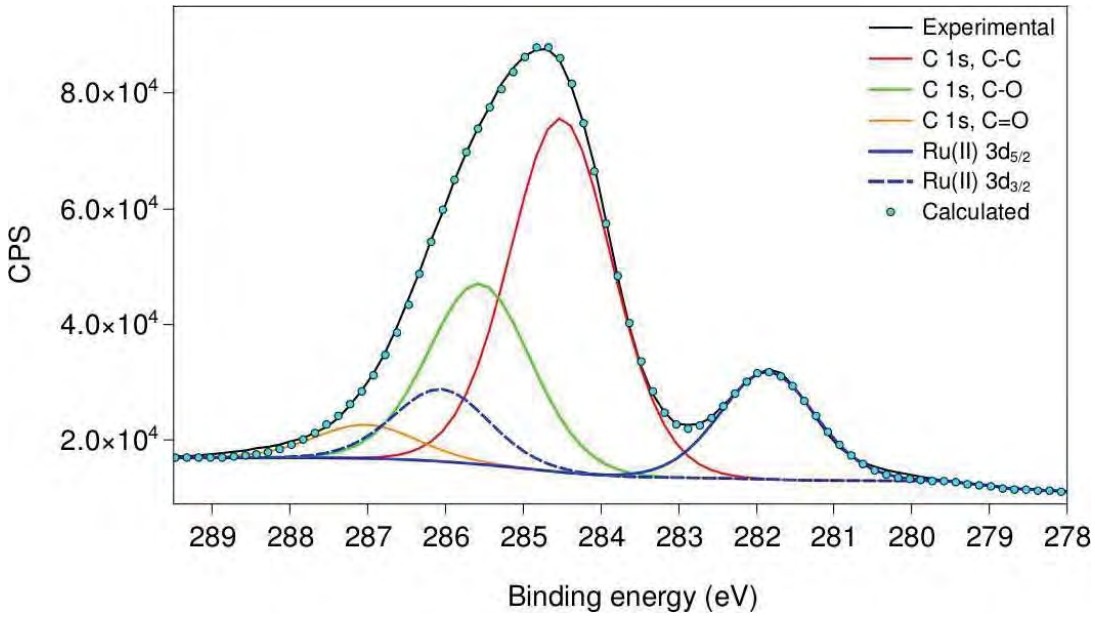

Fig. A20. XPS spectra of **4** (a) Ru ($3d_{5/2}$,$3d_{3/2}$)

.

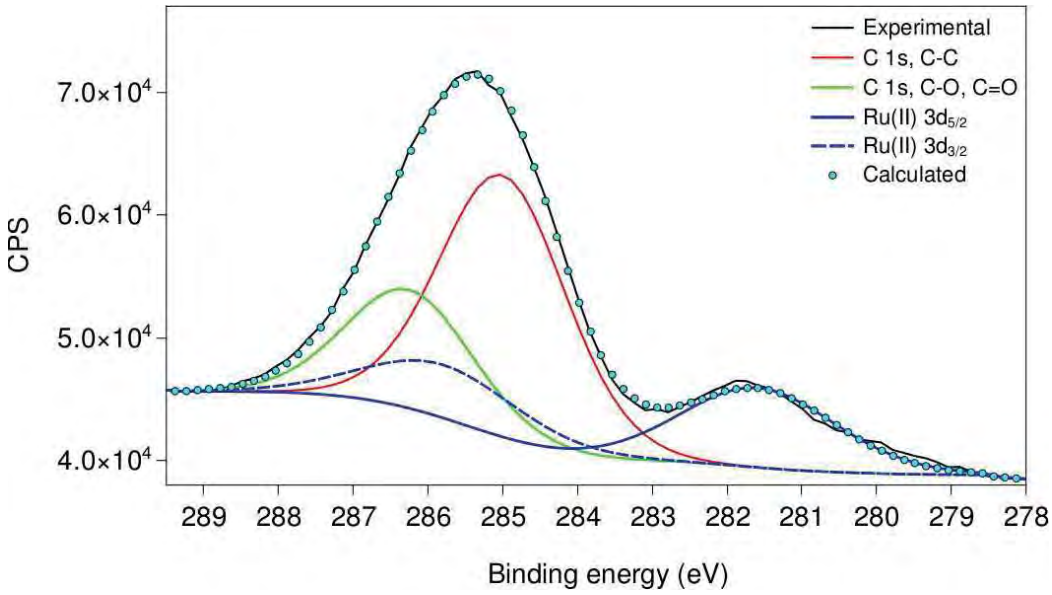

Fig. A21. XPS spectra of **UCNP@4** Ru ($3d_{5/2}$,$3d_{3/2}$).

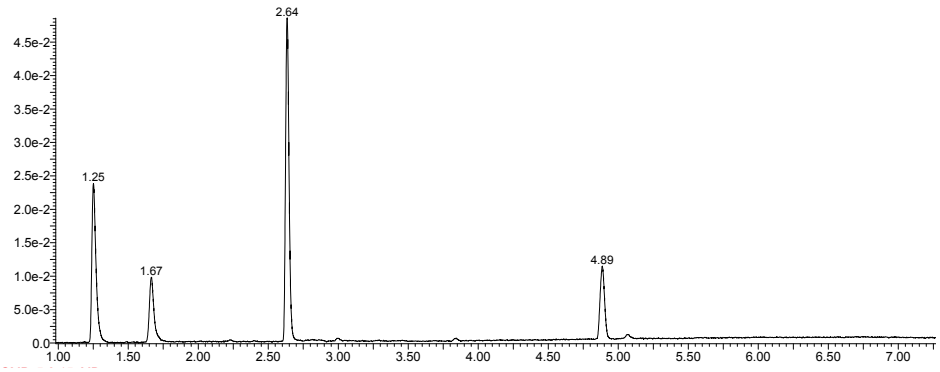

Fig. A22. Chromatogram of supernatant of **UCNP@4** in water after irradiation at 980 nm (8.1 $W \cdot cm^{-2}$). Before injection into UPLC-MS, the sample was sonicated and ultracentrifugated.

Retention time (RT) of hydrolyzed **4** is 4.9 min, RT of deprotected **4** is 2.6 min, RT of deprotected P-Trz-Py is 1.7 min and RT of $[(\eta^6\text{-}p\text{-cym})Ru(bpm)(H_2O)]^{2+}$ is 1.3 min.

ESI-MS (m/z) of deprotected **4** $[C_{28}H_{32}O_3N_8PRu]^+$ expected = 661.14 found = 661.19, ESI-MS (m/z) of deprotected P-Trz-Py $[C_{10}H_{14}N_4O_3P]^+$ expected = 269.08 found = 269.10, ESI-MS (m/z) of $[(\eta^6\text{-}p\text{-cym})Ru(bpm)(H_2O)]^{2+}$ $[C_{18}H_{21}N_4ORu]^+$expected = 411.08 found = 411.11.

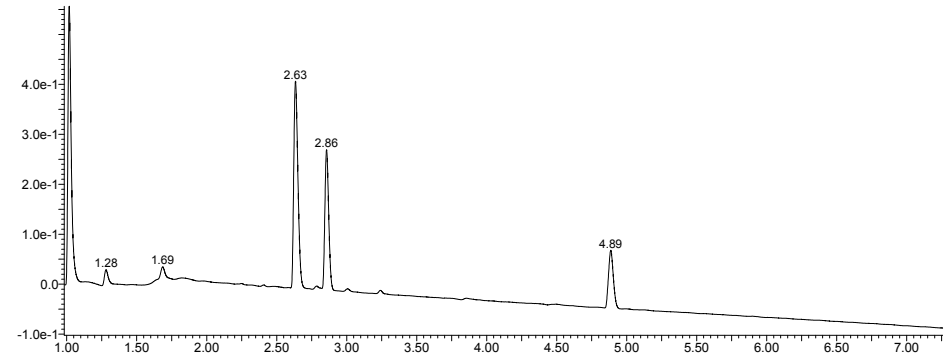

Fig. A23. Chromatogram of supernatant of **UCNP@4** in water after irradiation in presence of GMP. Before injection into UPLC-MS, the sample was sonicated and ultracentrifugated.

Retention time (RT) of hydrolyzed **4** is 4.9 min, RT of adduct $[(\eta^6\text{-}p\text{-cym})Ru(bpm)(GMP)]^{2+}$is 2.9 min, RT of deprotected **4** is 2.6 min, RT of deprotected P-Trz-Py is 1.7 min and RT of $[(\eta^6\text{-}p\text{-cym})Ru(bpm)(H_2O)]^{2+}$ is 1.3 min and RT of GMP is 1.1 min.

ESI-MS (m/z) of adduct $[(\eta^6\text{-}p\text{-cym})Ru(bpm)(GMP)]^{2+}$ $[C_{28}H_{33}O_8N_9PRu]^+$ expected = 756.12 found = 756.16, ESI-MS (m/z) of deprotected **4** $[C_{28}H_{32}O_3N_8PRu]^+$ expected = 661.14 found = 661.19, ESI-MS (m/z) of deprotected P-Trz-Py $[C_{10}H_{14}N_4O_3P]^+$ expected = 269.08 found = 269.10, ESI-MS (m/z) of $[(\eta^6\text{-}p\text{-cym})Ru(bpm)(H_2O)]^{2+}$ $[C_{18}H_{21}N_4ORu]^+$ expected = 411.08 found = 411.11, ESI-MS (m/z) of GMP $[C_{10}H_{15}N_5O_8P]^+$ expected = 364.07 found = 364.10.

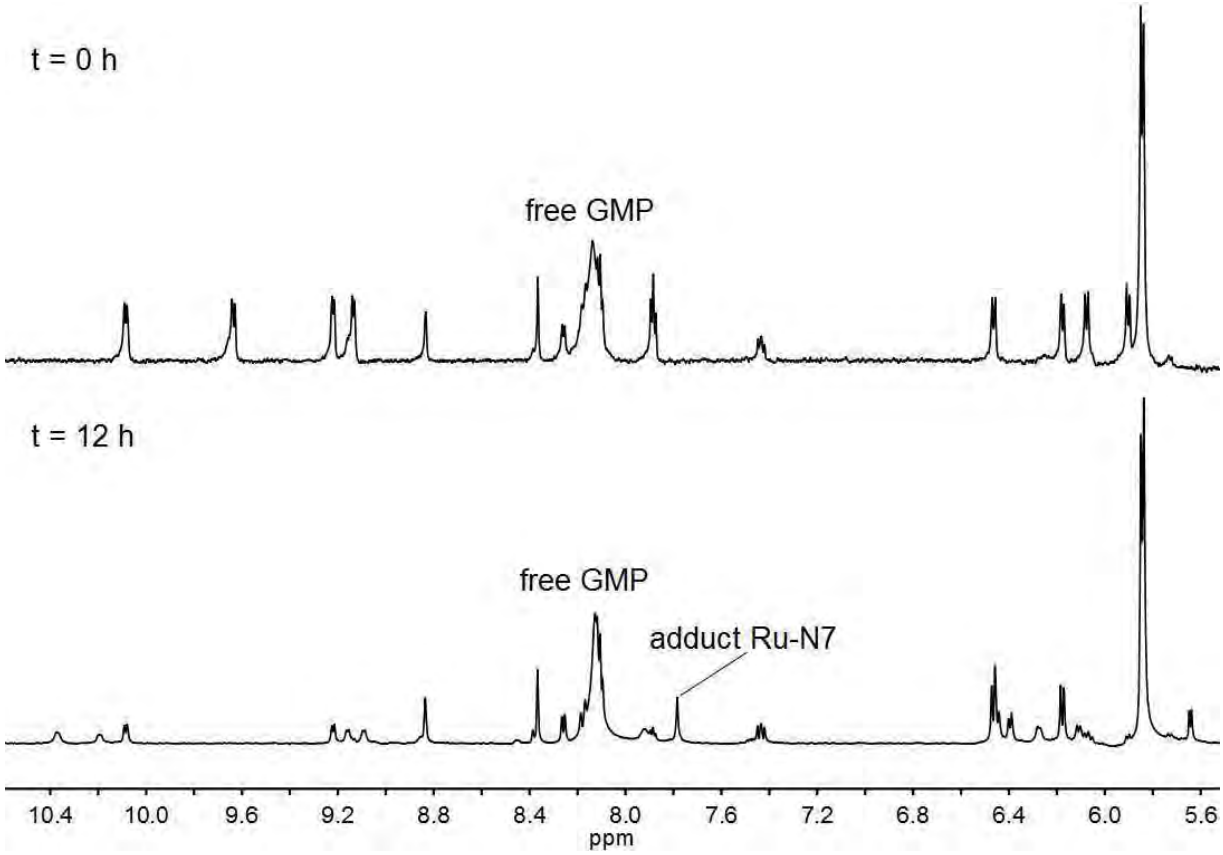

Fig. A24. ^{1}H NMR control spectra of **UCNP@4** in aqueous solution after irradiation at 980-nm in presence of GMP. The signal of the free GMP result broader than in previous NMR spectra due to the paramagnetic effect of UCNPs in solution.

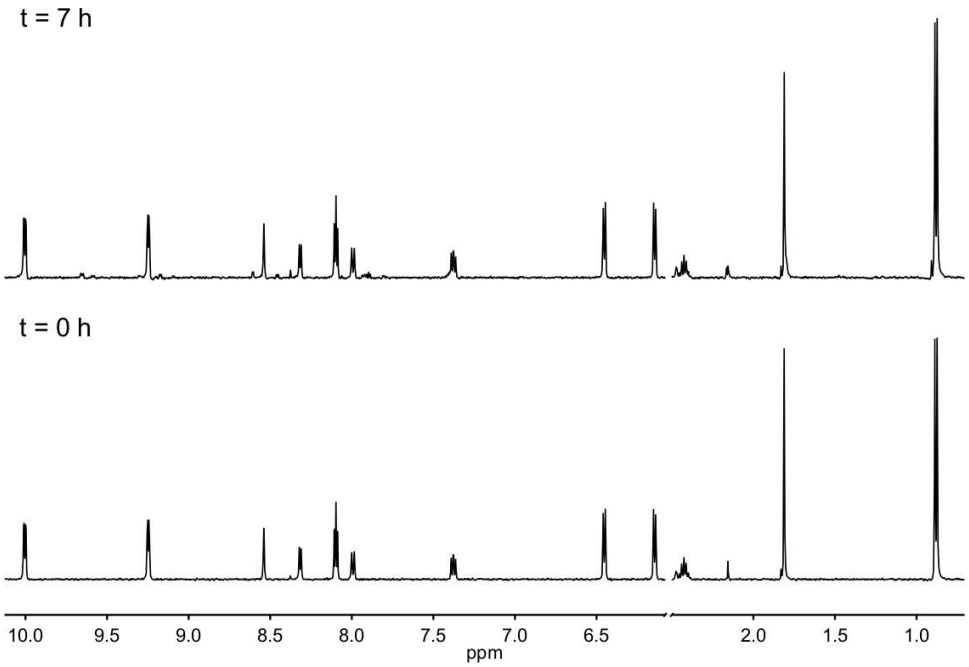

Fig. A25. ^{1}H NMR spectra of **2** in D_2O before (bottom) and after (top) 980 nm irradiation for 7 h (8.8 W cm^{-2}).

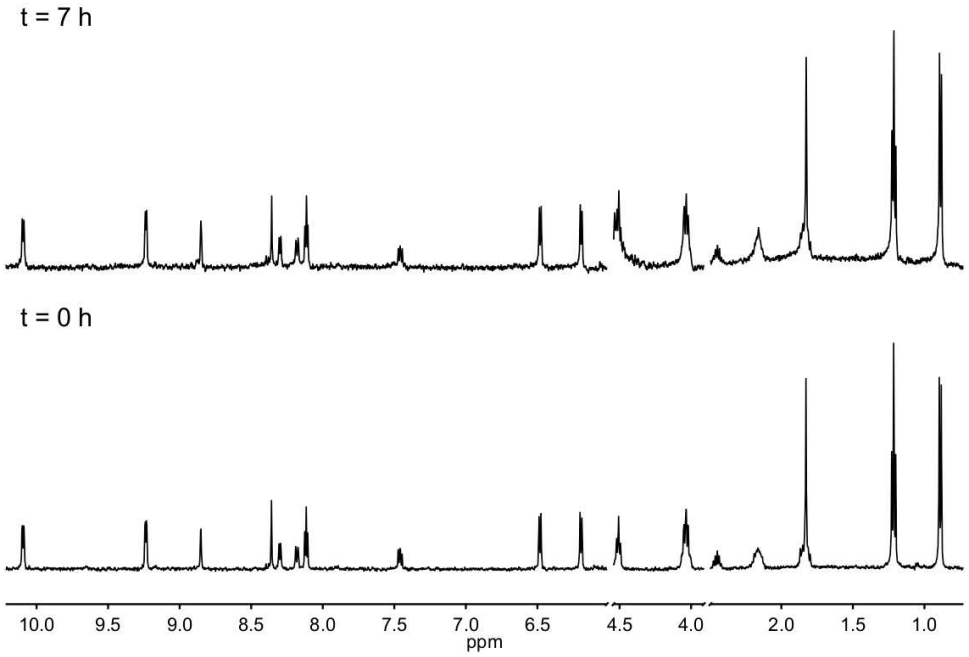

Fig. A26. ^{1}H NMR spectra of **4** in D_2O before (bottom) and after (top) 980 nm irradiation for 7 h (8.8 W cm^{-2}).